UNIVERSITY OF CALIFORNIA SAN DIEGO

Explosive Welding of Aluminum Plates: Experiments, Evaluation, and Modeling

A dissertation submitted in partial satisfaction of the requirements for the degree

Doctor of Philosophy

in

Structural Engineering

By

Kevin Arnett

Committee in charge:

Professor Gilbert A. Hegemier, Chair
Professor Lauren Stewart, Co-Chair
Professor Jiun-Shyan Chen
Professor Vitali Nesterenko
Professor Chia-Ming Uang

2019

The Dissertation of Kevin Arnett is approved, and it is acceptable in quality and form for publication on microfilm and electronically:

_____

_____

_____

_____
Co-chair

_____
Chair

University of California San Diego

2019

DEDICATION

To my family, Emily, Henry, and Catherine, you are the joy of my life. And to my parents and grandparents, who showed me the value of education and hard work, and set me on this wondrous course in life. I love you all.

TABLE OF CONTENTS

SIGNATURE PAGE iii

DEDICATION iv

TABLE OF CONTENTS v

LIST OF ABBREVIATIONS x

LIST OF SYMBOLS xii

LIST OF FIGURES xv

LIST OF TABLES xxii

ACKNOWLEDGEMENTS xxiv

VITA xxviii

ABSTRACT OF THE DISSERTATION xxix

1. INTRODUCTION 1

1.1 MOTIVATION 1

1.2 OBJECTIVES 2

1.3 OUTLINE 3

2. BACKGROUND 6

2.1 THE HISTORY OF EXPLOSIVE WELDING 6

2.1.1 Pre-World War II Building Blocks 6

2.1.2 Post World War II Backdrop of Explosive Metalworking 8

2.1.3 Discovery and Industrialization of Explosive Welding 11

2.1.4 Initial Investigations and a Rise of Awareness 13

2.1.5 Industrialization, Research, and International Collaboration 18

2.1.6 Notable Research and Events in a Matured Industry in the 1980s & 1990s . 24

2.1.7 Research, Collaboration, and Other Business: 2000s to the Present 27

2.2 FUNDAMENTALS AND MECHANICS OF EXPLOSIVE WELDING 30

2.2.1 Explosive Welding Fundamentals 31

2.2.2 Process Description and Welding Design Parameters 38

2.2.3 Bond Interfacial Wave Formation 56

2.2.4 Bond Metallurgical Characterization 85

3. EXPLOSIVE WELDING TESTS 94

3.1 WELD DESIGN 97

3.1.1 Welding Window Development 97

3.1.2 Welding State Selection 98

3.1.3 Final Choices for Test Configurations 108

3.2 DATA COLLECTION AND INSTRUMENTATION 112

3.2.1 Time of Arrival Pins 112

3.2.2 Flash Radiography (X-Ray) 116

3.3 TEST RESULTS 118

3.3.1 Full Specimen Tests 118

3.3.2 Subscale, X-Ray-Only Specimens 133

3.4 Analysis: Comparing Measured Results to Forecasted Values 140
3.4.1 Flyer Plate Velocities 140
3.4.2 Weld Velocities 146
3.4.3 Impact Angles 147
3.4.3 Summary 147
4. MECHANICAL VERIFICATION OF WELD QUALITY 148
4.1 Industry and Academic Standards for Evaluation 148
4.2 Selection of Tensile Shear Tests for Weld Evaluation 154
4.3 Specimen Preparation 156
4.3.1 Design of the Test Standard 156
4.3.2 Fabrication of Specimens 162
4.4 Effects of the As-Clad Condition on Testing 162
4.5 Testing 165
4.5.1 Testing Systems and Process 165
4.5.2 Macro-Level Results 170
4.5.3 Digital Image Correlation Results 173
4.6 Discussion of Test Results 193
5. METALLURGICAL OBSERVATIONS 195
5.1 Metal Composition and Chemistry 195
5.2 Macro & Meso Scale Observations of Welded Specimens 198

5.2.1 Macro Observations 198

5.2.2 Macro/Meso Scale Observations 199

5.3 MICROSCALE OBSERVATIONS VIA SCANNING ELECTRON MICROSCOPE 206

5.4 NANO-SCALE OBSERVATION OF THE 8° SAMPLE 212

6. NUMERICAL METHODS FOR EXPLOSIVE WELDING 217

6.1 THEORETICAL BACKGROUND FOR LS-DYNA MULTI-MATERIAL ALE 217

6.1.1 Kinematics, Material Derivatives, and Conservation Laws in ALE 218

6.1.2 Numerical Algorithms for Evaluation 221

6.1.3 The Multi-Material Formulation 222

6.1.4 Coupled Eulerian-Lagrangian 225

6.2 MODEL DETAILS AND PARAMETERS 226

6.2.1 Material Models and Properties 226

6.2.2 Geometry, Elements, and Boundary Conditions 229

6.2.3 Euler-Lagrange Coupling, Mesh Motion, and Hourglass Control 230

6.3 CHALLENGES IN MODELING 233

6.4 MODELING RESULTS 234

6.4.1 Macro-Level Comparisons to Experiments 234

6.4.2 Modeled Result for Welding Parameters 235

6.4.3 Prediction of Jetting 237

6.4.4 Wavelength and Amplitude Prediction 243

6.4.5 Other Modeling Connections to Theory 245

6.4.6 Temperature Predictions 251

6.5 Discussion of Explosive Welding Modeling 253

7. CONCLUSION 255

7.1 Summary And Conclusions 255

7.2 Recommendations for Future Work 258

REFERENCES 260

LIST OF ABBREVIATIONS

AIME	American Institute of Mining, Metallurgical, and Petroleum Engineers
ALE	Arbitrary Lagrangian Eulerian
AP&CC	American Potash and Chemical Company
ARA	Applied Research Associates
ARPA	Advanced Research Projects Agency
ASB	Adiabatic Shear Band
ASM	American Society of Metals
ASTM	American Society for Testing and Materials
CEER	Center for Extreme Events Research
CNC	Computer Numerical Control
DARPA	Defense Advanced Research Projects Agency
DIC	Digital Image Correlation
DMC	Dynamic Materials Corporation
DOD	Department of Defense
DRI	Denver Research Institute
EBSD	Electron Backscatter Diffraction
EDX	Electron Dispersive Spectroscopy
EFI	Explosive Fabricators Incorporated
FEM	Finite Element Method
HEL	Hugoniot Elastic Limit
ISZ	Intensive Shear Zone
ICBM	Intercontinental Ballistic Missile
JC	Johnson-Cook
JWL	Jones-Wilkins-Lee
LSTC	Livermore Software Technology Corporation
LWG	Line Wave Generator
M/U	Make-up
MDF	Medium Density Fiberboard
MIL	Military

MM-ALE	Multi-Material Arbitrary Lagrangian Eulerian
MPP	Massively Parallel Processing
NASA	National Aeronautics and Space Administration
NMAP	Nonlinear Meshfree Analysis Program
PETN	Pentaerythritol tetranitrate
PTA	Terephthalic Acid
QBI	Quintessential Bending Incompressible
RKPM	Reproducing Kernel Particle Method
SEM	Scanning Electron Microscope
SUPG	Streamline Upwinding Petrov-Galerkin
TEM	Transmission Electron Microscope
TOA	Time of Arrival
UMIST	University of Manchester Institute of Science and Technology
USAF	United States Air Force
VOD	Velocity of Detonation

LIST OF SYMBOLS

Upper Case Latin Characters

C1, C2	Tensile shear test control specimens
C2	1/12” Explosive Thickness used on 0.5° and 1.5° welds (2.1167 mm)
C6	0.25” Explosive Thickness used on 2.5° & 8° welds (6.35 mm)
$\frac{\boldsymbol{D}}{\boldsymbol{Dt}}[\cdot]$	Material time derivative of a generic scalar quantity
D_{CJ}	LS-DYNA detonation velocity of explosive notation
E	Energy
$\sqrt{2E}$	Gurney Energy
F_u	Ultimate tensile strength
H_v	Vicker’s Hardness
HEL	Hugoniot Elastic Limit
J_2	Second invariant of the deviatoric stress tensor
$J_2^{\varepsilon\prime}$	Second invariant of the deviatoric strain tensor
L	Lap distance for lap shear/tensile shear test specimen
P_{CJ}	Chapman-Jouget Pressure of detonating explosive
R	Ratio of mass of explosive per mass of flyer plate
R_w	Welding Reynold’s number for flow classification
S	Stagnation Point
T^*	Homologous temperature in JC constitutive equation, °K
U, V	Velocity
V_c	Alternate Notation Collision Point/Weld Velocity
V_d	Velocity of Detonation
V_F	Fluid Velocity. Plate (typically flyer) velocity in steady state coordinate system
V_j	Jet Velocity
V_p	Flyer Plate Velocity
V_T	Transition velocity from smooth to wavy bond interface
V_w	Collision Point/Weld Velocity
$\boldsymbol{X}$	Reference coordinates of initial material points in Lagrangian system

Lower case Latin Characters

a	Peak amplitude
$\boldsymbol{c}$	Convective velocity, $\boldsymbol{c} \equiv \boldsymbol{v} - \hat{\boldsymbol{v}}$, of material in ALE mesh.
c	Acoustic speed/dilatational wave speed/intercept of v_p/v_s curve/generic wave speed
l_0	Length to arrival of rarefaction wave
m	Mass
m_j	Mass of the Jet
m_s	Mass of the Slug/Salient Jet (welded flyer & parent plate)
p	Pressure
p_S	Stagnation Pressure
t	Thickness or time
t_0	Time to arrival of rarefaction wave
t_f	Thickness of the Flyer Plate
t_j	Thickness of the Jet
$\boldsymbol{v}$	Material velocity gradient
$\hat{\boldsymbol{v}}$	ALE reference mesh velocity
v_p	Particle velocity
v_s	Shock Velocity
$\boldsymbol{x}$	Current spatial coordinate system

Greek & Other Characters

α	Flyer Plate Inclination
β	Impact Angle
γ_0	Gruneisen Gamma
γ, θ, α	Alternate Impact Angle Notation
Δ	Characteristic length for velocity profile
ε	Strain
ε_1, ε_2	Principle Strains
ε_{vm}	Von Mises strain
η	Material volume fraction

λ	Wavelength
ρ	Density
σ	Stress
σ'	Deviatoric stress
$\bar{\sigma}$	Average stress in mixed material element
σ_U	Ultimate tensile strength
σ_Y	Initial yield strength
$\boldsymbol{\phi}(\boldsymbol{X}, t)$	Mapping from material domain to spatial domain
$\hat{\boldsymbol{\phi}}(\boldsymbol{\chi}, t)$	Mapping from the ALE reference domain to the spatial domain
$\boldsymbol{\chi}$	Reference coordinates in the ALE reference domain
$\boldsymbol{\psi}(\boldsymbol{X}, t)$	Mapping from material domain to ALE reference domain
ω	Nonlinear coefficient in JWL Equation of State
Ω	Spatial domain of body in current coordinates
$\hat{\Omega}$	ALE reference domain of body
Ω_0	Material domain of body in initial reference coordinates
$\boldsymbol{\nabla}$	Spatial gradient operator

LIST OF FIGURES

Figure 2-1: Illustration in Charles Munroe's 1888 article 7

Figure 2-2: Selected figures from Birkhoff's 1948 work 8

Figure 2-3: Trona Ammonium Perchlorate advertisement 11

Figure 2-4: The first published documentation of explosive welding by Leroy Carl 12

Figure 2-5: Images from the 1959 *Steel* article on explosive forming 14

Figure 2-6: Figure showing the AP&CC explosive welding process 15

Figure 2-7: Diagram of Philipchuk's patent 16

Figure 2-8: Cowan, Douglass, and Holtzman's imagery 17

Figure 2-9: The New York Times business and financial section 18

Figure 2-10: Early DuPont cladding products. 19

Figure 2-11: Early pictures of the Pennsylvania DuPont Detaclad 20

Figure 2-12: Representations of the forces in atomic bonding 32

Figure 2-13: Depiction of ideal versus real metallic bonding 33

Figure 2-14: A taxonomy of welding 35

Figure 2-15: Smooth and wavy bonding interfaces 37

Figure 2-16: Primary flat plate geometric welding configurations. 38

Figure 2-17: Simplified and commonly assumed kinematics 39

Figure 2-18: The geometry of motion 41

Figure 2-19: An idealized model 43

Figure 2-20: More realistic depiction of flow 45

Figure 2-21: Welding processes in pressure, time, and temperture coordinates 46

Figure 2-22: Alternative welding window 47

Figure 2-23: Introductory weld windows 48
Figure 2-24: Explosive welding window as shown in Liu 51
Figure 2-25: Indentation mechanism sequence 58
Figure 2-26: Hunt's Kelvin-Helmholtz explanation 60
Figure 2-27: Scenario of the acoustic derivation. [101] 61
Figure 2-28: Progress of a dilatational wave 62
Figure 2-29: Comparison of turbulent vortices 63
Figure 2-30: Figure from von Karman for stability ratio 64
Figure 2-31: Velocity profiles post collision 65
Figure 2-32: Physical scenario for Zabusky and Deem 67
Figure 2-33: Blazynski's stress wave mechanism 69
Figure 2-34: Theoretical boundaries of wave formation 71
Figure 2-35: Welding window from Szecket's empirical data 74
Figure 2-36: Early finite difference simulation by Oberg 83
Figure 2-37: Hump configurations 85
Figure 2-38: Metallurgy of impact welding bonds at different scales from [149] 86
Figure 2-39: Welding showing grains far from bond, with details 87
Figure 2-40: Intense shear zone 89
Figure 2-41: Example phase composition of steel-steel welding 90
Figure 2-42: Grain structure of good bond 93
Figure 3-1: Example test specimen 95
Figure 3-2: Test specimen concept and implementation 96
Figure 3-3: Modeled Flyer Plate Velocity-Displacement Histories 100

Figure 3-4: Plate and Detonation Velocity Test 101
Figure 3-5: Plate Velocity Pin Arrays 102
Figure 3-6: Flyer plate oscilloscope data 105
Figure 3-7: Experimental weldability window 106
Figure 3-8: Welding anvil 109
Figure 3-9: Line wave generator 110
Figure 3-10: Line wave generator oscilloscope data 111
Figure 3-11: Oscilloscopes used 112
Figure 3-12: Sample pin schematics 114
Figure 3-13: TOA pin circuit diagram 115
Figure 3-14: Flash X-Ray system 116
Figure 3-15: 0.5° test that failed to collect any data. 119
Figure 3-16: Uncorrected 1.5° time of arrival data 120
Figure 3-17: Linear correction applied to 1.5° 121
Figure 3-18: Corrected 1.5° time of arrival data 122
Figure 3-19: 1.5° test 123
Figure 3-20: 2.5° Test Referenced TOA Pin Data 125
Figure 3-21: 2.5° Test Images. (In (b) weld direction is right to left) 126
Figure 3-22: 8° Test Reference TOA Pin Data. 128
Figure 3-23: 8° Test Images 129
Figure 3-24: 0.5° Non-annealed Referenced TOA Pin Data. 131
Figure 3-25: 0.5°, non-annealed, make-up test 132
Figure 3-26: 1.5° X-Ray only test. 134

Figure 3-27: 1.5° X-Ray image 135
Figure 3-28: Full 1.5° X-Ray cassette image interpreted 135
Figure 3-29: 0.5° X-Ray image 136
Figure 3-30: Annotated 0.5° X-Ray test 136
Figure 3-31: 2.5° subscale test X-Ray images. 138
Figure 3-32: Annotated 2.5° test 139
Figure 3-33: 8° subscale test X-Ray images. 140
Figure 3-34: Annotated 8° test 140
Figure 3-35: Cut plane referenced in subsequent figure 142
Figure 3-36: NMAP Cross-section modeling results. 143
Figure 3-37: Edge effect on TOA pin measurements 143
Figure 3-38: Longitudinal correction 145
Figure 4-1: Standard cladding shear test from ASTM A263-5 149
Figure 4-2: Bending ductility test 150
Figure 4-3: MIL Standard J-24445A ram tensile test 152
Figure 4-4: Alternative mechanical bond tests in research 153
Figure 4-5: Tensile shear test specimen 157
Figure 4-6: Anticipated deformed shape of the specimen 158
Figure 4-7: Modeling result for proposed configuration 160
Figure 4-8: Fabrication of tensile shear specimens 161
Figure 4-9: Residual deformations in tensile shear samples 163
Figure 4-10: Modeling of weld samples 164
Figure 4-11: Test systems used during mechanical evaluation 166

Figure 4-12: Image pixel, subset, and motion basics 169
Figure 4-13: Maximum forces in specimens. (2.5° scenario had no testable specimens) 171
Figure 4-14: 0.5° load versus time plot 172
Figure 4-15: 1.5° load versus time plot 173
Figure 4-16: VIC-2D region of interest 174
Figure 4-17: Subset and step selection 174
Figure 4-18: Control 2 specimen at maximum load 178
Figure 4-19: Control specimen 2 at last significant capacity. 179
Figure 4-20: Control 2 von Mises strain profile at maximum loading 180
Figure 4-21: Control 2 showing von Mises strains after max load 181
Figure 4-22: 0.5° specimen von Mises strains at max load 182
Figure 4-23: 0.5° von Mises strain at last significant loading 183
Figure 4-24: 0.5° weld surface von Mises strains at maximum loading 184
Figure 4-25: 0.5° von Mises strains at the weld surface 185
Figure 4-26: 1.5° von Mises strain before loss of capacity 186
Figure 4-27: 1.5° test von Mises strains after capacity loss 187
Figure 4-28: 1.5° test weld surface strains before and after failing 188
Figure 4-29: 8° test showing von Mises strains at maximum loading 189
Figure 4-30: 8° test at point of last significant resistance 190
Figure 4-31: 8° test von Mises strains along the weld surface, at max loading 191
Figure 4-32: 8° test at last significant resistance 192
Figure 5-1: Al 6xxx Solidus and Solvus ternary diagrams 195
Figure 5-2: Liquidus ternary diagram 196

Figure 5-3: Quasi-binary phase diagram for aluminum and magnesium silicide 196
Figure 5-4: Specimen sample locations 200
Figure 5-5: Sample preparation 201
Figure 5-6: Optical image of the 0.5° bond 202
Figure 5-7: Optical image of 1.5° weld 202
Figure 5-8: Optical image of 2.5° specimen 203
Figure 5-9: Optical image of 8° specimen 204
Figure 5-10: Full length of the 2.5° weld 204
Figure 5-11: 0.5° specimen SEM image 207
Figure 5-12: 1.5° specimen melt and void 208
Figure 5-13: 1.5° specimen microcracks and melt layer 208
Figure 5-14: 2.5° specimen in the vicinity of the weld 209
Figure 5-15: 2.5° specimen melt pocket 209
Figure 5-16: 8° specimen near good bond by a vortex 210
Figure 5-17: 8° images nearer the top of a wave crest 211
Figure 5-18: 8° Focused Ion Beam preparation 213
Figure 5-19: TEM sample extraction preparation 214
Figure 5-20: Mounted TEM sample 214
Figure 5-21: Stitched TEM image of the bond zone 215
Figure 5-22: Band of fine grains in the bonding zone. 216
Figure 6-1: Mapping between ALE domains 218
Figure 6-2: Multiple materials in an ALE/Eulerian element 224
Figure 6-3: Example weld 2D modeling geometry 229

Figure 6-4: Prediction of edge failure based on modeling 234
Figure 6-5: Jet thickness from modeling 238
Figure 6-6: Modeling of 0.5° 239
Figure 6-7: Modeling of the 1.5° 240
Figure 6-8: Modeling of 2.5° case 241
Figure 6-9: Modeling result for the 8° case 242
Figure 6-10: 2.5° wave and amplitude measurement positions 243
Figure 6-11: 8° wave and amplitude measurement positions 243
Figure 6-12: Velocity wakes behind the collision point 246
Figure 6-13: Support for the “hump” 247
Figure 6-14: Shear shock front 248
Figure 6-15: Acoustic wave theory assessment 249
Figure 6-16: Flyer acoustic wave front 250
Figure 6-17: 0.5° temperature distribution 251
Figure 6-18: 1.5° temperature distribution 252
Figure 6-19: 2.5° temperature distribution 252
Figure 6-20: 8° temperature distribution at t = 11 μs 253

LIST OF TABLES

Table 2-1: Reference Explosive Welding Texts 30

Table 2-2: Pairs of dissimilar metals 37

Table 3-1: Experimental Conditions 96

Table 3-2: Jones-Wilkins Lee Explosive Burn parameters 99

Table 3-3: General Material and Johnson-Cook Parameters for Aluminum 6061-O 99

Table 3-4: Aluminum equation of state parameters 99

Table 3-5: Experimental Velocity of Detonation 102

Table 3-6: Plate velocity data 104

Table 3-7: Regions of good welding 108

Table 3-8: Additionally required tests due to equipment malfunction. 118

Table 3-9: 1.5° Raw Corrected TOA pin data. 124

Table 3-10: 2.5° Raw TOA Pin Data 127

Table 3-11: 8° Raw TOA Pin Data 130

Table 3-12: Make-up 0.5° Raw TOA Pin Data 133

Table 3-13: Flyer plate velocities based on longitudinal pin method (mm/μs) 145

Table 3-14: Plate velocity estimates using geometric analysis 146

Table 3-15: Weld velocities from different sources 147

Table 3-16: Measured impact angles 147

Table 4-1: Tensile Shear Test material model parameters 161

Table 4-2: Average Stress Results 171

Table 5-1: Al 6061 elemental composition.[210] 195

Table 5-2: Composition of Keller's reagent. [213] 201

Table 5-3: Comparison of measured wavelength and amplitude..... 206

Table 6-1: Weld parameter modeling results..... 236

Table 6-2: Modeled jet thickness..... 237

ACKNOWLEDGEMENTS

I have been the beneficiary of the work of many, many other people. Starting with my parents and grandparents who helped set me on a good course in life, through a long host of others. While I have done a share, I would not be where I am today without others.

I am very grateful for my advisors. To Gil Hegemier, I'd like to say how immensely grateful I am for the time you've invested in me. With all you've accomplished at this point in your career, you clearly had no reason you needed another PhD student, and when you brought me in, you didn't have to dedicate the time that you have to my education. The project I've worked on has broadened my knowledge in a lot of ways that have been a true pleasure, and similarly enjoyed working through plasticity under your direction. I've enjoyed all the conversations we've been able to have, whether about science, politics, vaccinations, or the joy of finding parking at UCSD. I'm very grateful.

To Lauren Stewart, thank you for your time and patience with me. The blast course you worked me into at the start of my studies was exactly the type of knowledge I hoped to gain here. You helped me ensure I was set up with a good slate of courses, and bore with me as I got my feet underneath me and worked through a rather painful course at the start that got to me more than it should have. And thank you for ensuring at the end that I got the last bit of resources I needed to complete things. I understand that others simply don't stop asking for your time, and I appreciate all you've willingly given to me.

To Professor J. S. Chen, thank you for all the time you invested in me and in this project. I first heard of "meshfree methods" in around 2011 on a trip to ERDC, and it was immediately a very highly intriguing white whale for me to chase. After meeting your former student, again at ERDC, while I was learning about the best places I could study the things I was interested in, I

feel very fortunate to have been able to take three of your computational courses and progress as far as I have in this area. You shared the resources of your group, most notably your computing resources, very generously, and by granting me space in 412, welcomed me into a group of peers I did not otherwise have at UCSD.

Professor Vitali Nesterenko, I cannot thank you enough for feedback, guidance, and reviews you gave to me concerning my progress in this study. As someone who ran labs at Novosibirsk that specialized in this field, and who studied under Andrei Deribas, I am exceptionally lucky to be able to have you on my committee for this topic. But on top of your credentials, your generosity and understanding have truly been a gift.

Thank you to Professor Uang as well for serving on my committee. As a former, and potentially future steel instructor, I feel very lucky to have had the opportunity to meet you and benefit from your advice.

I would like to thank Professor Hyonny Kim for your advice and generosity as I worked through some resource shortages. Your willingness to allow me the use of some of your equipment and to permit your students help me through my testing process has been critical factor in what I've been able to achieve. Your connections to other members of the staff ensured I had the mechanical tests I needed, and I'm not sure how I would have generated my chapter 5 without your help.

In this regard, further thanks is due to Steve Porter, for several hours dedicated to helping me fabricate test specimens, and to Eric Kim and Kostas Anagnostopoulos who spent several more helping me to learn the details of and execute my tests.

I'd like to thank Professor Marc Meyers. Although I failed to do a good job finding an opportunity to introduce myself until very late in my time here, my experience has nonetheless

been tremendously enriched. As with Professor Nesterenko, your background in the area of my study is nothing short of superlative. I am very grateful, after making my introduction into this area by reading your articles and your text, that I have been able to spend time learning from you and that you were willing to help me further the depth of my work by graciously providing the means to conduct and include a small TEM study as a part of my effort. Also, thanks to Zezhou Li for many hours of work dedicated to helping me get the TEM sample in a busy time of his own work.

I would like to thank Professor Veronica Eliasson for the time and resources you've provided to me. Your advice on contacts within MAE were highly valued, and your generosity with the use of image correlation licenses and permitting your students to help are gratefully acknowledged. To Will and Rod, thank you for the time you devoted to helping me looking into microscopy options and in the conduct of digital image correlation, which was a significant part of this work.

I'd like to thank Scott Hardesty, as well as Courtney, Dan, and Peter at Applied Research Associates in Denver. It was a very fun experience to get back out on a demo range, and this time to experience a civilian, research-oriented process. The weld tests would not have happened without you.

Thank you to Michael May and Kalin Shanklin at Decisive Testing, Inc, as well as Emily Mathison at General Atomics. I appreciate your patience and professionalism in helping me obtain optical and SEM microscopic images of the samples.

I would like to thank the Asahi-Kasei Corporation whose funding supported the explosive welding experiments in this work.

Thank you to Certified Metalcraft of El Cajon for donating the annealing heat treatment to my control tensile shear specimens.

I would also like to thank Chris Conley, Paul Mlakar, Brock Barry, Craig Quadrato, COL Fred Meyer, and Aaron Freidenberg. Your mentorship and friendship during my time at USMA and/or remotely from USMA to UCSD have also enriched my experience here.

To Jon Baek, your thanks sits at the boundary between those who were instrumental in my success, to the degree that I've achieved it, in this study on explosive welding, and those peers who vastly enriched my experience outside of work. Paired to jointly work on this at the start of the study by our advisors, you are both one of my true friends from my time here and a person to whom I owe a great deal of thanks for your assistance and work associated with this project. It has been a pleasure to get to know you and Youngeun.

And finally, I'd like to thank some of my other friends here at UCSD. Marco and Jake, you were both tremendous TA's and patient system administrators with me, and I'm grateful for your friendship. Jake it was a great part of my time here to jointly chase the two Henry's around the path at South Mesa, and to get to know your family. To Mat Reynolds, it has been a true pleasure getting to know you and work through some coursework alongside you. I wish you and Erin luck in the future. Lastly, to my office mate Manuel, thank you for sharing tips when I was new and for pushing to try extra things, as well as for all the coursework we did, each facing our respective wall until we had a point to compare.

I sincerely hope that I am able to maintain some degree of contact with everyone mentioned above, but it has not seemed to work that for me thus far in life. I will still try, but if life gets in the way, I will still always be grateful. For each person, my short few sentences don't seem to have done it justice. I hope all can see my thanks are in earnest.

VITA

2001	Bachelor of Science, United States Military Academy
2001-2009	United States Army
2010-2011	Master of Science, University of California Berkeley
2011-2014	Instructor and Assistant Professor, United States Military Academy
2014-2016	United States Army
2019	Doctor of Philosophy, University of California San Diego

PUBLICATIONS

Quadrato, C.E. and Arnett, K. (2014), "Determining Unbraced Lengths in Continuous Girders Subjected to Warping Restraint" *Proceedings of the Annual Stability Conference*, Structural Stability Research Council *(SSRC)*, Toronto, Canada, 25-28 March 2014.

Barry, B., Meyer, K., Arnett, K., and Spittka, B. (2013), "Competition-Based Learning Activities within Civil Engineering Education: A Critical Review of Current Options." American Society for Engineering Education 2013 National Conference, Atlanta, GA.

Quadrato, C.E. and Arnett, K. (2013), "Calculating the Impact of Partial Warp Restraint on Steel Girder Elastic Buckling Strength" *Proceedings of the Annual Stability Conference*, Structural Stability Research Council *(SSRC)*, Saint Louis, MO, 16-20 April 2013.

Arnett, K. and Quadrato, C. 2012. "Building Information Modeling: Design Instruction by Integration into an Undergraduate Curriculum." American Society for Engineering Education 2012 National Conference, San Antonio, TX.

ABSTRACT OF THE DISSERTATION

Explosive Welding of Aluminum Plates: Experiments, Evaluation, and Modeling

by

Kevin Arnett

Doctor of Philosophy in Structural Engineering

University of California San Diego, 2019

Professor Gilbert Hegemier, Chair
Professor Lauren Stewart, Co-Chair

Explosive welding is a field with a wide variety of applications of great value, such as corrosion resistant cladding and bi-metallic joints. It occupies a special place in the available metal joining techniques. Dissimilar metal welding is possible in metal pairings that don't support other conventional bonds, and it can produce superior area welds regardless of the metal parts to be joined. The objectives of this dissertation were to further the understanding of explosive welding in general, as well as the empirical understanding of welding of Aluminum

6061-O, and to investigate the use of LS-DYNA's Multi-Material Arbitrary Lagrangian-Eulerian formulation as a potential tool for the design of explosive welds. In the course of the work, the theory on formation of bond interfacial waves was identified as an area where there was not an apparent consensus, and this was addressed in light of both recent works and information from this study.

For this dissertation, an experimental program of explosive welding tests, mechanical weld verification, and metallurgical observation were undertaken in order to add to the data available for this type of welding. Nine different explosive welding tests were conducted covering four scenarios, which were combinations of different explosive thicknesses and flyer inclination angles. Tensile shear tests with digital image correlation were used to test the welds, and optical microscope, Scanning Electron Microscope, and Transmission Electron Microscope images were used to investigate the nature of the bond. The numerical investigation was conducted and compared to both experiment and initial modeling results.

The results reinforce the need for well-developed and material specific welding windows, adding additional data for the joining of Aluminum 6061-O. The endorsement of the continuous Kelvin-Helmholtz jet wake as the source of instability was supported with modeling results. The Multi-Material Arbitrary Lagrangian Eulerian modeling with Euler-Lagrange Coupling was demonstrated to yield results comparable to research codes for welding parameters, to be able to capture jetting, and provide meaningful temperature results. Bond interfacial waves were characterized with some success as well, concluding that this modeling technique is a viable means to assist in the design of explosive welds.

1. INTRODUCTION

1.1 MOTIVATION

As is clear from the vitae page, the author has spent a significant period of time in the US Army. A specific goal of the doctoral studies undertaken was to give back to an institution responsible for many benefits accrued over the years. The choice to try to compete for selection for study in the Structural Engineering Department at UCSD was informed by its reputation for protective blast design. The author is not just in the Army, but is also member of the Army Engineer Regiment, having served in various Combat Engineering roles where protection and explosives work are key components of the job. As an Engineer Officer, the author worked with explosives as early as the late 1990s, and this included the use of standard and improvised shaped charges. Though the selection of the present topic was not initially envisioned, it both provided a means to learn about many of the fundamental areas required for in-depth protective structural design and provided a great connection to and knowledge about the theory associated with shaped charges, which the author has been using or supervising, off and on for over 20 years. The behavior of metal lined shaped charges and metals in explosive welding are very similar, as will be shown.

Aside from the author's personal and institutional goals, the explosive welding of metals has a much broader set of industrial applications. In 2016, the Asahi Kasei Corporation was in coordination with the UCSD Center for Extreme Events Research, CEER, in order to arrange an experimental program. Asahi Kasei uses explosive welding in several areas including their BACLAD line of products, and they are one of a few key international firms with a long history in the industry.

A big part of the interest in explosive welding comes from its ability to join dissimilar materials that are otherwise difficult or incompatible to weld. In general cladding purposes, explosively welded products are used to produce composite clads that can combine corrosive resistant properties of more expensive metals with the structural capabilities of less expensive metals. With that general theme, they are employed in boilers, heat exchangers (including in nuclear power plants), and terephthalic acid reactors, among other applications.

Explosive welding is also used in bimetallic joints for connecting two different metals seamlessly. This need arises in maritime applications, combining aluminum and steel. Aluminum is used for weight savings and other benefits, and bimetallic joints enable a seamless connection where steel is still required. In cryogenic or liquid natural gas systems, aluminum is often relied upon in vacuum tight piping for areas exposed to critically low temperatures. In other portions of the system it is economical to switch to steel components. A steel to aluminum, vacuum tight transition joint is a critical component for these systems. Additionally, bimetallic joints have applications in electrical systems or in electrolytic processing where a transition between metals is desired with the best conductivity and structural properties possible. Further explosive welding has had many applications in space programs over the years.

1.2 OBJECTIVES

At the start of this study, a host of research objectives were envisioned. As can happen this list included things that didn't prove feasible to accomplish, and didn't include things that ended up proving fruitful to pursue during the course of the study.

The items that were addressed were significant. One goal, significantly achieved, was to further the understanding of the process, mechanism, and effects of explosive welding of aluminum plates. Another was to identify the effects of explosive welding on the material

properties and microstructure of aluminum alloy 6061-O welds. Most significantly, the capability for numerical modeling and prediction of welding and weld interface properties was demonstrated in a unique way.

There were a number of goals that proved beyond reach. Improving and comparing constitutive models for use in numerical modeling of explosive welding was not achieved. Nor was the author able to progress into an exhaustive welding study that would have allowed implementation and testing of more precise experimental techniques, as well as permitted the collection of more data for a more precisely defined welding window for 6061-O aluminum.

However, in the course of the study other pursuits presented the opportunity for this work to serve purposes not fully envisioned at the start of the effort. While a number of books exist on the topic of explosive welding, the latest English text was published in 1983, and all subsequent advances were primarily in articles. The details of the formation of interfacial bonds were considered unresolved in the published books. Attempting to successfully argue for a mechanism that satisfactorily accounts for the behavior, became an objective. This needed to be informed by physical and numerical evidence, as well as by current literature on this and related fields. Another objective became identifying whether a commercially available code could serve as a suitable design aid. The investigation of the use of the commercial software LS-DYNA as a potential practical tool for the design of welds uncovered the useful application of unexpected techniques, and became an area where more predictive capability was achieved than initially anticipated.

1.3 OUTLINE

This dissertation is divided into 7 chapters. Chapter 2 is a background chapter. A strong effort was made to produce an interesting and comprehensive review of the history of explosive

welding through the present. Academic and commercial developments in multiple global regions are discussed. The fundamentals of welding and explosive welding are also covered in detail. The typical fluids-based explanation using geometrical and material-based parameters for defining weld conditions is elaborated, and welding windows are discussed for use in designing explosive welds. A summary of theories on bond interfacial wave generation is covered, and in addition, a discussion of empirical relations of note is included as well. Lastly, an overview of some metallurgical considerations on the nature of bonding is covered through a more contemporarily referenced discussion.

In Chapter 3, the details of the explosion welding test program conducted with CEER for Asahi Kasei is covered. Aspects of the weld design selected are discussed. Data collection, instrumentation, and test results are also presented and analyzed.

Chapter 4 covers the details of the mechanical evaluation of the welds from the test program discussed in Chapter 3. Some background for defining a successful weld as well as a discussion of resource availability explain the test plan. Then specimen preparation is documented and discussed. Lastly test results are shown and analyzed.

The contents of Chapter 5 cover the metallurgical observations of the welding tests. Large scale down to nano-scale observations are made with the objective of relating them to both numerical predictions and prior works.

Chapter 6 is focused on the use of LS-DYNA's Multi-Material Arbitrary Lagrangian-Eulerian formulation with Euler-Lagrange Coupling as a tool for predicting explosive welding behaviors. The theoretical details of the modeling are summarized and contrasted with other commonly referenced ALE approaches. Then macro to meso scale results from the modeling are compared to both empirical predictions and results from earlier chapters. Additional insights that

the modeling can provide to bond wave formation are discussed, and a summary of modeling considerations is provided for this approach.

The last chapter provides a summary of the work, highlighting key connections between the results or ideas of different chapters, and then provides recommendations for future work.

2. BACKGROUND

2.1 THE HISTORY OF EXPLOSIVE WELDING

2.1.1 PRE-WORLD WAR II BUILDING BLOCKS

The use of explosives for working effects on metals or for concentrated/shaped effects extends far back into history. Before the second world war, it was largely empirically driven for cratering, quarrying, and military munitions applications as the science of explosives developed. The first use of explosives to create metal fragmentation from hollow cannon balls occurred in the early 18th century by the French and, famously, by LT Shrapnel of British artillery [1, pp. 217–218]. In 1888, Charles Munroe published an article that was the first English speaking account of what came to be known as the "Munroe Effect" in the U.S. Munroe demonstrated that cavities within explosives allowed the concentration of their blast effect. He famously stamped metal with "U.S.N", the U.S. Navy markings on the bottom of the gun-cotton explosives he used, as shown in Figure 2-1 below. This was some of the first documented US explosive metalworking [2]. Some historical works indicate German mining engineer Franz von Baader was the earliest documented expert to employ shaped charge techniques. He did so for mining in 1792 and may have observed similar stamping effects in 1799 [3]. Lieutenant M. von

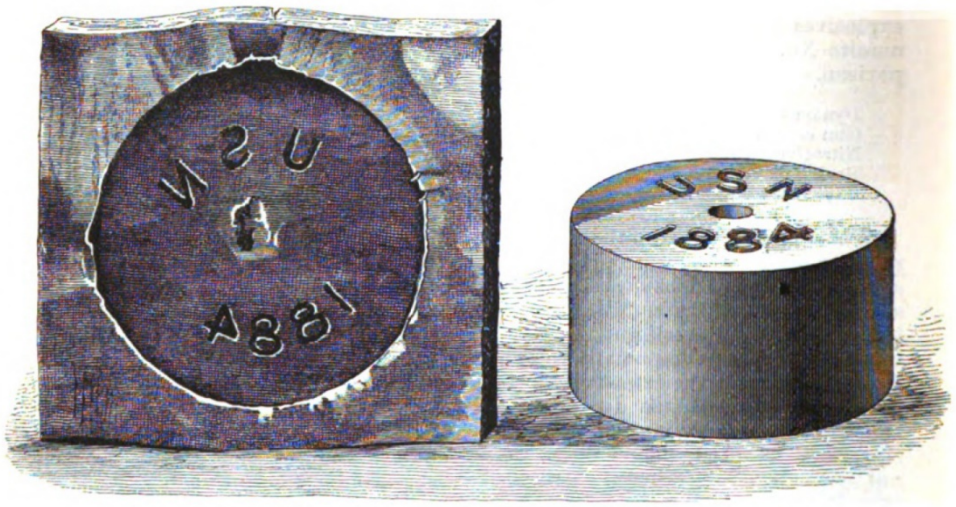

Figure 2-1: Illustration in Charles Munroe's 1888 article showing a cylinder of gun-cotton imprinted with US Navy markings and the resulting effect on a plate of iron.

Foerster also preceded Munroe with high explosive gun-cotton produced stamping in Germany in 1886[3].

The scientific ability to analyze these events also began to significantly evolve during and near the start of the 20th century, though they didn't directly contribute at the time. Evidence indicated the static and dynamic mechanical properties of materials were different as early as the late 1800s, but these results weren't immediately included in detailed analysis for impulsive loading [1, p. 7] [4, p. 5]. Despite the development of the science, progress continued on an empirical basis, with patents for explosive working of metals appearing as early as 1898 for explosive expansion of bicycle tubes in Britain. The US issued patents for forming sheet metal in 1909, and the French explosively formed gun emplacement shields around the same time[5, p. 2]. As early as the first World War, observers noted the welding of metal shrapnel to other metals surfaces, but no investigation was made into this phenomenon at the time [6, p. 7]. In the 1930s some other early explosive forming was conducted in the shallow cupping of steel plates for ordnance applications [7, p. 3].

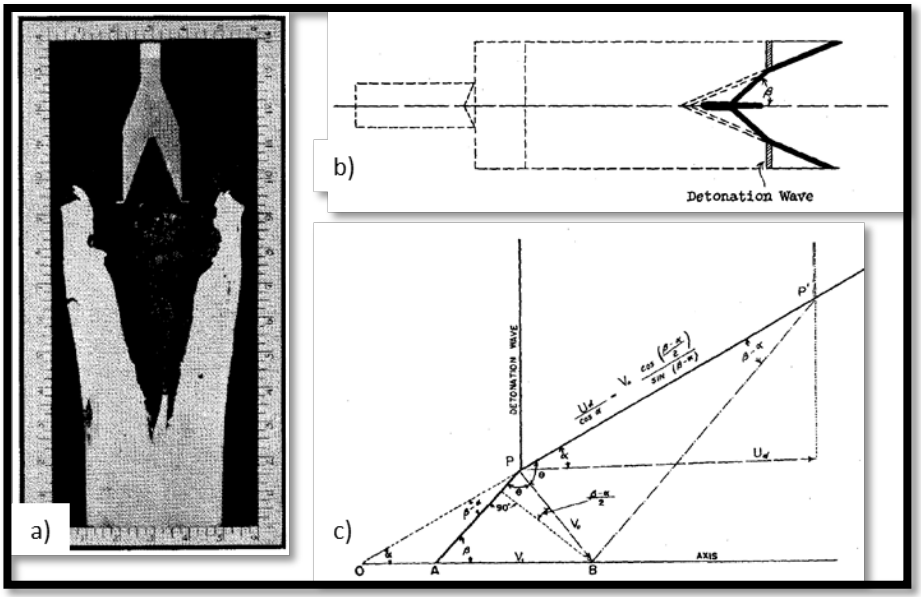

Figure 2-2: Selected figures from Birkhoff's 1948 work that established the first English speaking account of the mechanics of metal-lined shaped charges.

In the lead up and start of World War II, Thomanek in Germany and Mohaupt (a Swiss researcher who carried his work from Switzerland to France, and then in 1940, to the US) had introduced metal liners to shape charge munitions for increased penetration effects on metals and other targets [3]. However, in the US it wasn't until Birkhoff published his famous work [8] in 1948 (sample figures shown below in Figure 2-2) that a publicly released and robust theoretical analysis of lined shaped charges existed. Birkhoff's research is highly referred to[1] and relevant to the mechanics of explosive welding, but it did not directly lead to either explosive welding, nor to broader explosive metalworking for commercial purposes.

2.1.2 Post World War II Backdrop of Explosive Metalworking

After World War II, the confluence of the development in solid mechanics with the intense Cold War missile and aviation competition, supercharged the need for knowledge in the area of impulsive and other extreme loading of metals. The German V2 opened the door to

[1] The hydrodynamic jetting analysis has been so widely applied that it has even been used to attempt explanation of the formation of the moon.[231]

ballistic rockets. Jet and rocket engines, as well as nuclear weapons, made the knowledge of the dynamic behavior of metals of paramount relevance. These capabilities required engineers to understand behaviors under extreme loads, strain rates, temperatures, and under short durations, in order to extend missile and aviation capabilities. In the US, the Air Force was formed, the speed of sound broken, and the ability for mid-air refuel realized. Further, swept wing planes became preferred for sub and supersonic flight and hydrogen bombs were tested, all by 1952. By 1957, the launch of Sputnik and the USSR's first ICBM further increased the sense of urgency in the US, spawning the creation in quick succession of the Advanced Research Projects Agency (ARPA; the early name for DOD's DARPA) and NASA.[2]

In this backdrop, explosive metalworking emerged as a significant industry. Work done in the late 1940s on explosive hardening allowed industrial implementation in the 1950s. This was for steels subject to severe abrasion like railroad frogs, rock-crusher jaws, and other digging and grinding implements [4, p. 8]. Explosive forming presented itself as a capital-light method for prototyping unusual shapes, which was highly attractive for aerospace applications. By the late 1950s, explosive powder compaction and explosive forming became required capabilities for aerospace parts, especially missile domes [4, pp. 8–12], [5, p. 2]. By 1960, eighty government funded explosive metalworking programs were underway in the US [5, p. 2]. As the aviation industries of many countries grew in size and sophistication, the potential value of advanced metal working capabilities had expanded. Complicated shapes and new metals could dramatically increase the capital costs for prototyping systems, and explosive forming offered

[2] Both the US and USSR went on to use explosive welding for their space programs. The US applied it specifically in a titanium-steel transition joint for use in the Apollo spacecraft [51], for use in general joining, and for use as a remote joining capability.[194], [232] In the USSR the Institute of Hydrodynamics produced bimetallic sheets for Sergei Korolev, a key figure in the USSR space program.[26]

the potential to both replicate existing capabilities more cheaply and extend capabilities beyond the state of the art [7, p. 4].

The development of mathematical and modeling capabilities for elastic and inelastic solid mechanics further enabled the development of new analyses. Post WWI, Bridgeman, Prandtl, and Reuss had extended and burnished St. Venant and von Mises' plasticity theory for metals. Post WWII, Prager, Drucker, Hill, and Koiter, refined this knowledge, expanding the theoretical capabilities of solid mechanics. Kolsky published *Stress Waves in Solids* in 1953, further enhancing the state of engineering knowledge for dynamic systems.

Military, state, and private sponsored research continued on metallurgical considerations as well. In the US, Drucker's work at Brown was often funded by the military, and at China Lake, CA, Pearson and Rinehart had begun working on explosive effects on metals before 1951. From 1951 to 1955, they published eight joint or individual papers on work hardening, impulsive loading behavior, and scabbing of metals under explosive attack in the Journal of Applied Physics [9]–[16]. They also published in the Journal of the Acoustical Society of America [17] and authored a full text on impulsive loading, *Behavior of Metals Under Impulsive Loads* [1]. The USSR had extensive programs as well, and in 1957, the Institute of Hydrodynamics, Siberian Branch of the USSR Academy of Sciences was founded. It began work on explosive studies with M. L. Lavrentyev, father of Russian shape charge technology, in the lead. This institute was later re-designated to include his name, and the Lavrentyev Institute of Hydrodynamics exists today in the Siberian Branch of the Russian Academy of Sciences. Amongst the groups poised to benefit, private chemical and explosives companies, such as the American Potash & Chemical Company (AP&CC), E. I. du Pont de Nemours Company (DuPont) and the Hercules Powder Company [18], also conducted research on explosive

metalworking. Philipchuk of AP&CC and Cowan, Douglass, and Holtzman of DuPont, who filed the first patents on the explosive welding process were examples of these private researchers. It is possible that AP&CC got some information about the military research on explosive metalworking from their Trona, CA facility by Searles Lake where they manufactured borax, potash, and other chemicals. Trona was the site of their founding, became branding for other products like their rocket propellant shown in Figure 2-3 below, and is a short drive from the Naval Weapons Station at China Lake where Pearson and Rinehart worked.

Figure 2-3: Trona Ammonium Perchlorate advertisement in a 1961 Aviation Week and Space Technology catalogue from the American Potash and Chemical Company that was founded 10 miles from China Lake, CA. [238]

2.1.3 Discovery and Industrialization of Explosive Welding

It was this general environment of experimentation with metals and explosives that generated the industrial discovery of explosive welding. The first discovery of explosive

welding was published by Carl (see Figure 2-4 below) in 1944 [19], but it went largely unnoticed, much like the anecdotal observations in World War I. It is also reported that M. A. Lavrentyev observed that metal welded during his 1944-1946 experiments on shaped charges, but the wavy interface was focused on rather than the welding/joining, and it was not recognized as a potential commercial welding process [20]. Though the work of Birkhoff and the independent work of Lavrentyev in the USSR [21] on lined shape charge analysis proved critical in explaining the process, it was applied after the fact to explosive welding. Birkhoff's work did identify the "newly formed slug" as a recoverable body, suggesting a recognition that the two parts of the liner were fused, but this was not recognized as a possible joining technique at the time, just as in the case of Lavrentyev.

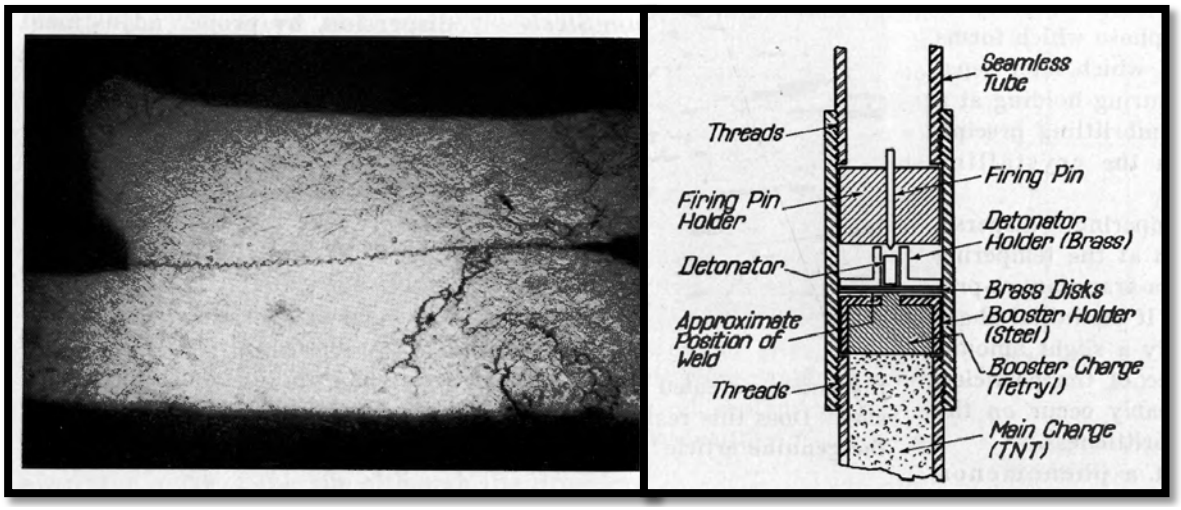

Figure 2-4: The first published documentation of explosive welding by Leroy Carl. On the left is an image of Carl's welded samples of half-hard brass. At right, a schematic of the set up where this accident occurred, with the brass disks bordered in red by the author.

The actual discovery by those who developed explosive welding occurred independently in several locations in the late 1950s. In all cases, the discoveries were accidents in forming or compaction that generated an incidental weld. John Pearson notes many different clues to the process, from welding in ordnance tests, to using an overcharged system in explosive forming,

but he specifically cites a study on powder compaction that he and Edward LaRocca published in 1958 as an example of a case where press misalignment resulted in accidental welds [4, p. 10], [22]. Richard Zabelka provides a figure showing welding of low-carbon steel resulting from test work associated with an experimental warhead, and cites it as an unexpected bond that "attracted immediate attention"[23, p. 3].[3] Vasil Philipchuk credits Frank Bois of AP&CC with detecting the welding principle while forming an aluminum blank into a deep U channel in an early article in *Steel*[4][24]. John Douglass at E. I. du Pont de Nemours Company observed welding during explosive forming tests and is credited with sparking that company's initial drive to investigate the process [25]. In the USSR, E. I. Bichenkov and Yu. A. Trishin, brought a sample of "stuck together pieces of steel and copper" to Andrei Deribas in 1960 [26]. Deribas, after reviewing the sample, showed it to V. S. Sedykh, a welding specialist and senior researcher, leading eventually to their 1962 initial publication [27]. From these initial discoveries, many other institutions began conducting work, such as Davenport and Duvall at Stanford, and Tardiff in Canada.

2.1.4 Initial Investigations and a Rise of Awareness

Once these initial discoveries occurred and preliminary investigations were conducted, a short period ensued, punctuated by a few key patents in the U.S., where news about explosive welding got out to a broader audience. In January 1959, the trade magazine *Steel* published an article highlighting some of the key work occurring in explosive forming with contributions from John Rinehart, John Pearson, and Vasil Philipchuk, see Figure 2-5 below [28]. Then in April,

[3] Richard Zabelka's 1960 Master's of Science Thesis at UCLA is the first university work on the topic of explosive welding. It is important and interesting to note that John Pearson was on his committee.[23] Though two references from closely connected sources offer different triggering events, the timeline is consistent with the compaction test sparking Dr. Pearson's interest, and in any case shows the prevalence of accidental welds in this testing environment.

[4] Further accounts and reports of this discovery by Philipchuk were published in *American Machinist*[233] and in a series of Creative Manufacturing Seminars held in Detroit and elsewhere by the American Society of Tool and Manufacturing Engineers (now the Society of Manufacturing based in Michigan) in 1961. This early 1962 work[234] by Donald Davenport of the Stanford Research Institute cites these 1960-61 articles.

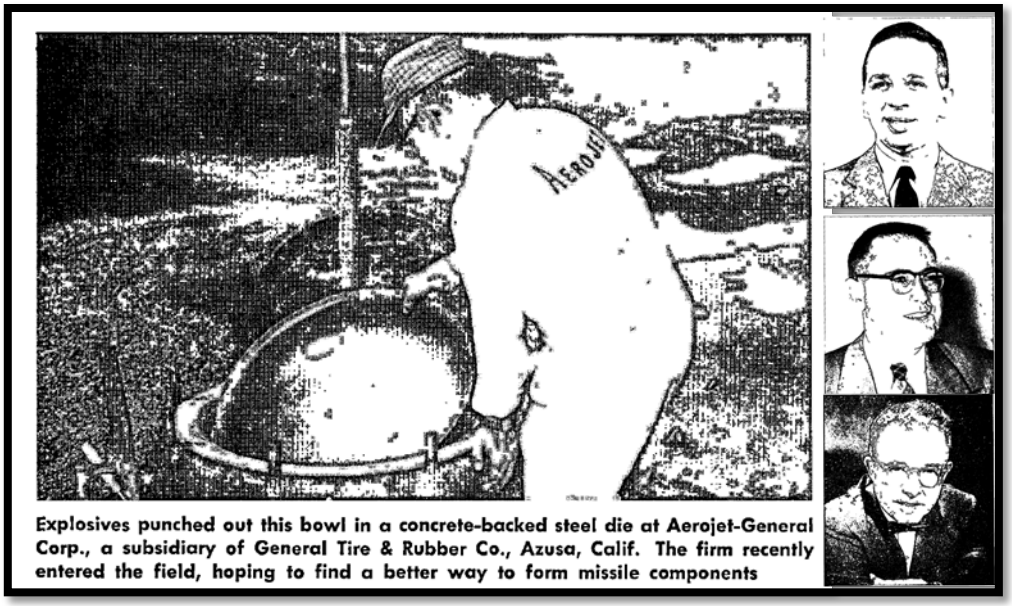

Figure 2-5: Images from the 1959 *Steel* article on explosive forming with contributions from two key independent developers of the explosive welding technique. Pictures at right from the article are, top to bottom, Vasil Philipchuk, John Pearson, and John Rinehart [28].

Welding Engineer profiled Philipchuk, producing one of the first instances of marketing the capability to a larger trade audience [29]. By November, as if realizing they'd just missed an opportunity with their explosive forming article, another article was published in *Steel*, revisiting Pearson and Philipchuk's work, but this time with a detailed look at explosive welding (see Figure 2-6 below) [24]. In September 1960, Pearson published about explosive metal working in

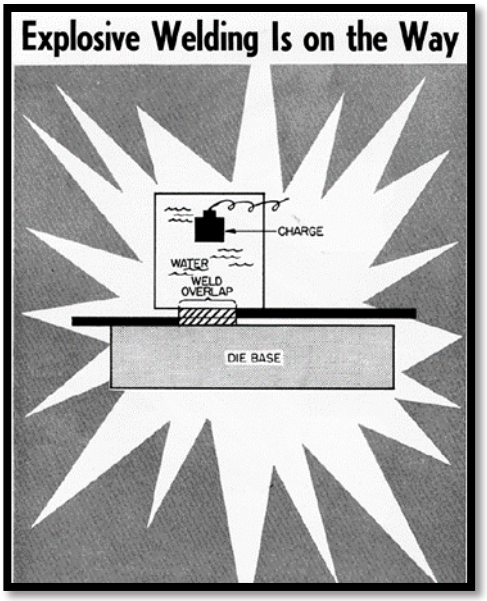

Figure 2-6: Figure showing the AP&CC explosive welding process from Vasil Philipchuk's article "Explosive Welding is on the Way" in *Welding Engineer* from April of 1959. [29]

the American Institute of Mining, Metallurgical, and Petroleum Engineers' (AIME[5]) *Journal of Metals*. This work contains a section with substantive detail that is one of the earliest journal article references to explosive welding [30].[6] This article, likely reporting work detailed in Zabelka's thesis, highlights the fact that surface jetting is involved and makes the connection to lined shaped charge technology and the associated hydrodynamic relationships. Zabelka's work and reference to Walsh, Shreffler, and Willig [31], Abrahamson[7] [32], and Birkhoff [8], demonstrate this connection had been unequivocally made. In 1962, V. Sedykh, Andrei Deribas, Ye. Bichenko and Yu. Trishin published the first work in the USSR covering explosive welding in the Russian Journal of Welding Production [27]. Though not delving into the details, this work recognized the connection to surface jetting as well.

[5] This society was later renamed, and is currently known as The Minerals, Metals, and Materials Society (commonly abbreviated TMS, but with more effect in their logo).

[6] Figure 20 of this article is actually the same micrograph from Figure 1 of Zabelka's Master's Thesis.[23]

[7] Zabelka found a lab report of the same title from Abrahamson from March of 1958, which is assumed to be the original date Abrahamson's work was completed.

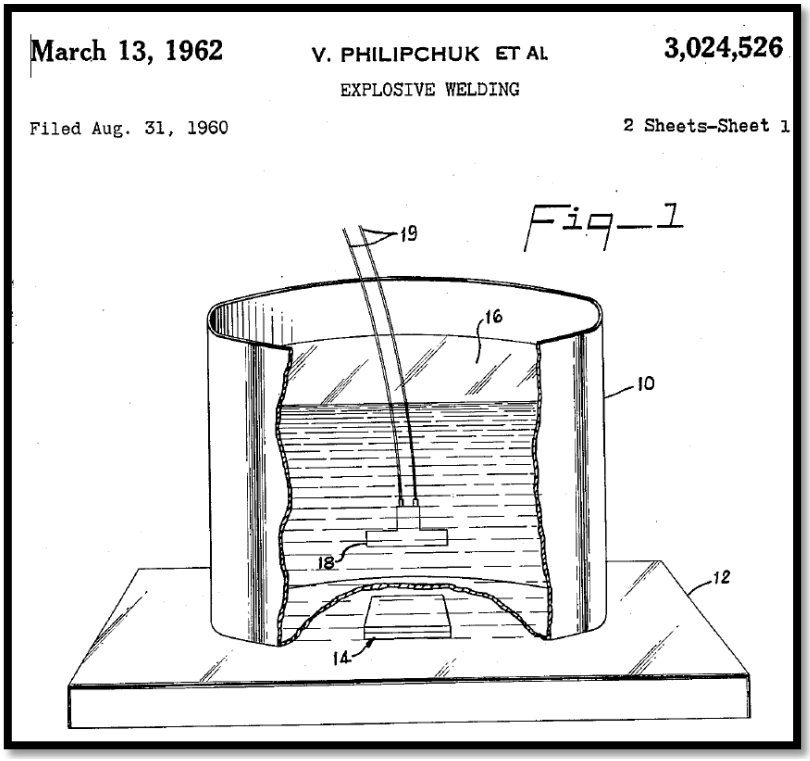

Figure 2-7: Diagram of Philipchuk's patented explosive welding process, taken from his 1962 patent.[33]

Philipchuk was the first to file and be granted a patent, filing in August of 1960 and having his patent granted in 1962 [33]. The problem was that Philipchuk's technique was not ideal a did not perform optimally. The processes he outlined primarily relied on water or another hydraulic fluid to transfer the impulse to the metals rather than putting the explosive in direct contact with a metal as shown above in Figure 2-7. Cowan, Douglass, and Holtzman filed for an explosive welding patent two months after Philipchuk in 1960, but they were not granted their official patent until 1964 [34]. Their patent demonstrated substantial knowledge of jetting and other aspects of the explosive welding process. As shown in Figure 2-8, their process is much more closely aligned with modern practice. Their patent was detailed and thorough, but did not lay out a theoretical basis for what was happening, reserving that for journal publication. The

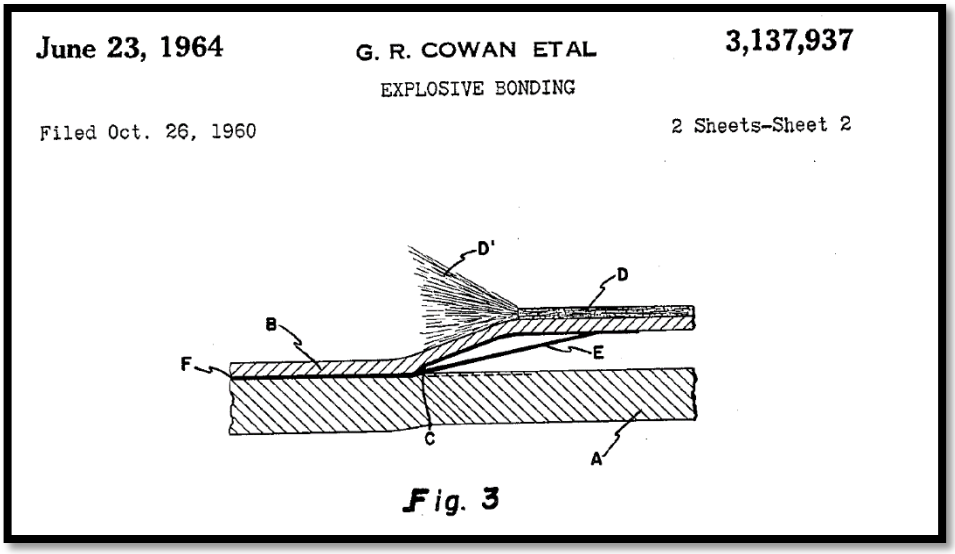

Figure 2-8: Cowan, Douglass, and Holtzman's imagery and details proved much more aligned with subsequently accepted research and publications about the explosive welding process.

patent was assigned to E. I. du Pont de Nemours Company where they were employed, planting the seeds for the single largest explosion cladding company in existence today. In 1961, Popoff, also employed by DuPont, filed a patent for explosive welding in cylindrical geometries, and the patent was granted one month after the first DuPont patent in 1964 [35]. Cowan, Douglass, & Holtzman and Popoff likely worked together as portions of Popoff's patent are identical word for word with the earlier patent of Cowan, Douglass, and Holtzman. It was this work at DuPont


BUSINESS The New York Times. FINANCIAL

U.S. ACTS TO BAR BIG PHONE MERGER

Negro Graduates Meeting Job Recruiters

ARGENTINA EYEING U.S. OIL HOLDINGS

STOCKS CREEP UP AT SLUGGISH PACE

BRAZIL APPROVES SUGE POWER PLAN

EXPLOSIVES USED TO JOIN METALS

Du Pont Receives Patent for Cladding Process

By STACY V. JONES
Special to The New York Times

WASHINGTON, June 19—E. I. du Pont de Nemours & Co., will receive a patent next week for a process of joining metals by the use of high explosives.

Du Pont has found the method especially useful for cladding—coating one metal with a thin layer of another to gain corro-

Training in Job-Hunting

Figure 2-9: The New York Times business and financial section front page from June 20, 1964 publicizing DuPont's explosive welding patent and process.[25]

that gained the first wide spread recognition of the technology as well. On the same day they reported the passage of the Civil Rights Bill by the US Senate, the New York Times covered the patent by Cowan Douglass, and Holtzman three days before it was granted, see Figure 2-9 above [25].

2.1.5 Industrialization, Research, and International Collaboration

From the early 1960s through the early 1980s, explosive welding experienced an "explosion" of industrialization, research, and international collaboration/discussion. The industrialization that occurred largely set the stage for much of the current landscape of the explosive welding market. Du Pont lead the way with initial production in the United States. In the early 1960's they began investment in facilities near Dunbar, Pennsylvania [36]–[38]. They

found many unique and innovative ways to profit with the new technology, often exploiting its flexibility and their first adopter status.

One notable example of DuPont's early innovations with explosive welding was their production of US coins using the cladding process. Beginning in 1959 the US began to experience coin shortages [39]. The US Mint increased production of coins in response. However, they were not only unable to keep up with demand, but also drove the price of silver up to a point that it was worth more in bullion than the face value of the coins it was used to make. This led to the Coinage Act of 1965 where the composition of US coins officially changed, beginning the use of a clad coin setup. DuPont generated early profits fabricating these coins. They were able to immediately produce clad coins during their development and initial rollout, before increased capacity was otherwise available through capital intensive means [36].

Figure 2-10: Early DuPont cladding products. Left: a terephthalic reactor ready for delivery. Right: a metal leaching autoclave in production. Images courtesy of John Banker, of Clad Metal Consulting, an early DuPont employee. [36]

DuPont also expanded into production of bi-metal sheet cladding products marketed under the brand Detaclad. By 1966, DuPont's Detaclad was in full production and DuPont had identified a large majority of the currently profitable explosive welding applications [36]. They produced titanium clad terephthalic acid (PTA) reactors, titanium-clad metal leaching autoclaves, and clad tube sheets. Examples are shown in Figure 2-10 above. The facilities and capital investment made by DuPont was extensive, as shown by Figure 2-11 below. In fact, the initial

production facilities were so large and effective that they still exist largely intact under different ownership. In addition to direct production, DuPont also licensed technology globally to Nobel Explosives, UK; Nitro Nobel, Sweden; Dynamit Nobel, Germany; Nobel Bozelle, France; Explosive Fabricators Incorporated, USA; Asahi Explosives, Japan; and IDL, India [36]. All of these companies eventually became competitors.

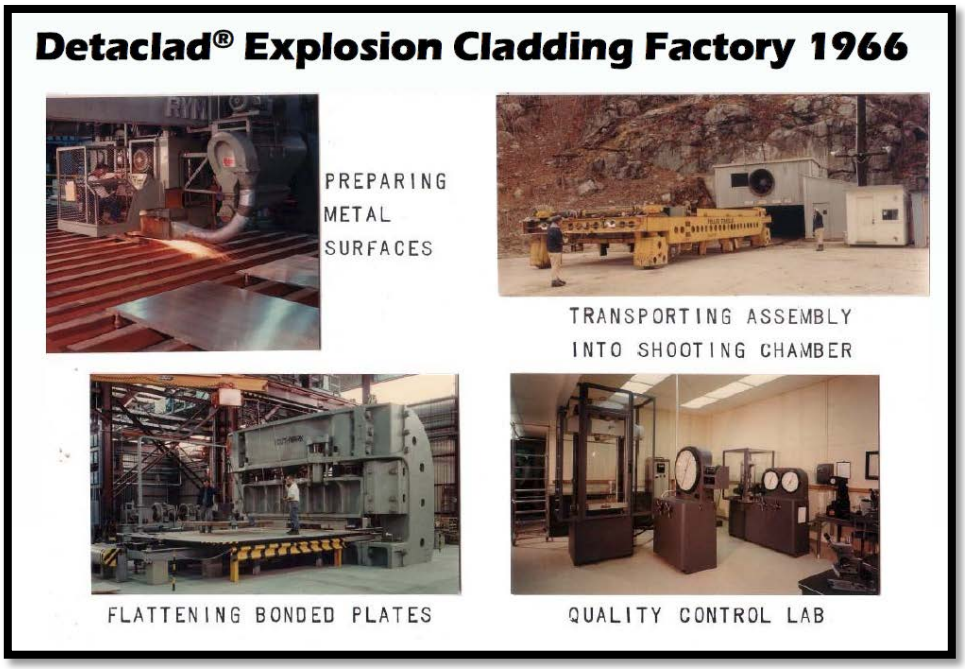

Figure 2-11: Early pictures of the Pennsylvania DuPont Detaclad explosion cladding facilities. [36]

Other US companies emerged in the market as well. In 1965 Martin Marietta, a Denver aerospace firm had a number of explosive metalworking patents [40], [41] and they also had a fledgling explosive welding division. Explosive Fabricators, Incorporated[8] (EFI) was formed that year, acquiring their cladding operations [42]. In the 1970s and into the 1980s, US explosive welding companies were competitive in similar metal cladding before hot roll bonding technology developed to replace their capability [36].

[8] Explosive Fabricators, Incorporated later changed their name to the Dynamic Materials Corporation.

Starting in the 1960s, as industrialization surged, so also did research and publications. Cowan, Douglass, and Holtzman's 1963 paper was the first US journal work to refer to Birkhoff's metal lined cavity analysis in analyzing explosive welding and to explicitly apply the hydrodynamic framework to the explosive bonding situation in detail [43]. Their work went well beyond any other explosive welding work at the time, applying hydrodynamic theory to both subsonic and supersonic flow regimes and their relation to the bonding process. The book *Explosive Working of Metals* by Pearson and Rinehart was also published in 1963. This is an extensive work on explosive metalworking, with a significant section on explosive welding; the first such treatment in a book [7]. Deribas had already published work in a journal by [27]1962 as well, and by 1972, he had published his book (only available in Russian) *The Physics of Explosive Hardening and Welding* [44]. Roughly starting in the 1960s, key international researchers began their work in explosive welding. Bernard Crossland of the Queens University, Belfast in Northern Ireland completed significant work by 1964 [45]. His research career in this topic would culminate in his extensive book, *Explosive Welding of Metal and its Application* [6]. In the U.K., Tadeusz Z. Blazynski, later in 1983 editor of the another extensive explosive welding book, *Explosive Welding, Forming, and Compaction*, had published by 1967 [46].

As international researchers emerged, a concomitant coalescence of regional centers of expertise emerged, often sponsored by sustained or intermittent state funding. In the USSR, the Institute of Hydrodynamics played an obvious and central role. In Japan, the Japanese Welding Society provided a forum for work that sparked their industry; an initial publication was the first of many to come [47]. In the US in 1965, ARPA sponsored the establishment of the Center for High Energy Forming in Colorado under the direction of the Army Materials and Mechanics Research Center. The Center was initially formed as a joint effort between the Denver Research

Institute[9] of the University of Denver and Martin Marietta, a nearby aerospace company [48]. Arthur A. Ezra, who initially worked for Martin Marietta and then later became the Chair of the Department of Mechanical Sciences and Environmental Engineering, Denver Research Institute, University of Denver, was the first researcher in explosive forming at Martin Marietta [5, N. About the Author]. By 1973, he had published *Principles and Practice of Explosive Metalworking* that contains a full chapter[10] on explosive welding.

The Denver Research Institute, Center for High Energy Rate Forming became a huge engine for explosive welding research in the US. Dr. Steve Carpenter, an Assistant Professor of Physics, and Robert Wittman, a Research Metallurgist, produced work and publications that are extensively cited in the field of explosive welding, and more broadly, in all types of impact welding. They collaborated with DOD and military service research agencies, as well as work with Vonne Linse of Battelle in 1967 [49]. Under US Air Force funding, an eight year study began by 1969, involving the US Air Force Academy, the Air Force Frank J. Seiler Research Lab, the Denver Research Institute, private companies, and Los Alamos National Lab [50]. This is the single most thorough and quantitative research report the author has found on explosive welding. Notably, Prof. Marc Meyers of UCSD graduated with his PhD from this University of Denver program in 1974, spawning his career in dynamic behavior of materials. The center officially finalized its contractual work in 1974 [48], although center members remained active for some time afterwards in government sponsored work (such as the USAF contract above).

In all of these different locations and more, a dizzying array of research topics were explored by many prominent researchers. Flat, cylindrical, and more advanced geometries were

[9] This sub-organization of the University of Denver included departments related to physical sciences, but has since been dissolved.

[10] In his acknowledgements, Ezra thanks Steve Carpenter and Robert Wittman[51] for writing this chapter. He also thanks John Pearson for advice, guidance, and support in writing the full text.

successfully joined. The exploration of welding windows, including empirical and other relationships for quantifying the windows, occurred [49], [51], [52], In the late 1960s and throughout the 1970s, the mechanism of bonding and wave formation became a big focus, [53]–[64]. The uses for nuclear power plant heat exchangers began to be explored in the late 70s[65], and carried into the early 80s. The use of gas guns for developing weld window characteristics emerged [66]. Researchers such as Blazynski (Leeds) and El-Sobky (Manchester Institute of Science and Technology (UMIST)) remained active in the UK, with S.T.S Al-Hassani publishing from UMIST in 1981. Crossland helped guide the work of Frank McKee and later Alexander Szecket in the use of gas guns for weld window research at the Queen's University, Belfast. This was an era of tremendous and broadening innovation in this research area.

This significant burst of international research generated a similar burst of international conferences (in attendance, not just in name) where all the notable countries and researchers above participated in a very open exchange of ideas and accomplishments. The Denver Research Institute launched the earliest of these in 1967. The first International Conference on High Energy Rate Forming sparked a series that would last over a decade with subsequent meetings in 1969, 1971, 1973, 1975, 1977, and 1981. Several of the conferences were held in Leeds, England[11], making the trip shorter for European researchers, especially the groups from the Manchester and Leeds areas, as well as Crossland and coworkers from Northern Ireland. Though held in the US and UK, notable researchers from the USSR, Germany, and Japan were frequently among the conference attendees. In 1970, a series of international conferences began in eastern Europe in the Czechoslovak Socialist Republic (CSSR). This meeting, each titled a *Symposium on the Use of Explosive Energy in Manufacturing Metallic Materials of New*

[11] Specifically, the fourth and seventh conferences were hosted in Leeds.

Properties and the Possibility of Applications Thereof, was held every three years, with the last occurring in 1988. As in the case of the western conference series, this series was well attended by US, UK, and Japanese researchers, in addition to researchers from eastern Europe.

2.1.6 Notable Research and Events in a Matured Industry in the 1980s & 1990s

By the end of the 1970s, the industry associated with explosive welding had largely matured. Areas of significant research, identifying new applications or weld combinations, remained, though not matching the pace of earlier work. In many ways the earlier academic collaboration that brought the field to fruition began to take a backseat to a focus on regionalization and commercialization of the technology.

The 1980s brought some interesting and new developments in applications and research. One of the most significant commercial trends in the 1980s was when Explosive Fabricators Inc in the US began marketing stainless steel and nickel alloy clad, competing with other production techniques, and gaining ground with quality and other criteria beyond price [36]. Additionally, the US Army briefly investigated uses for float bridge repair [67]. For research topics, discussion of whether bonding occurred in an instantaneous melted stated versus a solid state began in the 1980s, whereas the process had been primarily considered a solid state process up to that point [68]. Also, the formation of waves continued to be a topic of research with new models proposed by researchers Jaramillo, Szecket, and Inal, who could trace their research lineages back to Crossland [69],[70], [71].

In the 1990s, much new research focused on the use of emerging computational capabilities and microscopy techniques for understanding explosive welding. To an extent some regionalization began to occur in terms of collaboration and conferences. Starting in the 1980s, US academic research in explosive welding began to wane, perhaps for competitive reasons, and

that remained the case into the 1990s. However, in 1980, the EXPLOMET series on the *Metallurgical Effects of High Strain-Rate Deformation and Fabrication*, organized by Marc Meyers and Lawrence Murr, kicked off in the US in Albuquerque, New Mexico. Though there was substantial international participation, all EXPLOMET conferences were held in the US and the focus slightly de-emphasized explosive welding. This conference series was held again in 1985 and1990, and, as was noted in a report to US Army funders, the focus continued to shift away from explosive welding, forming, and cladding [72]. In the 1990 conference, EXPLOMET organizers initiated the John Rinehart award, designating Andrei Deribas as a co-recipient of the first award for his "seminal contributions to the theory of explosive welding" among other contributions.[12] In Europe in 1985, DYMAT, another regional organization for the dynamic behavior of materials, was established [73]. They initiated a conference series and remain an active organization to date.

By end of the 1980s, the explosive welding industry was well established, and by the 1990s, DuPont as well as Asahi Chemical Industry Co Ltd, EFI, and various European Nobel companies that used DuPont patents had built up a reliable market. DuPont and EFI[13] were the main US companies producing explosively welded cladding. These businesses had gained significant depth and sophistication, as they competed amongst other explosive welding companies, and more broadly in cladding, with companies using other cladding techniques.

In 1995, the US International Trade Commission received a trade complaint from Lukens about less than fair value imports of clad steel plate from Japan that was eventually substantiated

[12] The other co-recipient was Mark Wilkins from Lawrence Livermore National Labs. The award was given out each of the two more times the conference was held; in 1995 (El Paso, TX) and 2000 in Albuquerque, NM. Then the award moved to being awarded at conferences of the Minerals, Metals, and Materials Society (TMS) through 2007, and then in 2009, responsibility for the award transferred to DYMAT.

[13] It was in 1994 that the name change from EFI to Dynamic Materials Corporation (DMC) occurred.

[37]. Lukens used a roll bond technique for their cladding or subcontracted explosion cladding work to DuPont that they could then roll to smaller gauges. Other US companies other than Lukens, who responded to the investigation were Ametek and Vessel (both roll-bond companies), and DuPont and DMC (both explosive cladders). Although, in 1995 all Japanese firms listed as dumping product used roll-bonding technology, DMC and DuPont benefitted, and this determination has been reviewed four times since (most recently December 2018). It is still in effect [37], [74]–[77]. Though Asahi-Kasei (formerly Asahi Chemical Co[78]) was listed as a respondent to the third review of the anti-dumping action, it was the only explosive cladding competitor listed and was only listed one time (the fourth review hid all Japanese respondents). At least in the steel cladding subset of the explosive welding business, the above referenced US producers have been protected for nearly 25 years from cladding competition.

This coincided with the growth of the US market. In 1996 DMC bought out DuPont's DetaClad cladding division. In 2001 it bought the French producer Nobelclad (which had previously bought the Swedish explosive cladding company Nitrometall), and by the 2013 review of the USITC intervention, DMC had acquired the German subsidiary DynaPlat. Just before the financial crash of 2005, DMC commanded 95% of the domestic US market and two thirds of the world market in cladding, with their only major competitor being Japan's Asahi-Kasei [38], [42]. Other smaller domestic firms also entered the market though. Regal Technology Corporation was formed in 1992 with Von Linse[14] as CEO, but reportedly stopped producing explosive cladding in 2017. High Energy Metals was formed in 1997 in Sequim, WA, when David Brasher and Donald Butler left Northwest Technical Industries after a firm buyout.

[14] Linse was an early researcher in explosive welding, publishing as early as 1967, and worked for the Battelle Memorial Institute, a nonprofit research institution that has managed certain Department of Energy national labs.

They attempted to acquire Northwest Technical Industries from its owner and their boss, Al Hair, but Pacific Aerospace and Electric (PacAero) came and made a higher offer [79]. PacAero still has a "Bonded Metals Division," which they market as "formerly known as Northwest Technical Industries." It also operates in Sequim, WA [79], [80].

2.1.7 Research, Collaboration, and Other Business: 2000s to the Present

From the 2000s to the present there has been a continued focus on explosive welding and other related work. This has occurred in the US, in Europe, and elsewhere. The nature of this work varied. Much work continued to focus on understanding the nature of the bond. This included attempting to more clearly define when it will occur, attempting to understand and predict the formation of interfacial waves, and attempting to understand other details of the mechanism such as the role of adiabatic shear, potential melting, or even a more physics-based approach to predict bonding. A large body of work has also emerged that focused on computational modeling of the process, as well as on evaluation of the product or newly produced products. Additionally, the field was enriched by the emergence of new, but intimately similar fields and an expansion into countries that previously hadn't developed expertise.

As the EXPLOMET series of conferences entered the latter half of their existence, the US group The Minerals, Metals, and Materials Society began including a section on dynamic behavior of materials in their annual meetings. This occurred in 1994, 1998, 2003, and 2007. These events saw the overlap of researchers prominent in the EXPLOMET series with a slightly different audience including Prof. Glenn Daehn of Ohio State University. As the US codified better fuel economy requirements for autos, funding was also identified to further that aim.[15] Prof. Daehn, working in the Materials Science and Engineering Department, began looking at

[15] The following are three publications with funding of this type.[175], [235], [236]

joining technologies that facilitated joining steel and aluminum for lighter automobiles, implemented high speed forming techniques, and otherwise generally aimed to further a Midwest manufacturing revival using technology. In the initial Colorado-hosted High Energy Rate Forming conferences of the 1970s, there were mentions of electro-magnetic forming, and it was included in A.A. Ezra's book as well. However, technological improvement began to make it more feasible in the 90s and 2000's. Prof. Daehn's work began to delve into high-velocity and electromagnetic forming [81]. These areas are highly interrelated to explosive welding.

In 2001 the beginnings of the International Impulse Forming Group were sown, and in 2008 they held their 3rd International Conference. The group maintains strong ties between western Europe and the US, and is a great source for contemporary impact welding research. Prof. Daehn is a member of their scientific advisory board. This group has been on the edge of two new forms of welding, intimately related to explosive welding: Magnetic Pulse Welding and, first presented in 2013 by Prof. Daehn and associates, Vapor Foil Actuated Welding [82]. Since the turn of the century there has been a remarkable increase in the amount of published work on magnetic pulse welding [83]. Both processes mainly differ from explosive welding in that their flyers generate their impact velocity with a different means. Without explosives, they are easier to operate on a smaller scale and better suited to automation for manufacturing. The advent of these fields means that in understanding the bond that occurs for explosive welding, a now larger set of works need to be reviewed.

In eastern Europe, the fall of communism slowed the pace of collaboration from the Czechoslovakian conferences that ended in the 1980s. However, it did not stop that collaboration, and in some cases, it opened up free market opportunities. The Czechoslovakian conferences were significant forums with great contributions, and provided a closer and easier

outlet for the work Russian researchers carried on. The Lavrentyev Institute of Hydrodynamics in Novosibirsk continued work into this time period and by 2006, they organized the resumption of eastern European conferences. They started a series under the name Explosive Production of New Materials (EPNM). The series began its numbering as the 8th in order to continue the numbering from the Czechoslovakian series. Though there was a large break between the 7th conference in 1988 and the resumption under a new title in 2006, the initial EPNM conferences set the stage for many other developments. Several other regional countries had developed expertise and the locations of practice had also expanded within Russia. In addition to Novosibirsk, a significant region of explosive welding research existed in Volgograd, Russia.

With the dissolution of several of the communist governments the door opened for some private commerce in eastern Europe that may not have flourished earlier. For example, Explomet, a Polish explosion welding company, was founded in 1990, and Bitrub International, Ltd was founded in Barnaul, south of Novosibirsk in 1992. Innovations in the region continued, notably developing steel/titanium joining in an argon environment [26] in the early 2000s, and the EPNM conference series continues as a marketing platform, with the most recent occurring in May of 2018. These conferences and others have provided additional outlets for an expanding set of researchers. In this time period, Japan continued its history of significant contributions, working on modeling and other technique developments. Further, many other countries began to make frequent contributions. Amongst the published works on the topic China, India, Turkey, Iraq, and Iran, as well as a wider set of European countries have become contributors to the body of knowledge.

2.2 FUNDAMENTALS AND MECHANICS OF EXPLOSIVE WELDING

With the long history in this field, there has been significant time for development of the fundamental mechanical principles. It is intended provide an extensive review of this subject matter, but with focus on key topics of debate and areas relevant to research that was conducted in this effort. There will inevitably be gaps, in either emerging or well-established topics, where the reader will be referred to literature. Obviously emerging topics require journal research, but for the established content, several texts exist from several pioneers in the field, which could serve as great starting points. The following texts are comprehensive texts that either wholly or in part cover explosive welding, listed in order of publication in Table 2-1, below.

Table 2-1: Reference Explosive Welding Texts

Explosive Working of Metals, John S. Rinehart and John Pearson, 1962.[7]
The Physics of Explosive Hardening and Welding, Andrei Deribas, 1972.[44][16]
Principles and Practice of Explosive Metalworking, A. A. Ezra, 1973.[5]
Explosive Welding of Metals and its Application, Bernard Crossland, 1982.[6]
Explosive Welding, Forming, and Compaction, T.Z. Blazynski, ed., 1983.[4]
Explosion Welding of Metals, I.D. Zakharenko, 1990.[84] [17]

The text by Crossland was relied upon extensively, both as an introduction to the field, and as a reference of continued depth and detail as the study progressed. The compilation by Blazynski contains contributions from many notable names in the field and contains a comparable wealth of data. The works by Ezra and also Rinehart and Pearson are valuable earlier contributions, but

[16] This work only available in Russian.
[17] This work only available in Russian.

their focus on explosive welding is more limited. The texts in Russian have not been reviewed personally, but are both from accomplished researchers; Andrei Deribas especially is tremendously accomplished in the field. Additionally, a shorter summary can be found, authored by Liu et al for the American Society of Metals [85]. This review will cover explosive welding fundamentals, a description of the process and its design parameters, wavy bond interface formation, and characterization of the metallurgical bond.

2.2.1 EXPLOSIVE WELDING FUNDAMENTALS

Explosive welding[18] is a subset of metal joining processes, and specifically, a sub category of welding. As such, it important to understand the fundamentals of welding, to appreciate explosive welding's place in the taxonomy of welding, and, in a summary manner, appreciate the distinguishing features of the bond.

[18] Explosive welding can sometimes be referred to as explosive cladding. Cladding more generally is plate metal that is made up of two or more distinct-material layers of bonded by any generic means.

2.2.1.1 Metallic Bonding and Welding Details

At the atomic level, metals are bound together in one of the primary inter-atomic bonds. At the atomic level bonding represents an equilibrium position where attractive and repulsive forces achieve a minimum potential energy as shown in Figure 2-12. While many students are introduced to ionic and covalent bonds in their first chemistry class, perhaps hearing a mention of Van der Walls forces as secondary bonds, metallic bonding may not quite get the same billing.

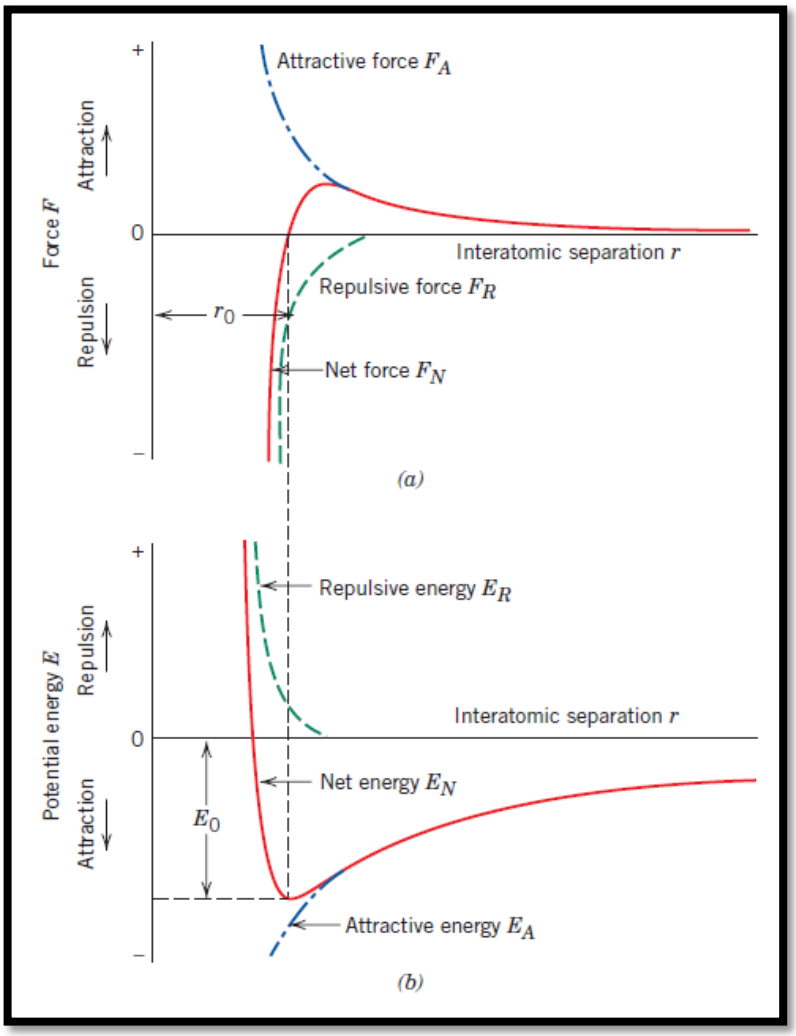

Figure 2-12: Representations of the forces in atomic bonding from Callister. [86] (a) A plot of the attractive, repulsive and net forces. (b) The potential energy associated with the forces involved, highlighting the equilibrium position.

However, it is the third primary bonding mechanism and the one at play in holding together metals. In metallic bonding, the atoms generally have a central positively charged core, while the one or two, 2s valence electrons at their outermost level participate in the "sea of electrons" that glue the positive cores together in some form of crystal structure. The reader is referred to Callister [86], or other introductory materials sciences texts for more detail. At first blush, all that is required for bonding is to get atoms close enough to allow these metallic bonding forces to take over. However, there are multiple other complicating factors.

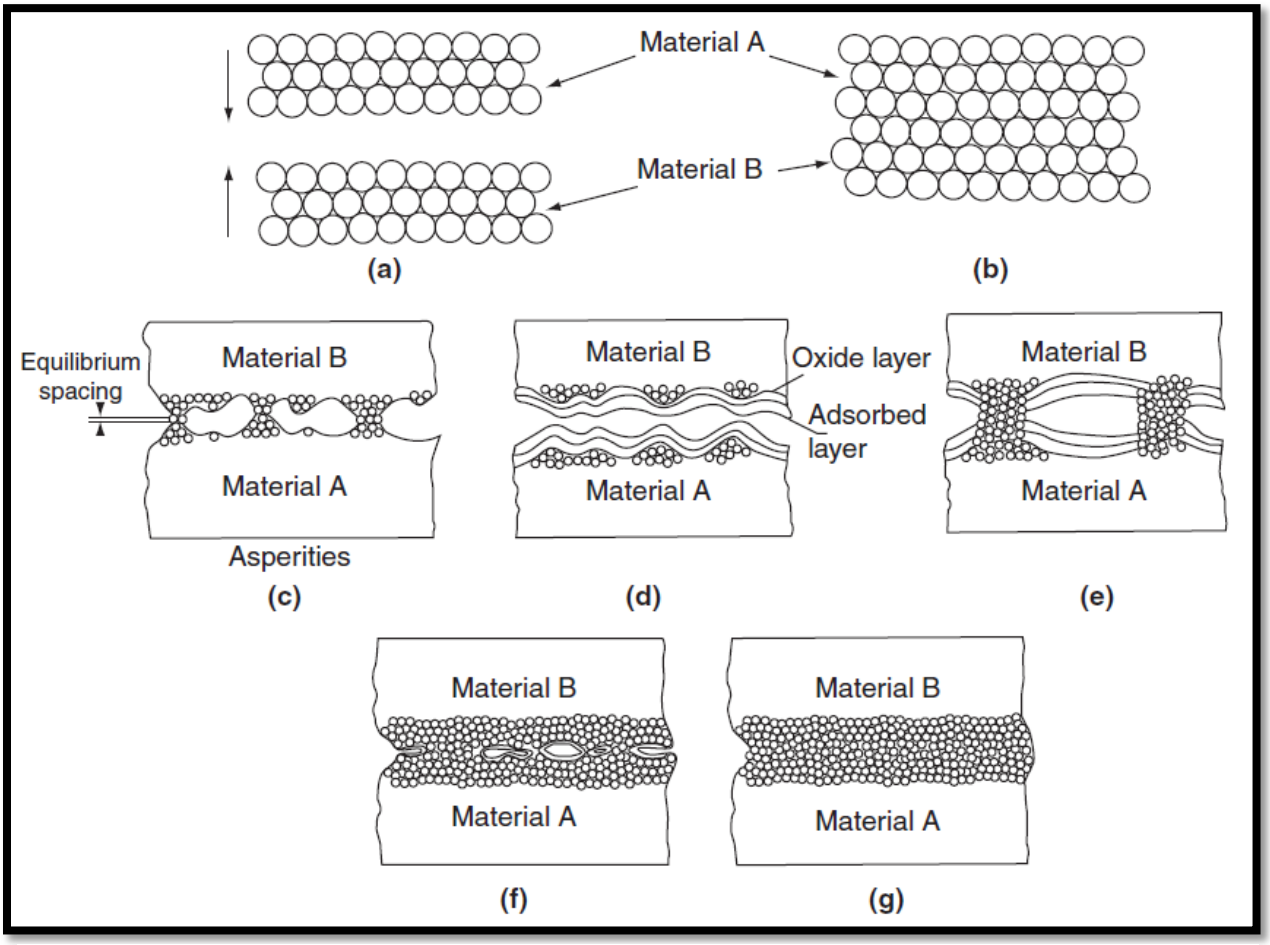

Figure 2-13: Depiction of ideal versus real metallic bonding of metal crystal structures. (a) and (b): Ideal crystal bonding where the joining surfaces close to a distance at a small fraction of nanometers allowing attractive atomic forces to complete the bond. (c) Asperities, or real surface irregularities can prevent atomic closeness over very high proportions of "flat" surfaces. (d) Oxides and potentially other contaminants often exist at the exposed surface of metals preventing contact of the two crystal structures. (e), (f), and (g): Potentially defective ways bonds can occur as a result. From [87].

In real joining, both the presence of contaminants and the true surface finish of materials come into play as shown in Figure 2-13. With regard to the surface finish, it is important to understand asperities. Asperities are surface irregularities at the atomic level that remain on surfaces machined to the strictest possible tolerance. If two of these "flat" surfaces are pressed together, it is estimated that only 1 in 10^6-10^8 atoms come into close contact. Additionally, oxides often form at the surface of metals, which put a different compound at the surface of the metal and prevent a metallic bond from taking place [87]. Different types of welding use different means to overcome these main obstacles, but it is also important to note that in dissimilar materials different crystal structures and other factors can impose additional barriers to bonding.

2.2.1.2 A Taxonomy of Welding

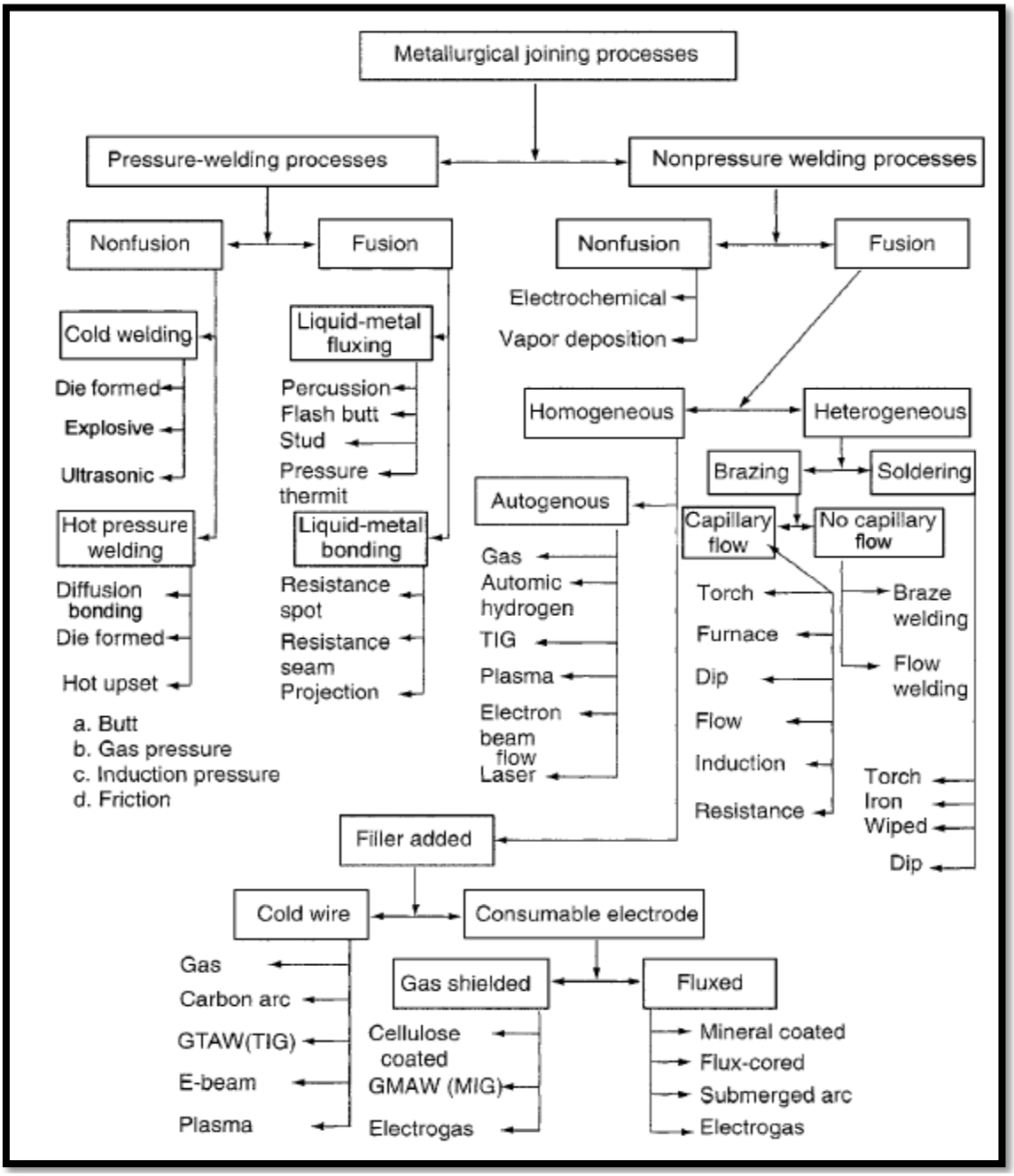

Figure 2-14: A taxonomy of welding processes according to Messler. [239]

Explosive welding is one among many welding techniques that successfully generate metallic bonding on previously existing metal surfaces. There are multiple ways to categorize welding techniques, but the most instructive, in the opinion of the author, is by organizing them according to the fundamental means they overcome the asperities and oxide contaminants that

otherwise limit joining. Messler compiled such a breakdown for the American Society of Metals, shown in Figure 2-14, which at its uppermost two levels separates processes based on their use of pressure and melting to overcome asperities and contaminants. The first means shown, "pressure" welds use high pressures and plastic deformations to deform asperities out of the way, breaking up oxides, and allowing bonding. Fusion processes, on the other hand, use melting (of either the metals to be joined or a filler) to close atomic distances and float impurities to the surface of the new bond. Pressure welds sometimes enjoy only partial success in making effective joints, and depending on the specific process may not produce as strong of a bond. Fusion welds are the more common variety of welds and are the ones engineers and the public are most familiar with. If a critique was to be made of the taxonomy in Figure 2-14 related to explosive welding, the author would suggest that a unifying category of "Impact Welding" be substituted for explosive welding, which would consist of explosive welding, magnetic pulse welding, laser impact welding, and vapor foil actuated welding.[19]

2.2.1.3 Summary of Bonding Features

Explosive welding, and all categories of impact welding, share several key distinguishing characteristics. They are placed in the non-fusion portion of the taxonomy as the joining does not explicitly rely on heat transfer into the metals, nor macro level melting as a means for generating bonds, but rather the intense pressures and deformations of impact. Though there are severe deformations in the region of the bonding zone, at a certain distance the metal grain structure can be largely unaltered, and the process can generate a bond stronger than the base metal. When done correctly, the technique does not have susceptibility to Heat Affected Zones, which can plague and limit fusion processes due to the sustained high temperatures and melting

[19] In defense of Messler, magnetic pulse welding, laser impact welding, and especially vapor foil actuated welding are much more recent technological developments.

that is involved. The process actually generates a metal jet between the plates, which removes the layers containing asperities and contaminants, allowing the pressures and shearing of impact to close the distance for bonding. The metals transition from largely undisturbed grains of the base metal, to highly elongated, sheared, and smaller grains near the bond. At the bonding surface the metals join with the other material in a layer that is only resolvable with Transmission Electron Microscopes. In certain cases, there are melt pockets, but in good welds these are not detrimental. The bond interface can also be smooth or wavy as shown in Figure 2-15. The process also enables the joining of many dissimilar metals that other processes cannot achieve as shown in Table 2-2.

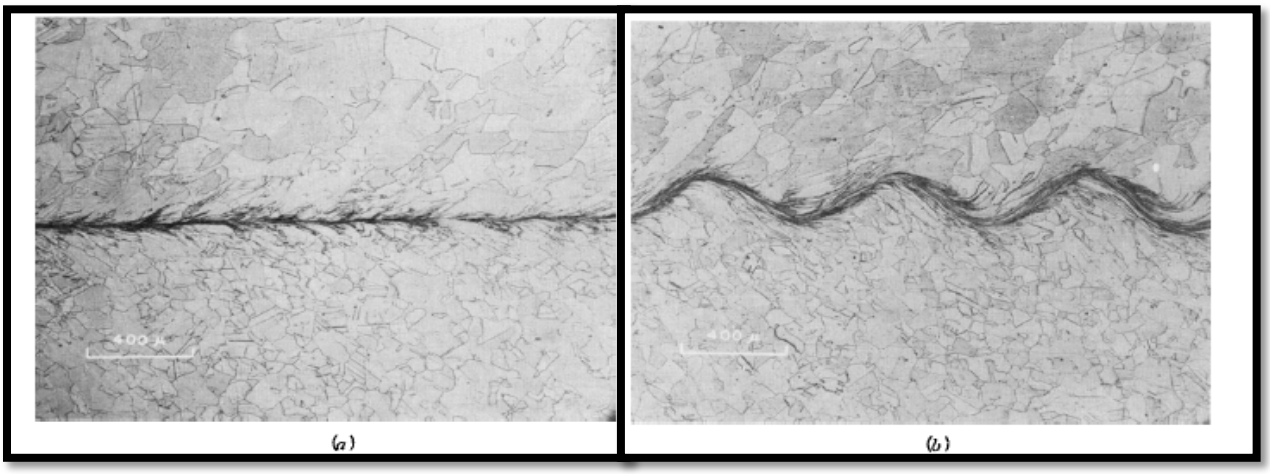

Figure 2-15: Smooth and wavy bonding interfaces possible in explosive welding. [54]

Table 2-2: Pairs of dissimilar metals that have been welded using explosive welding [85].

	Metal 2														
Metal 1	**Zr**	**Mg**	**Co alloys**	**Pt**	**Au**	**Ag**	**Nb**	**Ta**	**Ti**	**Ni alloys**	**Cu alloys**	**Al alloys**	**Stainless steels**	**Alloy steels**	**Carbon steels**
Carbon steels	X	X	X	...	X	X	X	X	X	X	X	X	X	X	X
Alloy steels	X	X	X	...	...	...	X	X	X	X	X	X	X	X	...
Stainless steels	X	...	X	...	X	X	X	X	X	X	X	X	X	...	...
Aluminum alloys	X	X	...	...	X	X	X	X	X	X	X	X	...	...	...
Copper alloys	X	...	...	...	X	X	X	X	X	X	X	...	...	...	...
Nickel alloys	X	X	X	X	X	...	X	X	X	X	...	...	...	...	...
Titanium	X	X	...	...	...	X	X	X	X	...	...	...	...	...	...
Tantalum	X	...	...	...	X	...	X	X	...	...	...	...	...	...	...
Niobium	...	...	...	X	...	...	X	...	...	...	...	...	...	...	...
Silver	...	...	...	...	...	X	...	...	...	...	...	...	...	...	...
Gold	...	...	...	...	...	...	...	...	...	...	...	...	...	...	...
Platinum	...	...	...	X	...	...	...	...	...	...	...	...	...	...	...
Cobalt alloys	...	...	X	...	...	...	...	...	...	...	...	...	...	...	...
Magnesium	X	X	...	...	...	...	...	...	...	...	...	...	...	...	...
Zirconium	X	...	...	...	...	...	...	...	...	...	...	...	...	...	...

2.2.2 Process Description and Welding Design Parameters

In the course of establishing the body of knowledge in the field of explosive welding, researchers identified common successful configurations, converged on a shared understanding of the best description of the process using a fluid analogy. They built upon this foundation to develop the concept of a weldability window that is used to identify input-parameter-based regions of successful welding for the design of welds. In this work, the welding of planar geometries will be the focus, but cylindrical and even more complex geometries can be achieved.

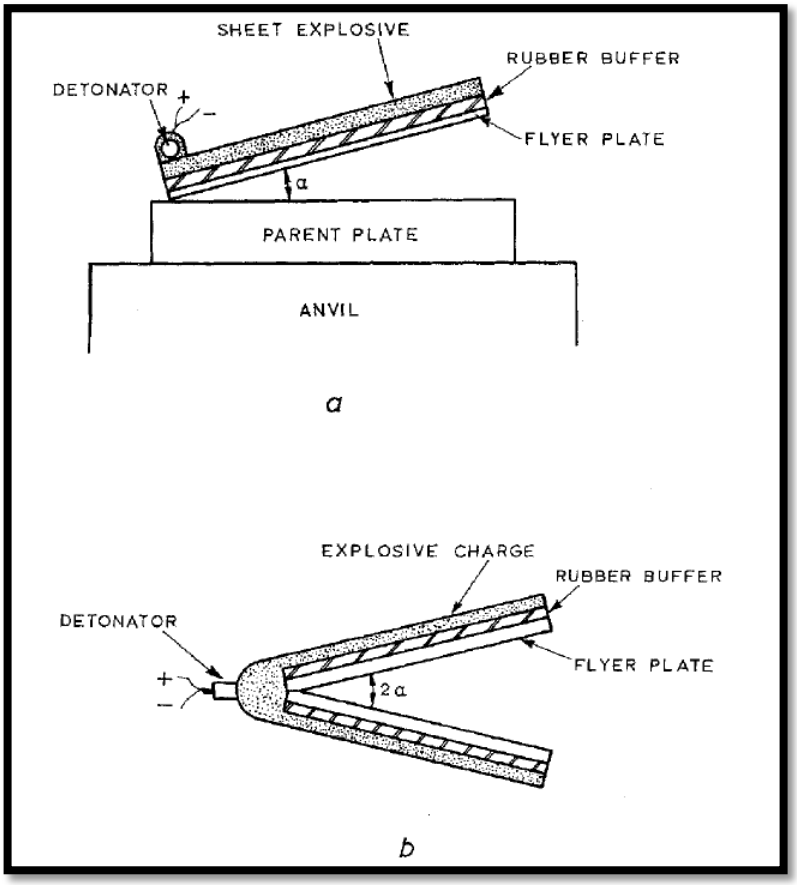

Figure 2-16: Primary flat plate geometric welding configurations. (a) Asymmetric welding. (b) Symmetric welding. (Symmetry only intended with respect to geometry; not material properties) [45]

2.2.2.1 Typical Welding Geometries and the Kinematics of the Process

The basic geometric arrangements for planar welding are shown in Figure 2-16. When viewed in a two-dimensional cross section, it isn't possible to distinguish between a planar and a cylindrical configuration despite obvious differences in three dimensions. In a cylindrical case, a 2D representation could look similar to Figure 2-16a, but with an axis of rotation oriented horizontally above the flyer plate and explosive. More advanced and complicated geometries have been welded. For examples, see figures shown in the book by Ezra [5, pp. 210–219].

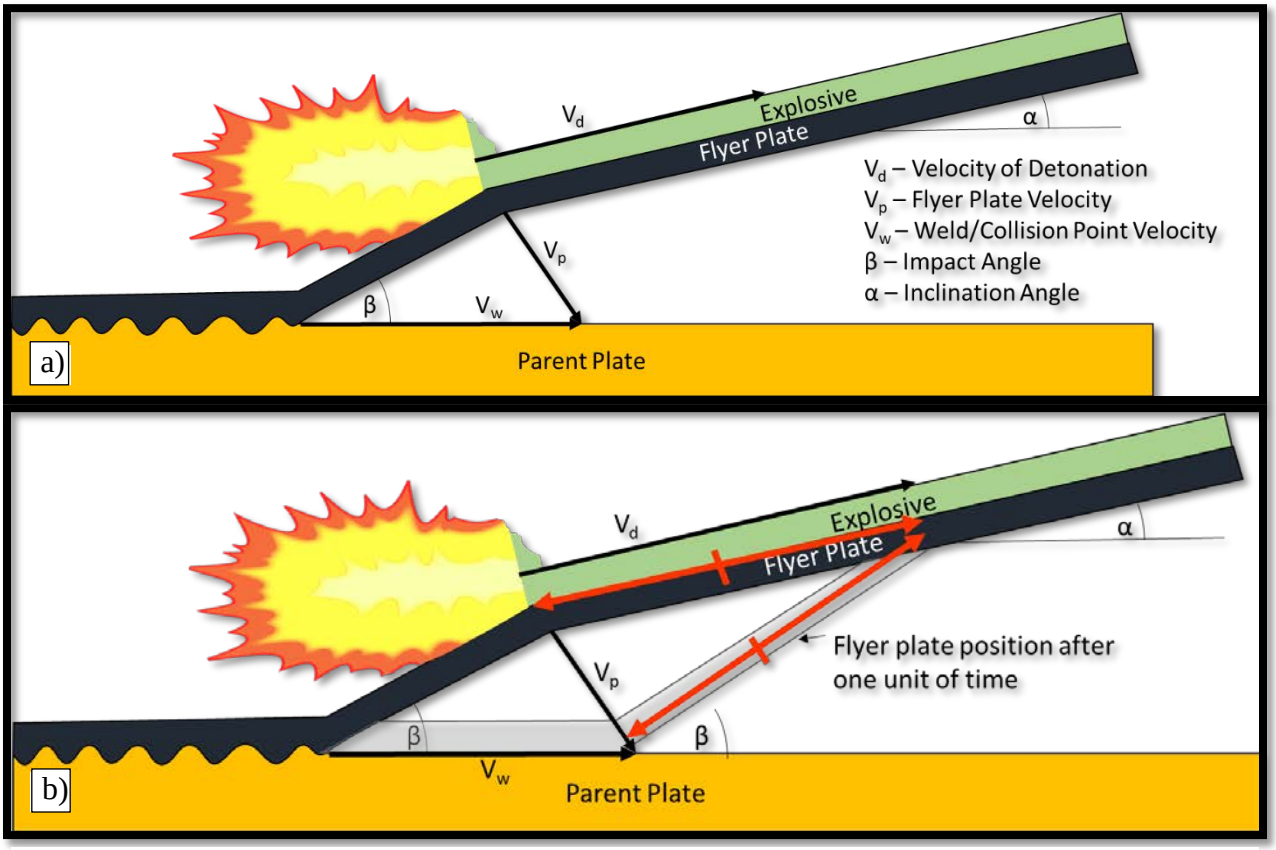

Figure 2-17: Simplified and commonly assumed kinematics of explosive welding motion. (a) The process at time t during execution with relevant approximate angles, and velocities labeled. (b) The process at time t and then at time t +1 unit of time (shaded segments that meet at the V_p and V_w vector tips). In red, a key assumption is that the length of the flyer plate that is put into motion is fixed and has appeared to hinge only at the new detonation point.

In Figure 2-17, the welding process is shown only partially executed. Although the welding event appears nearly instantaneous to the observer, it is actually finite in time, occurring

over a period of micro seconds, depending upon the dimensions to be welded. Figure 2-17(a) lists the idealized geometry, which ignores certain physical curving that inevitably occurs. The flyer plate (sometimes called the prime metal) is propelled by explosive, where the detonation progresses down the length of the flyer. Regions are shown where the flyer has already impacted and welded, where it is in flight downward, and where it has yet to be accelerated by the detonation. The bottom plate is known as the parent plate (sometimes also the backer or target plate), and rests on an "anvil" serving the purpose to eliminate end product gross deformations. The initial angle of inclination for the flyer, α, can be non-zero, but for many practical reasons to be detailed later, it is often equal to zero. Under the acceleration of the detonating explosive, the angle of the flyer plate is changed so that it is inclined at a new angle, the impact or collision angle, β[20], relative to the parent plate. The explosive is assumed to detonate at a constant rate, V_d, and the plate is also assumed to have an average velocity vector represented by V_p. The point at which the flyer plate has just touched the parent plate is the collision or impact point, and the rate it moves down the parent plate is termed the velocity of welding or velocity of collision, V_w or V_c.

Having established the starting point of typical welding configurations, the progression of the process can be detailed. What follows is primarily based on Birkhoff's work [8].

Figure 2-17b represents the average kinematics that are assumed by moving one unit forward in time from Figure 2-17a. In this scenario, all the magnitudes of all the velocities become numerically equal to the corresponding distance they have travelled in the unit of time. This geometry is further elaborated in Figure 2-18, and it is assumed the reader will be able to quickly follow the geometry that is shown in specifying all the different resulting angles. This

[20] γ is also a popular variable for this angle.

allows the establishment of relationships between the velocities. Starting with triangle CDF, it is clear that the following relationship holds:

$$\sin\left(\frac{\beta-\alpha}{2}\right) = \frac{\frac{1}{2}V_p}{V_d} \tag{2-1}$$

Using triangles ABS and BCS, equating relations for adjoining segment BS yields:

$$V_w \sin(\beta) = V_p cos\left(\frac{\beta-\alpha}{2}\right) \tag{2-2}$$

Again, this geometry was established by Birkhoff, and is one of several commonly assumed governing relationships, which essentially make different assumptions about the direction of the flyer plate velocity. This and other commonly assumed relations are shown in El-Sobky's contribution to Blazynski's compilation [4, p. 198].

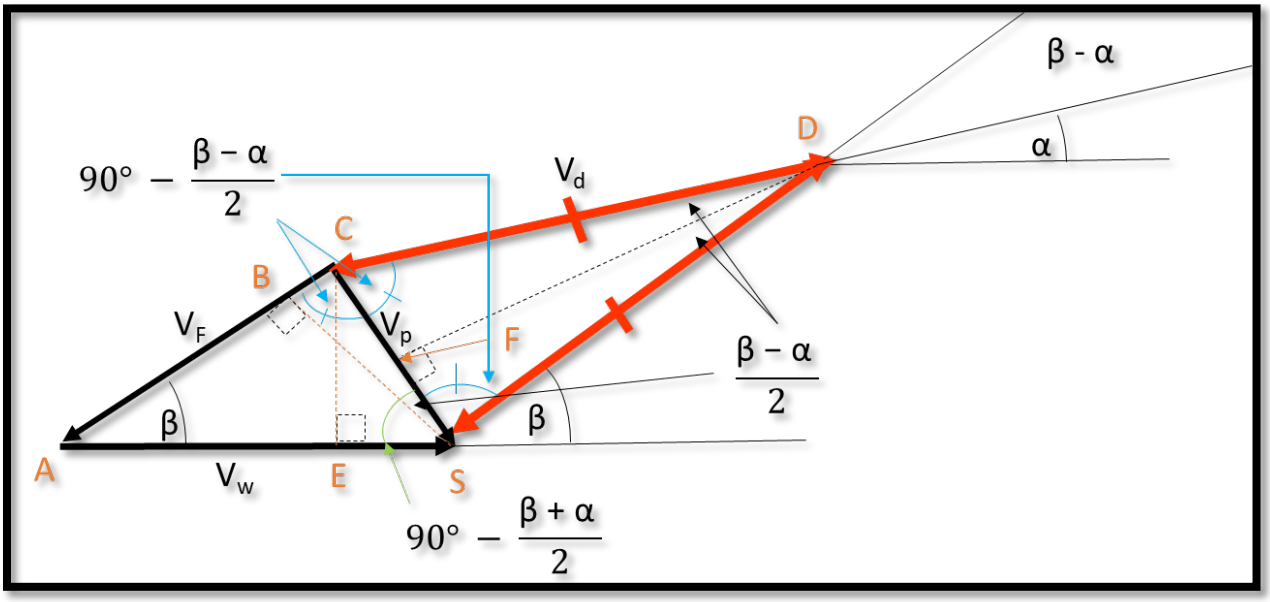

Figure 2-18: The geometry of motion assumed in the passage of one unit of time, with the key assumption that length of the flyer does not change. (segment CD at time t versus segment SD at t +1) This results in the plate velocity bisecting the interior angle ACD. In a unit of time the distance traveled becomes numerically equal to the respective velocities.

2.2.2.2 The Fluid Analogy and Jetting

Up to this point, the description of the kinematics has been articulated using a coordinate system that is fixed in space with an observer of the welding event. Upon connecting this welding mechanism to Birkhoff's explanation of shape charges [8], it became clear that the same fluids-based analysis could be applied. Explosive welding is best explained using an analogy based upon the flow of fluids in an inviscid and incompressible state, which uses a coordinate system that moves with the collision point. It is a very common reaction to balk at the idea that this inviscid fluid model can be an appropriate description of the behavior of metals, yet this analogy has stood the test of time.

In this approach, the velocity of the collision point, *S*, is zero, and instead the parent plate moves (to the left in Figure 2-18) past it at a speed of V_w. The flyer plate motion, rather than down and to the right as shown in Figure 2-18, becomes the flow velocity V_F that is shown moving down and to the left in this traveling coordinate system. Using segment triangles ACE and CES, and equating expressions for segment CE, an equation relating this flow velocity to other parameters can be formulated. With the added idealized assumption that the parent plate is rigid, a steady flow fluids problem is presented in Figure 2-19 that enables several very valuable first order approximations.

$$V_F \sin(\beta) = V_p cos\left(\frac{\beta + \alpha}{2}\right) \tag{2-3}$$

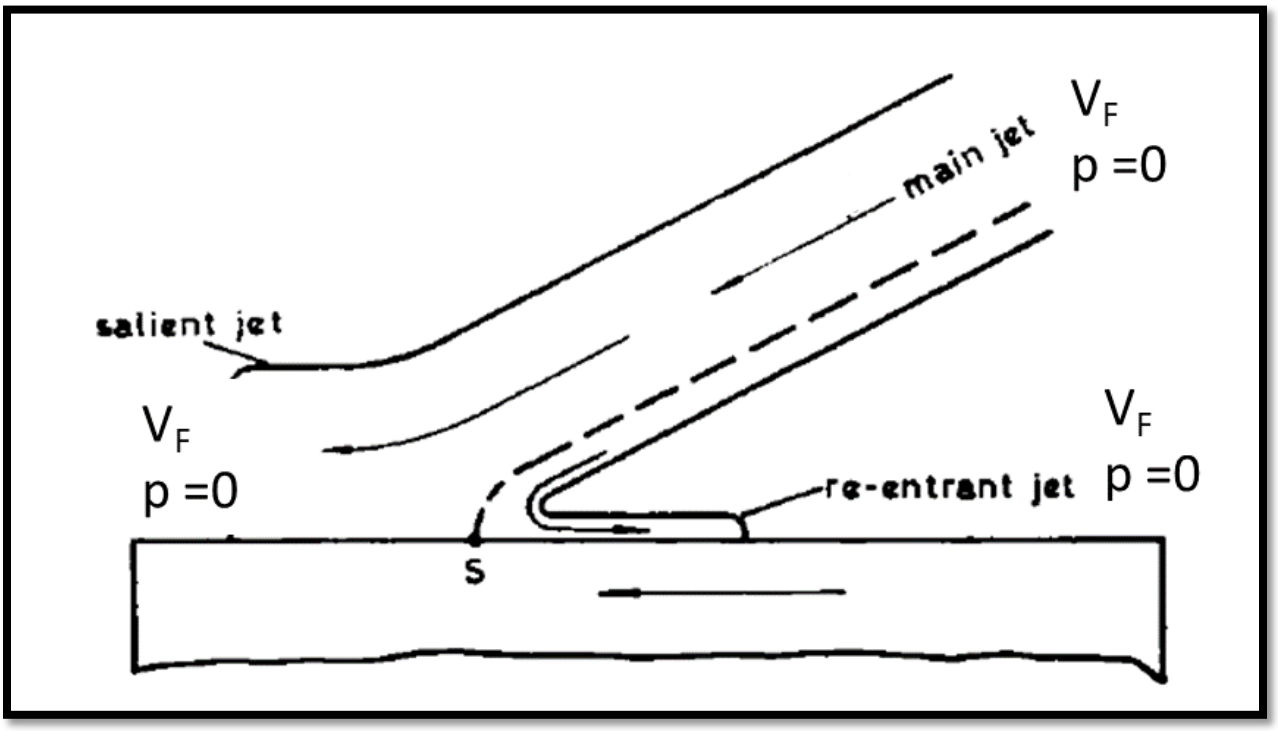

Figure 2-19: An idealized model assuming inviscid and incompressible fluid flow. Figure adopted and modified from [240]. The first similar figure can be found in [32].

The streamlines of the flyer plate flow in Figure 2-19 are divided by the streamline ending at point *S*, the stagnation point. Material up and to the left of that streamline separates to the left forming the salient jet or slug, and material to the bottom right becomes the re-entrant jet (commonly just "jet"). In this configuration, the Euler-Bernoulli equations for the conservation of energy apply directly along a streamline as shown in Equation (2-4).

$$p + \frac{1}{2}\rho V_F^2 = constant\ on\ streamline \tag{2-4}$$

In Equation (2-4), p is pressure and ρ is material density. This illustrates what is shown in Figure 2-19, which is that if velocity goes to zero, all energy is converted to pressure. Alternatively, if we are infinitely away from the stagnation point, we can assume that the flow returns to speed V_F, and the pressure to zero, or the reference pressure. Stagnation pressure is

then shown in Equation (2-5) after equating portions of Equation (2-4) for point *S* and the point where reference pressure is assumed and V_F is the velocity.

$$p_S = \frac{1}{2}\rho V_F^2 \tag{2-5}$$

If we are using the portion of the jet that returns to zero/reference pressure, we can establish an estimate for the velocity of the jet, which is shown in Equation (2-6).

$$V_j = V_w + V_F \tag{2-6}$$

Given our incompressible assumption, ρ never varies from initial mass over a fixed differential volume, and this scenario can be considered representative of what occurs to a fixed mass for a differential length of flow of the flyer.

Taking the approach of considering a fixed mass, an equation expressing conservation of linear momentum in the horizontal direction can be expressed in Equation (2-7).

$$m \cdot V_F \cos(\beta) = m_s V_F - m_j V_F \tag{2-7}$$

Here m is the full original mass of the segment, m_s is the mass of that segment that flows into the salient jet, and m_j is the mass that flows into the re-entrant jet in Equation (2-8).

$$m = m_s + m_j \tag{2-8}$$

Combining these two expressions and noting with our assumption of incompressibility that a fixed volume can be chosen to be a unit area times the thickness of the plate or jet, these equations result in expressions for the mass or thicknesses, of the jet and slug relative to the original mass or thickness of the flyer *(*m or t_f).

$$m_j = \frac{m}{2}(1 - \cos(\beta)) = m \cdot sin^2\left(\frac{\beta}{2}\right)$$
$$t_j = \frac{t_f}{2}(1 - \cos(\beta)) = t_f \cdot sin^2\left(\frac{\beta}{2}\right) \quad (2\text{-}9)$$

Note the second version of Equation (2-9) is a simplification by a power reduction trigonometric identity, which is included for reference later. All in all, this idealized model provides many useful estimates of the behavior of explosive welding, even though it isn't exactly what is known to occur. For example experimental jet velocities reported in [88] were roughly 26% slower than the hydrodynamic prediction on average.

It was long acknowledged that the idealized model did omit real behaviors. Notably, it is assumed the parent plate is rigid and does not contribute to the jet. This has been shown to not be the case, for example in [89], [90]. Figure 2-20, below, was one early depiction of a more detailed flow.

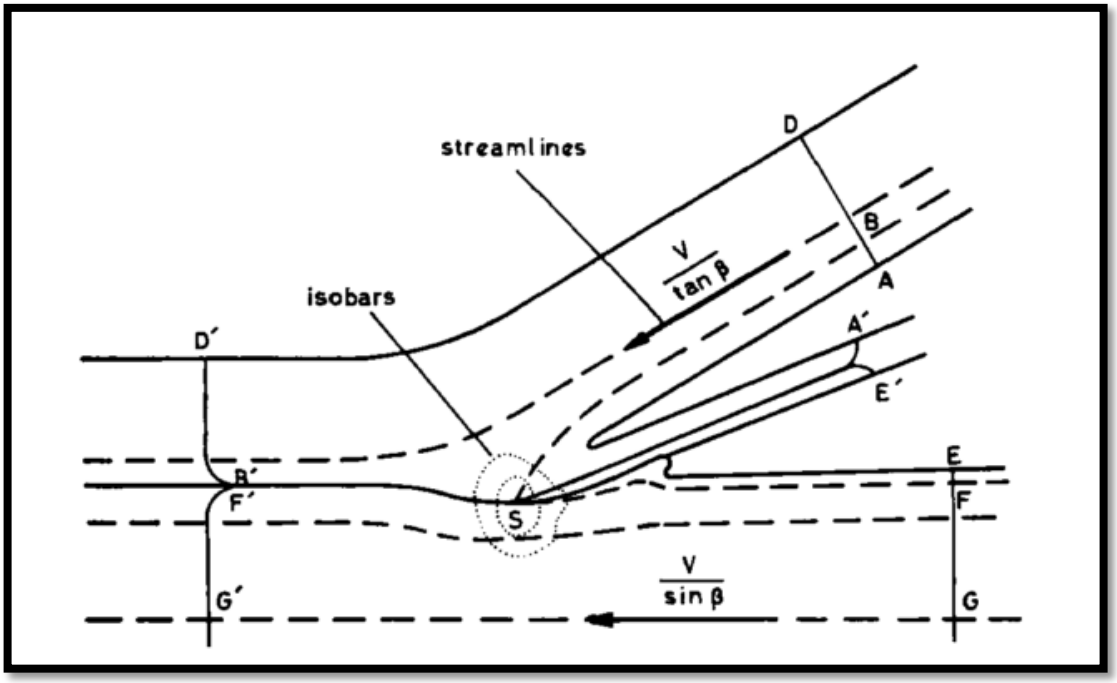

Figure 2-20: More realistic depiction of flow in coordinate system moving with the collision point. [240] Note in this case the direction has been assumed to be normal to the flyer for the plate velocity.

2.2.2.3 The Weldability Window and the Design of Planar Welds

As the understanding of the explosive welding process became more established, research began to focus less on what was happening during explosive welding and more on how to predict when a positive result could be expected. Different researchers suggested many different things. Though some current researchers are focused on trying to shift the bonding criteria into more fundamental physical and thermodynamic parameters such as that shown in Figure 2-21, researchers in the late 1960's and early 1970s were focused on things they could reliably measure. As the behavior of explosives was something very difficult to control and quantify, a number of researchers listed explosive loading (i.e. explosive mass versus flyer mass) as a metric. It was common to provide flyer plate standoff prescriptions [6, pp. 87–91]. Also the parameters used in the hydrodynamically-based equations above became critical. Empirical limits began to be tracked, and while some researchers preferred to use the velocity of the plate,

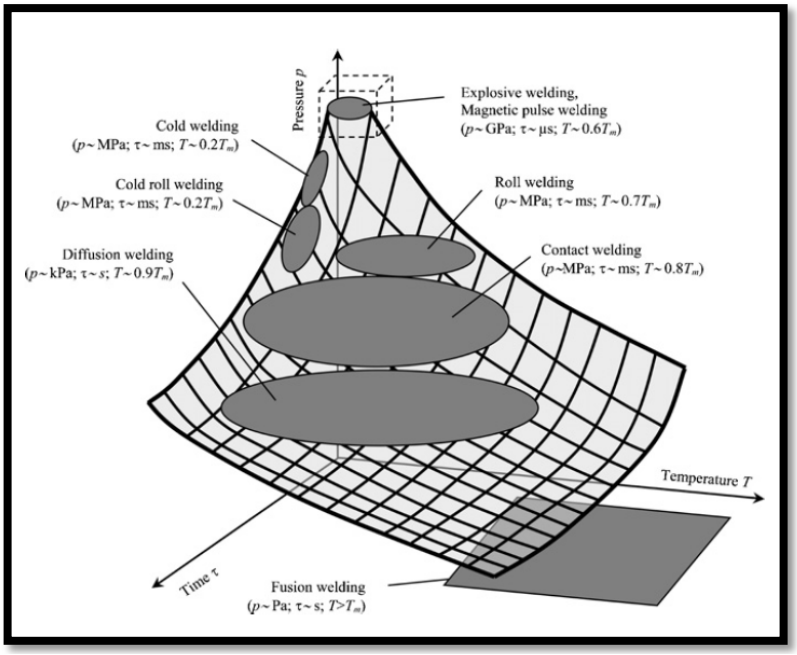

Figure 2-21: Welding processes in pressure, time, and temperture coordinates, proposed by Lysak and Kuzmin [121], in a part of their work to propose welding based on criteria such as pressure deforming impulse and temperature distribution during welding.

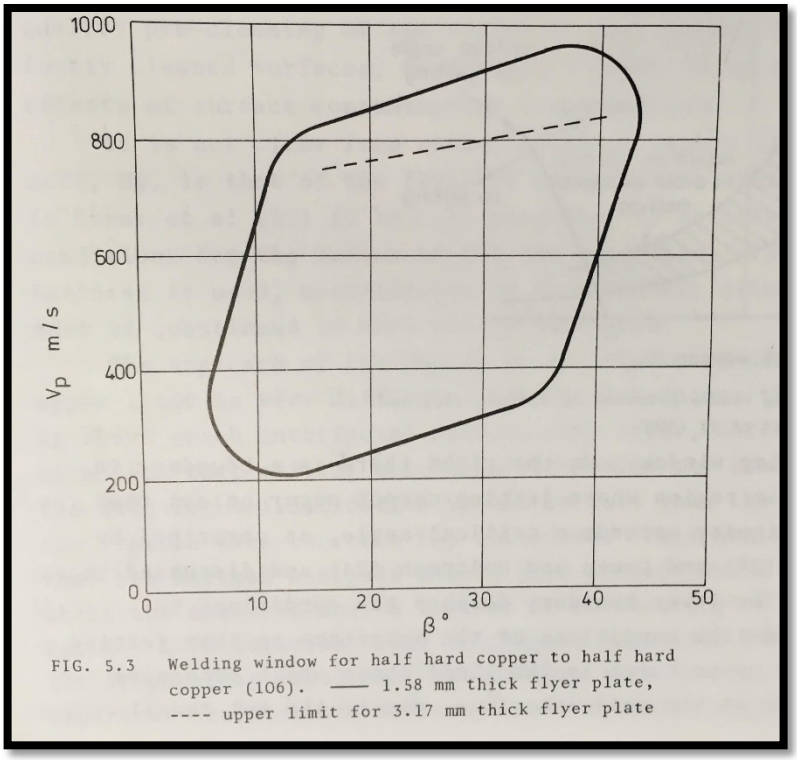

Figure 2-22: Alternative welding window based on flyer plate velocity, V_p, and impact angle, β, developed by Szecket in work with Crossland and McKee. [6], [120], [241]

V_p, and the impact angle, β, as shown in Figure 2-22, eventually, empirical limits of a welding window came to commonly be presented in terms of weld velocity, V_w, and impact angle, β.

Although Crossland credits Deribas and Wittman for the use of these coordinates [6, p. 96], that may have been done due to their influence within the field and their specific contributions to the use of this space, rather than on them being the first to to present it in 1973 and 1975. In fact, in 1971, researchers used weld velocity, V_w, versus impact angle, β, coordinates in discussing other important factors [54], and then in 1972, Zakharenko appears to have been the first to "… determine in these coordinates the region of conditions under which there will take place welding of the material." [91] In 1973 though, Wittman's presentation of this welding window was detailed with a full set of proposed boundaries. It also presented an argument on how this space eliminated variables related to the specific explosive and explosive

loading, as well as to the initial inclination of the plates, α [92]. Deribas et al, in 1975, proposed specific additional formula to identify upper and lower boundaries [93].

This welding window quickly became the standard for recording the bounds of effective welding. It was bounded by a critical flow transition weld velocity, $V_{w,}$ on the left[21] and a maximum weld velocity on the right that was based on impact angle and the speed of sound in the metals involved. On the bottom, a pressure and plate-velocity-based curve provided a lower bound, and another curve based on the maximum plate velocity before deleterious effects served as the upper bound. This general technique for recording and predicting the weldability of metals remains as the industry standard today, with minor variations. Each boundary will be detailed below.

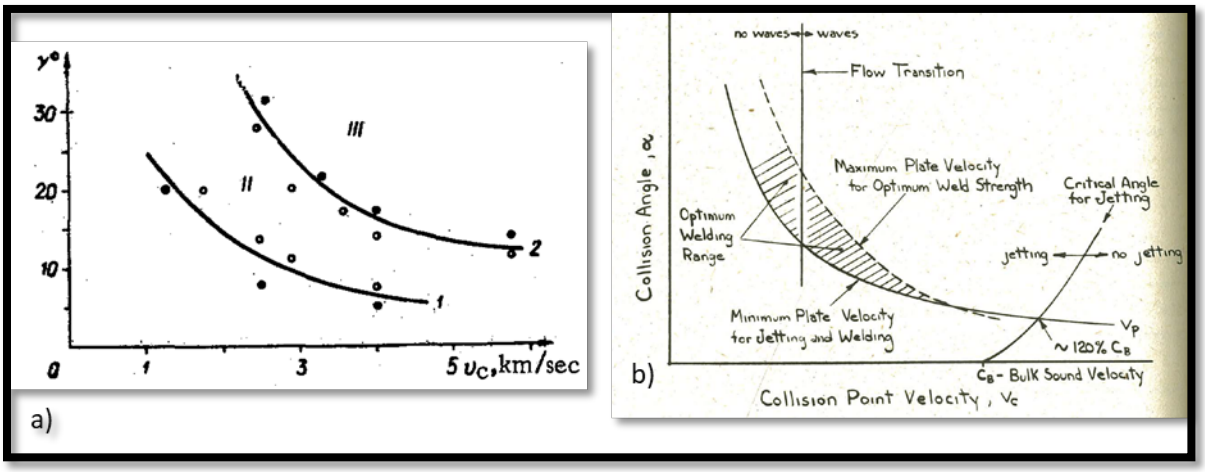

Figure 2-23: Introductory weld windows in weld velocity, V_w, versus impact angle, β, space. a) Zakharenko's first use with upper and lower boundaries [$V_w \leftrightarrow v_c$, $\beta \leftrightarrow \gamma$] [91] b) Wittman's proposed window showing all four common limits. [$V_w \leftrightarrow v_c$, $\beta \leftrightarrow \alpha$] [92]

- Lower Boundary: Minimum Plate Velocity to Achieve Critical Impact Pressure

For the lower boundary, sufficient momentum and kinetic energy must be imparted into the flyer plate prior to impact. This is required in order to achieve a minimum critical impact

[21] The left limit has developed more disagreement over time. It was based on an assumption that wavy welds were required for strong bonds, which has become disputed.

pressure at the stagnation point, in accordance with the hydrodynamic analogy [see Equations (2-5) and (2-3)]. Wittman proposed an expression for this limit based on a value five times the Hugoniot Elastic Limit (HEL) of the material, or in its absence, based on its ultimate tensile strength, σ_U, as shown in Equation (2-10)[22]. [92]

$$V_p = \sqrt{\frac{5 \cdot HEL}{\rho}} \approx \sqrt{\frac{\sigma_U}{\rho}} \tag{2-10}$$

Deribas subsequently proposed the relationship shown in Equation (2-11) in 1975, where H_V is the Vicker's hardness of the softer material, ρ is its density, and k is an empirical constant varying from 0.6 for perfectly cleaned surfaces to 1.2 for unprepared surfaces [93].

$$\beta = k \sqrt{\frac{H_V}{\rho \cdot V_w^2}} \tag{2-11}$$

- Right Boundary: Maximum Weld Velocity and Associated Minimum Angle

For the right boundary, shock behavior must be accounted for. If the welding or flow velocity, V_w or V_F[23], exceeds the bulk/dilatational speed of sound in any of the metals involved, this creates shock fronts ahead of the collision point during welding. Walsh, Shreffler, and Willig in general, and Cowan and Holtzman for explosive welding, showed that if these shock fronts are attached to the collision point, then there is no high-pressure region in the metal adjacent to free air/space in order to allow jetting. [31], [43] In either metal, once the weld velocity, V_w, reaches the metal's speed of sound, in order to detach the shock, the metal must have its flow diverted by a minimum angle from the flow of the outgoing slug. Cowan and

[22] For use in Equation (2-2).

[23] These values are quite close and are often used interchangeably, especially since more common parallel arrangements make these values equal.

Holtzman provide the details for finding this limit using the material's Hugoniot data in conjunction with conservation of mass and momentum equations and a geometric relation to the minimum angle [43]. Some authors use other simplified metrics including limiting the weld velocity to 1.25 times the speed of sound in the metal. Others suggest a simple linear relationship as shown in Equation (2-12), where β is in radians and V_w is in mm/μs [94], [95]. Equation (2-12) is included for illustrative purposes and has not been found outside of the references cited.[24]

$$V_w = \frac{\beta}{10} + 5.5 \tag{2-12}$$

- Upper Boundary: Maximum Kinetic Energy Before Excessive Melt/Brittle Compounds

As the flyer plate is propelled faster, it gains kinetic energy. Upon impact, if there is too high of a speed, the kinetic energy of motion generates too much heat in the metals, and it can lead to melting. Melting obviously is not always detrimental to welding, or else all fusion welding categories from Figure 2-14 would not exist. However, there are two limits that

[24] Both references cite [32], but it is not apparent where this equation is in Abrahamson's work and it may be another's derivative of his presentation. It is clear the last term should be the metal's sonic speed. It is included as an illustration of an alternative between a detailed analysis and a wrote factor of 25%.

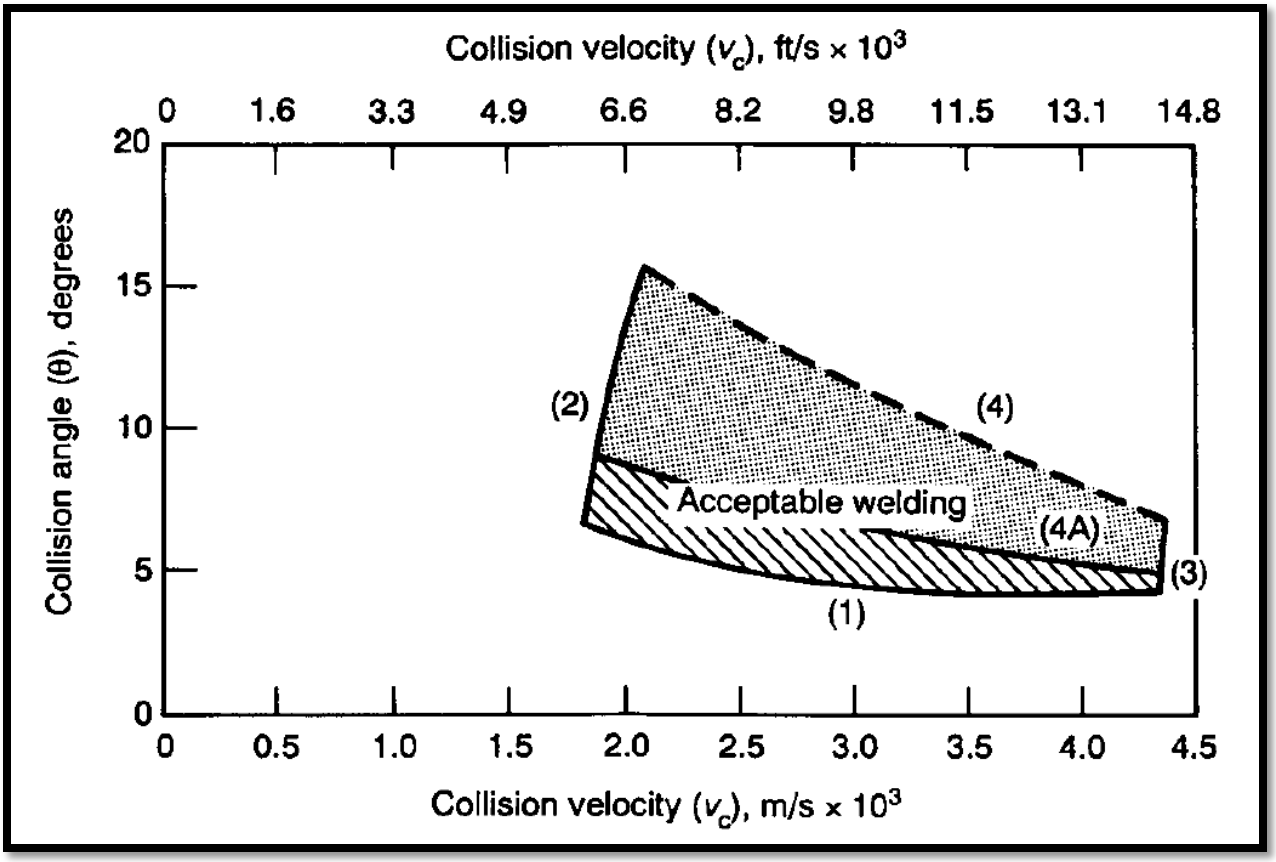

Figure 2-24: Explosive welding window as shown in Liu, Banker, and Prothe depicting two upper limits based on the types of metals welded (4A vs 4). [85]

come into play. The first (4A in Figure 2-24), occurs when one is welding metals prone to forming brittle intermetallic compounds [85]. In this scenario, impact welding may be one of the few (or the only) viable means of welding because when mixed in a molten or near molten state, the metals form compounds that alter the bond to an unusable state. The second is more similar to the limits on heating in fusion welds. Namely, a number of common issues from heat affected zones appear: grain growth after recrystallization, re-dissolution and phase change of precipitates for metals that are precipitate hardened, and for large melt pockets/layers, contraction during solidification leaving cracks and voids. An expression for this limit can is shown in Equation (2-13), from Wittman[92], but Deribas also has a similar expression [93].

$$V_p = \frac{1}{N}\frac{\sqrt{T_{mp}C_B}}{V_w}\frac{\sqrt{kCC_B}}{\sqrt[4]{\rho t_f}} \quad (2\text{-}13)$$

Here, T_{mp} is melt point, C_B is the bulk/dilatational speed of sound in the metal, k is the thermal conductivity, C is the specific heat of the material, ρ is the metal density, V_w is weld velocity, and t_f is the thickness of the flyer plate.

- Left Boundary: A Complicated Case of Competing Issues

Although in Figure 2-23 Wittman shows a vertical line for flow transition, with some acceptable welding still occurring at lower welding speeds, V_w, many have taken the flow transition as a bounding limit for good welding. Clearly Wittman did not necessarily agree, and this boundary is still not definitively resolved in current literature, foreshadowing some discussion in Chapter 4.[25] Wittman, included this transition based on the work of Cowan, Bergman, and Holtzman. Neither the requirement of a wavy interface as a threshold for good bonding, nor the fixed weld velocity as a transition from a smooth to wavy bond are universally accepted. It is interesting to note that Deribas did not typically include this limit in the welding windows he would depict, as late as 1989 [96]. Both wave formation and the nature of the bonding interface will be discussed in detail later in Section 2.2.3 and 2.2.4.

In the absence of a wavy bond interface as a requirement resulting in the left limit, it is clear that there are practical considerations that come into play, without generating an exact limit on the left side of the window. The shape of the lower boundary increasingly requires larger impact angles, β, as the weld velocity, V_w, decreases. Achieving these larger angles at some point either requires inclining the flyer plate or finding slower detonating explosives. Aside from the point that other researchers have suggested maximum impact angles in general [4, p.

[25] In short, the criteria for successful welding varies with its anticipated requirements in use.

203], inclining the flyer can have impacts in large cladding as standoff increases too much [6, pp. 115–116], and there is a minimum on the detonation velocities of acceptable explosives. These considerations have not been formalized, but clearly limit the left hand bound of the welding window, even in the absence of the wavy weld criteria.

- Design of Welds

Crossland and Blazynski offer the most detailed compilations of the considerations for designing welds, but it is intended to provide the quick version for a researcher trying to achieve their first successful bond. Once a pair of metals, either similar or dissimilar, are selected for welding, the immediate task is identifying the empirical weld window for the materials. In the absence of an existing empirical window, one can be assembled using material properties. Equations (2-11) and (2-13) can specify the upper and lower boundaries based on material properties. Either Hugoniot data and the process of Cowan and Holtzman [43] can specify the right boundary, or a crude metric such as 1.25 times the speed of sound or a variant of Equation (2-12) can be used. If a distinction between smooth or wavy bonding is desired, either an empirical data set or the relation shown in Section 2.2.3.2 and Equation (2-17) below, can be added to the window to inform that decision.

With a window in hand, a designer can start to address the independent variables they have. Namely the flyer inclination, α, the plate velocity, V_p, and the selection of the explosive. There are a few considerations to include. First, the selection of flyer inclination, as mentioned above, has effects on the standoff at the end of the plate, with too much standoff causing problems such as whipping the end of the plate [6, pp. 115–116]. Second, the velocity of the plate can be tailored based on the amount of explosive used. And third, the type of explosive sets your detonation velocity, with minor variation based on explosive thickness. In short, you

have three independent variables, initial flyer plate inclination, α; flyer plate velocity, V_p; and explosive detonation rate, V_d. The plate velocity must be between your lower and upper bounds, Equations (2-11) and (2-13), but where is your choice.

For selecting the plate velocity desired, there are a number of additional details to consider for arriving at your required specifications. A specific flyer plate velocity traces out a curve that is shifted up or down from boundary 1 or Equation (2-11). For a given flyer plate velocity, V_p, you can change your welding condition along that curve either by varying the explosive detonation velocity, V_d, or by varying the flyer plate initial inclination, α. Modeling with appropriate explosive parameters for a given explosive and explosive thickness can successfully predict the flyer plate's velocity versus time distribution, allowing both identification of the terminal velocity and the required standoff to achieve that velocity. Alternatively, the modified Gurney equation for the open-faced sandwich configuration can be employed to estimate the terminal velocity of the flyer, and a rule of thumb based on flyer thickness can be applied. An example standoff rule of thumb listed by Crossland is that standoff be greater than 50% of the flyer thickness (i.e. $d > \frac{1}{2} t_f$ where t_f is thickness of the flyer). The open-faced sandwich Gurney equation mentioned above is Equation (2-14) below. It is based on the Gurney energy, $\sqrt{2E}$, which is tabulated for many explosives, and the ratio of the mass of explosive to the mass of the flyer plate per unit area, R.

$$V_p = \sqrt{2E}\left\{\frac{\left(1+\frac{2}{R}\right)^3+1}{6\left(1+\frac{1}{R}\right)}+\frac{1}{R}\right\}^{-\frac{1}{2}} \tag{2-14}$$

For selecting your explosive, there are some considerations that are flexible, but in many ways, there are more limitations. Due to the right limit of the welding window, for example

Equation (2-13), and the relations in Equations (2-1) & (2-2), certain explosives that are otherwise desirable start become problematic. Sheet explosives which are easier to control, handle, and have more uniform, quality-controlled characteristics, also have significantly higher detonation velocities, which quickly surpass your bulk sound speed/impact angle limitation. Further, even if those explosives are used, they often deliver a given impulse with a shorter time duration (i.e. increased force), which can cause local damage if the flyer plate is unprotected. This can also generate reflected rarefaction waves that cause flyer plate spalling and even failure of some bonds. Especially for large plate cladding (a common application), detonation velocities around and under 4 mm/μs are preferable [6, p. 39].

Accounting for these factors, a designer selects parameters to choose their optimal weld conditions within the welding window. Additional considerations for the finer points still have to be determined. Buffers between the flyer plate and the explosive can limit damage to the flyer plate. The detonation front can be arranged to traverse the flyer plate in a specific direction/configuration for more process control, but initiation from a single point, allowing radial detonation, produces acceptable welds as well. Establishing the spacing between the flyer plate and the parent plate can be done with external devices, but sometimes the sag due to gravity in the flyer plate can be problematic. In that case though, spacers placed between the flyer and parent plate have been shown not to significantly affect the result, as they are expelled by the jet. Spall bars can be placed on the end of the flyer plate in order to further protect the edges of the flyer plate as the shock gets to the end of the plate. The preceding considerations are addressed in more detail by Crossland [6, pp. 117–124]. Additionally, as alluded to in the specification of Equation (2-11), the surface cleanliness of the welded plates should be considered.

The last choice to be made is what to use as an "anvil" for the welding process, i.e. what supports the bottom of the flyer plate. This is often done with rigid/deep and stiffer plates, but, at the other end of the spectrum, welding has been achieved in free flight. [70], [97] Air suspended welding is not likely to be practical, but it goes to show that welding can be successful without a rigid metal anvil. It is common to also use compacted sand or earth as an alternative [98]. Although Crossland does not spend much time discussing the anvil, suggesting its main consideration is economic and aimed at limitation of residual deformations, he does note compacted sand is effective [6, pp. 120–121]. However, according to Chadwick in [4, pp. 248–249], the selection of an anvil can have important effects based on its characteristic impedance[26], and he too suggests compacted sand.

2.2.3 Bond Interfacial Wave Formation

The wavy nature of many explosive welding bonds has intrigued, baffled, and otherwise occupied researchers for many years, since it was first observed. This wavy bond interface is a manifestation of a phenomenon first observed as wavy surfaces in general impact events [32], [99]. Within the field of explosive welding, this was among the first mysteries, and it has remained among the most persistent in terms of the duration it has lacked an articulated mechanism of formation. In fact, current literature for all kinds of impact welding will often delve into analysis explaining the formation of waves (e.g., see [100]). Beyond climbing the mountain because it is there, understanding this phenomenon is important as many believe that welding with wavy bonds is superior to welding with smooth ones, perhaps due to a degree of interlock or increased surface area. Another point to consider is that parameters in smooth welding are often at the margins of the welding window, where random variations in the

[26] The effect of acoustic waves will be discussed more later. They are believed to be quite significant.

parameters can lead to a lack of bonding more quickly. While research, to be discussed later, has eroded support for some of the concerns with smooth welding mentioned above, the topic has continually maintained the focus of researchers for over 50 years.

2.2.3.1 A Summary of Competing Theories

As it is clear to see upon reviewing Table 2-1, it has been quite a long time since a comprehensive review of explosive welding has been compiled into a comprehensive text. It is left then to a reader to cover a wide breadth of literature, since 1983 when Blazynski published his compilation. The mechanism of wave formation has a few competing explanations, which will be listed chronologically. The oldest, often described as the indentation mechanism was based on work by Abrahamson[32], whose liquid-putty experiment informed his analogy that the flyer material would create an indentation underneath the collision point simultaneously resulting in a "hump" in front of the jet. Periodic perturbations would result in fluctuations that would become frozen into the interfacial boundary waves. Bahrani, Black, and Crossland, [55] built upon this idea envisioning a complete sequence of steps they thought could generate the interfacial boundary waves. Hunt proposed a Kelvin-Helmholtz instability, acting in front of the collision point [53]. Godunov, Deribas, Zabrodin, and Kozin articulated a theory formulated including the effects of acoustic rarefaction waves (i.e. elastic dilatational waves) [101]. Cowan, Bergmann, and Holtzman made an analogy to with the von Karman vortex street, plus other significant contributions in a 1971 paper [54]. This was essentially very similar to a discussion by Kowalick and Hay published just a few months earlier and appears to have been independent [57]. In 1975, Robinson proposed a schema that applied a different kind of Kelvin-Helmholtz instability, which was described as acting behind the collision point [63]. Also in 1975, Blazynski first proposed a stress wave mechanism based on different types of stress waves,

primarily dilatational, but with different ideas than shown by Godunov [4, Ch. 8.2.2], [62]. In 1978, although previously supporting the von Karman vortex street linkages [58], Reid seconded Robinson's formulation, linking it to his earlier work, and describing it as a wake instability mechanism, with references to Birkhoff's wake theory [60]. The last and latest contribution to be listed is also the least cited, but offers some unique insights as well. Gupta and Kainth propose a step further on Reid's discussion, identifying a swinging wake mechanism, furthering the analogy to Birkhoff's periodic wake theory [102].

- Indentation Mechanism

This theory is still highly referenced to date, as it offers very qualitatively appealing images and explanations of the progression of interfacial wave generation. Figure 2-25 below,

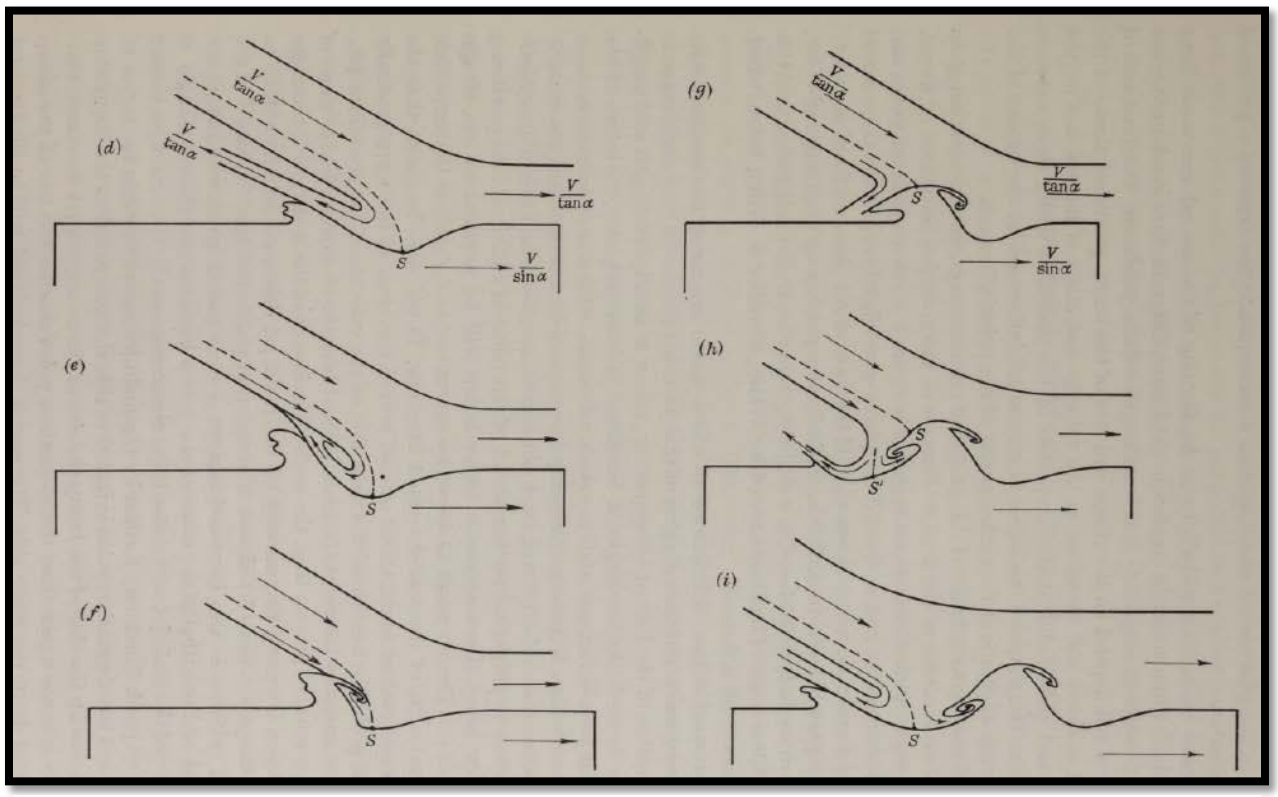

Figure 2-25: Indentation mechanism sequence. [55]

shows the sequence that was presented.[27][55] In this sequence, the flyer plate flow depresses the parent plate beneath the stagnation point (d) causing a hump that directs the jet upward. The existence of a hump was shown in Abrahamson's work that included a set of liquid and putty jet experiments, but he considered it more of a steady state [32]. In the Bahrani mechanism, eventually, (e) the hump diverts the jet far enough to encounter the flyer's incoming flow. This generates a backwards facing vortex (f) that cuts off the streamline to the stagnation point causing the stagnation point to jump to the top of the wave (g). This begins to generate a front facing vortex, (h), which leads the stagnation point to slip down into the trough of the wave, completing one cycle (i). The mechanism qualitatively discusses the relative shearing between the flyer and parent plate shown in the flow in Figure 2-25 as well. This mechanism remains popular to refer to as the actual mechanism, with very current citations [103], [104]. However, it is quite telling that Crossland, one of the coauthors of the paper that introduced this idea, by the time of authoring his text said this mechanism "… does not provide an adequate explanation of the underlying wave mechanism."[6, p. 28]

- Kelvin Helmholtz in Front of the Collision

Hunt's idea relied upon the classic Kelvin-Helmholtz instability mechanism where there is a velocity discontinuity between two fluids, such as that shown in Figure 2-26 below [53].

[27] Note they assume a velocity normal to the flyer plate surface.

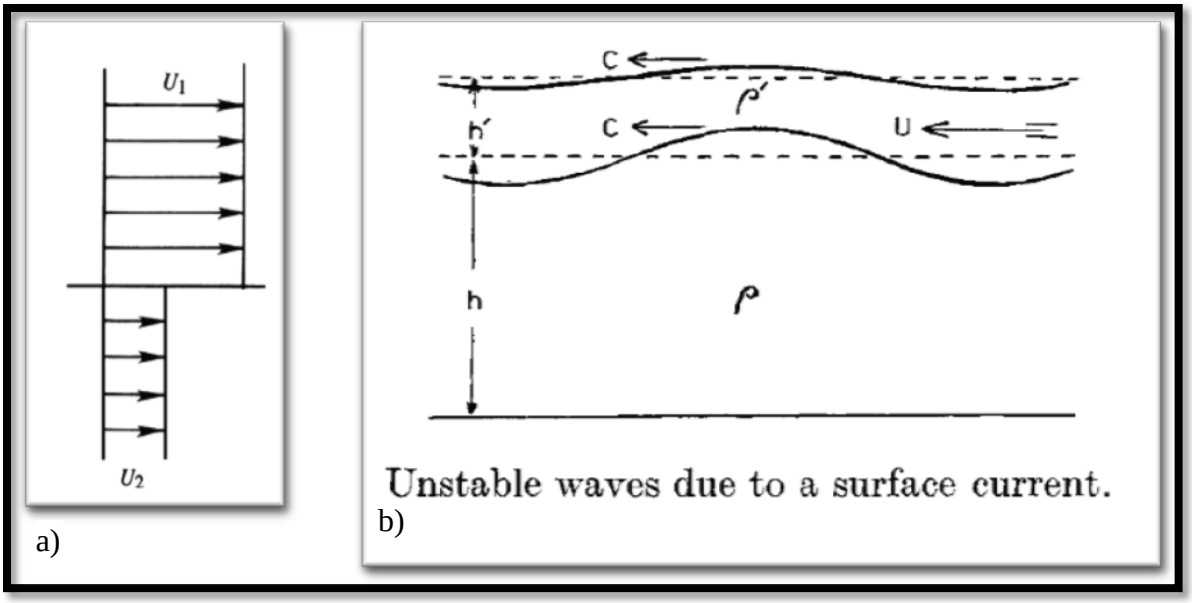

Figure 2-26: Hunt's Kelvin-Helmholtz explanation. a) Velocity distribution of two fluid layers with a flow discontinuity between flow at velocity *U1* (top) and *U2* (bottom). Adapted from [107, p. 538]. b) Hunt's scenario with the jet traveling over the parent plate at velocity *U*. [53]

In Hunt's analysis, the jet was assumed to flow much like it is shown in Figure 2-19, directly adjacent to the flow of the incoming parent plate. This is the same scenario as shown in Figure 2-26 b) from Hunt's work. This analysis had the added benefit of accounting for the effect of different densities, which clearly affected the weld shape.

- Linear Acoustic Analysis w/ Initiation due to Rarefaction Wave Arrival

The work of Godunov, Deribas, Zabrodin, and Kozin focused on understanding the waves by applying a solution based on a linear acoustic analysis. This assumed an inviscid flow and applied the equations of continuity/conservation of mass and equilibrium to a superimposed steady state and perturbed flow field [101]. Analytical solutions were found using the complex plane for the scenario of plates impacting as shown in Figure 2-27 below, in certain cases using potential and stream functions, φ and ψ. Both like and differing densities were derived, and an expression for the curvature of the free surface in the vicinity of the origin *O* was derived, which bore a remarkable resemblance an empirical expression predict wavelength to be presented in later in Section 2.2.3.2, Equation (2-19). In other words, this solution appears to be unstable to perturbations, and the curvature of this perturbed flow near the contact point appears to be a characteristic length that relates to actual wavelengths of experimentally measured interfacial waves. Additionally, the most highly cited aspect of this work was the effect of a reflected rarefaction wave shown and explained in Figure 2-28.

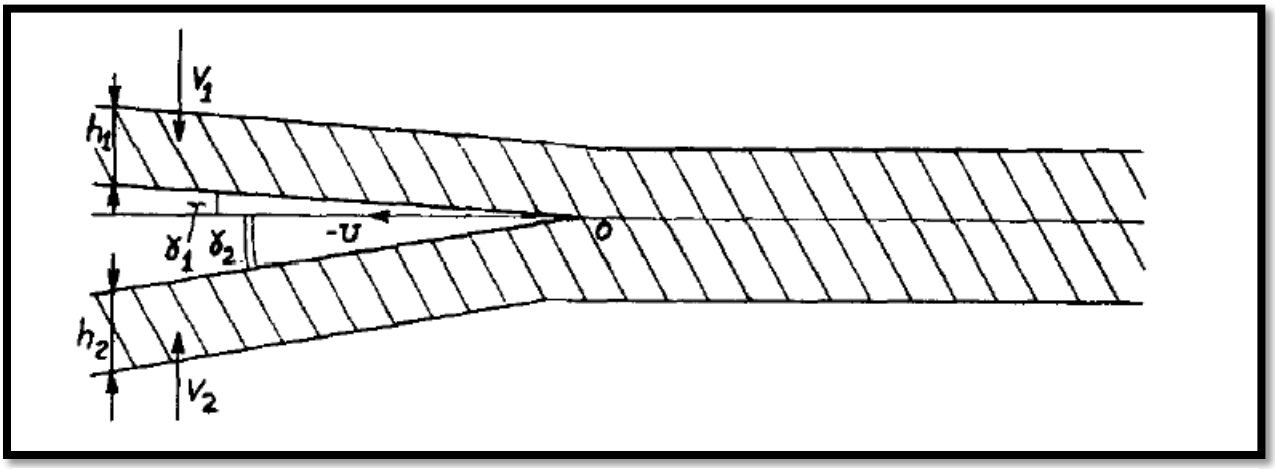

Figure 2-27: Scenario of the acoustic derivation. [101]

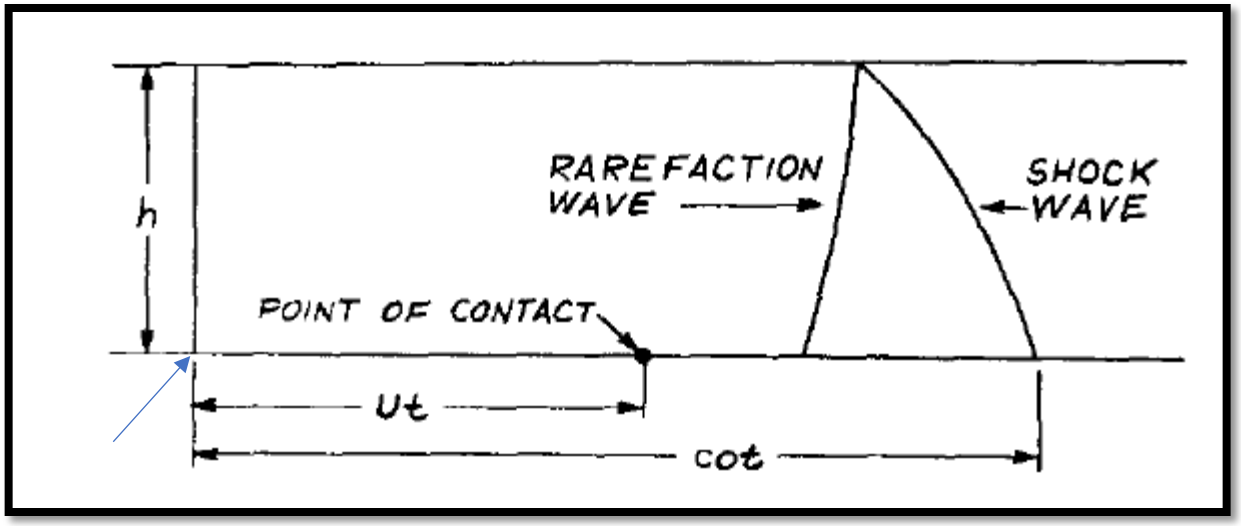

Figure 2-28: Progress of a dilatational wave and the point of contact with time. The contact point which is the source for the shock wave and its reflected rarefaction wave is the far left point identified with the blue arrow. Since then, time t has passed. The velocity of the contact point is U (i.e. $V_w \leftrightarrow U$), and the speed of the dilatational wave is c_0. The bottom dimension that looks like "cot" is intended to be c_0t. With t << than shown in the figure, the rarefaction wave will not have even formed, but with an intermediate t, it will first strike the contact point at Ut. [101]

This analysis, articulated in the caption shows that after a fixed time, a rarefaction wave will arrive at the collision point. Though they did not experimentally verify it in this reference, they hypothesized that the arrival of this wave served as an initiation of waves, or as the perturbation

$$l_0 = V_w t_0 = \frac{2hV_w}{\sqrt{{c_0}^2 - {V_w}^2}} \tag{2-15}$$

required for their instability to take effect. This arrival time is shown above in Equation (2-15), where l_0 is the length required for arrival of the rarefaction, t_0 is the time for arrival, V_w is the weld speed, and c_0 is the acoustic speed in the metal. They further showed that if they machined a ledge into the parent plate of the same amplitude as the normally manifested bond interfacial waves, they could trigger waves earlier than normal and immediately after the step.

- Waves as a Manifestation of von Karman Vortex Streets

Both Cowan, Bergmann, and Holtzman, as well as Kowalick and Hay, made the comparison between the shape of the highly turbulent bond interfacial waves in explosive welding and the vortices developed in von Karman vortex streets [54], [57].

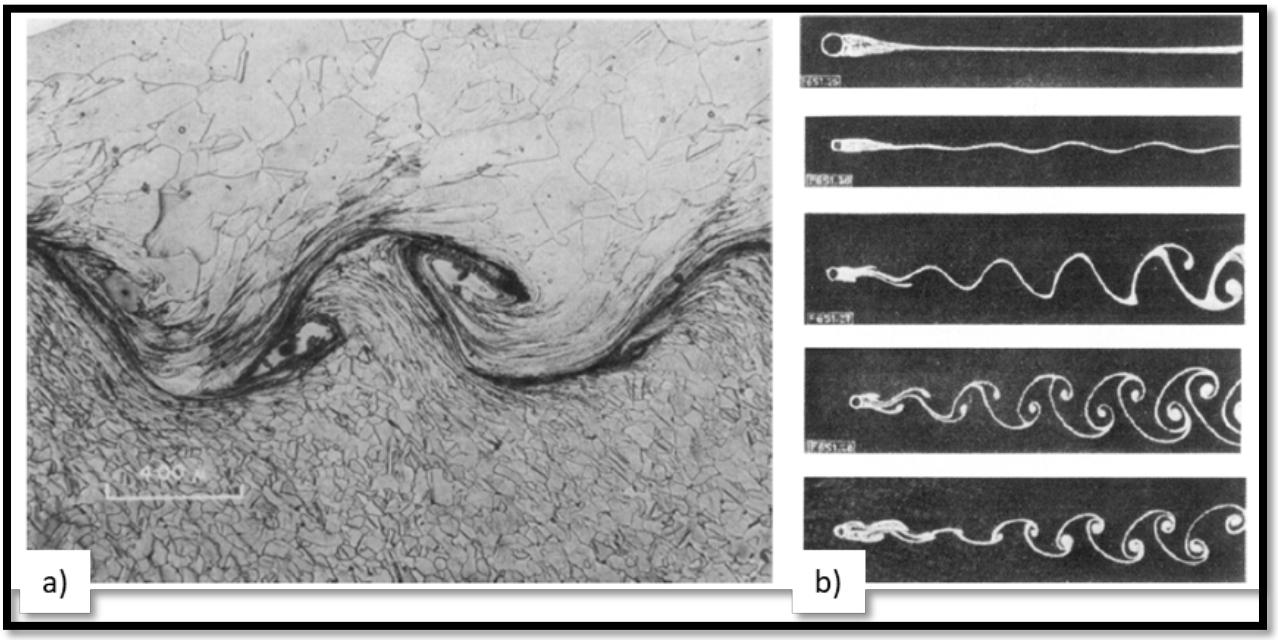

Figure 2-29: Comparison of turbulent vortices in explosive welding interfacial waves with flow developed behind cylindrical obstructions resulting in von Karman vortex streets. a) Weld sample. [54] b) Fluid flow experiment with increasing Reynolds number from to bottom resulting in a vortex street. [242]

The comparison between the waves in Figure 2-29 a) and b) are striking. Cowan, Bergmann, and Holtzman used several related concepts from fluids in order to attempt to make use of the apparent similarity between bond wave formation and fluid flow after flowing around an obstacle. This included an attempt to establish a welding Strouhal number, a welding Reynold's number to be discussed in Section 2.2.3.2, and relations for wavelength and amplitude. They noted that the ratio of weld interfacial wave amplitudes to wavelengths was

roughly constant[28] and that the ratio of impact angle squared (β^2) to wavelength was "quite good" as a predictive factor relating those values.

It is important to note that von Karman's ratio is not directly applicable to the ratio of explosive welding bond amplitude to wavelength. Figure 2-30 below is from von Karman's first paper on the stability of vortices. As noted in the figure, it is clear that the amplitude measured in explosive welding interfacial bonds would not correspond to von Karman's vertical vortex spacing, *h* [105]. As a result, comparisons of the von Karman ratio to impact welding amplitude-to-wavelength ratios should not be expected to result in exact matches.[29]

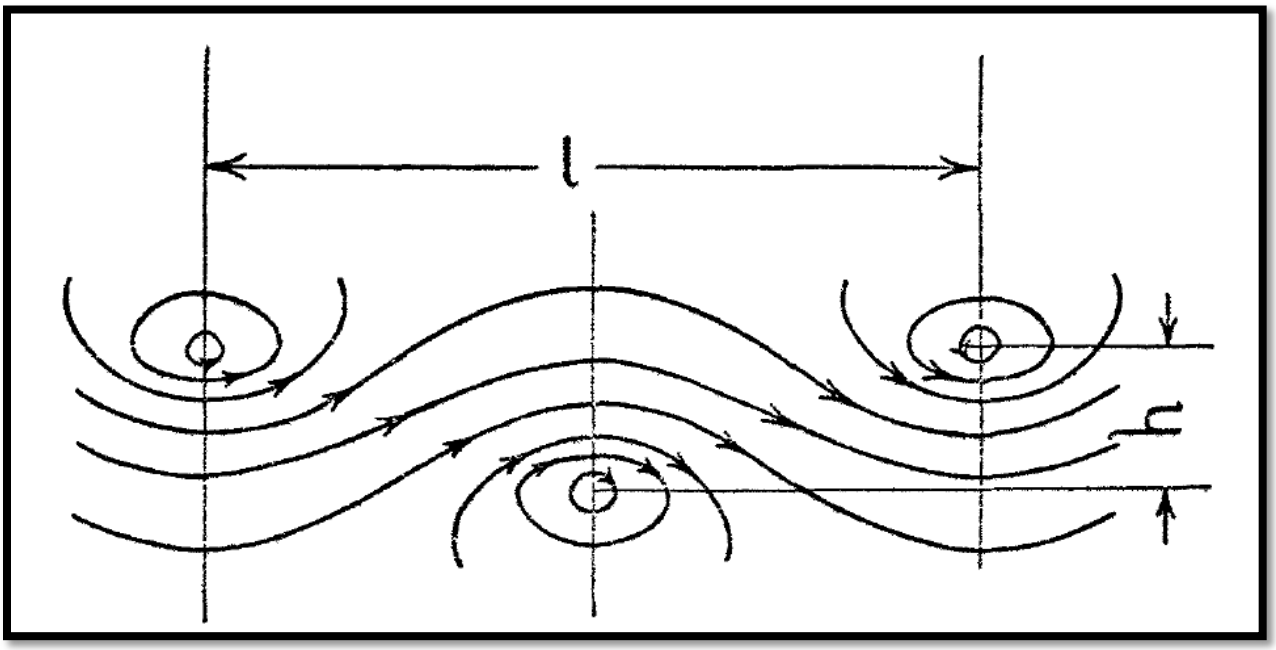

Figure 2-30: Figure from von Karman for stability ratio. His parameters were measured relative to vortex centers. For explosive welding, l would reasonably correspond to wavelength, λ. However, h, the vertical vortex spacing dimension would not correspond to explosive welding bond wave amplitude, a. Looking at Figure 2-29, the vortices are clearly within the bounds of the interface amplitude. [105]

[28] It was unclear to the author on reading the reference, but the amplitude referred to appears to be a peak amplitude rather than peak-to-peak. Some other authors refer to "2a", rather than just "a".

[29] The ratio for von Karman that is typically quoted, 0.28, was actually arrived at in his second paper of the same title. The second paper just doesn't contain any figures.[133]

- Kelvin-Helmholtz Instability Behind the Collision and from Varying Velocity Profiles

In 1975, Robinson presented one of the more powerful explanations of what generated the instabilities leading to bond interfacial waves [63]. While the work of Hunt [53] assumed

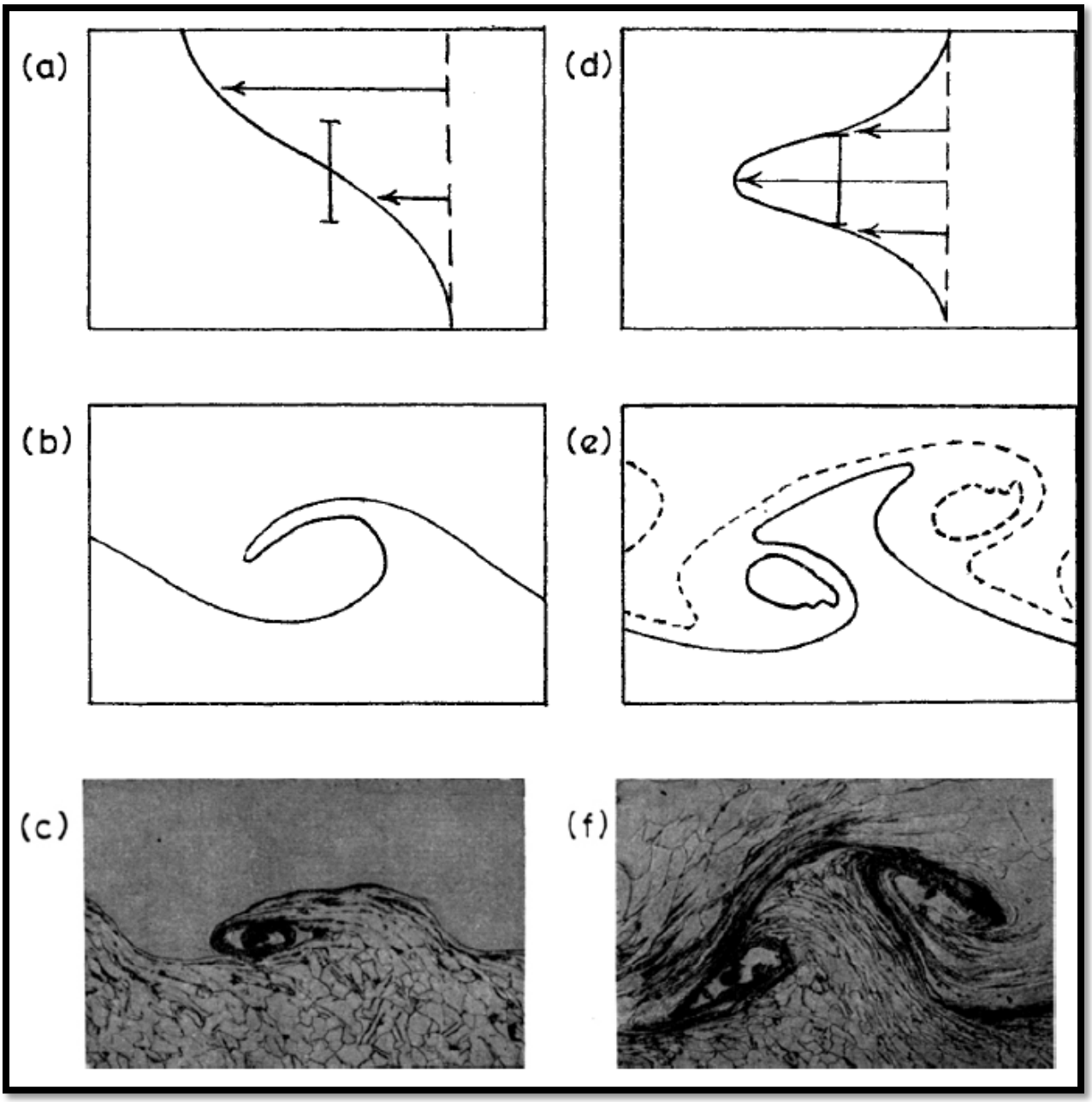

Figure 2-31: Velocity profiles post collision. [63] a) A single inflection point, continuous profile. b) Resulting breaking wave modeling result. c) Similar structure in explosive welding sample. d) Double inflection point on continuous profile similar to a jet or a wake. e) Model result from d. f) Potentially related explosive welding interfacial wave structure. Note the vertical bars in (a) and (d) that identify the characteristic dimension of the velocity profiles.

that the instability was initiated in front of the collision point, Robinson's focused behind the collision point. While the jet flow in Figure 2-19 and Figure 2-26b) is drawn as a solid layer adjacent to the parent material, there is no reason to believe that is the true behavior. In fact, early streak photography and flash X-Rays of explosive welds[61], [88] show that this is uniformly not the case. However, it is quite clear that the interfacial layers of the plates are in contact after colliding.

Robinson made the comparison between two different velocity profiles and possible results, shown in Figure 2-31. Figure 2-31 (d) could be due to a jet or the wake made by the recent passage of a disturbance/obstacle with a set characteristic dimension. In fact, the result shown in Figure 2-31 (e) resulted from the analysis of the evolution of a wake formed by a thin plate in a continuous parallel flow done by Zabusky and Deem [106]. The similarities to the velocity profile in explosive welding begin to become apparent as we realize that by the hydrodynamic analogy, the region of the stagnation point would instantaneously have little to no velocity and would generate a similar wake as that shown in Figure 2-32.

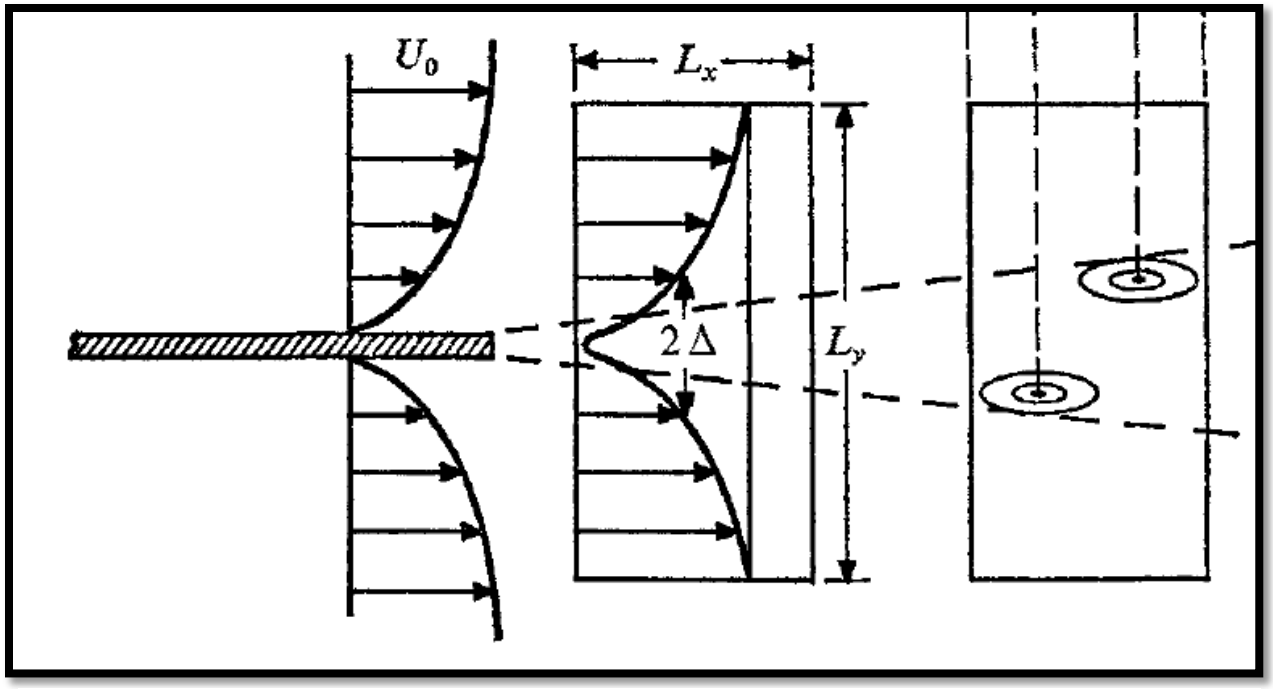

Figure 2-32: Physical scenario for Zabusky and Deem's model for Figure 2-31 (e). [106]

Aside from the location of the velocity profile (i.e., not in front of the collision point), this is a different mechanism from that relied upon by Hunt. Hunt's analysis uses a velocity profile discrete discontinuity shown in Figure 2-26 a), while Robinson's analysis is based on a continuous velocity profile as shown in Figure 2-31 (a) and (d). In some ways the analysis is similar to that of Godunov et. al above, as it derives a solution using field equations for an inviscid fluid. Robinson, however uses potentials and also incompressibility to derive his solution, still accounting for shearing motions to establish stability conditions. While Hunt's formulation is often termed a Kelvin-Helmholtz instability, Robinson is referring to the more general case of a continuous distribution of velocity that generates a similar instability and is also termed a Kelvin-Helmholtz instability [107, p. 563]. While the formulations for Hunt's scenario, are unstable with respect to disturbances of any wavelength in certain cases, Robinson's scenario has *most* unstable wavelengths [107, pp. 541, 566]. In this case with continuous velocity distributions, Rayleigh's inflection point criteria (strengthened by Fjortoft) indicate an inflection

point in the velocity profile is a necessary (but not sufficient) condition for instability of inviscid parallel flows, and both velocity profiles in Figure 2-31 meet the strong necessary condition of Fjortoft.

While regular fluids would have their resulting waves gradually diffuse to viscous effects, Robinson clearly discussed how this was limited by the transition from inviscid to viscous/plastic flow, and then to elastic conditions rather quickly. The region/size of the flow that were experiencing critical pressures and strain rates, directly effecting how long the unstable waves have to evolve. Reid, initially a fan of the von Karman vortex street analogy, came to support Robinson's analysis [60].

One other recent contribution that deserves mention is the work by Nassiri and his team of advisors [108]–[110]. They conducted a linear stability analysis, similar to that of many earlier researchers such as Robinson, but they were able to expand their formulation to include viscous effects, use some different assumptions, and further the predictions about the wavenumbers that were the most unstable as perturbations to the flow of the wake. This addresses similar velocity profiles in the same wake location, but with the added improvement of including viscous effects. This appears to be a significant improvement on the analysis, and reinforces Robinson's general approach.

- Stress Wave Mechanism

In 1975 Blazynski presented a stress wave mechanism for wave formation[62]. The strength of this analysis is that waves of different types were considered. Shear waves were differentiated from surface waves and dilatational waves, with a recognition of the distinct speed of propagation for each. This work also discussed how wave impulses fan out radially from their source, and should also given credit for its consideration of elastic and plastic waves in general.

Blazynski's mechanism discusses waves formed on the free of surface of the plates (see point 1 in Figure 2-33) resulting only from the effects of dilatational waves. He proposes that these free surface waves will exist as a source of continuous surface instability for the formation of bond interfacial waves.

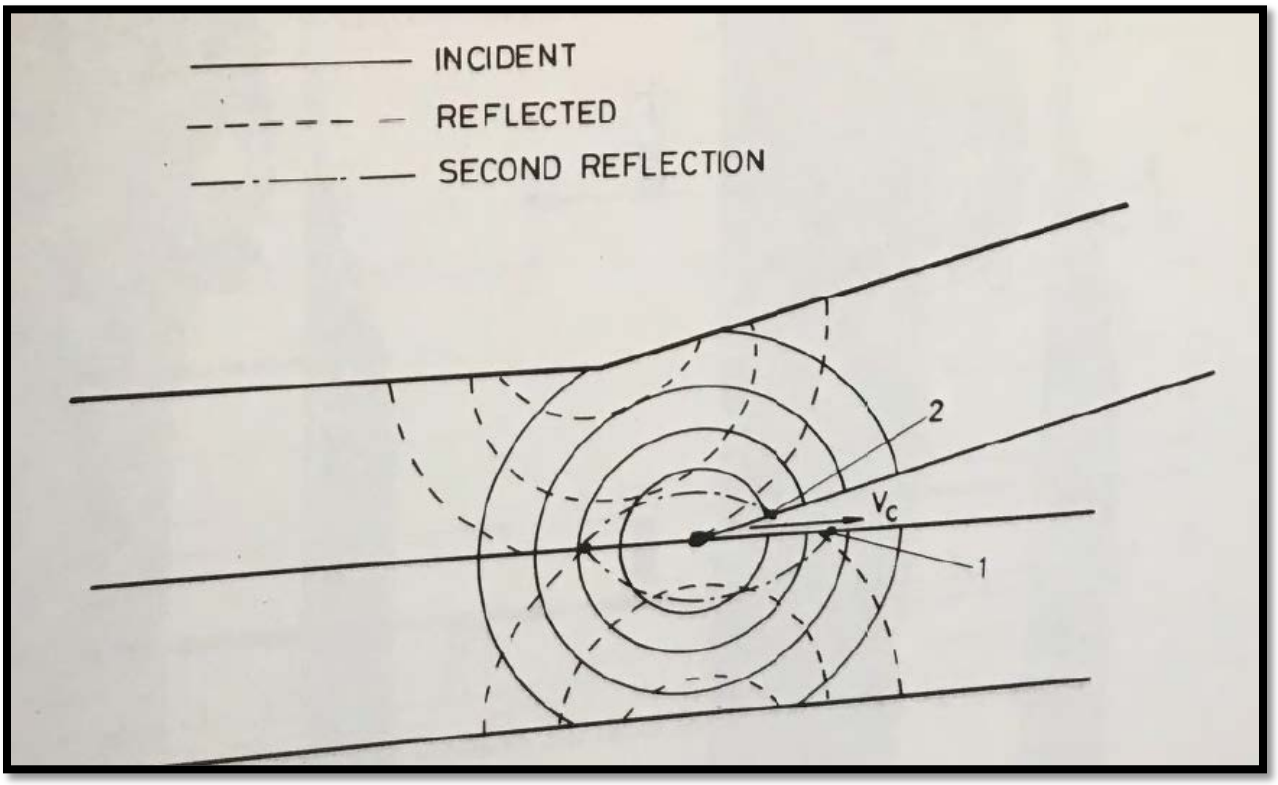

Figure 2-33: Blazynski's stress wave mechanism's surface wave analysis. [62]

- Swinging Wake Mechanism

Reid was the first to suggest a swinging wake mechanism [58]. He later linked it to the theory of Robinson [60]. Botros and Groves also explored this model [111]. Building on work by Birkhoff and Reid, Gupta applied a swinging wake mechanism where a restoring force acts on the "wake" forcing it toward an equilibrium position at the original wake center [102]. This force is generated by an equivalent "aerofoil", and can address movement between fluids of different densities.

2.2.3.2 Prediction of Interfacial Waves and Wave Characteristics

- Transition from Smooth to Wavy Bonding Interfaces

As it must be abundantly clear, the topic of the wavy interface has been ubiquitous in explosive welding research. In addition to a search for a theoretical explanation of their formation and characteristics, empirical relations have been sought. As noted above, welds with a wavy interfacial bond were considered to be superior by many.

One of the first questions researchers tried to answer was when will waves be formed. As seen from Wittman's welding window above in Figure 2-23, the left limit of welding proposed was a set velocity of welding, V_w, below which they did not expect wavy interfaces at the bond.

This limit was first proposed by Cowan, Bergman, and Holtzman in 1971 [54]. They arrived at this limit as they were making observations about turbulent fluid flow and turbulent flow in explosive welding, and these comparisons led them to further relate interface waves to the formation of von Karman vortex streets in Section 2.2.3.1 above. In von Karman vortex street formation, the flow is described by a Reynolds number as a means to distinguish what kind of flows will have the turbulent behavior. Cowan, Bergmann, and Holtzman noted this connection and sought a Reynolds number they could apply in explosive welding. They noted the fundamental notion of the Reynold's number, R_e, is the ratio of the inertial forces to viscous forces in a Newtonian fluid. Taking the leap to more of a Bingham plastic of sorts, they arrived at the statement (using explosive welding flow in the slug), shown on the right of Equation

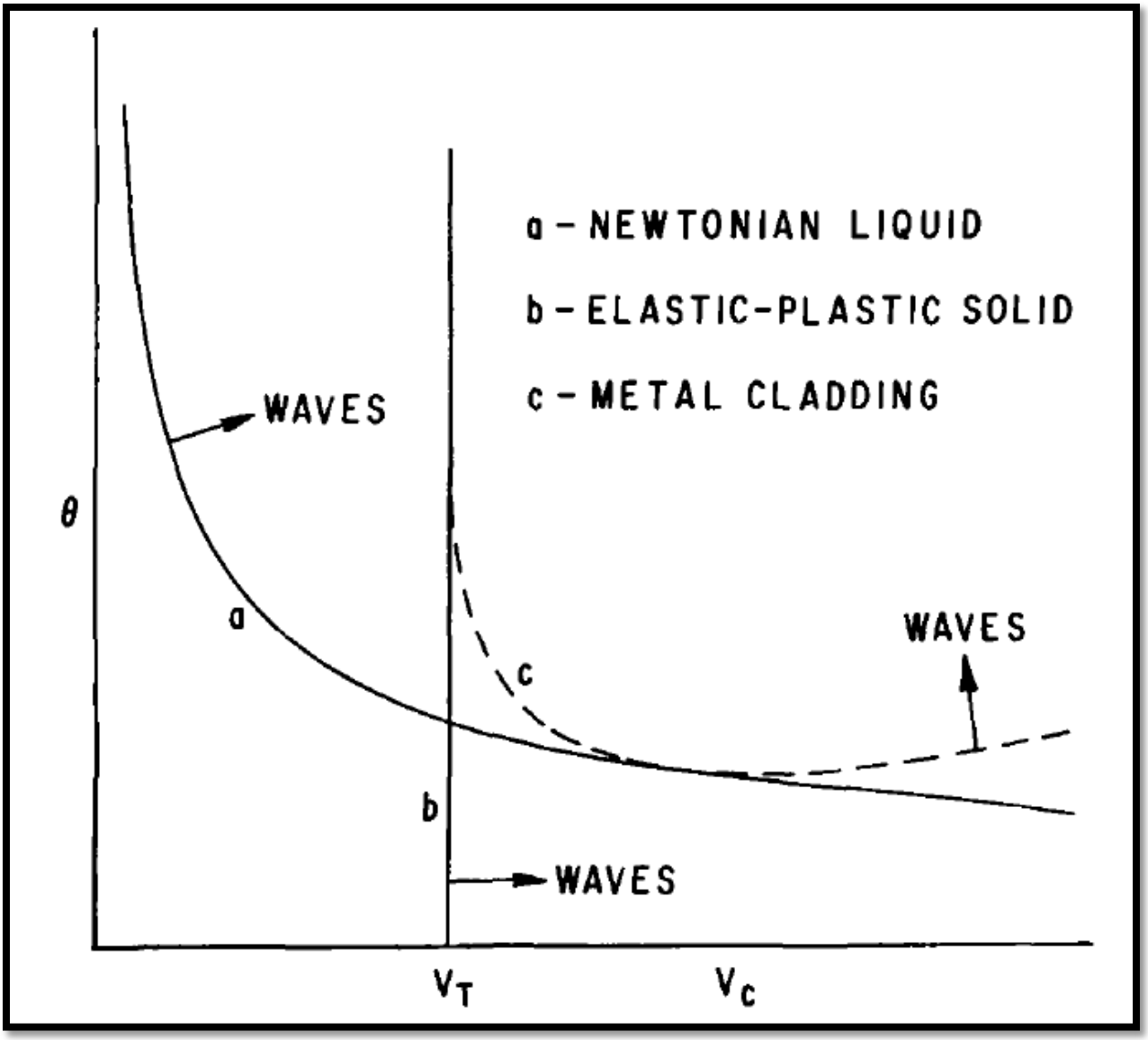

Figure 2-34: Theoretical boundaries of wave formation as impact angle and flow velocity vary, as presented by Cowan, Bergmann, and Holtzman. (a) The boundary for a Newtonian fluid. (b) The boundary they proposed for elastic-plastic solids. (c) The boundary they claim to be typically observed.

(2-16) for an ideal elastic-plastic solid. In this equation V_w is welding velocity/slug flow velocity, ρ is material density, d is the characteristic length, P_s is the stagnation pressure of

$$R_e = \frac{V_w \rho d}{\mu} = \frac{\frac{1}{2}\rho V_w^2}{\frac{\mu V_w}{2d}} \propto \frac{P_s}{Y} \tag{2-16}$$

flow, and *Y* is the material yield/flow stress. Cowan, Bergmann, and Holtzman then looked for ways they could propose an analogous Reynold's number for explosive welding, since the Reynold's number served to mark the boundary to turbulent flow in traditional fluids. They further compared the theoretical boundaries of interfacial wave formation in the collision of Newtonian fluids, elastic-plastic or Bingham fluids, and the interfacial waves observed in explosive welding, as shown in Figure 2-34. They reasoned it could therefore serve to mark the boundary of turbulent flow in welding. In keeping with the conceptual definition of the Reynold's number shown in Equation (2-16), they proposed that the Reynolds number for explosive welding flow would be expressed as shown in Equation (2-17), where R_w is the

$$R_w = \frac{(\rho_f + \rho_p)V_w^2}{2(H_f + H_p)} \tag{2-17}$$

Reynolds number of the explosive welding flow, ρ_f and ρ_p are the densities of the flyer and parent plates respectively, and H_f and H_p are the diamond pyramid hardness of the flyer and parent plate metal, as proxies for the yield stress.[30] As the weld velocity increases,[31] so does the Reynolds number for this formulation.

Cowan, Bergmann, and Holtzman then undertook studies to identify a controlling Reynolds number that marked the transition from flat bonding interfaces to wavy bond interfaces in confirmation of their theory. It is important to note that all of their studies only made use of

[30] Note that factors of ½ in the numerator and denominator generated average densities and average hardness are cancelled out in the final form of Equation (2-17).

[31] They assumed parallel plate arrangements, in which case $V_w = V_F$, but even in inclined arrangements these values are close to begin with and behind the collision point the velocity fields in the flyer and parent plates begin to equilibrate. Additionally, for behavior behind the collision point, the velocity of the weld may be more appropriate in any case.

parallel welding and of the same impact angle (roughly 12°), which was arrived at by manipulating detonation velocities and flyer plate velocities as they gathered data for different weld velocities. With data shown for 11 different configurations, they arrived at an average critical weld flow Reynold's number of 10.6, to mark the transition from smooth to wavy welding. All of this was behind that vertical line in Wittman's window in Figure 2-23.

Based on its inclusion in early literature in the field, there are a wealth of papers that either evaluate and document the validity of this limit or apply it as an established condition [51], [85], [94], [95], [97], [98], [112]–[119]. However, starting around 1975, Crossland began working on the use of a gas gun as a means to economically evaluate empirical welding domains [66]. In 1979, a PhD student of his, Alexander Szecket completed a thesis, characterizing the weldability domain of different like-metal pairs [120] By the time of the publication of his text, Crossland felt that the transition boundary at a fixed welding velocity, V_w, was ". . . not substantiated . . ." [6, p. 100]. Aside from his dissertation and the mention in Crossland's 1982 text, Szecket's specific findings on the transition from smooth to wavy interfacial waves was not published in literature (especially using the β vs. V_w coordinates users were more familiar with) until 1987 [71]. Since then a number of other researchers picked up on the new idea or otherwise published supporting data, but it is still clearly not widely shared [121]–[127].

As an alternative/modification, to the transition model proposed by Cowan, Bergmann, and Holtzman, the paper by Jaramillo, Szecket, and Inal from 1987 published a sample welding window using more the common impact angle, β, and welding velocity, V_w, coordinates, as shown in Figure 2-35, below[71]. In addition, they discussed the rough empirical values that allow plotting of the transition zone for three like metal pairs (copper to copper, mild steel to

$$R_t = K_{E-P} = 122.32(\pm 16.9) - 19.35(\pm 3.65)\beta + 1.07(\pm 0.24)\beta^2 - 0.020(\pm 0.005)\beta^2 \text{ (Al-Al)} \quad (2\text{-}18)$$

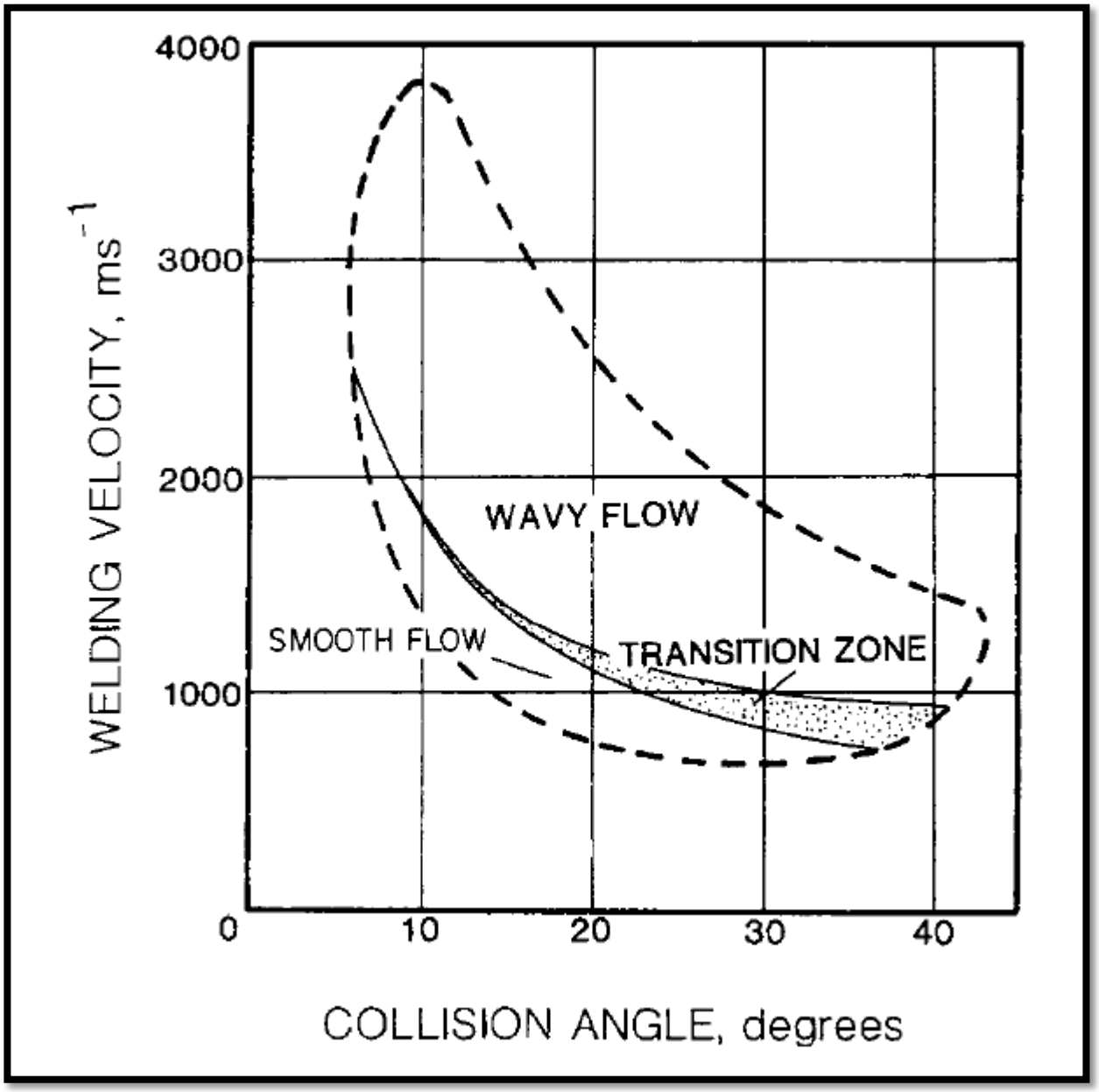

Figure 2-35: Welding window from Szecket's empirical data collection efforts from his 1979 thesis, as published by Jaramillo, Szecket, and Inal. Note, to be different, they transposed the usual axes. [71]

mild steel, and aluminum 2024 to itself; Al to Al shown in Equation (2-18)). They termed the result of these equations "elastic-plastic deformation theory" rather than choosing to explicitly retain the nomenclature of the critical Reynold's number. They added caveats that rather than an

abrupt value at high impact angles, where there was a transition stage and the switch from laminar to turbulent gradually/variably occurred for welding experiments.

Specific, independent work confirms that a constant weld velocity is not adequate to describe the boundary,[121] and a separate independent study also suggests similar conclusions about the appropriateness of an equation such as Equation (2-18). Additionally, Carvalho, Mendes, Leal, Galvao, and Loureiro proposed another metric, a Wave Interface Factor as an alternative to predict bond interfacial waves for dissimilar metals.[32]

- Prediction of Bond Interfacial Wavelength

The above quasi-empirical relations add refinements and zones of behavior to the welding window. However, there are more details that can be predicted, in order to develop a full understanding of the process. Several authors made efforts to quantify the wavelength of bond interfacial waves. The first to present a possible predictive relation was Deribas, Kudinov, Matveenkov, and Simonov in 1968.[33][56] A host of others continued the pursuit through the turn of the century [53], [54], [58]–[60], [97], [101], [102], [111], [128]–[131]. However, for the purposes of evaluations to be conducted in this work, Deribas' original proposal from [56], shown in Equation (2-19), will be used. It has stood the test of time, likely due to its

$$\lambda = 26 \cdot t_f \cdot sin^2\left(\frac{\beta}{2}\right) \tag{2-19}$$

combination of simplicity and physical relevance. The reader is referred to Equation (2-9) in the form based upon thickness. It is clear that the relationship proposed by Deribas is based upon

[32] The factor, a product of the density ratio and the melt temperature ratio, from flyer to parent is always 1 for like metals. Their proposed criteria would always predict wavy interfaces for like metals, which seems limiting.

[33] Narrowly. Hunt's work was published in April of 1968, while Deribas et. all published in March, if the author has interpreted numbering correctly.

the thickness of the outgoing jet, which other researchers in the list of citations above showed is also related to the thickness of the wake.

- Bond Interfacial Amplitude and its Relation to Wavelength

Klein appears to have been the first to show that the ratio of lateral and longitudinal distance between waves in typical explosive welding scenarios are roughly the same [132]. Deribas, Kudinov, Matveenkov, and Simonov compiled a set of data from previous work, analyzing what it predicted for the ratio [56], [64]. The provided several example ranges (middle value = their mean): Steel-Steel 0.1<0.17<0.25, Copper-Copper 00.15<0.25<0.35, D16T-D16T 0.14<0.2<0.25. Then in 1971, both Cowan, Bergmann, and Holtzman, as well as Godunov, Deribas, and Kozin made similar observations [54], [131]. Cowan et. all gave an example value of 0.20 for nickel/steel welding, and observed the ratio to be nearly constant, except when flow is near the transition region with smooth interfacial boundaries or for very small impact angles. Godunov et. all list a value of 0.25. By 1973, Deribas had settled on the value of 0.25. This ratio held for Reid, but he also noted the comparison to the stable von Karman vortex street ratio, though as noted above there are some differences [58]. In 1912, von Karman derived the ratio of stable vortices as $\frac{h}{l} = \frac{1}{\pi} acosh\left(\sqrt{2}\right) \approx 0.28$ [133]. He had, just weeks before published an article on the same topic, of the same name that provides the figure associated with this derivation, Figure 2-30, indicating *h* as the spacing transverse to the flow away from the wake, with *l* as the direction between centers parallel to that flow [105]. Although Deribas dismissed this connection as not all wavy bond interfaces have vortexes, it is remarkable that the ratios are so similar, and as shown in Figure 2-29 b), even in standard fluids, the vortex street is one end of the spectrum after starting from laminar flow, and smoother waves of similar proportions appear in the intervening Reynold's numbers.

2.2.3.3 Proposed Connections and Synthesis of Existing Theories

In describing the formation of bond interfacial waves, many authors have made very substantial contributions. However, despite all of that great work, the topic of wave formation remains an area where many researchers and practitioners in the field have yet to reach a consensus opinion. It is telling that as recently as December 2018, articles have been published evaluating one of Reid's empirical relationships for wavelength and the effect of flyer plate thicknesses on the weld [124]. This contribution comes from a set of authors with substantial experience and credibility in the field as well, but it nonetheless includes a rundown of the differing wave formation theories and mechanisms, without particularly strong assertions about how the mechanisms may fit together. There are a number of likely reasons for this. The behaviors in explosive welding cover a very broad field of knowledge and phenomena, and at a rather complex level. A full understanding requires advanced comprehension of fluid mechanics (including stability analysis relying upon complex number eigenvalue analysis), solid mechanics, physical modeling, elastic and plastic waves, shock behavior, explosives, material science and metallurgy, thermodynamics, advanced instrumentation, and computational mechanics. This broad sweep has intensely tried the author's abilities. After nearly 50 years of the existence of the field, the bulk of which included a push to understand interfacial waves, a proposal such as this is surer to expose flaws of understanding than to stand intense scrutiny, but that will, at least, be of value to the author if nothing else succeeds.

The proposed connections of the various theories outlined above will break down various factors in interfacial wave formation. There are many competing factors, and much like many advanced, irregular problems, perfect solutions likely only exist for such a narrow subset of parameters that a successful unifying explanation may not exist in explicit, closed-form detail.

However, the author believes it is possible to present and connect the source of instabilities, the physical perturbations that trigger initial wave growth, the resulting wave pattern, and the mechanism that caps the extent of wave amplitude growth before they are locked in.

As far as the instabilities that are generated, the proposal first articulated by Robinson is of critical importance. Wave generation behind the collision point from a shear related stability analysis was a critical step. From the fluid analogy, the flow behind the stagnation point in the welding process would clearly decrease its velocity[34] (hence its stagnation) relative to the flow around it, and the appreciation of the wake velocity profile this produces has significant power. The flow is similar to that shown in Figure 2-31 (d), which is similar to the fluid flow around a thin plate. Linear stability analysis of a perturbed flow, generating complex potential and stream functions, as well as complex wave speeds, takes a basic physical flow, and quantifies scenarios where perturbing waves set off an unstable growth that continues until linear relationships breakdown. The exact solution of this sort of analysis is complicated, which is why Robinson, Abe, and Nassiri, with their respective variations on the included factors had to resort to numerical solution (directly or indirectly). [63], [109], [134] This is a Kelvin-Helmholtz instability, but of a continuous varying flow rather than a discrete discontinuity, distinguishing it from Hunt's analysis. The necessary condition for instability of Rayleigh's criteria[107, p. 573] (namely an inflection point in the velocity profile) applies with two inflections, so that Figure 2-31 (a) and (b) both meet the criteria.[35] This addresses the criticism by some about Kelvin-Helmholtz instabilities not applying to symmetric collision scenarios. Specifically, they likely confuse this type of Kelvin-Helmholtz scenario with that presented by Hunt. Additionally, this

[34] In the steady-state coordinate system traveling with the collision point.

[35] Kundu refers to an even stronger criteria necessary condition discovered by Fjortoft,[107, p. 574] which both Figures meet as well.

analysis still possesses the ability to explain an instability in the superposition of the velocity profiles of Figure 2-31 (a) and (b). While the author believes that Hunt got the location of his instability (i.e. in front of the collision) wrong, the even simpler derivation of unstable scenarios with its assumptions are instructive, where a velocity profile like Figure 2-26 (a) can be viewed as an extreme or preceding version to the profile Figure 2-31 (a). This classic Kelvin Helmholtz, in common welding configuration has a lot explanatory power, as the flyer arrives at the collision point at a slightly slower flow speed than the parent (see Equations (2-2) and (2-3) solved for V_F & V_w), and the velocity discontinuity generates the dominate breaking wave of Figure 2-31 (b). The complex wave speed solution for the classic case accounts for instabilities for differing discrete velocities, but it also predicts instability for different densities [107, p. 541].[36] All of these mechanisms, which admittedly allow for several variants, generate the conditions for unstable growth under a perturbation.

As with the conditions for unstable wave growth, the author believes there are many varying ways perturbations can trigger the instability. However, the main explanation proposed relies primarily upon the insights from Deribas' acoustic explanation with some added ideas. Deribas' idea of a fixed time to wave initiation has seen some support in literature (such as [135] It emphasizes the role of dilatational waves as initiation mechanisms. While Blaznyski's theory suggests a different course (ahead of the collision point) for dilatational waves to come into play, his work also supports the idea of these waves as a potential perturbation [62]. Szecket, Vigueras, and Inal essentially propose a similar process where the rarefaction reflected back

[36] What is intriguing is that there is a direction associated with this instability. For standard fluids in the classic relationship, that direction is supplied by gravity. A denser material on bottom is the stable configuration. However, work by Carvalho highlights this is reversed for explosive welding, where if the denser material is in the flyer (i.e. on top), that is the scenario where waves are not formed.[126] He does also attribute part of this to melt temperature.

from the free surface of the flyer returns to initiate waves in their 1986 work [69]. Plaksin describes a pulsating nature in the detonation of certain explosives that could produce similar perturbations [136]. Both Szecket and Deribas demonstrated that a perturbation such as a step machined into the materials can initiate the waves, providing evidence that perturbations have an effect in the first place [101], [137]. Szecket's work interestingly showed that substitution of a different material could also serve as this trigger as well.

However, as a way to qualify the assertions of Szecket and Deribas, it is important to note the cases that seem to differ. Both Szecket and Deribas focus on rarefaction returning from the free surface of the flyer. It is interesting to consider that particle motion from a compressive wave in the parent reflected from a rigid base will be in the same direction as the motion of Szecket and Deribas' rarefaction wave. They likely used data from normal scenarios where the parent plate was thicker than the flyer, in which case a dilatational wave traveling in the flyer would return first, assuming similar materials. Interestingly, Jaramillo's work from 1987, where the parent plate was suspended in the air (removing the rigid base consideration above and introducing another rarefaction source), indicated that for ratios of parent thickness over flyer thickness up to 1.6, the observed wavelength varied with the ratio [70]. The thicker parent plate did not affect the wavelength above a ratio of 3 in his data. Similarly, Wronka found that the base plate did matter to the wavelength, but not after a passing a certain thickness [138]. Further, he claimed, with experimental and analytical arguments, that the acoustic properties and the corresponding reflection of waves mattered as well, and he produced further arguments about the importance of the effect of dilatational waves [130] More compelling evidence of the effect of dilatational waves are found in [139], [140], where vibrational excitations were applied to welding samples, changing the bond interfacial waves of otherwise identical welds. It seems

apparent that the different configurations of dilatational waves are the main perturbations for bond interfacial waves. Different geometries, materials, and boundaries necessarily affect the arrival and type of waves, but the picture that emerges is that this is the controlling excitation mechanism. Some of the early agreement on the influence of the flyer was likely due to unintentional and consistent similarities of the relative natures of the parent and anvil.

With the source of initial instability and the source of perturbation addressed, the next component is a description of the resulting waves. It is here that a place for the von Karman vortex street connection exists. Early references to this mechanism often failed to address the fact that von Karman's analysis was largely focused on the stable configuration of the spacing of the vortices, *h/l*, see Figure 2-30, above. Once vortices are formed, this analysis and ratio serves to constrain amplitude by wavelength or vice versa. By a bit of a stretch, admittedly, this seems to also somewhat relate to the ratio of less turbulent waves.

However, if the von Karman ratio or a similar value (e.g. near 0.25) is accepted, it only can fix one of the two resultant variables of wavelength and amplitude. It remains after identifying sources of instability, perturbations, and a restricting ratio, to fix either amplitude or wavelength. It is here that the combined effects of the most unstable wavenumbers and the swinging wake mechanism come into play.

As far as the most unstable wavenumber, both Robinson and Nassiri arrived at the conclusion that certain wavelengths were more unstable. This idea is supported in standard fluid mechanics texts, such as Kundu, as well [107, Ch. 11.7]. Robinson formulated two least stable wavelengths, λ, based on the characteristic length, Δ, (i.e. wake thickness which is relatable to the jet thickness): $\lambda = 14.1\Delta$ or 7.8Δ. Nassiri's analysis was based upon numerical analysis and material properties, and so is less general, but he did arrive at the least stable wavelengths being

around $\lambda = 8.4\,\Delta$. This would serve to somewhat limit the wavelengths, and then via the amplitude/wavelength ratio, it would control the amplitudes.

The other means that is likely the most concrete is the swinging wake mechanism, first adopted from Birkhoff's work by Reid, and then later expanded upon and detailed by Gupta. [58], [60], [102] This mechanism accounts for dissimilar materials and the varying wake thickness as the impact angle changes. This model predicts the degree of distortion for dissimilar materials, provides an estimate of the amplitude to wave ratio, and provides a practical cap on the amplitude due to the nature of the restoring force and wake. With the wake width fixed, the airfoil has a set amplitude upon which it is violently propelled back across the wake, and that then fixes the wavelength that can exist via the amplitude to wave ratio.

In summary, the varying types of Kelvin-Helmholtz instabilities set the conditions for unstable wave formation behind the collision point, based on the wake velocity profiles expected for a given weld. Dilatational waves affected by the geometry, materials, and boundaries of the flyer, parent, and anvil, as well as any other wave source provide the perturbation. The amplitude to wavelength ratio, similar to the von Karman value, constrains the geometry of waves that can occur. A combination of the waves excited (perhaps the most unstable) and the limit imposed on the amplitude of waves by the swinging wake mechanism provide the final constraint on the bond interfacial waves. This explanation may not satisfy like a simple linear equation, but the author believes it to be plausible, comprehensive, and connective of the important parts of historical theories. Further, although it does not yield simple equations, it does allow numerical/computational modeling, as all of the above factors derive from first principles physics such as the conservation laws that are part of solid mechanics based codes.

2.2.3.4 On the “Hump” Near the Collision Point

Beginning with Abrahamson’s work, the notion of a hump adjacent to the collision point was introduced [32]. Bahrani et. al adopted and modified this notion to try to explain the formation of bond interfacial waves, as detailed above in Section 2.2.3.1 [55]. Although the author does not subscribe to the details of that mechanism, numerous works support the idea that a hump is formed near the collision point. Suggestively, Blazynski’s work with a liquid analogue does show a surface wave forming in front the point of contact [141], [142] With the advent of better modeling methods, a number of numerical studies also predicted a hump. Oberg, one of the earliest numerical studies found by the author, recounts a report by Botros & Groves suggesting the hump would be more or less under the stagnation point, and their simulation corroborated that idea [143]. They attempted to coin a definition of a “dynamic

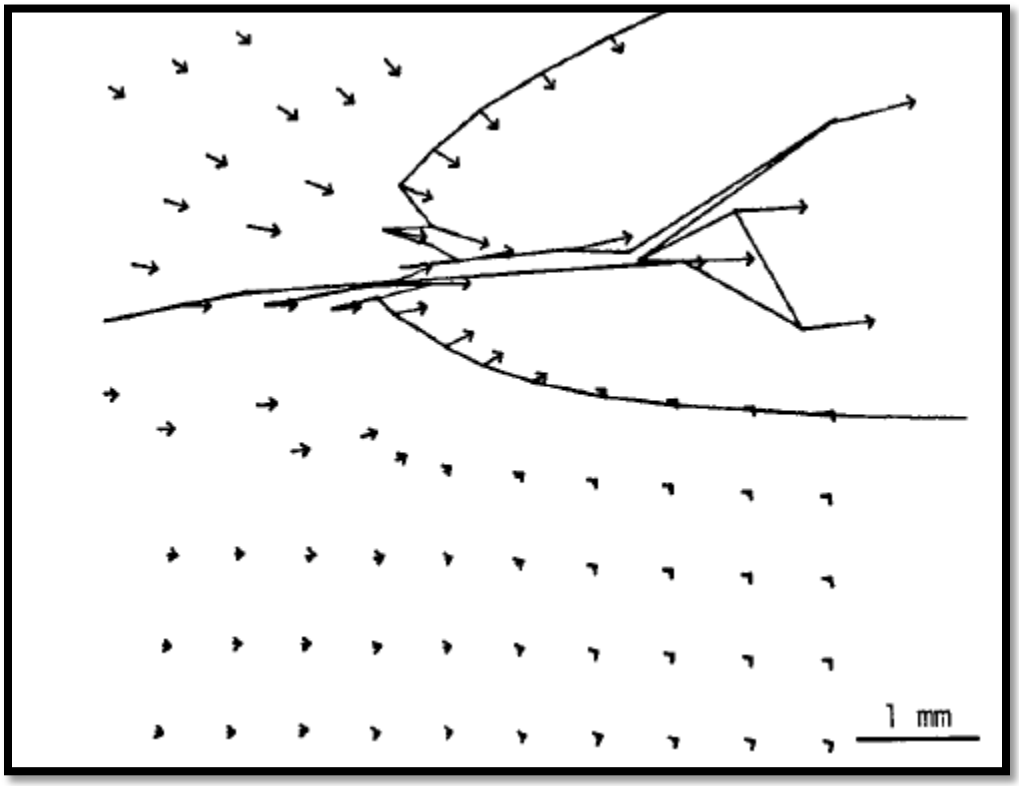

Figure 2-36: Early finite difference simulation by Oberg, Schweitz, and Olofsson showing a hump. [143]

impact angle" distinct from the one defined in Section 2.2.2.1, which does not account for any curvature in the local region of impact. This distinction does not appear to have been widely understood and adopted. More recently, in 2005, Mousavi and Al-Hassani completed modeling using AUTODYN that depicts and supports a similar hump formation [144].

After a review of this "hump", it does appear to be a legitimate physical phenomenon, based mainly on modeling results. As opposed to the idealized scenario in Figure 2-19 where there appears no means for the parent plate to contribute to jetting, the hump presents a scenario where material from the parent plate could be placed between, and roughly on a line normal to, its free surface and the stagnation point. The formation of this hump qualitatively makes sense with Blazynski's analogue and with Rayleigh surface waves. Though the bulk of the discussion on material waves focuses on dilatational waves (and is perhaps is confused with references to bond/interface waves), other physical waves obviously occur and are believed to be important. Simonov presented a criteria for bonding in 1991 based on the shear wave speed of the material [145]. In his proposed formulation, the weld velocity, V_w, is required to be faster than the speed of shear waves in the material. While Mousavi and Al-Hassani's experimental work show this criteria does not always predict bonding,[144] that does not preclude it from being a necessary condition. Referring to Meyers,[146] it is clear that shear waves are slower than dilatational waves and slightly faster than Rayleigh surface waves. Simonov's criteria then set the stage for a shear shock wave, (which would be captured by constitutive models with strain rate effects) and hence a Rayleigh shock wave that can travel faster than normal at a steady position relative to the collision point. Kakizaki et. all's work further demonstrate its effect via modeling, as shown in Figure 2-37 [90].

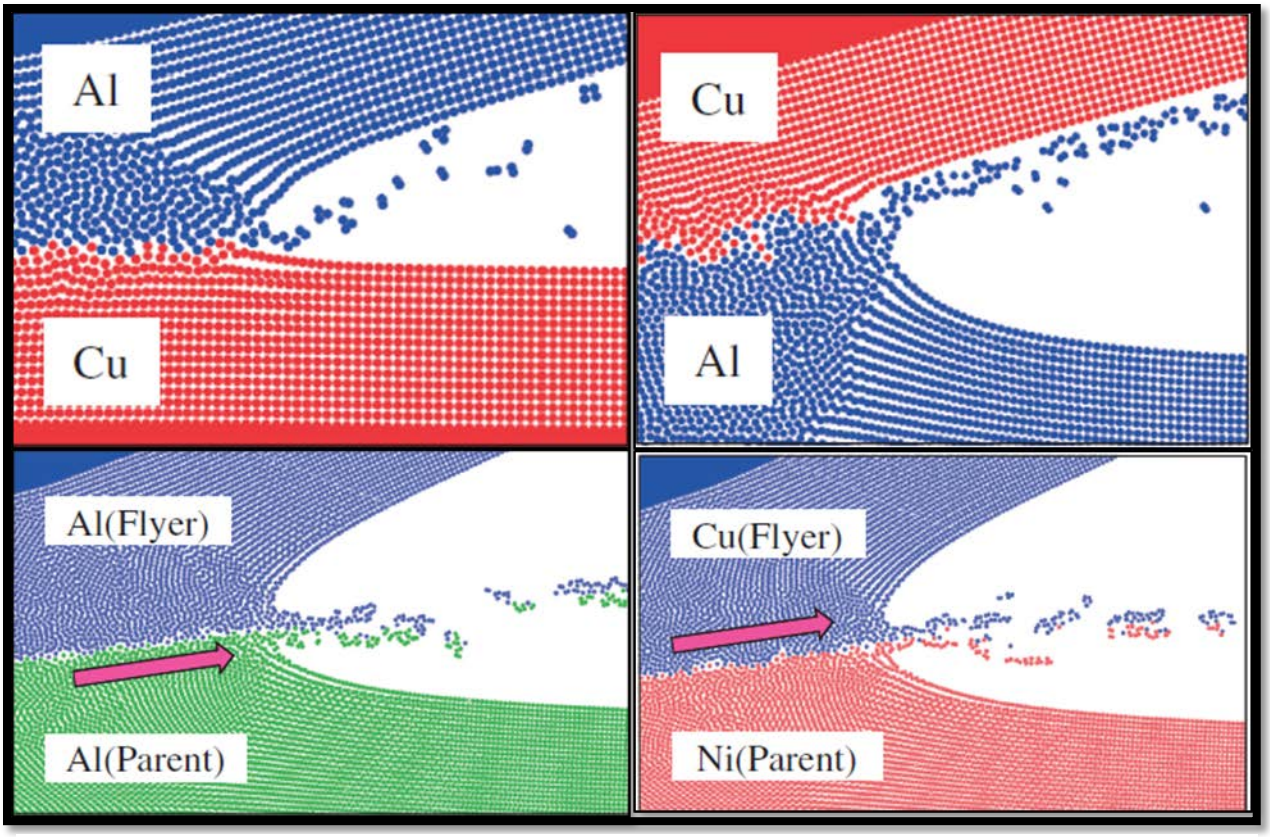

Figure 2-37: Hump configurations showing that it favors formation in denser material or equilibrates for more similar densities. Compiled from modeling by Kakizaki, Watanabe, and Kumai. [90]

2.2.4 Bond Metallurgical Characterization

In section 2.2.1, the fundamentals of the metallurgical bond were introduced. Highlights of the bond were discussed in section 2.2.1.3, introducing the overall grain characterizations and showing the smooth versus wavy interfaces in Figure 2-15. The formation of bond interfacial waves was discussed in section 2.2.3. What remains is to characterize the metallurgical and mechanical effects of the welding process.

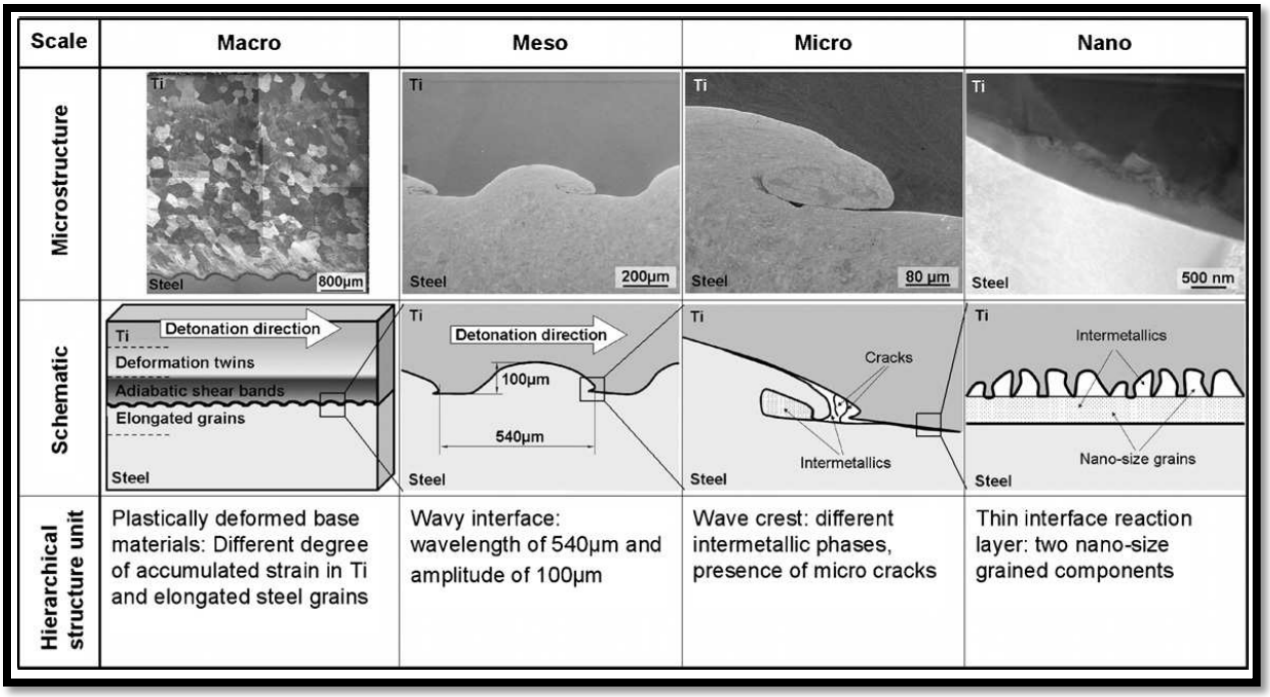

Figure 2-38: Metallurgy of impact welding bonds at different scales from [149].

Important characteristics appear at different scales of reference. Figure 2-38, from Song, Kostka, Veehmayer, and Raabe, is a good breakdown of important characteristics as smaller and smaller details are uncovered. Mechanical characteristics including hardness, fracture characteristics, and ductility, as well as grain sizes will be discussed at the macroscopic level. The effect of melting, the grain characteristics near the bond, and the impact of turbulent waves will be discussed at the combined meso and microscale. And the nature of the smooth interface that appears in the smooth bond, as well as in portions of wavy bonds, will be discussed at the nanoscale, including a discussion of whether the bond is solid state, as is traditionally believed, or is characterized with nanoscopic melt.

2.2.4.1 Macroscale

As has already been highlighted, and can be viewed in Figure 2-15 and Figure 2-39, the grain structure in explosive welding varies from a natural state as one progresses to the bond

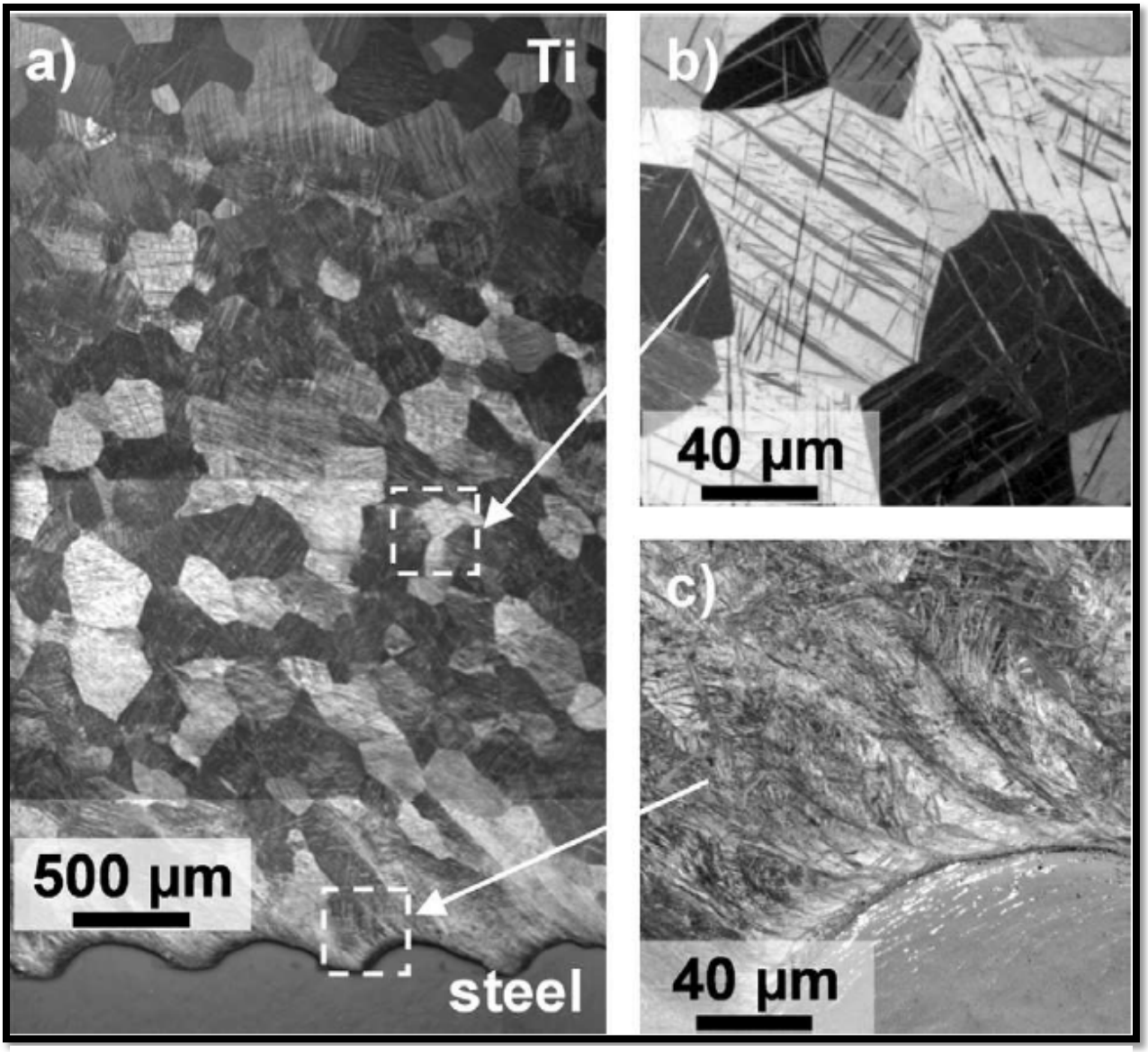

Figure 2-39: Welding showing grains far from bond, with details. a) Larger scale showing relation to bond has grains with diameter ≈ 50 µm. b) Closer view of larger grains that still contain deformation twins. c) Region nearest the bond of intense shear deformation containing adiabatic shear bands and high dislocation densities. [149]

region. The grains in the base metal are largely equiaxed, but may have deformation twins dependent on the degree of shock hardening that occurred and the nature of the metal [147]–[149]. Microhardness measurements are typically taken across the bond layer. Examples of this are widespread, e.g. [127], [150]–[157]. One publication even provided a hardness map [150]. Typically, the microhardness increases in the vicinity of the bond zone, although in some cases,

due to either melting or a degree of annealing due to excess energy, there can be a dip in hardness at the bond layer [5, p. 201], [6, p. 193]. Commonly, the shear stiffness and the ductility of the bond are of interest, and so common clad standards specify shear tests that stress the bond and also tests that require bending around a radius for ductility [158], [159]. Although, wavy bonds are often favored and considered strong, it has also been shown that smooth bonds can be effective. They also present less risk of brittle intermetallic compounds [157], [160], [161]. Certain multilayer composites generated by multilayer explosive bonding have shown increase fatigue crack resistance [162]. Also, the bond layer has a strong effect upon the propagation of cracks in good welds. It is posited that the directional nature of the elongated grains and their particular angle in a wavy interface provide an anisotropic condition, and the angle of propagation can change more than 90° to follow the bond layer for a period of time [163].

2.2.4.2 Mesoscale and Microscale Melting and Distortions

As one starts to look more closely at the meso and micro scales, many details emerge that illuminate why there is often increased hardness in the vicinity of the bond. As seen qualitatively in Figure 2-40 a), and with microscope images in Figure 2-40 b), there is a zone, clearly visible due to the grain refinement and distortion, with intense plastic deformation. As seen in Figure 2-40 b), the amplitude of a wavy interface pattern is captured within this zone. The size of this zone has been shown by Bondar and Nesterenko to be correlated with the thickness of the jet from Equation (2-8), $t_f \cdot sin^2\left(\frac{\beta}{2}\right)$. [164] Within this zone, there is intense distortion and elongation of the grains. Adiabatic shear bands, as shown in Figure 2-40 c), commonly occur, and as corroborated by Zareie Rajani and Akbari Mousavi [155]. In certain

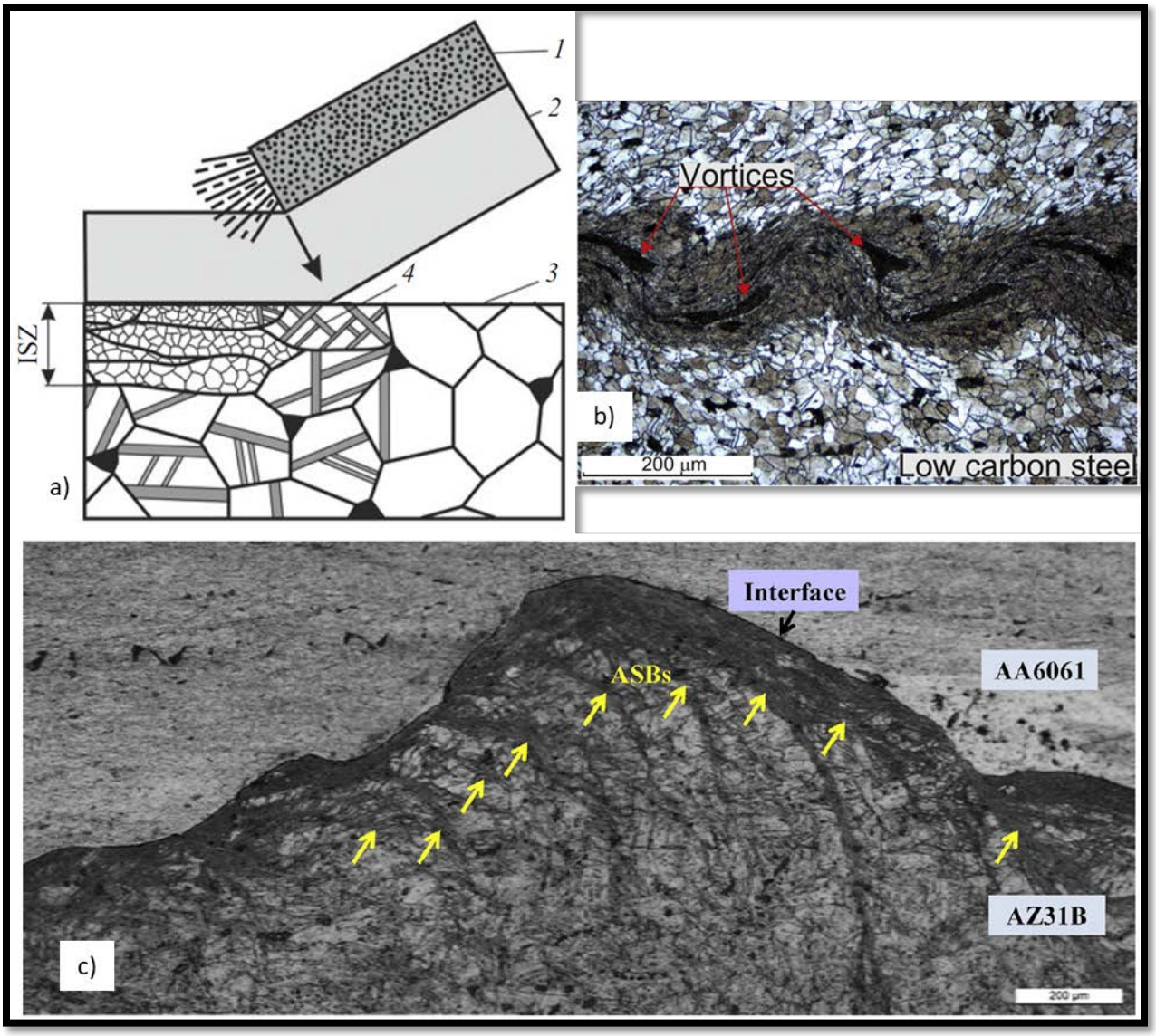

Figure 2-40: Intense shear zone with small grains and adiabatic shear bands. a) Qualitative illustration of grain changes. [148] b) Optical image highlighting region of intense shearing based on smaller, distorted grains.[177] c) Another example of aluminum welding where adiabatic shear bands can be seen next to yellow arrows.[104]

cases, grains in this region can undergo dynamic recrystallization, as noted by Bondar [165] and discussed in [166], [167].

Within this zone of intense plastic deformation, either the smooth or wavy interface is contained. The wavy interface can be smooth, as more or less shown in Figure 2-15 b), or it can be turbulent, with vortices, as shown in Figure 2-31 (c) and (f). In either the smooth or the wavy

configuration, it possible to have a layer or pockets of melt (for example, see [168]). When full melted layers are manifest, it is often a sign that the welding state was too close to the upper bound of the welding window.

Melt at this scale can cause a number of problems. First, for dissimilar metals, certain combinations can form intermetallic compounds if put into a melted state, thereby facilitating diffusion and chemical reactions. Even without intermetallic compounds, Figure 2-41 shows how polymorphic crystalline phase change can be rampant, generating metastable or other phases that can have undesirable effects. Second, after melting it is common for pores as shown in Figure 2-41, or cracks to form in the melt upon cooling [118]. However, melt can typically be controlled and prevented. If just in isolated vortices, it is often not large enough to produce cracks and pores during cooling, or if it does, it is infrequent enough that long lengths of very high-quality bond can compensate for any existing deficiencies. In the absence of melt, at this meso/micro scale, the bond interface is not resolvable (i.e. with optical or SEM resolutions). The

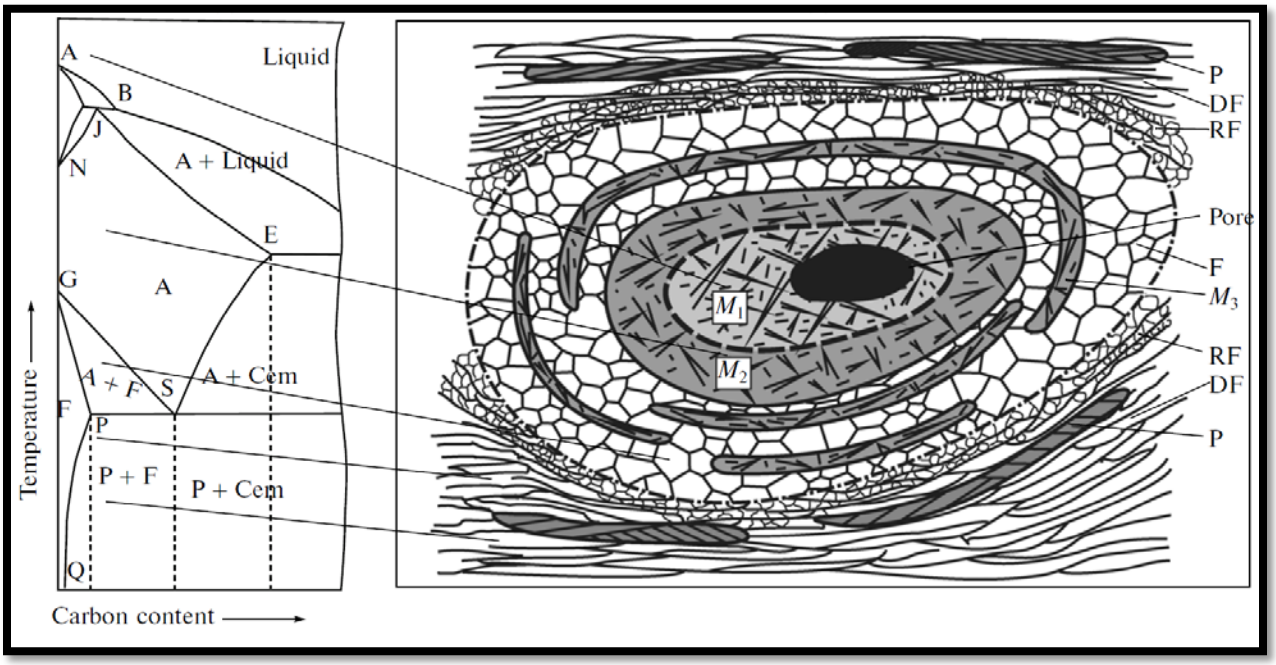

Figure 2-41: Example phase composition of steel-steel welding. F, ferrite; P, pearlite; M_1, M_2, and M_3, martensite; DF, deformed ferrite; RF, recrystallized ferrite; and C, cavity. [243]

bond shows little to no diffusion of one material into the other, which is why this has been historically considered a solid-state bonding process. Electron dispersive spectroscopy (EDX) analyses that can identify different elements are routinely conducted to attempt to detect evidence of diffusion. Typical dissimilar metal profiles at a "non-melt" interface will transition from one material to the other in around 5 μm or less [150].

2.2.4.3 Nanoscale Analysis of the Bond Interface and Ultra-fine Melt Layer

As presented above in Section 2.2.4.2, in regions of strong bonding without significant melt layers (i.e. even at the peaks and troughs of otherwise turbulent bond interfacial waves), the details and morphology of the interface is actually an abrupt but finite transition from one material to the other, sometimes referred to as the interlayer or interpass. This appears to have been first identified in work by Hammerschmidt and Kreye in 1981 with early transmission electron microscope (TEM) work [68]. Hammerschmidt and Kreye challenged the notion that the bond interface was characterized by a solid-state nature, instead claiming that the interlayer was in fact a fine layer of melting varying from 500 nm to 5 μm wide. This flew in the face of orthodoxy and inertia in the academic community. Many, even those applying TEM analysis, still don't always refer to the bond as having a layer of melting [149], [152], [169]–[172]. However, much more recent work that capably analyzes the interlayer at sufficient resolution often concludes that this layer experiences a sequence of rapid melting then solidification [154], [173]–[177]. Paul et. all even show melt layers as small as 20 nm, with fine crystallites smaller than a few tens of nanometers "'immersed' in the solidified melt" [154]. Considering the rough scale of an atomic radius is 1/6 of a nanometer and example crystal unit cell lengths are on the order of 0.5 nanometers, this provides room for tens of layers in a crystallite.

This type of melting would involve rapid heating and subsequent quenching. On this there is and has been consensus for some time. Hammerschmidt and Kreye reported this in 1981 (rapid heating and cooling on the order of 10^5 K/s,) and there has not been major dispute [68]. Paul and others have reported that these rates could be on the order of 10^9 K/s for heating, with cooling near 10^5-10^7 K/s [154], [177]. This is consistent with the identification of adiabatic shearing as a primary functioning mechanism in the creation of the bond [178]. It is also consistent with the findings of Bondar in 1995, who referred to this as a plastic-strain localization band [165].

The identification of the bond boundary with TEM does yield some consistent characteristics. There are a number of studies that identify regions of nano-sized grains, regardless of material type [152], [154], [172], [174], [179]. Grain sizes decrease from the size in the base metal state to the nano-size at the edge of the bond, similar to the progression shown in Figure 2-38 on the right as you move up from steel to the next layer. This could be associated with arrival at the plastic-strain localization band and a region of dynamic recrystallization [166], [167]. At this point heading deeper into this “good bond”, there appear to be differences of significance based upon the materials joined and perhaps the amount of energy in that region of the bond. In one case of like metal welding, the grain morphology progressed similar to the right side of Figure 2-42 [172]. This boundary of nano-sized grains progressing to a possible higher temperature mixing or melting layer at the center of the interlayer is similar to that discussed by Paul [154].

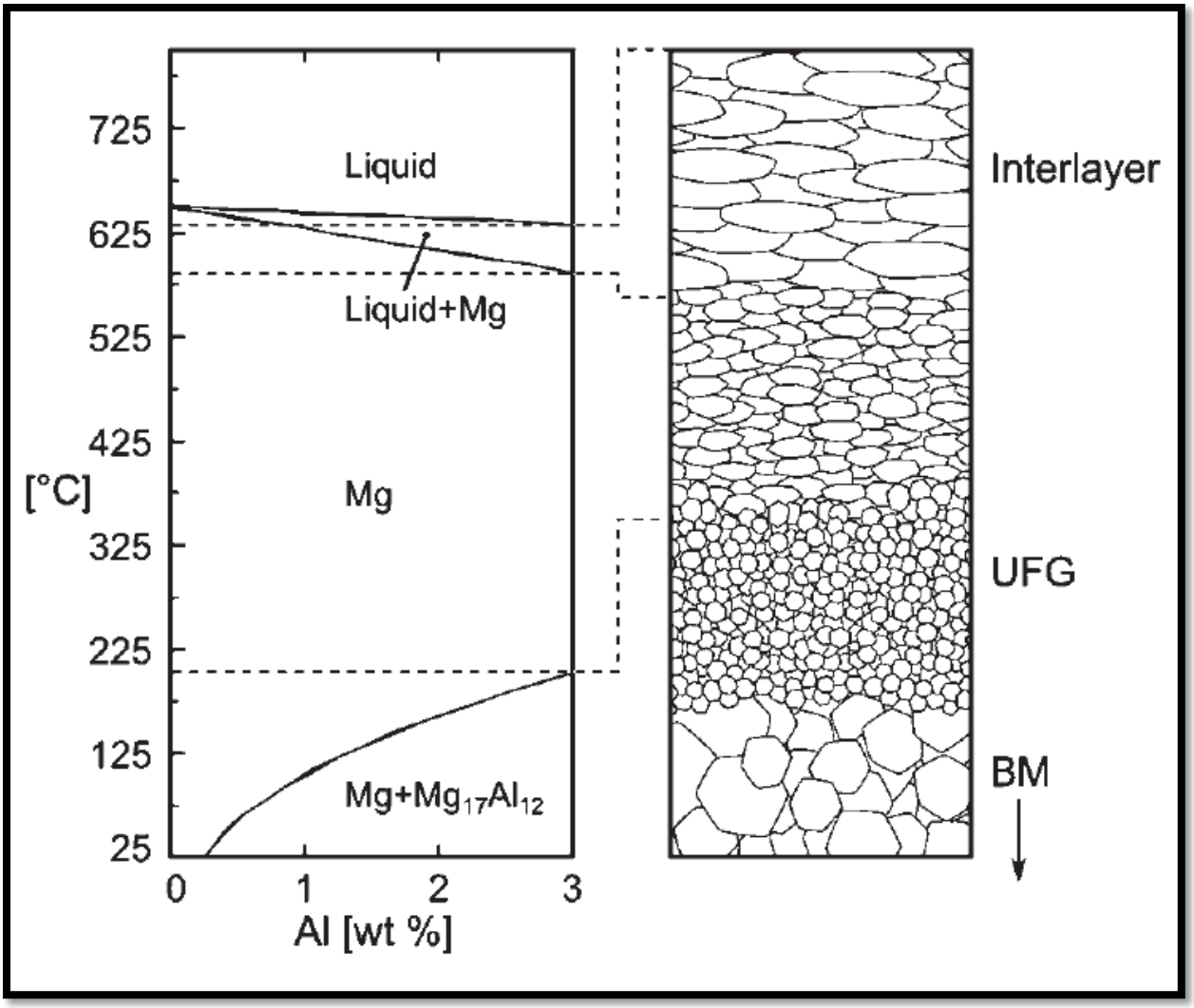

Figure 2-42: Grain structure of good bond proposed by Berlin for Magnesium Alloy AZ31. The qualitative grain sizes are shown at right, associated with phase and temperatures at left, with the top being a plane/line of symmetry passing back towards the upper base metal. [172]

3. EXPLOSIVE WELDING TESTS

As has been noted, in the spring of 2017, this project was initiated between the University of California San Diego Center for Extreme Events Research (CEER) and the Asahi Kasei Corporation. The intent was to perform four simulation guided explosive welding tests, as an integrated experimental and computational investigation. Supporting modeling using the Nonlinear Meshfree Analysis Program (NMAP)[180], a Reproducing Kernel Particle Method research code, was used in support of the test design.

Four explosive welding tests were performed with 10.75 in. x 3 ft. x 0.25 in. thick 6061-O aluminum plates (as used in a similar study in [181]). The plates were subjected to appropriate explosive amounts as shown in Figure 3-1 below and in Table 3-1. Time-of-Arrival (TOA) Pins monitored the progress of sheet explosive detonations and welding of the test specimen plates. A unique test setup was designed to attempt to protect these pins from weld jetting that overlapped the flyer plate beyond the sides of the parent plate as shown in Figure 3-2. A flash X-Ray system, which generates a nominal 25 nanosecond duration X-Ray energy pulse, and high-speed video were used to capture the motion of high-speed objects. The flash X-Ray system allowed the measurement of impact angle and collision velocity, as well as the generation of other information about plate deformations and interface conditions. The explosive amount and standoff distance of the four explosive welding tests were guided by NMAP analyses by CEER with initial corroborating CTH modeling at ARA. Additional experimental parameter verification was conducted prior to the main test series.

Figure 3-1: Example test specimen (8 degree without explosive and explosive instrumentation.)

Table 3-1: Experimental Conditions (Data that differs for the parent plate noted separately in blue)

Test No.	Cladding (flyer) (*parent*)* Plate Dimension	Cladding (flyer) Plate Thickness	Cladding (flyer) Plate Material	Type of Explosives	Initiation	Thickness & Width of Explosive	Stand-off Distance	Initial Plate Angle (α)	Measurement	Velocity of Flyer Plate (estimate)	Impact Angle (estimate)	Collision Point Velocity (estimate)
1	10.75 in.× 36 in. 6.5 in x 36 in	1/4 in.	6061-O Al	PETN-based	LWG	2.1 mm thick 10.5" wide	3.175 to 11.2 mm (linearly)	0.5°	• Deformation of Cladding plate (TOA) • X-Ray	380 m/s	3.6°	6000 m/s
2	10.75 in.× 36 in. 6.5 in x 36 in	1/4 in.	6061-O Al	PETN-based	LWG	2.1 mm thick 10.5" wide	3.175 to 27.1 mm (linearly)	1.5°	• Deformation of Cladding plate (TOA) • X-Ray	380 m/s	4.6°	4700 m/s
3	10.75 in.× 36 in. 6.5 in x 36 in	1/4 in.	6061-O Al	PETN-based	LWG	6.35 mm thick 10.5" wide	3.175 to 43.1 mm (linearly)	2.5°	• Deformation of Cladding plate (TOA) • X-Ray	920 m/s	10°	5300 m/s
4	10.75 in.× 36 in. 6.5 in x 36 in	1/4 in.	6061-O Al	PETN-based	LWG	6.35 mm thick 10.5" wide	0 to 127.3 mm (linearly)	8°	• Deformation of Cladding plate (TOA) • X-Ray	920 m/s	15.5°	3400 m/s

* flyer plates with larger width than the parent plates to protect these pins from the weld jetting

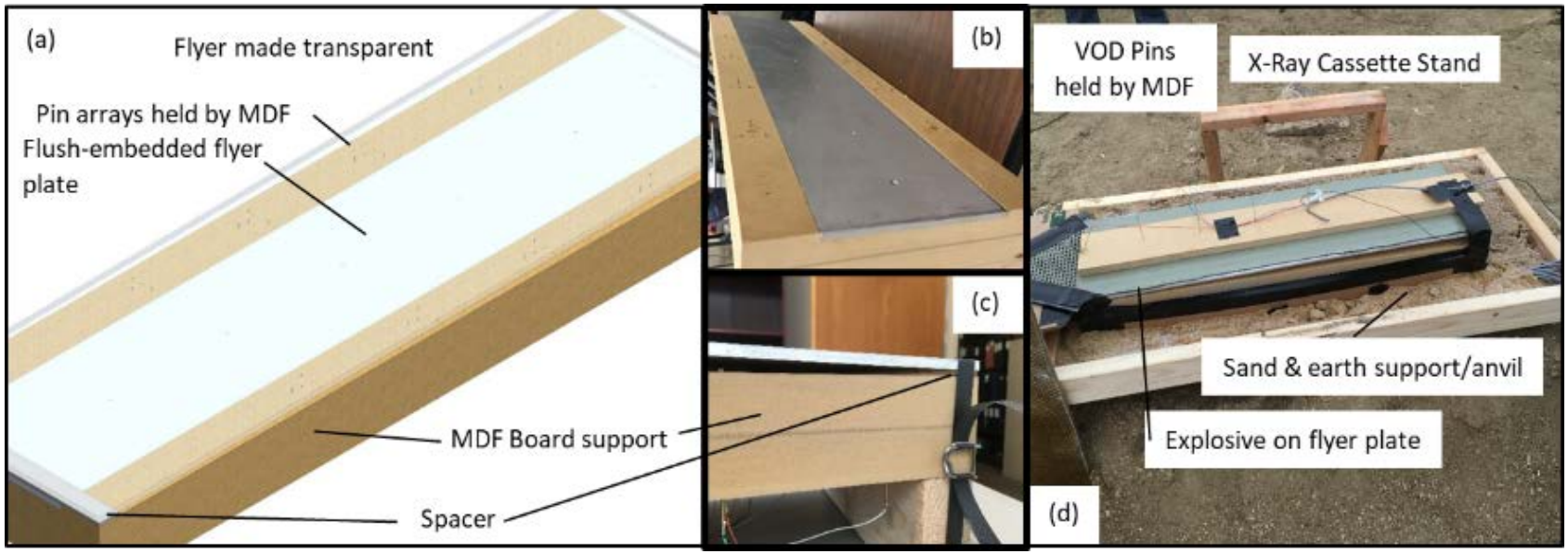

Figure 3-2: Test specimen concept and implementation. (a) Isometric plan. (b) Specimen without flyer plate (c) Specimen with flyer secured and range ready. (d) 1.5 deg specimen s prior to detonation and placement of X-Ray cassette.

3.1 WELD DESIGN

3.1.1 WELDING WINDOW DEVELOPMENT

As noted in Section 2.2.2.3, the first step in the design of welds requires the establishment of a welding window. In this case, since the welding of Aluminum 6061-O was the focus, the welding window established in [181] was used as the starting point. In that study, the lower boundary was established using material properties and Equation (2-11), established by Deribas [93]. The upper boundary was an alternative to Equation (2-13), established by Deribas in the same paper, but modified as suggested by Crossland [6, p. 98]. Crossland noted that a series of material properties were included in Deribas' original formulation, only to be multiplied by an empirical constant, *k*. His modification was then to conflate all the material constants with the empirical constant, leaving only the varying plate thickness and weld velocity terms, as shown in Equation (3-1) below. In this equation, β is impact angle, t_f is the thickness of the flyer, V_w is the velocity of welding, and *k* is the empirical constant (unique to this equation).

$$sin\left(\frac{\beta}{2}\right) = \frac{k}{t_f^{0.25} V_w^{1.25}} \tag{3-1}$$

Establishment of the value of *k* was not discussed by Deribas, but is obviously a critical step. Wittman's Equation (2-13) also requires the establishment of an empirical constant, *N*. Neither author explicitly recommends how to establish their constants, but it is clear they require the conduct of experiments. Wittman did use his equations and experimental data to make comparisons between metals. In making those comparisons, Wittman chose to compare values at a weld velocity, V_w, equal to ½ the speed of sound in the metal. Crossland stated that this proves to be a good single weld velocity to use for establishing a value for the constant, *k*, that can then be assumed to apply to a permissible domain of weld velocities [6, p. 98]. Grignon has upper limits for two plate thicknesses in [181], but it is unclear exactly how the constant, *k*, was

evaluated in that work. Based on that fact, and the discovery that the available sheet explosive thicknesses appeared to generate plate velocities such that the welding state was very near the bottom boundary of the weld window, it was assumed that the upper boundary would not be a limiting factor and was therefore disregarded. The left boundary for the window was based on practical limits and will be discussed later, while the right limit was not explicitly developed with Hugoniot data; rather a rule of thumb was investigated.

3.1.2 Welding State Selection

Upon the development of a welding window, Section 2.2.2.3 then suggests some latitude in choosing the individual independent variables. In the case of this study, the first choice was driven by explosive selection. As an initial study, the decision was made to use explosives that ARA already had available to decrease costs as capability was demonstrated to Asahi Kasei. This fixed the detonation velocity, V_d, and due to two available thicknesses of the sheet explosives, gave discrete possible plate velocities for the ¼" plate that had been proposed to Asahi Kasei. This left the inclination angle, α, as the sole independent variable where there was discretion. The immediate task upon making it to this point was to establish the plate velocities that would be achieved.

3.1.2.1 Flyer Plate Velocity-Displacement Modeling and Experimental Verification

- Explosive Characterization

The explosives selected were Donovan PETN-based sheet explosive with nominal dimensions of 2 mm (C2) and 6 mm (C6). Actual dimensions were based on US imperial units at 1/12 in and 1/4 in respectively (2.116 mm and 6.35 mm). The explosive was fabricated by Donovan Commercial Industries and had the same make-up and performance characteristics as equivalent products from suppliers like Ensign-Bickford (Primasheet). They contained 64%

PETN, 25.75% Citroflex (acetyl tributyl citrate or ATBC), and 10.25% Nitrocellulose, coming in 10.5" wide sheets. The manufacturer's specification listed the detonation velocity, V_d, as 7.00 mm/μs and the density as 1.48 g/cm^3. Cheetah 8.0 was used to analyze the explosive and develop parameters for the Jones-Wilkins-Lee Equation of State. The resulting parameters are shown in Table 3-2.

Table 3-2: Jones-Wilkins Lee Explosive Burn parameters

A (GPa)	B (GPa)	C (GPa)	R_1	R_2	ω	ρ_0 (g/cc)	E_0 (KJ/cc)	P_{CJ} (GPa)	D_{CJ} (m/s)
712.61	27.644	1.600	5.782	1.941	0.359	1.48	7.820	18.50	7000

- Aluminum Modeling and Parameters

Within NMAP, the aluminum 6061-O material was modeled using the Johnson-Cook constitutive relation for the deviatoric behavior of the material. This accounted for hardening, strain-rate effects, and temperature effects in loading [182]. The Johnson-Cook fracture model, which similarly accounts for the state of stress, the plastic strain rate, and the temperature, was used as well [183]. The equation of state, or pressure-volume-temperature relationship, was the Gruneisen equation of state. The parameters used are shown below in Table 3-3 and Table 3-4. The equations and details will be presented later in Section 6.2.1.

Table 3-3: General Material and Johnson-Cook Parameters for Aluminum 6061-O

ρ (gm/cm^3)	T_m (K)	T_{rm} (K)	G (GPa)	A (MPa)	B (MPa)	c
2.7	926	294	25.94	60	500	0.02
n	m	D1	D2	D3	D4	D5
0.3	1.0	-0.77	1.45	-0.47	0.011	1.6

Table 3-4: Aluminum equation of state parameters for the Gruneisen model.

c (mm/μs)	γ_0	a	S_1	S_2	S_3	E_0 (MPa)
5.293	1.97	0.48	1.345	0	0	0.0514

- Predicted Velocity-Displacement Relation

Modeling was initially conducted in CTH by ARA to predict the velocity-displacement time history, and NMAP simulation was produced shortly thereafter. At this stage of the project, the use of 1/8" thick aluminum flyer plates was still under consideration. The results of these simulations are shown in Figure 3-3 below. For the ¼" plate (that was eventually used), the

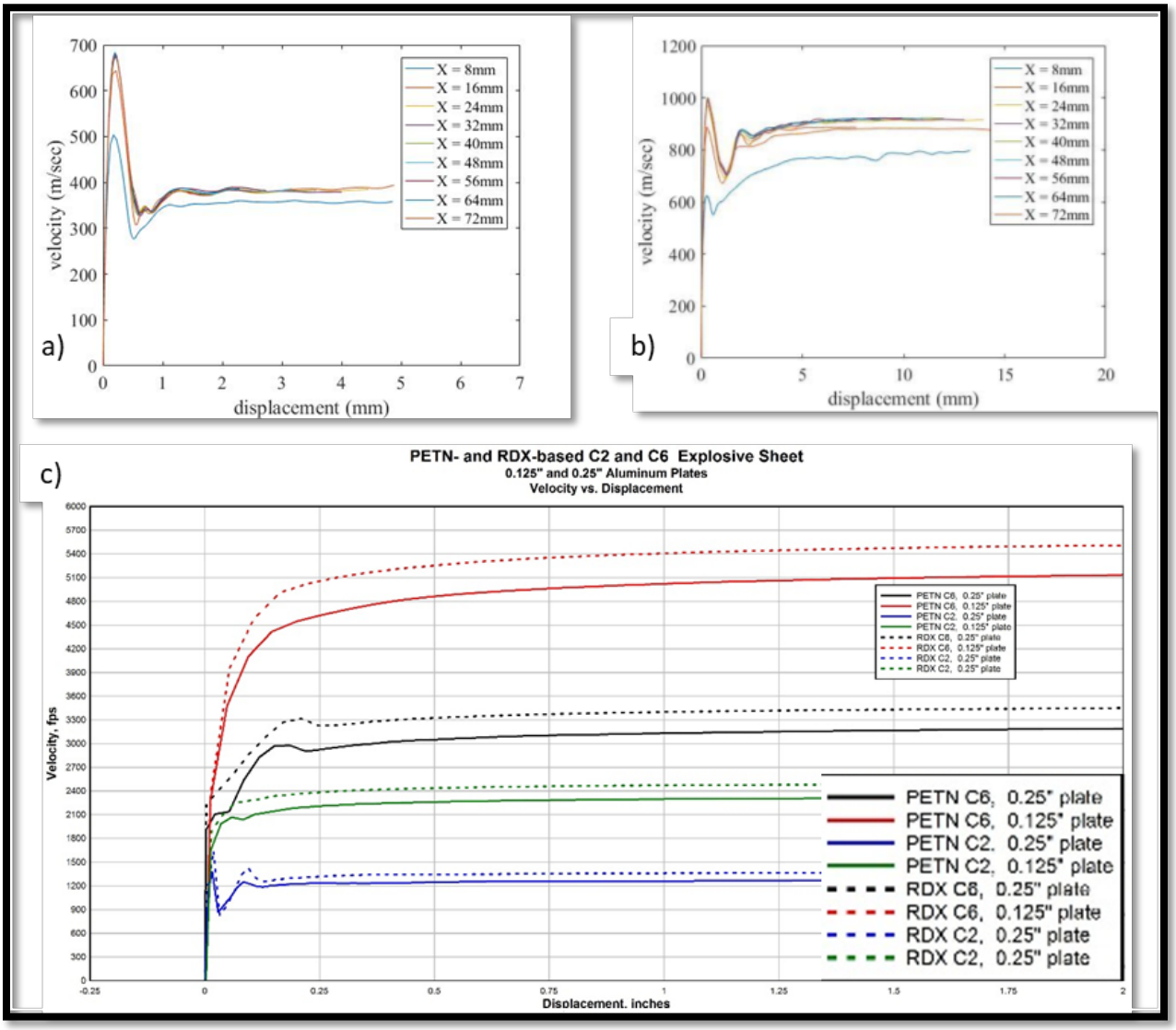

Figure 3-3: Modeled Flyer Plate Velocity-Displacement Histories. a) NMAP result for 1/4" plate with a C2 thickness [1/12" of explosive]. b) NMAP result for a 1/4" plate with a C6 thickness [1/4" of explosive]. c) CTH modeling results for 1/4" and 1/8" flyer plates and C2 or C6 thicknesses, per the legend.

NMAP generated values of flyer plate velocity, were V_p = 0.380 mm/μs for the C2 thickness and V_p = 0.920 mm/μs for the C6 thickness. These values were used in Equations (2-1) and (2-2) for identifying potential welding states for use on the welding window, and they compare favorably with the blue and black lines in Figure 3-3 c) from CTH.

- Verification of Detonation Velocity and Plate Velocity Modeling

On June 19, 2017 preliminary tests were conducted to confirm explosive characteristics and plate velocities. The specimen, is shown below in Figure 3-4 (a) & (b). The time of detonation front arrival at different pins is shown in Figure 3-4 (c) from the oscilloscope waveform data. These values were tabulated below in Table 3-5, where the average velocity was calculated. This provided an experimentally measured velocity of 7.06 mm/μs.

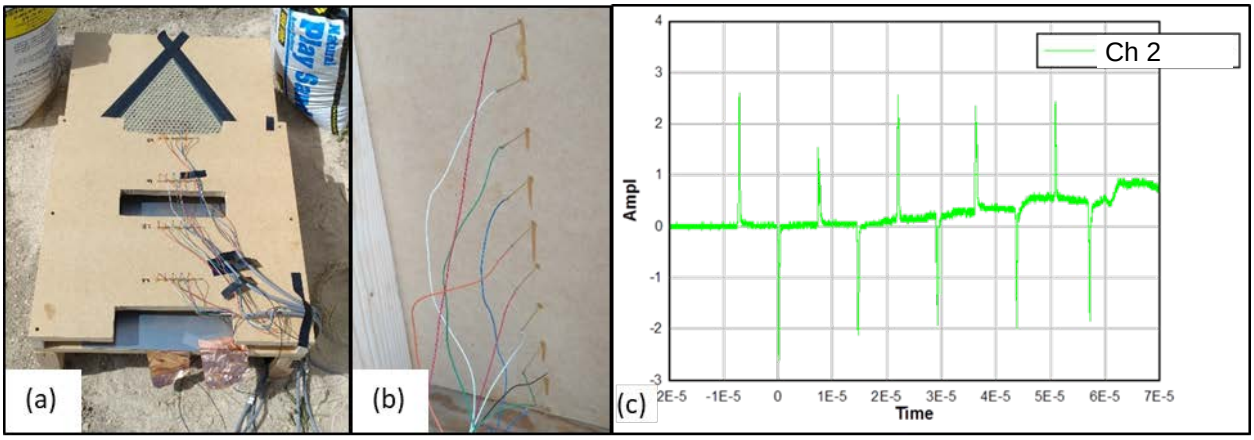

Figure 3-4: Plate and Detonation Velocity Test. (a) 19 June Test (C2 explosive thickness on bottom pushing 1/8 in. flyer up into V_p pin arrays). b) V_d pins on bottom of specimen shown in a). c) V_d data plotted, where spikes represent voltage discharges measured by the oscilloscope upon contact with the explosive.

Table 3-5: Experimental Velocity of Detonation data and calculated velocities. Distance between the heights of the pins are shown next to the Time of Arrival (TOA) based on voltage spikes.

	C2 PETN Sheet Explosive		Slope: 7.05 mm/μs
	Distance, mm	TOA, μs	
0	0	-7.2624	
1	50.8	0.0156	
2	101.6	7.2896	
3	152.4	14.6016	
4	203.2	21.8936	
5	254	29.1676	
6	304.8	36.1456	
7	355.6	45.6656	
8	406.4	50.7536	
9	457.2	57.0456	

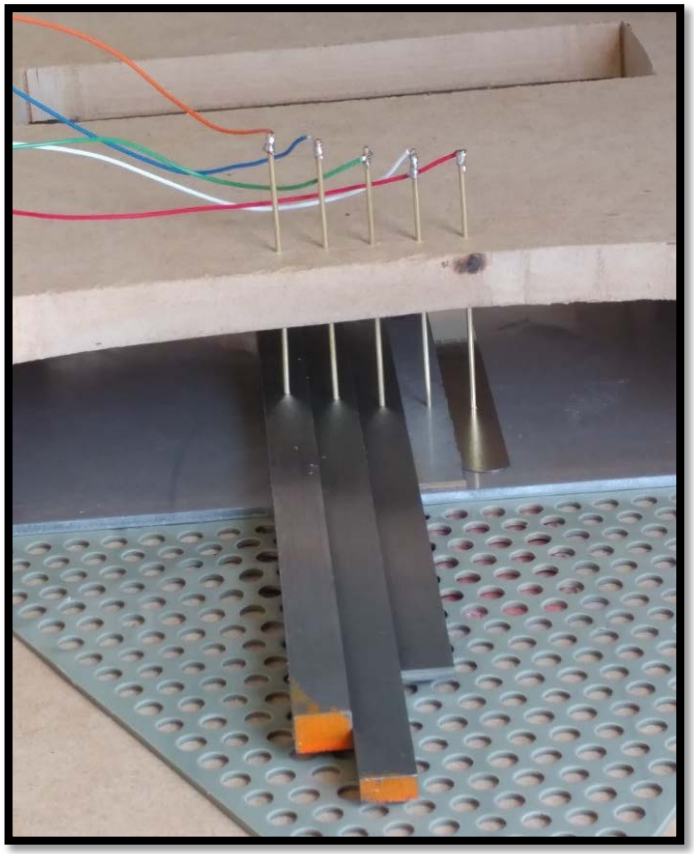

Figure 3-5: Plate Velocity Pin Arrays. The pin arrays in the explosive flyer plate test were spaced from the aluminum plate using precision ground bar stock (shown in place), in order to best measure the distance traveled before contact with the pin.

The same test specimen from Figure 3-4 was used to experimentally measure the flyer plate velocities. Looking closely at Figure 3-4 a), it is possible to make out that five lines of time of arrival pins that were spaced down the length of the 1/8" plate, while Figure 3-5 shows a close-up of a sample array. The horizontal arrays allowed the time of arrival of the flyer plate to be measured at different heights for the same longitudinal distance, providing a discrete displacement time history for the plate, assuming no curvature in the transverse direction. Table 3-6, below, shows the tabulated values of the displacement data, as well as the average velocity that was calculated as a result at each longitudinal distance. Figure 3-6 shows a plot of the oscilloscope data for the test. This data served as validation for the computational models in NMAP and CTH, enabling selection of flyer plate velocities for use in identifying the state of welding.

Table 3-6: Plate velocity data from the June 19, 2017 test with a 1/8" plate and a C2 (1/12") thickness of explosive.

Movement of 3.175 mm Al Plate (6061-T6)						
Horiz. Distance, mm	Vert. Dist., mm	Time, μs	Δt, μs	Speed, mm/μs	Average Speeds, mm/μs	
50.8	0.08	0.20162	0		Avg. Spd	0.64
	1.602	2.6236	2.42198	0.628411	Fit:	0.9995
	3.2	5.1936	4.99198	0.62179		
	6.371	10.3416	10.13998	0.615967		
	9.536	14.9316	14.72998	0.689542		
152.4	0.08	14.6736	0		Avg. Spd	0.62
	1.602	17.2996	2.626	0.579589	Fit:	0.9997
	3.2	19.9776	5.304	0.596714		
	6.371	25.0716	10.398	0.622497		
	9.536	29.9996	15.326	0.642248		
254.0	0.08	29.0376	0		Avg. Spd	0.63
	1.602	31.7256	2.688	0.56622	Fit:	0.9985
	3.2	34.4596	5.422	0.584492		
	6.371	39.3776	10.34	0.644774		
	9.536	43.9636	14.926	0.690144		
355.6	0.08	43.8056	0		Avg. Spd	0.66
	1.602	46.1136	2.308	0.659445	Fit:	0.9986
	3.2	48.7596	4.954	0.60393		
	6.371	53.7556	9.95	0.634708		
		Average P3 to P5:		0.660486	mm/μs	

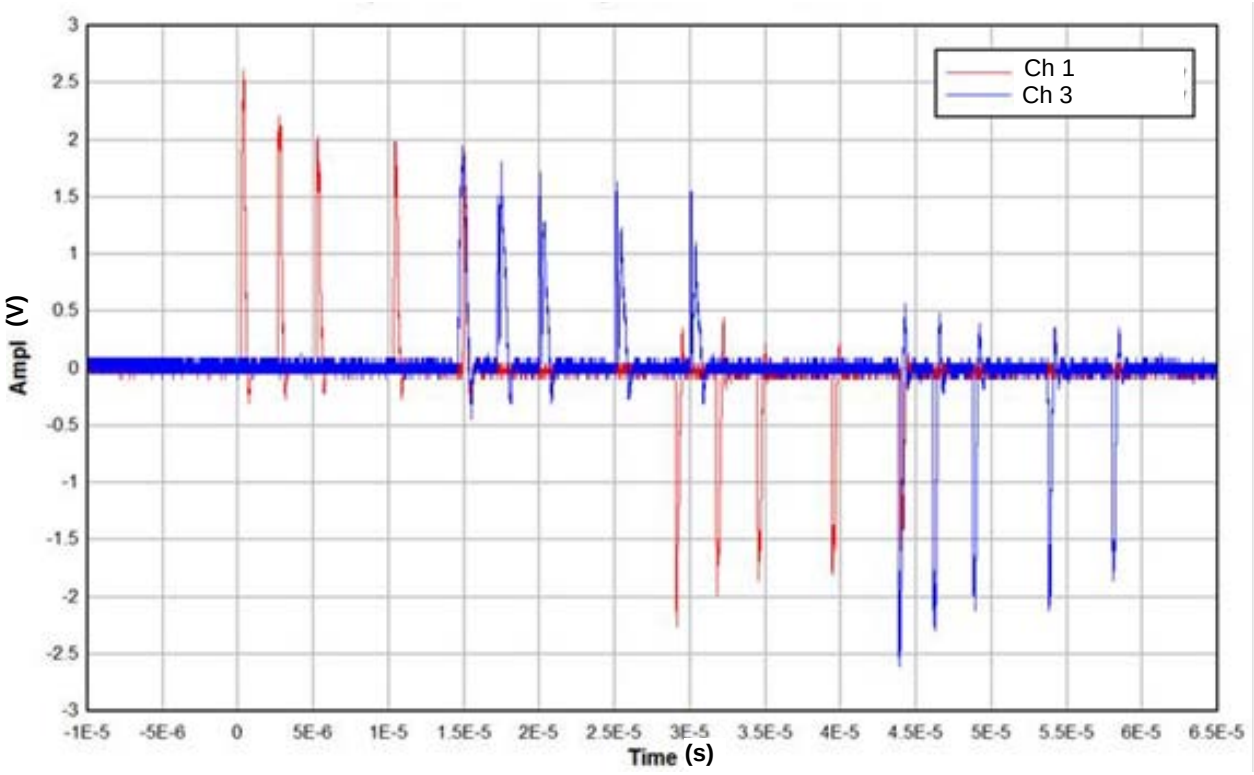

Figure 3-6: Flyer plate oscilloscope data, showing the voltage spikes upon contact. Two channels for data acquisition were used. Voltage discharge sign (±) only reflects details of the wiring diagram.

3.1.2.2 Accessible States within the Weldability Window

With the explosive detonation velocity, V_d, and the flyer plate velocity, V_p, predictions confirmed, potential states of welding could be generated. Equation (2-1) allowed selection of the impact angle, β, as a function of flyer plate inclination, α. Figure 3-7 below, shows the result of using our confirmed detonation velocity and flyer plate velocities to generate different impact angle options. Discrete values for the flyer plate inclination are plotted and labeled along the continuously varying set of options. The figure shows the result for the two different plate speeds. Additionally, the sonic speed of aluminum is shown on the figure for reference. For the lower thickness of explosive, the lower boundary for a cleaned surface was just exceeded, and for the thicker amount, the reduced cleaning value was just passed. It was this result that drove the assumption that the upper boundary of welding did not warrant further exploration.

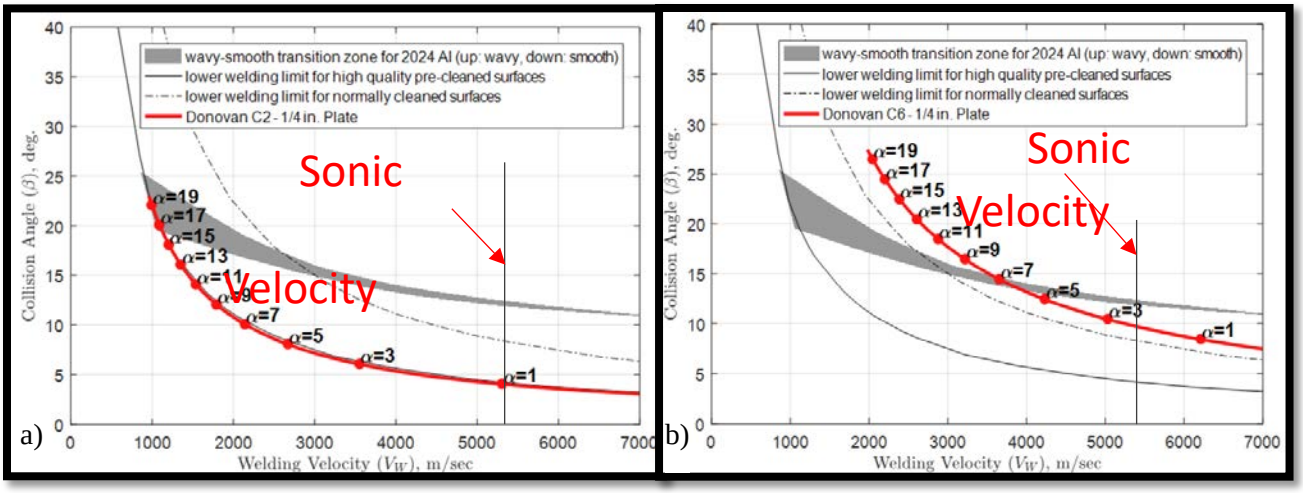

Figure 3-7: Experimental weldability window with potential experiments as a function of the ¼" flyer plate inclination angle, α (degrees), shown in red. a) Result plotted for the C2 explosive thickness [1/12"/2.116 mm]. b) Result plotted for the C6 thickness of explosive [1/4"/6.35 mm].

With direction to conduct four tests using varying explosive thickness, it was decided to conduct two tests at each thickness of explosive. Within each set of tests for a given thickness, discretion was provided for the flyer plate inclination. It became clear that due to the high velocity of detonation for the available explosive, it would be required in all cases to incline the flyer plate in order to achieve a weld.

For the 2 mm thickness of explosive, based on the estimated velocity of the flyer plate, an initial plate angle α = 1.0° results in a collision point velocity of roughly 5300 m/s, which is also the approximate acoustic speed of aluminum. As discussed in Section 2.2.2.3, this enters the region of behavior where dilatational shock fronts must be considered. While in Section 2.2.2.2 rules of thumb, simplified equations (such as Equation (2-12)), and detailed analysis based upon material Hugoniot data were referred to as possible means for selecting the right limit, it is also true that some references recommend keeping the weld velocity lower than the sonic velocity in the material [6, p. 88]. The flyer plate inclination angles chosen were 0.5° and 1.5°, in order assess the impact of crossing this threshold. The weld velocity for α = 0.5° is 6.03 mm/μs. This is roughly 14% greater than the sonic speed of aluminum, while still less than the rule of thumb

limit in Section 2.2.2.3, which caps the weld velocity at 25% greater than the speed of sound. The inclination $\alpha = 1.5°$ generates a weld velocity of $V_w = 4.69$ mm/μs. The tests provide an opportunity to contrast the results as the sonic speed of the material is exceeded.

For the tests using the 6.35 mm of explosive, a clear opportunity was presented to evaluate the applicability of the Al 2024 smooth-wavy transition boundary generated by Jaramillo, Szecket, and Inal[71] to Al 6061-O. However, as previously indicated, increased standoff distance detrimentally affects the quality of welding. A limit of 25 mm was suggested, as shown in [6, p. 115]. Using that limit, it was clear that, especially in the case of the C6 explosive thickness, good welding would only be expected on a smaller portion of the 36" plate to be used. An inclination angle $\alpha = 7.0°$ is roughly the lower bound before entering the smooth-wavy weld transition region, as shown in Figure 3-7 b). In order to get the maximum amount of plate below the standoff limit, while still keeping the weld velocity below the acoustic speed of aluminum, an angle of $\alpha = 2.5°$ was chosen for one test. This places the weld velocity at $V_w =$ 5290 m/s, compared to the estimated value of 5293 m/s for the acoustic speed. Then an angle of $\alpha = 8°$ was selected for the final test in order to pass into the wavy bond region, with as little inclination as possible.

The considerations above account for the schedule of tests conducted, as shown in Table 3-1. Due to the inclined nature of the plate orientations and the suggested 25 mm limit for standoff, the regions of expected good welding were tabulated in Table 3-7.

Table 3-7: Regions of good welding assuming a 25 mm standoff is the maximum bound for good welding.

Test No.	Thickness of Explosive	Stand-off Distance	Initial Plate Angle (α)	Estimated Weld Limits
1	2.1 mm	3.175 to 11.2 mm (linearly)	0.5°	Complete weld
2	2.1 mm	3.175 to 27.1 mm (linearly)	1.5°	Good through 32.8 inches
3	6.35 mm	3.175 to 43.1 mm (linearly)	2.5°	Good through 19.7 inches
4	6.35 mm	0 to 127.3 mm (linearly)	8°	Good through 6.1 inches

3.1.3 Final Choices for Test Configurations

3.1.3.1 Choice of Anvil

Due to considerations of cost and simplicity, as well as the recommendations of several authors, an anvil consisting of compacted sand upon a compacted earth subbase was chosen. Figure 3-8 below, shows the anvil and how it accommodated instrumentation. In order to ensure access to TOA pins for electrical connections, the plates were mounted on on-edge 2x4's. The edge was then enclosed with cardboard, for sand placement in and around the wires. A notch in the cardboard was added to pass out the bundled leads. The specimen was turned upside down, and upon filling with a compacted sand layer, the tray was placed upside down on top of that, allowing the whole assemblage to be rotated right-side up. Then placement of the remaining confining sand was possible. This tray was then placed on built up compacted earth in order to get the final required height for other instrumentation.

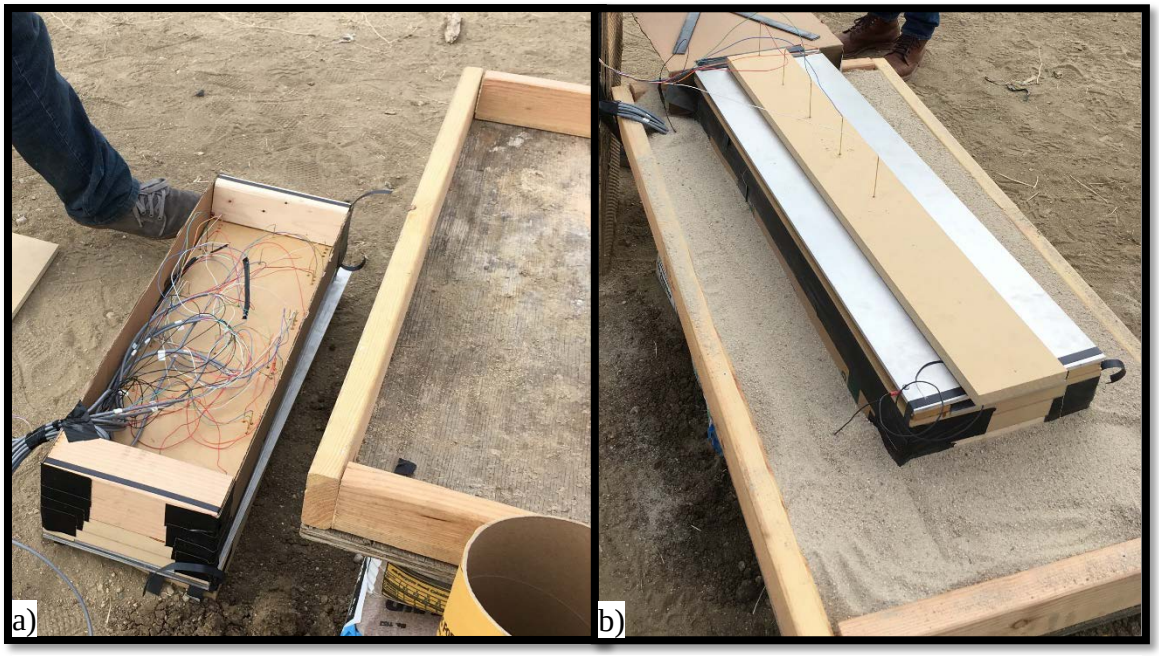

Figure 3-8: Welding anvil, used for tests. a) Tray and underside of sample frame, showing TOA pin connections, to be filled with moist sand. b) Filled tray and placed sample awaiting explosives.

3.1.3.2 Line Wave Generator

As noted in Section 2.2.2.3, Design of Welds, while detonation at a single point with a radial detonation pattern produces acceptable welds, it is possible to further control that process if desired. In this case, in order to support measurements, we wanted to render the process such that a 2D representation would be adequate for describing what happened in the event. As a result, a technique was used to try to ensure that the initiation of the explosive occurred along the entire leading edge, rather than at a single point.

Shown in Figure 3-9, a line wave generator employs a pattern of successive circular voids to slow the progress of the detonation front in the center, relative to the edges such that at the end of the charge, the detonation front is approximately linear. Figure 3-9 a) is from the line wave generator tested on June 19, 2017 in order to confirm its performance. Three channels were used and connected to foils that closed circuits with TOA pins (not shown). One pin for each channel

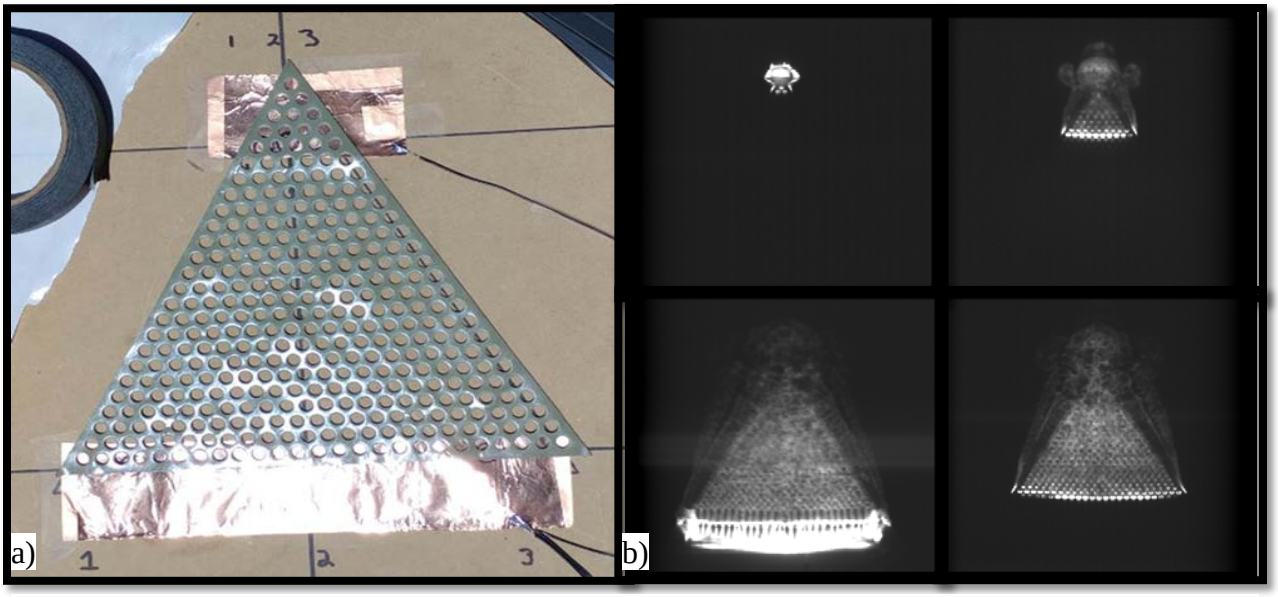

Figure 3-9: Line wave generator used in explosive welding tests. a) Line wave generator used in June 19, 2017 test showing foils for measurement circuits and labeled channels. b) Progression of an example line wave generator produced by the Australian DOD.

was at the top of the triangle as shown in the figure, and one pin for each channel was placed along the lower foil at the leftmost, center, and rightmost positions. Ideally, all pins trigger at the same time if a perfectly planar detonation front is generated. Figure 3-10 shows the recorded oscilloscope date for the line wave generator test. All three channels discharge nearly simultaneously, while the center channel discharges roughly 2 μs prior to the outer channels. This indicated that the center of the detonation front was about 12.7 mm ahead of the outer edges at the end of the event. Not shown in Figure 3-9 or Figure 3-10, confining steel plates were also placed on the edges of the line wave generator to further refine the effect of the explosive geometry. These plates are visible in Figure 3-8 b), and based on tests unrelated to this study, have been shown to produce a better effect by confining the outer edges of the explosive.

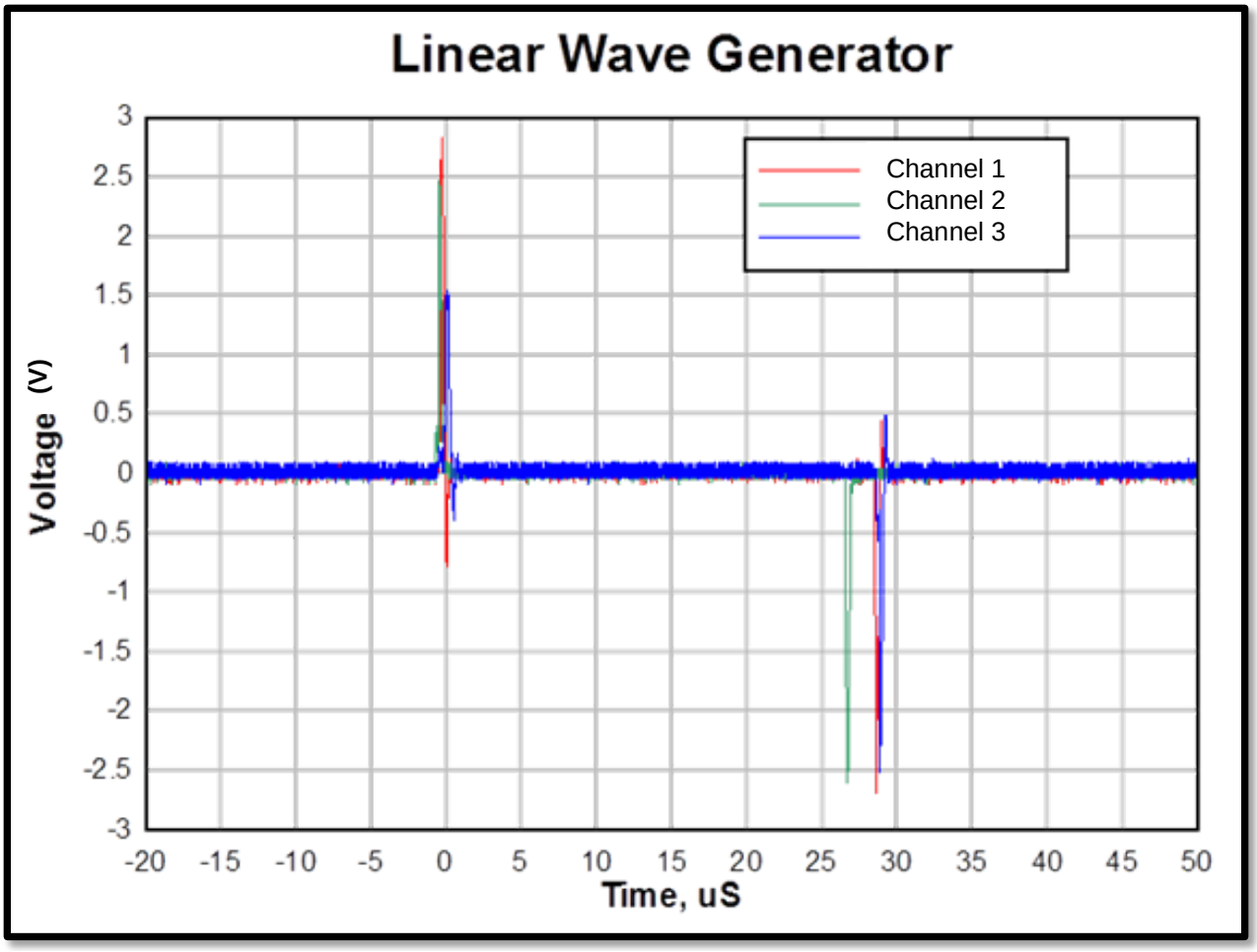

Figure 3-10: Line wave generator oscilloscope data showing each of the three channels per the color-coded legend, with the initial voltage discharge and the final discharge for each channel. Channel 2, the center channel triggers about 2μs prior to the outer channels, indicating a somewhat symmetric curve with about 12.7 mm of relative longitudinal difference in the detonation front at the end of the event.

3.1.3.3 Attempted Avoidance of TOA Pin Damage

Especially for taller pins, intended to measure the earliest arrival of the flyer plate in the actual welding tests, the effect of the weld jet became a concern. NMAP simulations showed that the potential for pin damage existed prior to their function, which intuitively follows what one would expect. A study by Khanzadeh et. all, used an oversized flyer plate as a part of their setup, which inspired a decision in the arrangement for this test setup [98]. For the overlapping sections without a parent plate of comparable density and ductility, it was posited that jetting would not form. The proposed solution was to fabricate the parent plate two inches narrower on

each side, as shown in Figure 3-2 a) and b), allowing for the placement of the taller TOA pin arrays along the outer edges of the event.

3.2 Data Collection and Instrumentation

In the initial proposal for testing, three means of data collection were proposed. Velocity measurements using TOA pins, flash radiography for imaging of the in-progress event, and high-speed video. Varying degrees of success were achieved with each technique. Additionally, wide view camera shots were taken, primarily for purposes of trouble shooting in the event of test malfunctions.

3.2.1 Time of Arrival Pins

The TOA pins were circuit closure pins with 5 volts applied across the open circuit.

3.2.1.1 Data Recording

Figure 3-11 below, shows the oscilloscopes used during actual weld event testing; six

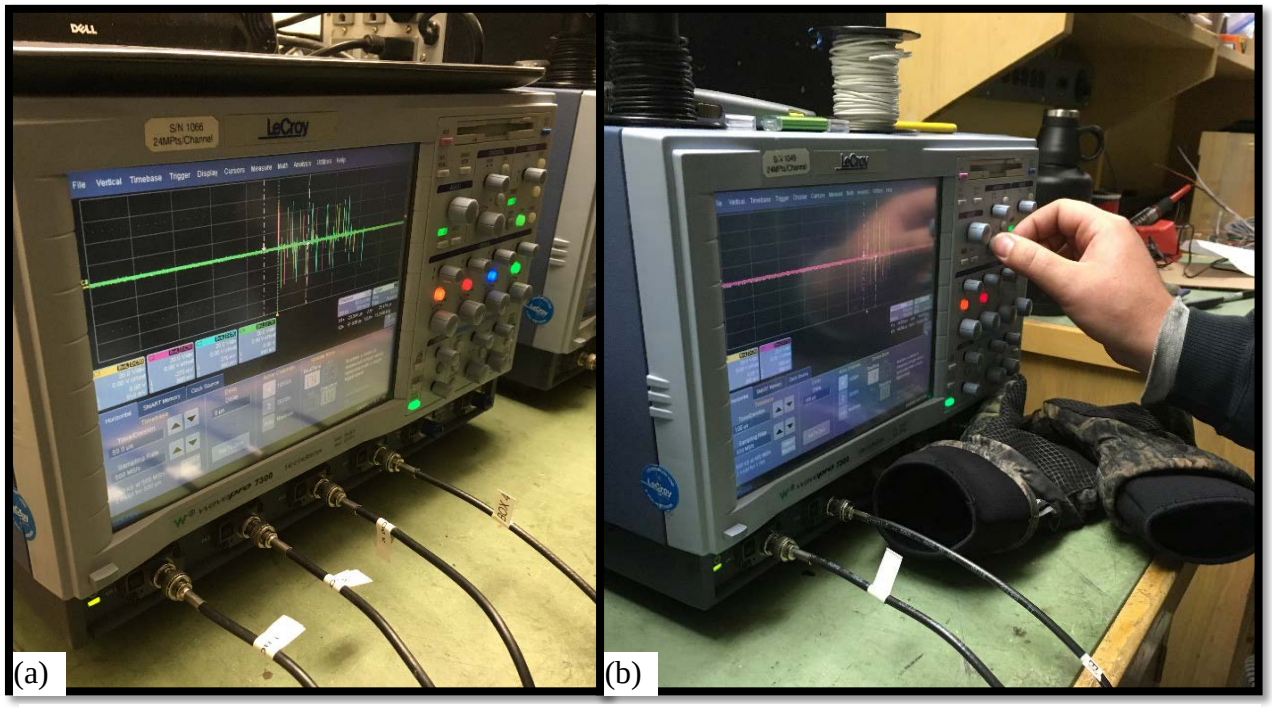

Figure 3-11: Oscilloscopes used show six (4 and 2) channels feeding in for measurement.

total channels of digital data were collected. The first TOA pin (flush pin in array group A on channel/box 1) served as a trigger to start data acquisition, and then ≈10 gigasamples/second were recorded data for the event. The two oscilloscopes were linked together in order to get six total channels for recording.

3.2.1.2 Pin Layout and Spacing

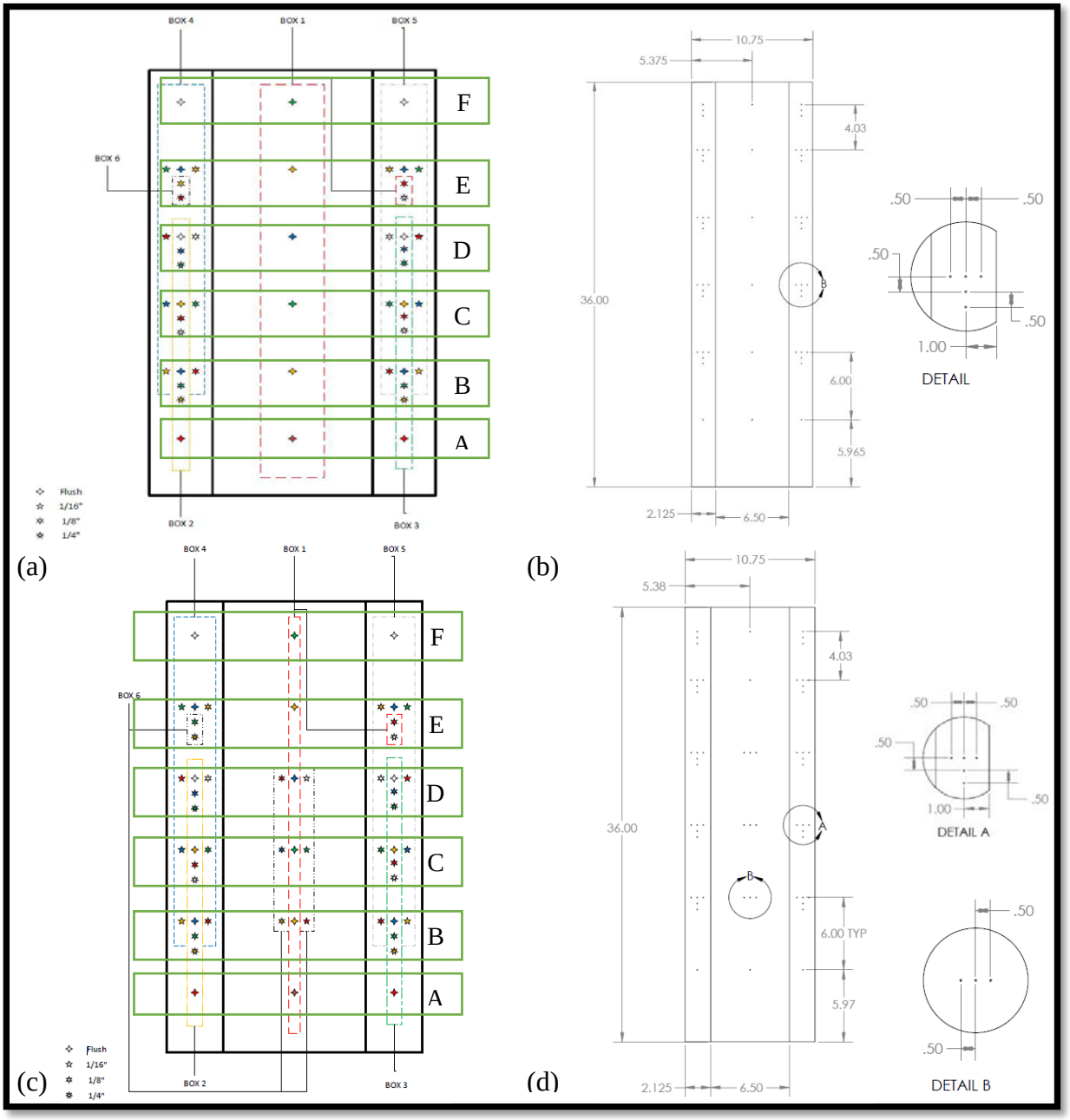

Figure 3-12: Sample pin schematics. (a) Schematic of 1.5° and 2.5° test pin arrays. Data collection channels shown at left with pin channels annotated with dashed boxes and pin array groups annotated by letter in solid green boxes. (b) 1.5° test view with dimensions. (c) Schematic of 8° and 0.5° (non-annealed) test pin arrays, annotated as in (a). (d) 0.5° non-annealed test view with dimensions.

Figure 3-12 above, shows sample data channels and pin layouts (referencing the pin heights; flush pins were 0.001" above the plane of the parent plate surface). The TOA pin leads,

along with a ground/neutral line connected to the flyer plate were wired back to junction boxes in a protected location adjacent to the test site. When VOD pins were used to measure the velocity of detonation of the explosive, a continuous strip of foil conductor was placed between the explosive and the Medium-density fiberboard (MDF) pin holder block, and this foil was connected to the neutral line. Each junction box was then connected with a single line shown

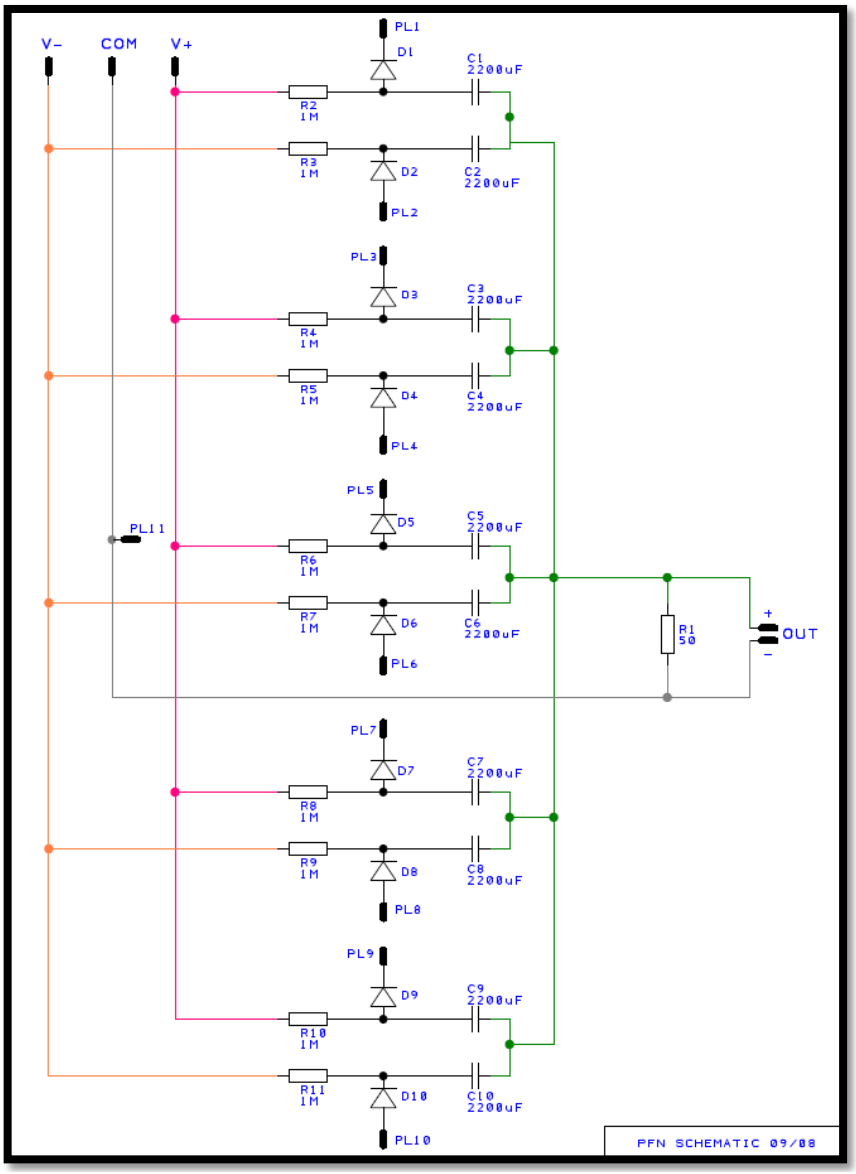

Figure 3-13: TOA pin circuit diagram, that was the pulse forming network for each channel. Each channel was capable of recording 10 discharge signals, 5 positive, and five negative. R→Resistor, C→Capacitor, D→Diode, PL→Pin Line

in Figure 3-11, entering into a single recorded channel. In each channel, the junction box was wired as shown in Figure 3-13, enabling each channel to record 10 data points.

3.2.2 FLASH RADIOGRAPHY (X-RAY)

Figure 3-14: Flash X-Ray system used in testing. a) Charging components. b) Discharge delay system. c) Protective cover guarding X-Ray head connecting to larger leads in a).

In this system a flash X-Ray triggered two times during an explosive event, capturing the progress of welding separated by about 12 inches along the length of the plates. The X-Ray heads shown in Figure 3-14 c) had to be carefully leveled manually. They were aimed at the leading edge, and the relative elevation of the head centerlines and the specimen were compared with a string level. This ensured that the burst would hit the plates at the appropriate elevation, in a direction parallel with the ground. The specimen itself was leveled, with its elevation and orientation consistent with the above considerations. Behind the specimen, on a simple stand shown in Figure 3-2 d), a fly-away cassette was placed that contained the X-Ray film. These cassettes did have vertical wires attached, spaced at 12" to give the image scale.

Due to the nature of this arrangement, reading and interpreting the X-Ray images can be particularly challenging. The X-Rays are blocked by denser material. Whiter pixels represent less exposed areas of film, and so appear where metal or dense explosives were encountered. However, because there were two pulses, there are two sets of shadows. The whitest location had X-Rays blocked in both flashes, intermediate densities or areas of the film where only one flash was blocked will be shades of grey, and only areas where the X-Rays had a free path in both events are completely dark and exposed. Both the shade, and the results must be viewed and then the exact materials encountered must be inferred.

The X-Ray triggering was the most problematic part of data collection. Four different triggers were utilized over the course of the testing. All triggers involved placement at a point on the flyer/explosive. That point was then used to calculate time delays for the firing of the two X-Ray heads (blue cylinders shown in Figure 3-14 c)). The calculations were based on geometric analysis using the test geometry, expected impact angle β, and expected velocities of detonation and welding. The original trigger not pictured was placed between the explosive and flyer of the

first test (0.5°, annealed). The second attempted to use a circuit closure using two separated foil layers on top of the explosive (exposed foil seen on the explosive in the top part of Figure 3-19 a)). The third method attempted to use a TOA pin w/ foil and is visible in the top part of Figure 3-21 a). The last method was a commercial switch placed between the explosive and flyer plate. Its lead and connection can be seen protruding to the right of the explosive in Figure 3-26 (a).

3.3 TEST RESULTS

While the initial test schedule is shown in Table 3-1, it became necessary to conduct additional tests due to the improper functioning of various systems, as shown in Table 3-8. As noted in Table 3-8, and true for all the originally planned tests, the flyer plates were 10.75" wide, while the explosive sheets were only 10.5" wide. However, despite some minor issues, the data obtained was of good quality.

Table 3-8: Additionally required tests due to equipment malfunction.

Test No.	Cladding (flyer) (parent)* Plate Dimension	Cladding (flyer) Plate Thickness	Cladding (flyer) Plate Material	Thickness & Width of Explosive	Initial Plate Angle (α)
5 M/U	10.75 in.× 36 in. 6.5 in x 36 in	1/4 in.	6061-T6 Al	2.1 mm thick 10.5" wide	0.5°
6 X-Ray	4.0 in x 18 in (both)	1/4 in.	6061-O Al	2.1 mm thick 4" wide	1.5°
7 X-Ray	4.0 in x 18 in (both)	1/4 in.	6061-O Al	6.35 mm thick 4" wide	2.5°
8 X-Ray	4.0 in x 18 in (both)	1/4 in.	6061-O Al	2.1 mm thick 4" wide	0.5°
9 X-Ray	4.0 in x 18 in (both)	1/4 in.	6061-O Al	6.35 mm thick 4" wide	8°

3.3.1 FULL SPECIMEN TESTS

3.3.1.1 Test 1: C2 & 0.5° Inclination, October 27, 2017

No data was collected successfully in this test due to trigger malfunction, but there was apparently successful welding (no cuts or other analysis conducted to confirm). A retest for this was conducted later as described in Section 3.3.1.5. See Figure 3-15 to view the end result.

Figure 3-15: 0.5° test that failed to collect any data.

3.3.1.2 Test 2: C2 & 1.5° Inclination, October 30, 2017

For this test the originally reviewed data appeared to have some issues that were clearly inconsistent with rationally explainable and related facts.

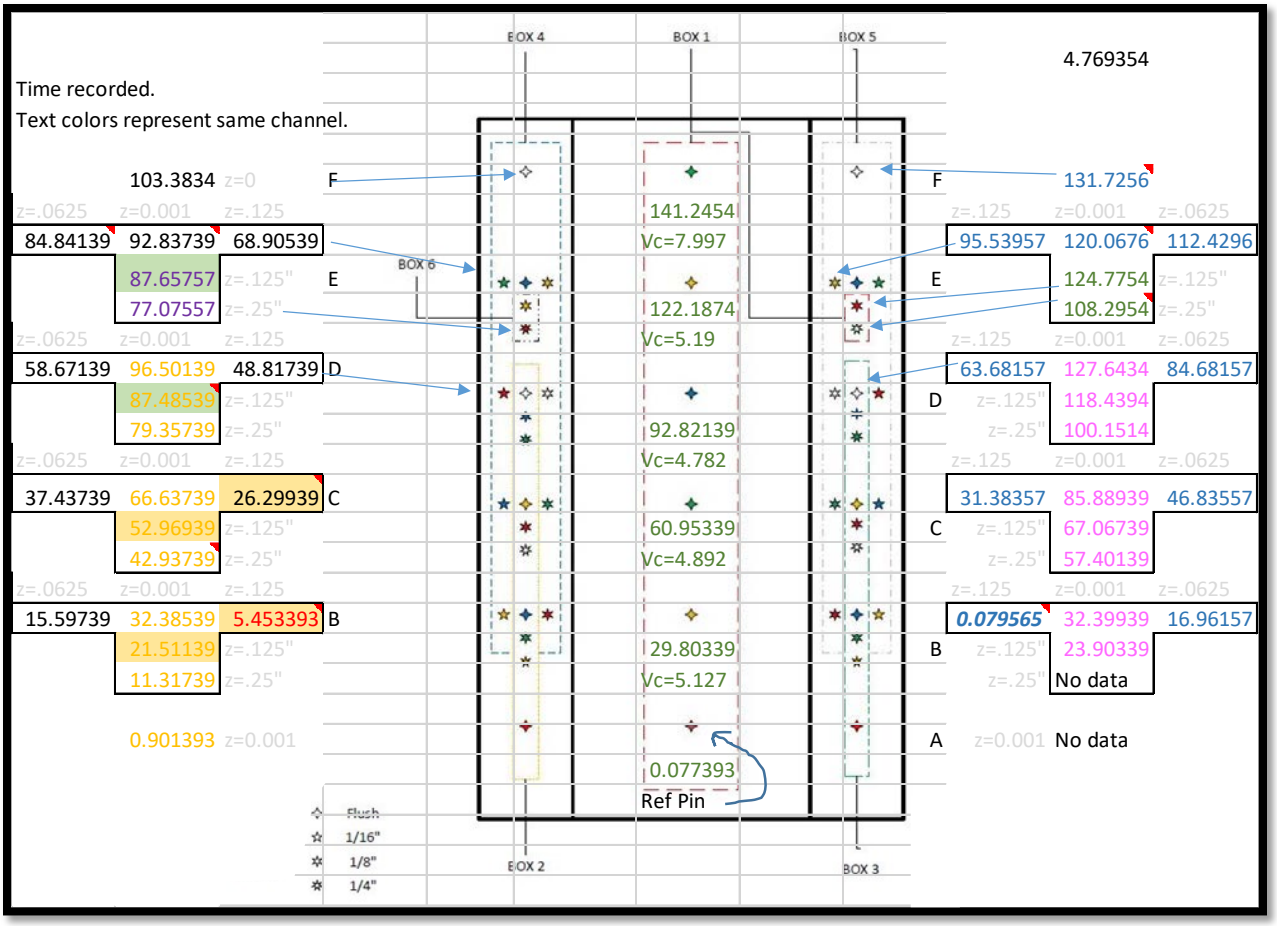

Figure 3-16: Uncorrected 1.5° time of arrival data for each pin. Time of arrival shown to the outside of the interior schematic, following the same spatial pattern as the pins. Pin heights shown in light grey in inches for ease of recall for each pin height. Array gr groups labeled with letters for reference in tabulated data.

- Disconnect in Time t = 0 μs

The color coding of the different data collection channels in Figure 3-16 helps to highlight an apparent time shift that was discovered. Upon review, it appeared as if time t = 0 was different for different channels. Channel 5 data on the right array group B starts at the 1/8" pin at roughly 0 μs, whereas it starts at 5.5 μs for the 1/8" pin on the left in array group B. The Line Wave Generator test on 19 June predicted symmetry about the centerline/longitudinal axis. Also note, that in array group B on the left, the 1/8" pin just mentioned at 5.5 μs is striking 16 μs earlier than the 1/8" pin closer to the start of detonation, but recorded on channel 2. The ¼" pin

in array Group E from channel 6 on the left strikes 2 μs before the last prior ¼" pin in array group D, but from channel 2. Similarly, the two pins form channel 1 on the right in array group E have a disconnect. This was identified and evaluated to identify causes and potential corrections. Spurious triggers and clearly inconsistent data were able to be corrected to some extent.

- Apparent difference in the measure of a unit of time between channels

After the aforementioned corrections were made, there were still some concerns. The correction of time t = 0 corrected the initial symmetry for the left and right, and mitigated the difference with the jump into array group E. However, there was still evidence of issues between channels, and an undue lack of symmetry at the end of the specimen. Though there is every reason to expect symmetry in the explosion on either side of the centerline, it was found that each channel still showed consistent, yet consistently different measures of the time it takes to

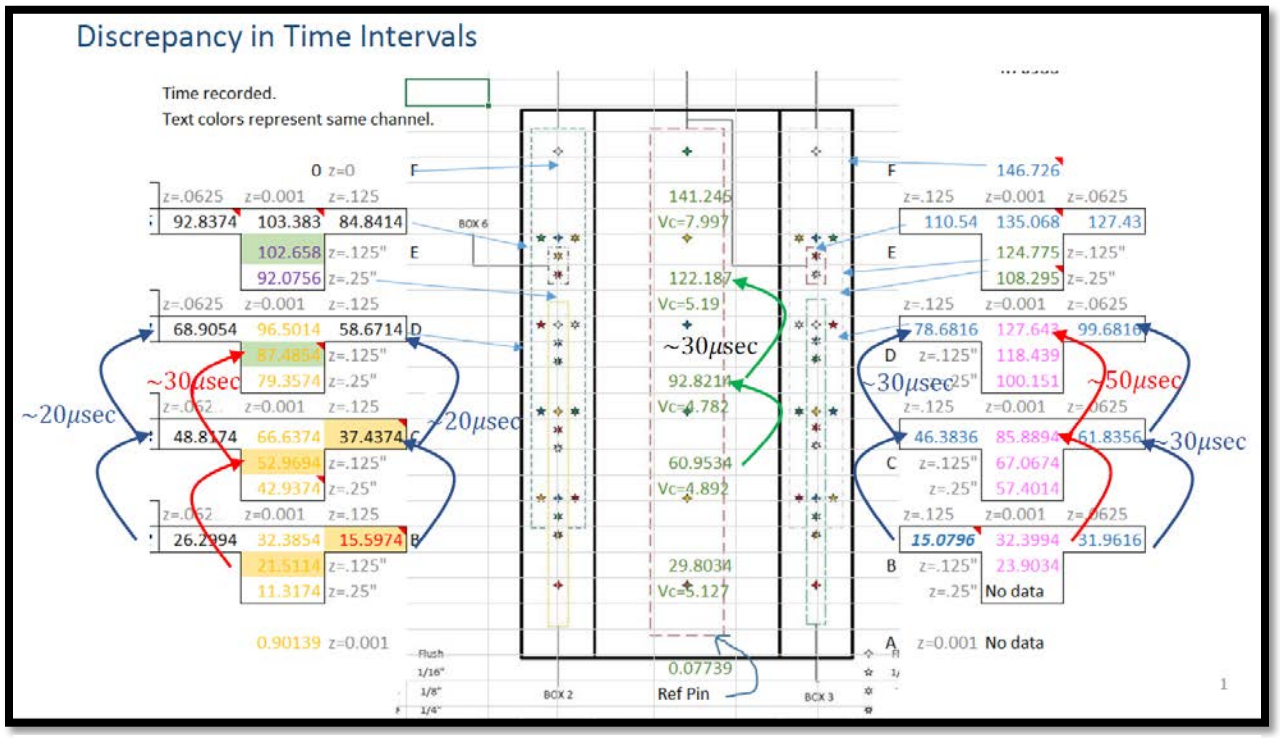

Figure 3-17: Linear correction applied to 1.5° differing channels, based on inconsistent time of arrivals within pin arrays and across the centerline as a line of symmetry.

progress from one array group to the next. This observation was investigated to find any potential causes, but no specific reason was identified. However, a linear correction was applied to the data, shown in above in Figure 3-17, and it has appeared to address the majority of all concerns with the data. The X-Ray heads failed to function for this test, but it did weld and the TOA data discussed above was collected. The information below in Figure 3-18 shows the corrected time of arrival data for the 1.5° test. V_w average values between flush pins in the centerline are shown.

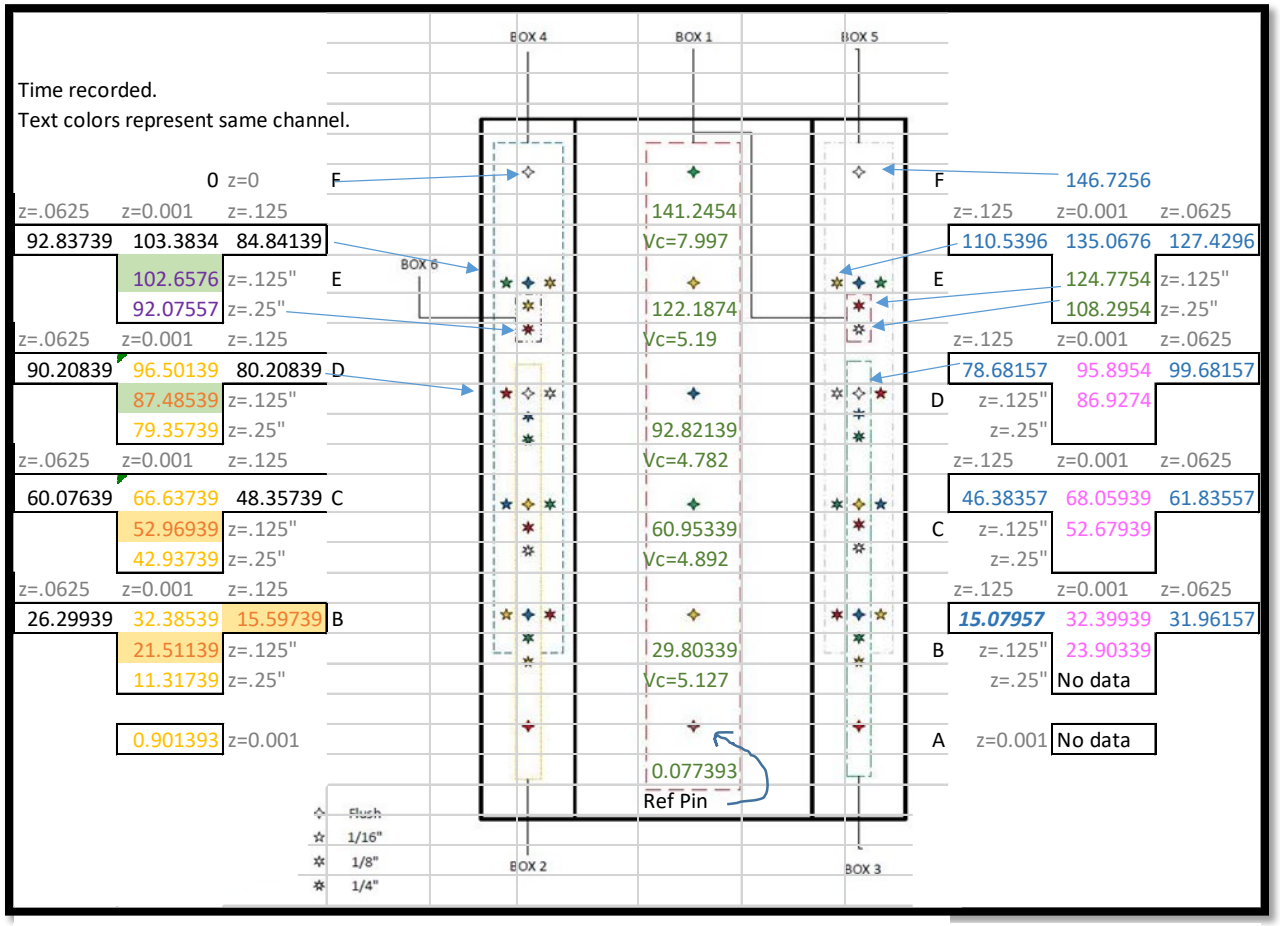

Figure 3-18: Corrected 1.5° time of arrival data referenced to its arrival locations schematically.

Figure 3-19: 1.5° test. a) Test before detonation. b) Post-welding result.

Table 3-9: 1.5° Raw Corrected TOA pin data.

					Weld			Plate		
Channel 6 VOD										
Pin Height	**Pin Group Letter**	**X distance from ref pin (mm)**	**' distance from ref pin (mn**	**Time (µS)**	**ΔD (mm)**	**ΔT (µS)**	**Velocity (mm/µS)**	**ΔD (mm)**	**ΔT (µS)**	**Velocity (mm/µS)**
0.001" (.0254mm)	A	0	0	-49.10443	0	-64.10443	7.112869999			
0.001" (.0254mm)	B	127	0	-31.18843	127	17.916	7.088635856			
0.001" (.0254mm)	C	254	0	-13.39843	127	17.79	7.138842046			
0.001" (.0254mm)	D	381	0	4.11557	127	17.514	7.251341784			
0.001" (.0254mm)	E	508	0	22.329565	127	18.213995	6.972660309			
Channel 1										
Pin Height	**Pin Group Letter**	**X distance from ref pin (mm)**	**' distance from ref pin (mn**	**Time (µS)**	**ΔD (mm)**	**ΔT (µS)**	**Velocity (mm/µS)**	**ΔD (mm)**	**ΔT (µS)**	**Velocity (mm/µS)**
0.001" (.0254mm)	A	0	0	0.07739344	0	0.07739344	5.073729532			
0.001" (.0254mm)	B	152.4	0	29.80339	152.4	29.72599656	5.126825595			
0.001" (.0254mm)	C	304.8	0	60.95339	152.4	31.15	4.892455859			
0.001" (.0254mm)	D	457.2	0	92.82139	152.4	31.868	4.782226685			
0.25" (6.35mm)	E	584.2	111.125	108.2954						
0.125" (3.175mm)	E	596.9	111.125	124.7754						
0.001" (.0254mm)	E	609.6	0	122.1874	152.4	29.36601	5.189673367			
0.001" (.0254mm)	F	712.08375	0	141.2454	102.48375	19.058	5.377466156			
Channel 2										
Pin Height	**Pin Group Letter**	**X distance from ref pin (mm)**	**' distance from ref pin (mn**	**Time (µS)**	**ΔD (mm)**	**ΔT (µS)**	**Velocity (mm/µS)**	**ΔD (mm)**	**ΔT (µS)**	**Velocity (mm/µS)**
0.001" (.0254mm)	A	0	111.125	0.9013934	0	0.9013934	4.797687961			
0.25" (6.35mm)	B	127	111.125	11.31739						
0.125" (3.175mm)	B	139.7	111.125	21.51139						
0.001" (.0254mm)	B	152.4	111.125	32.38539	152.4	31.4839966	4.840554455	1.5621	6.086	0.256671048
0.25" (6.35mm)	C	279.4	111.125	42.93739						
0.125" (3.175mm)	C	292.1	111.125	52.96939						
0.001" (.0254mm)	C	304.8	111.125	66.63739	152.4	34.252	4.449375219	1.5621	17.82	0.087659933
0.25" (6.35mm)	D	431.8	111.125	79.35739						
0.125" (3.175mm)	D	444.5	111.125	87.48539						
0.001" (.0254mm)	D	457.2	111.125	96.50139	152.4	29.864	5.103134208	1.5621	27.596	0.05660603
Channel 3										
Pin Height	**Pin Group Letter**	**X distance from ref pin (mm)**	**' distance from ref pin (mn**	**Time (µS)**	**ΔD (mm)**	**ΔT (µS)**	**Velocity (mm/µS)**	**ΔD (mm)**	**ΔT (µS)**	**Velocity (mm/µS)**
0.001" (.0254mm)	A	0	111.125		0	23.90339	4.817470509			
0.25" (6.35mm)	B	127	111.125							
0.125" (3.175mm)	B	139.7	111.125	23.90339						
0.001" (.0254mm)	B	152.4	111.125	32.39939	152.4	32.39939	4.703792263	1.5621	0.43782	3.567904618
0.25" (6.35mm)	C	279.4	111.125							
0.125" (3.175mm)	C	292.1	111.125	52.67939						
0.001" (.0254mm)	C	304.8	111.125	68.05939	152.4	35.66	4.273696018	1.5621	6.22382	0.250987336
0.25" (6.35mm)	D	431.8	111.125							
0.125" (3.175mm)	D	444.5	111.125	86.9273967						
0.001" (.0254mm)	D	457.2	111.125	95.8953967	152.4	27.83600667	5.474923247	1.5621	-3.7861733	-0.41258016
Channel 4										
Pin Height	**Pin Group Letter**	**X distance from ref pin (mm)**	**' distance from ref pin (mn**	**Time (µS)**	**ΔD (mm)**	**ΔT (µS)**	**Velocity (mm/µS)**	**ΔD (mm)**	**ΔT (µS)**	**Velocity (mm/µS)**
0.125" (3.175mm)	B	152.4	98.425	15.59739				0	5.453393	0.202503904
0.0625" (1.5875mm)	B	152.4	123.825	26.29939				1.5875	10.702	0.148336759
0.125" (3.175mm)	C	304.8	98.425	37.43739				0	26.29939	0.113579527
0.0625" (1.5875mm)	C	304.8	123.825	48.81739				1.5875	11.38	0.139499121
0.125" (3.175mm)	D	457.2	98.425	58.67139				0	48.81739	0.105863109
0.0625" (1.5875mm)	D	457.2	123.825	68.90539				1.5875	10.234	0.155120188
0.125" (3.175mm)	E	609.6	98.425	84.84139				0	68.90539	0.173329569
0.0625" (1.5875mm)	E	609.6	123.825	92.83739				1.5875	7.996	0.198536768
0.001" (.0254mm)	E	609.6	111.125	103.3834	152.4	6.88201	22.14469319	1.5621	10.54601	0.14812237
0.001" (.0254mm)	F	712.08375	111.125		102.48375	-103.3834	-0.991297926			
Channel 5										
Pin Height	**Pin Group Letter**	**X distance from ref pin (mm)**	**' distance from ref pin (mn**	**Time (µS)**	**ΔD (mm)**	**ΔT (µS)**	**Velocity (mm/µS)**	**ΔD (mm)**	**ΔT (µS)**	**Velocity (mm/µS)**
0.125" (3.175mm)	B	152.4	98.425	15.0795654				0	0.0795654	1.83096983
0.0625" (1.5875mm)	B	152.4	123.825	31.96157				1.5875	16.8820046	0.094035041
0.125" (3.175mm)	C	304.8	98.425	46.38357				0	31.38357	0.176862423
0.0625" (1.5875mm)	C	304.8	123.825	61.83557				1.5875	15.452	0.10273751
0.125" (3.175mm)	D	457.2	98.425	78.68157				0	63.68157	-0.168492461
0.0625" (1.5875mm)	D	457.2	123.825	99.68157				1.5875	21	0.075595238
0.125" (3.175mm)	E	609.6	98.425	110.53957				0	95.53957	0.149253625
0.0625" (1.5875mm)	E	609.6	123.825	127.4296				1.5875	16.89003	0.09399036
0.001" (.0254mm)	E	609.6	111.125	135.0676	152.4	39.17220333	3.89051386	1.5621	7.638	0.204516889
0.001" (.0254mm)	F	712.08375	111.125	146.7256	102.48375	11.658	8.790851776			
Channel 6										
Pin Height	**Pin Group Letter**	**X distance from ref pin (mm)**	**' distance from ref pin (mn**	**Time (µS)**	**ΔD (mm)**	**ΔT (µS)**	**Velocity (mm/µS)**	**ΔD (mm)**	**ΔT (µS)**	**Velocity (mm/µS)**
0.25" (6.35mm)	E	584.2	111.125	92.07557						
0.125" (3.175mm)	E	596.9	111.125	102.65757						

3.3.1.3 Test 3: C6 & 2.5° Inclination, October 30, 2017

The X-Ray heads did not function at the correct time for this test, producing a useless image. However, the specimen did weld, and there were no issues with the TOA data.

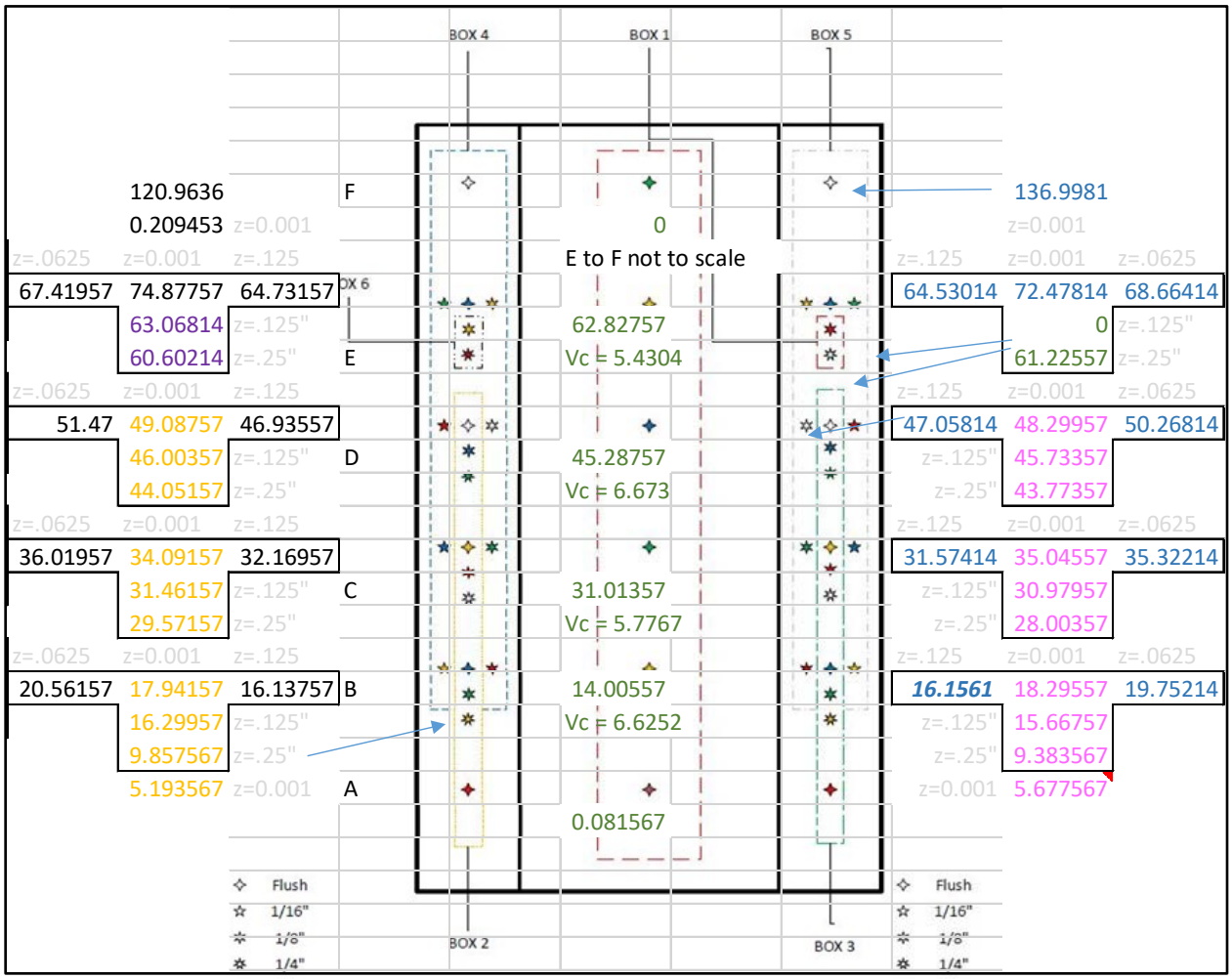

Figure 3-20: 2.5° Test Referenced TOA Pin Data

Figure 3-21: 2.5° Test Images. (In (b) weld direction is right to left)

Table 3-10: 2.5° Raw TOA Pin Data

2.5 Degree Plate Angle										
					Weld			Plate		
Channel 6 VOD										
Pin Height	**Pin Group Letter**	**listance from ref pin (n**	**istance from ref pin (m**	**Time (µS)**	**ΔD (mm)**	**ΔT (µS)**	**Velocity (mm/µS)**	**ΔD (mm)**	**ΔT (µS)**	**Velocity (mm/µS)**
0.001" (.0254mm)	A	0	0	-16.51186	0	-64.10443	7.307490074			
0.001" (.0254mm)	B	127	0	1.29414	127	17.806	7.132427272			
0.001" (.0254mm)	C	254	0	18.636136	127	17.341996	7.323263135			
0.001" (.0254mm)	D	381	0	36.43414	127	17.798004	7.135631614			
0.001" (.0254mm)	E	508	0	53.06014	127	16.626	7.638638277			
Channel 1										
Pin Height	**Pin Group Letter**	**listance from ref pin (n**	**istance from ref pin (m**	**Time (µS)**	**ΔD (mm)**	**ΔT (µS)**	**Velocity (mm/µS)**	**ΔD (mm)**	**ΔT (µS)**	**Velocity (mm/µS)**
0.001" (.0254mm)	A	0	0	0.08156693	0	0.08156693	3.98862619			
0.001" (.0254mm)	B	92.25	0	14.00557	92.25	13.92400307	6.625249904			
0.001" (.0254mm)	C	190.5	0	31.01357	98.25	17.008	5.776693321			
0.001" (.0254mm)	D	285.75	0	45.28757	95.25	14.274	6.672971837			
0.25" (6.35mm)	E	355.6	111.125	61.22557						
0.125" (3.175mm)	E	368.3	111.125							
0.001" (.0254mm)	E	381	0	62.82757	95.25	17.54	5.430444698			
0.001" (.0254mm)	F	667.63375	0		286.63375	-62.82757	-4.562228811			
Channel 2										
Pin Height	**Pin Group Letter**	**listance from ref pin (n**	**istance from ref pin (m**	**Time (µS)**	**ΔD (mm)**	**ΔT (µS)**	**Velocity (mm/µS)**	**ΔD (mm)**	**ΔT (µS)**	**Velocity (mm/µS)**
0.001" (.0254mm)	A	0	111.125	5.193567	0	5.193564	6.573761707			
0.25" (6.35mm)	B	69.85	111.125	9.857567						
0.125" (3.175mm)	B	82.55	111.125	16.29957						
0.001" (.0254mm)	B	95.25	111.125	17.94157	95.25	12.748003	7.471758518	1.5621	-2.62	-0.596221374
0.25" (6.35mm)	C	165.1	111.125	29.57157						
0.125" (3.175mm)	C	177.8	111.125	31.46157						
0.001" (.0254mm)	C	190.5	111.125	34.09157	95.25	16.15	5.897832817	1.5621	-1.928	-0.810217842
0.25" (6.35mm)	D	260.35	111.125	44.05157						
0.125" (3.175mm)	D	273.05	111.125	46.00357						
0.001" (.0254mm)	D	285.75	111.125	49.08757	95.25	14.996	6.351693785	1.5621	-2.3824	-0.655675088
Channel 3										
Pin Height	**Pin Group Letter**	**listance from ref pin (n**	**istance from ref pin (m**	**Time (µS)**	**ΔD (mm)**	**ΔT (µS)**	**Velocity (mm/µS)**	**ΔD (mm)**	**ΔT (µS)**	**Velocity (mm/µS)**
0.001" (.0254mm)	A	0	111.125	5.677567	0	5.193564	6.807271666			
0.25" (6.35mm)	B	69.85	111.125	9.383567						
0.125" (3.175mm)	B	82.55	111.125	15.66757						
0.001" (.0254mm)	B	95.25	111.125	18.29557	95.25	12.618003	7.548738101	1.5621	-1.4566	-1.072453977
0.25" (6.35mm)	C	165.1	111.125	28.00357						
0.125" (3.175mm)	C	177.8	111.125	30.97957						
0.001" (.0254mm)	C	190.5	111.125	35.04557	95.25	16.75	5.686567164	1.5621	-0.2766	-5.648118017
0.25" (6.35mm)	D	260.35	111.125	43.77357						
0.125" (3.175mm)	D	273.05	111.125	45.73357						
0.001" (.0254mm)	D	285.75	111.125	48.29957	95.25	13.254	7.186509733	1.5621	-1.9686	-0.793520169
Channel 4										
Pin Height	**Pin Group Letter**	**listance from ref pin (n**	**istance from ref pin (m**	**Time (µS)**	**ΔD (mm)**	**ΔT (µS)**	**Velocity (mm/µS)**	**ΔD (mm)**	**ΔT (µS)**	**Velocity (mm/µS)**
0.125" (3.175mm)	B	92.25	98.425	16.13757				0		-0.118691609
0.0625" (1.5875mm)	B	92.25	123.825	20.56157				1.5875	4.424	0.358838156
0.125" (3.175mm)	C	190.5	98.425	32.16957				0		-0.19894009
0.0625" (1.5875mm)	C	190.5	123.825	36.01957				1.5875	3.85	0.412337662
0.125" (3.175mm)	D	285.75	98.425	46.93557				0		-0.152787979
0.0625" (1.5875mm)	D	285.75	123.825	51.47				1.5875	4.53443	0.35009913
0.125" (3.175mm)	E	381	98.425	64.73157				0		0.400020367
0.0625" (1.5875mm)	E	381	123.825	67.41957				1.5875	2.688	0.590587798
0.001" (.0254mm)	E	381	111.125	74.87757	95.25	25.79	3.693291974	1.5621	7.458	0.209452936
0.001" (.0254mm)	F	667.63375	111.125	120.9636	286.63375	46.08603	6.219536593			
Channel 5										
Pin Height	**Pin Group Letter**	**listance from ref pin (n**	**istance from ref pin (m**	**Time (µS)**	**ΔD (mm)**	**ΔT (µS)**	**Velocity (mm/µS)**	**ΔD (mm)**	**ΔT (µS)**	**Velocity (mm/µS)**
0.125" (3.175mm)	B	92.25	98.425	16.1561362				0		-0.315495608
0.0625" (1.5875mm)	B	92.25	123.825	19.752136				1.5875	3.596	0.441462761
0.125" (3.175mm)	C	190.5	98.425	31.57414				0		-2.612279393
0.0625" (1.5875mm)	C	190.5	123.825	35.32214				1.5875	3.748	0.423559232
0.125" (3.175mm)	D	285.75	98.425	47.05814				0		-0.149485941
0.0625" (1.5875mm)	D	285.75	123.825	50.26814				1.5875	3.21	0.494548287
0.125" (3.175mm)	E	381	98.425	64.53014				0		0.396790324
0.0625" (1.5875mm)	E	381	123.825	68.66414				1.5875	4.134	0.384010643
0.001" (.0254mm)	E	381	111.125	72.47814	95.25	24.17857	3.939438933	1.5621	3.814	0.409570005
0.001" (.0254mm)	F	667.63375	111.125	136.9981	286.63375	64.51996	4.442559326			
Channel 6										
Pin Height	**Pin Group Letter**	**listance from ref pin (n**	**istance from ref pin (m**	**Time (µS)**	**ΔD (mm)**	**ΔT (µS)**	**Velocity (mm/µS)**	**ΔD (mm)**	**ΔT (µS)**	**Velocity (mm/µS)**
0.25" (6.35mm)	E	355.6	111.125	60.60214						
0.125" (3.175mm)	E	368.3	111.125	63.06814						

3.3.1.4 Test 4: C6 & 8° Inclination, December 20, 2017

The X-Ray head did not function on this test. This test did appear to weld effectively; largely for the whole length of the specimen. However, as is visible in (b), the specimen split, validating concerns with larger welding standoffs. In this test, as shown in Figure 3-22, a different placement of TOA pin arrays was attempted, using pins previously dedicated to measuring detonation velocity. The intent was to try capturing data without corruption by edge effects. Edge effects will be discussed in Section 3.4.1.1.

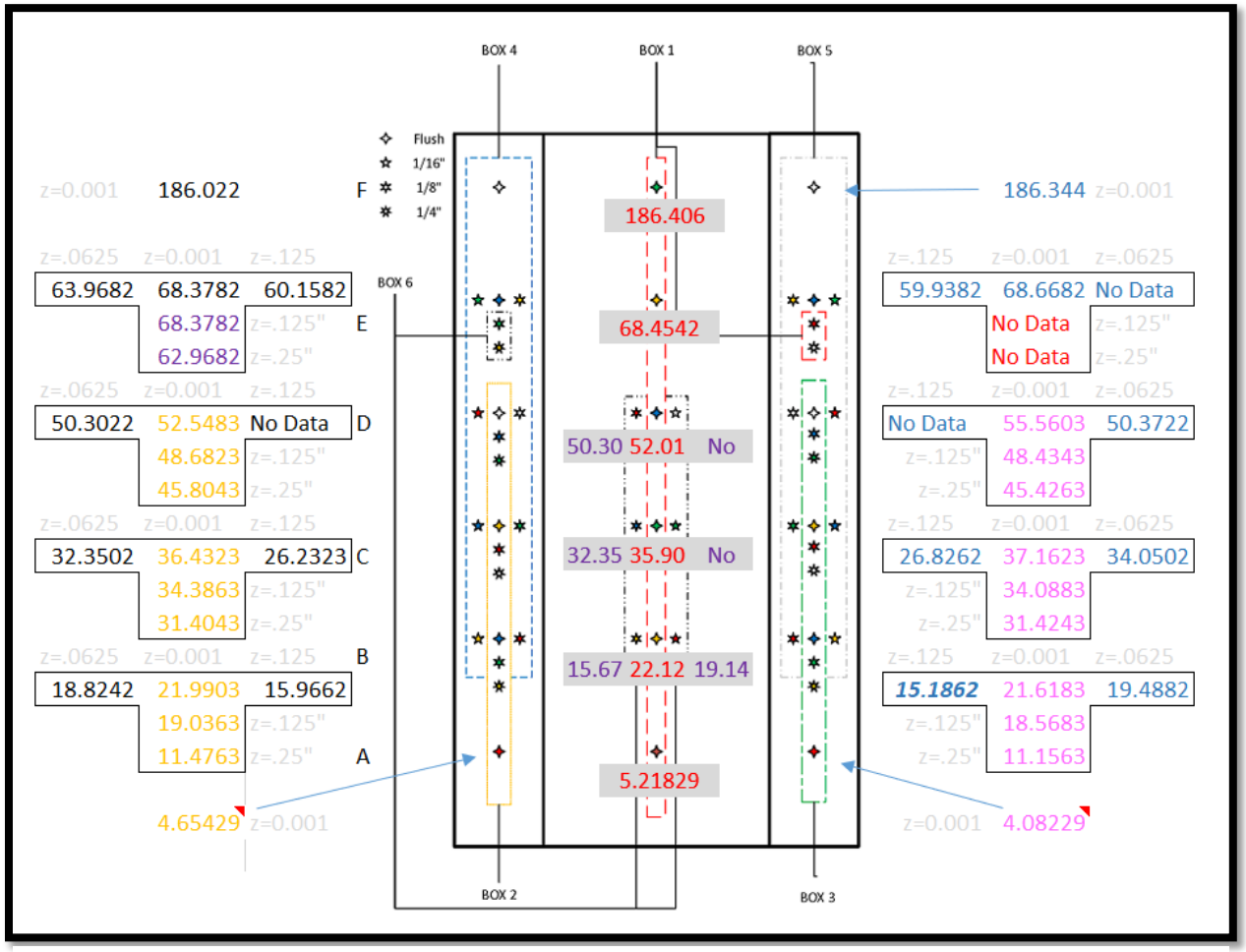

Figure 3-22: 8° Test Reference TOA Pin Data.

Figure 3-23: 8° Test Images

Table 3-11: 8° Raw TOA Pin Data

8 Degree Plate Angle										
					Weld			Plate		
Channel 1										
Pin Height	**Pin Group Letter**	**X distance from ref pin (mm)**	**Y distance from ref pin (mm)**	**Time (µS)**	**ΔD (mm)**	**ΔT (µS)**	**Velocity (mm/µS)**	**ΔD (mm)**	**ΔT (µS)**	**Velocity (mm/µS)**
0.001" (.0254mm)	A	0	0	5.218291						
0.001" (.0254mm)	B	76.2	0	20.98429	76.2	15.765999	4.833185642			
0.001" (.0254mm)	C	152.4	0	35.99629	76.2	15.012	5.075939249			
0.001" (.0254mm)	D	228.6	0	52.01229	76.2	16.016	4.757742258			
0.25" (6.35mm)	E	279.4	111.125							
0.125" (3.175mm)	E	292.12	111.125							
0.001" (.0254mm)	E	304.8	0	68.10229	76.2	16.09	4.735860783			
0.001" (.0254mm)	F	740.02	0	186.4063	435.22	118.30401	3.678827117			
Channel 2										
Pin Height	**Pin Group Letter**	**X distance from ref pin (mm)**	**Y distance from ref pin (mm)**	**Time (µS)**	**ΔD (mm)**	**ΔT (µS)**	**Velocity (mm/µS)**	**ΔD (mm)**	**ΔT (µS)**	**Velocity (mm/µS)**
0.001" (.0254mm)	A	0	111.125	4.654291						
0.25" (6.35mm)	B	50.8	111.125	11.47629						
0.125" (3.175mm)	B	63.5	111.125	19.03629						
0.001" (.0254mm)	B	76.2	111.125	21.99029	76.2	17.335999	4.395477872	1.5621	3.16605	0.493390818
0.25" (6.35mm)	C	127.15	111.125	31.40429						
0.125" (3.175mm)	C	139.73	111.125	34.38629						
0.001" (.0254mm)	C	152.4	111.125	36.43229	76.2	14.442	5.276277524	1.5621	4.08205	0.382675371
0.25" (6.35mm)	D	203.29	111.125	45.80429						
0.125" (3.175mm)	D	215.9	111.125	48.68229						
0.001" (.0254mm)	D	228.6	111.125	52.54829	76.2	16.116	4.728220402	1.5621	2.24605	0.695487634
Channel 3										
Pin Height	**Pin Group Letter**	**X distance from ref pin (mm)**	**Y distance from ref pin (mm)**	**Time (µS)**	**ΔD (mm)**	**ΔT (µS)**	**Velocity (mm/µS)**	**ΔD (mm)**	**ΔT (µS)**	**Velocity (mm/µS)**
0.001" (.0254mm)	A	0	111.125	4.082291						
0.25" (6.35mm)	B	50.8	111.125	11.15629						
0.125" (3.175mm)	B	63.5	111.125	18.56829						
0.001" (.0254mm)	B	76.2	111.125	21.61829	76.2	17.535999	4.345346963	1.5621	2.13005	0.733363067
0.25" (6.35mm)	C	127.15	111.125	31.42429						
0.125" (3.175mm)	C	139.73	111.125	34.08829						
0.001" (.0254mm)	C	152.4	111.125	37.16229	76.2	15.544	4.902213073	1.5621	3.11205	0.501952089
0.25" (6.35mm)	D	203.29	111.125	45.42629						
0.125" (3.175mm)	D	215.9	111.125	48.43429						
0.001" (.0254mm)	D	228.6	111.125	55.56029	76.2	18.398	4.141754539	1.5621	5.18805	0.301095787
Channel 4										
Pin Height	**Pin Group Letter**	**X distance from ref pin (mm)**	**Y distance from ref pin (mm)**	**Time (µS)**	**ΔD (mm)**	**ΔT (µS)**	**Velocity (mm/µS)**	**ΔD (mm)**	**ΔT (µS)**	**Velocity (mm/µS)**
0.125" (3.175mm)	B	76.2	98.425	15.96624						
0.0625" (1.5875mm)	B	76.2	123.825	18.82424				1.5875	2.858	0.555458362
0.125" (3.175mm)	C	152.4	98.425	26.23229						
0.0625" (1.5875mm)	C	152.4	123.825	32.35024				1.5875	6.11795	0.259482343
0.125" (3.175mm)	D	228.6	98.425	No Data						
0.0625" (1.5875mm)	D	228.6	123.825	50.30224				1.5875	#VALUE!	#VALUE!
0.125" (3.175mm)	E	304.8	98.425	60.15824						
0.0625" (1.5875mm)	E	304.8	123.825	63.96824				1.5875	3.81	0.416666667
0.001" (.0254mm)	E	304.8	111.125	68.37824	76.2	15.82995	4.813660182	1.5621	4.41	0.354217687
0.001" (.0254mm)	F	740.02	111.125	186.0222	435.22	117.64396	3.699467444			
Channel 5										
Pin Height	**Pin Group Letter**	**X distance from ref pin (mm)**	**Y distance from ref pin (mm)**	**Time (µS)**	**ΔD (mm)**	**ΔT (µS)**	**Velocity (mm/µS)**	**ΔD (mm)**	**ΔT (µS)**	**Velocity (mm/µS)**
0.125" (3.175mm)	B	76.2	98.425	15.18624						
0.0625" (1.5875mm)	B	76.2	123.825	19.48824				1.5875	4.302	0.369014412
0.125" (3.175mm)	C	152.4	98.425	26.82624						
0.0625" (1.5875mm)	C	152.4	123.825	34.05024				1.5875	7.224	0.219753599
0.125" (3.175mm)	D	228.6	98.425	No Data						
0.0625" (1.5875mm)	D	228.6	123.825	50.37224				1.5875	#VALUE!	#VALUE!
0.125" (3.175mm)	E	304.8	98.425	59.93824						
0.0625" (1.5875mm)	E	304.8	123.825	No Data				1.5875	#VALUE!	#VALUE!
0.001" (.0254mm)	E	304.8	111.125	68.66824	76.2	13.10795	5.813265995	1.5621	#VALUE!	#VALUE!
0.001" (.0254mm)	F	740.02	111.125	186.3442	435.22	117.67596	3.698461436			
Channel 6										
Pin Height	**Pin Group Letter**	**X distance from ref pin (mm)**	**Y distance from ref pin (mm)**	**Time (µS)**	**ΔD (mm)**	**ΔT (µS)**	**Velocity (mm/µS)**	**ΔD (mm)**	**ΔT (µS)**	**Velocity (mm/µS)**
0.125" (3.175mm)	B	76.2	12.7	18.96629						
0.0625" (1.5875mm)	B	76.2	12.7	24.96029				1.5875	5.994	0.264848182
0.125" (3.175mm)	C	152.4	12.7	34.43429						
0.0625" (1.5875mm)	C	152.4	12.7	40.46229				1.5875	6.028	0.263354346
0.125" (3.175mm)	D	228.6	12.7	51.37429						
0.0625" (1.5875mm)	D	228.6	12.7	54.96429				1.5875	3.59	0.442200557
0.25" (6.35mm)	E	355.6	111.125	71.00629						
0.125" (3.175mm)	E	368.3	111.125	74.87029				3.175	3.864	0.821687371

3.3.1.5 Test 5: C2 & 0.5° Inclination, December 20, 2017 (non-annealed plates)

This test was conducted after the initial 0.5° test failed to collect TOA pin data. It was attempted to get X-Ray images for this test, but the system failed to function again. This test did not weld, but it is very interesting to note the surface waves in Figure 3-25.

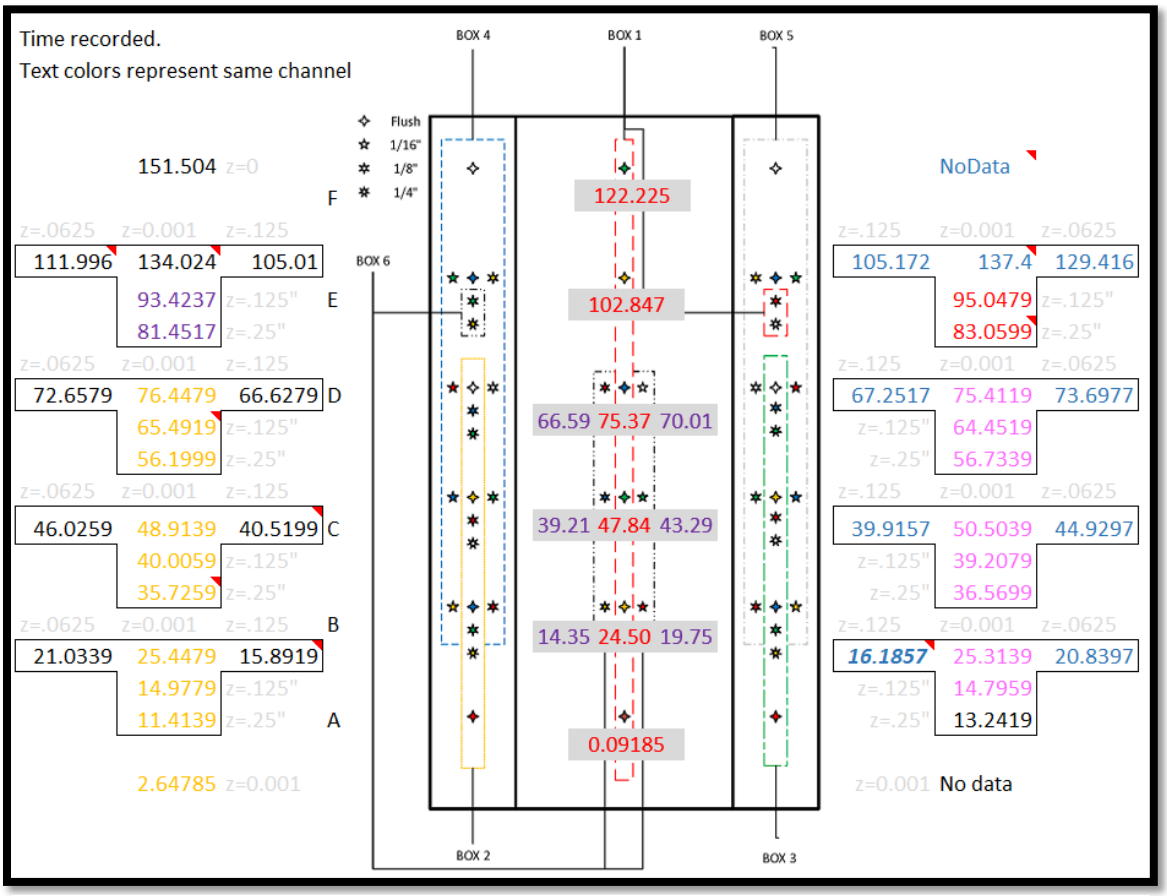

Figure 3-24: 0.5° Non-annealed Referenced TOA Pin Data.

Figure 3-25: 0.5°, non-annealed, make-up test that failed to weld

Table 3-12: Make-up 0.5° Raw TOA Pin Data

.5 Degree Plate Angle										
					Weld			Plate		
Channel 1										
Pin Height	**Pin Group Letter**	**X distance from ref pin (mm)**	**Y distance from ref pin (mm)**	**Time (µS)**	**ΔD (mm)**	**ΔT (µS)**	**Velocity (mm/µS)**	**ΔD (mm)**	**ΔT (µS)**	**Velocity (mm/µS)**
0.001" (.0254mm)	A	0	0	0.0918529						
0.001" (.0254mm)	B	152.4	0	24.50185	152.4	24.41	6.243343634			
0.001" (.0254mm)	C	304.8	0	47.84585	152.4	23.344	6.52844414			
0.001" (.0254mm)	D	457.2	0	75.37185	152.4	27.526	5.536583594			
0.25" (6.35mm)	E	584.2	111.125	83.05985						
0.125" (3.175mm)	E	596.9	111.125	95.04785				3.175	11.988	0.264848182
0.001" (.0254mm)	E	609.6	0	102.8479	152.4	27.4761	5.546648809			
0.001" (.0254mm)	F	712.08	0	122.2259	102.48	19.378	5.288471462			
Channel 2										
Pin Height	**Pin Group Letter**	**X distance from ref pin (mm)**	**Y distance from ref pin (mm)**	**Time (µS)**	**ΔD (mm)**	**ΔT (µS)**	**Velocity (mm/µS)**	**ΔD (mm)**	**ΔT (µS)**	**Velocity (mm/µS)**
0.001" (.0254mm)	A	0	111.125	2.647853						
0.125" (3.175mm)	B	127.15	111.125	11.41385						
0.125" (3.175mm)	B	139.7	111.125	14.97785						
0.001" (.0254mm)	B	152.4	111.125	25.44785	152.4	22.8	6.684211406	1.5621	4.414	0.353896692
0.125" (3.175mm)	C	279.4	111.125	35.72585						
0.125" (3.175mm)	C	292.1	111.125	40.00585						
0.001" (.0254mm)	C	304.8	111.125	48.91385	152.4	23.466	6.494502685	1.5621	2.888	0.540893352
0.25" (6.35mm)	D	431.8	111.125	56.19985						
0.125" (3.175mm)	D	444.5	111.125	65.49185						
0.001" (.0254mm)	D	457.2	111.125	76.44785	152.4	27.534	5.53497494	1.5621	3.79	0.412163588
Channel 3										
Pin Height	**Pin Group Letter**	**X distance from ref pin (mm)**	**Y distance from ref pin (mm)**	**Time (µS)**	**ΔD (mm)**	**ΔT (µS)**	**Velocity (mm/µS)**	**ΔD (mm)**	**ΔT (µS)**	**Velocity (mm/µS)**
0.001" (.0254mm)	A	0	111.125	0.7918529						
0.125" (3.175mm)	B	127.15	111.125	13.24185						
0.125" (3.175mm)	B	139.7	111.125	14.79585						
0.001" (.0254mm)	B	152.4	111.125	25.31385	152.4	24.522	6.214828237	1.5621	4.47418	0.349136602
0.125" (3.175mm)	C	279.4	111.125	36.56985						
0.125" (3.175mm)	C	292.1	111.125	39.20785						
0.001" (.0254mm)	C	304.8	111.125	50.50385	152.4	25.19	6.050019849	1.5621	5.57418	0.280238528
0.25" (6.35mm)	D	431.8	111.125	56.73385						
0.125" (3.175mm)	D	444.5	111.125	64.45185						
0.001" (.0254mm)	D	457.2	111.125	75.41185	152.4	24.908	6.118516139	1.5621	1.71418	0.911281196
Channel 4										
Pin Height	**Pin Group Letter**	**X distance from ref pin (mm)**	**Y distance from ref pin (mm)**	**Time (µS)**	**ΔD (mm)**	**ΔT (µS)**	**Velocity (mm/µS)**	**ΔD (mm)**	**ΔT (µS)**	**Velocity (mm/µS)**
0.125" (3.175mm)	B	152.4	98.425	15.89185						
0.0625" (1.5875mm)	B	152.4	123.825	21.03385				1.5875	5.142	0.308732011
0.125" (3.175mm)	C	304.8	98.425	40.51985						
0.0625" (1.5875mm)	C	304.8	123.825	46.02585				1.5875	5.506	0.288321831
0.125" (3.175mm)	D	457.2	98.425	66.62785						
0.0625" (1.5875mm)	D	457.2	123.825	72.65785				1.5875	6.03	0.263266998
0.125" (3.175mm)	E	609.6	98.425	105.0099						
0.0625" (1.5875mm)	E	609.6	123.825	111.9959				1.5875	6.986	0.227240195
0.001" (.0254mm)	E	609.6	111.125	134.0239	152.4	57.5761	2.646933925	1.5621	22.028	0.070914291
0.001" (.0254mm)	F	712.08	111.125	151.5039	102.48	17.48	5.862700229			
Channel 5										
Pin Height	**Pin Group Letter**	**X distance from ref pin (mm)**	**Y distance from ref pin (mm)**	**Time (µS)**	**ΔD (mm)**	**ΔT (µS)**	**Velocity (mm/µS)**	**ΔD (mm)**	**ΔT (µS)**	**Velocity (mm/µS)**
0.125" (3.175mm)	B	152.4	98.425	16.18567						
0.0625" (1.5875mm)	B	152.4	123.825	20.83967				1.5875	4.654	0.341104426
0.125" (3.175mm)	C	304.8	98.425	39.91567						
0.0625" (1.5875mm)	C	304.8	123.825	44.92967				1.5875	5.014	0.316613482
0.125" (3.175mm)	D	457.2	98.425	67.25167						
0.0625" (1.5875mm)	D	457.2	123.825	73.69767				1.5875	6.446	0.246276761
0.125" (3.175mm)	E	609.6	98.425	105.1717						
0.0625" (1.5875mm)	E	609.6	123.825	129.4157				1.5875	24.244	0.065480119
0.001" (.0254mm)	E	609.6	111.125	137.3997	152.4	61.9879	2.458546312	1.5621	7.984	0.195653808
0.001" (.0254mm)	F	712.08	111.125	NoData	102.48					
Channel 6										
Pin Height	**Pin Group Letter**	**X distance from ref pin (mm)**	**Y distance from ref pin (mm)**	**Time (µS)**	**ΔD (mm)**	**ΔT (µS)**	**Velocity (mm/µS)**	**ΔD (mm)**	**ΔT (µS)**	**Velocity (mm/µS)**
0.125" (3.175mm)	B	152.4	12.7	14.35167						
0.0625" (1.5875mm)	B	152.4	12.7	19.75767				1.5875	5.406	0.293655198
0.125" (3.175mm)	C	304.8	12.7	39.21167						
0.0625" (1.5875mm)	C	304.8	12.7	43.29767				1.5875	4.086	0.388521782
0.125" (3.175mm)	D	457.2	12.7	66.59967						
0.0625" (1.5875mm)	D	457.2	12.7	70.01767				1.5875	3.418	0.464452896
0.25" (6.35mm)	E	584.2	111.125	81.45167						
0.125" (3.175mm)	E	596.9	111.125	93.42367				3.175	11.972	0.265202138

3.3.2 SUBSCALE, X-RAY-ONLY SPECIMENS

These tests were conducted to capture X-Ray images from similar test specimens to the original full specimens. The specimens used were 4" x 18", but of the same thickness. These

tests were conducted at the same inclination angles as the full specimen tests. An additional purpose of the first test was to check out the trigger system, after multiple trigger malfunctions. When that appeared to work correctly, the 8° full specimen (above) was tested.

3.3.2.1 1.5°Degree Inclination, December 20, 2017

This was the first test conducted in December. It was used to confirm the X-Ray trigger. It did function effectively for this specific test, and so it was then used in the remaining full-size samples. Unfortunately, the system failed to function in those two tests on this day.

Figure 3-26: 1.5° X-Ray only test.

The measured impact angle is roughly 6.5° in the initial impact region and 5.2° in the second impact region, compared to the predicted 4.6° angle from the geometric analysis. There is some uncertainty in the measurement of the angles from the X-Ray images. Reviewing the impact zone captured in the first head (clearest in Figure 3-26), it is apparent there is a non-planar/wavy nature to the geometry of the in-flight flyer plate. Depending upon the exact points used for measurement, the angles in the first zone were as low as 4.9° and as high as 6.8°. Similarly, there is some variability in the measurement of the angle in the second impact zone.

The angles shown are the best estimate when one attempts to be more precise, which is limited by the graininess of the image.

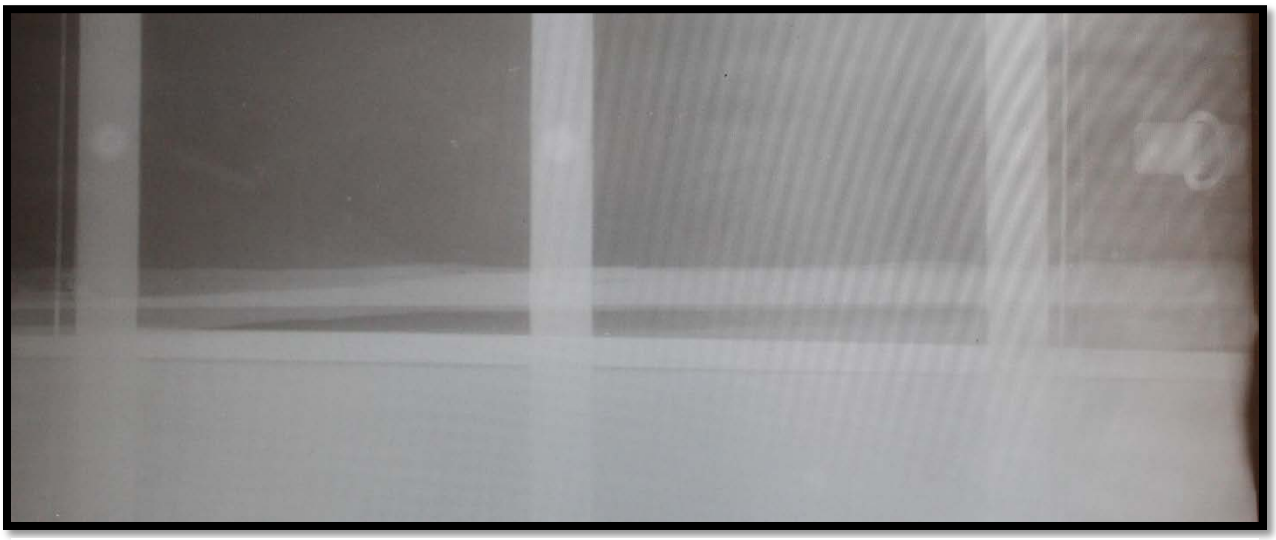

Figure 3-27: 1.5° X-Ray image captured on the cassette with X-Ray shadows from both X-Ray heads.

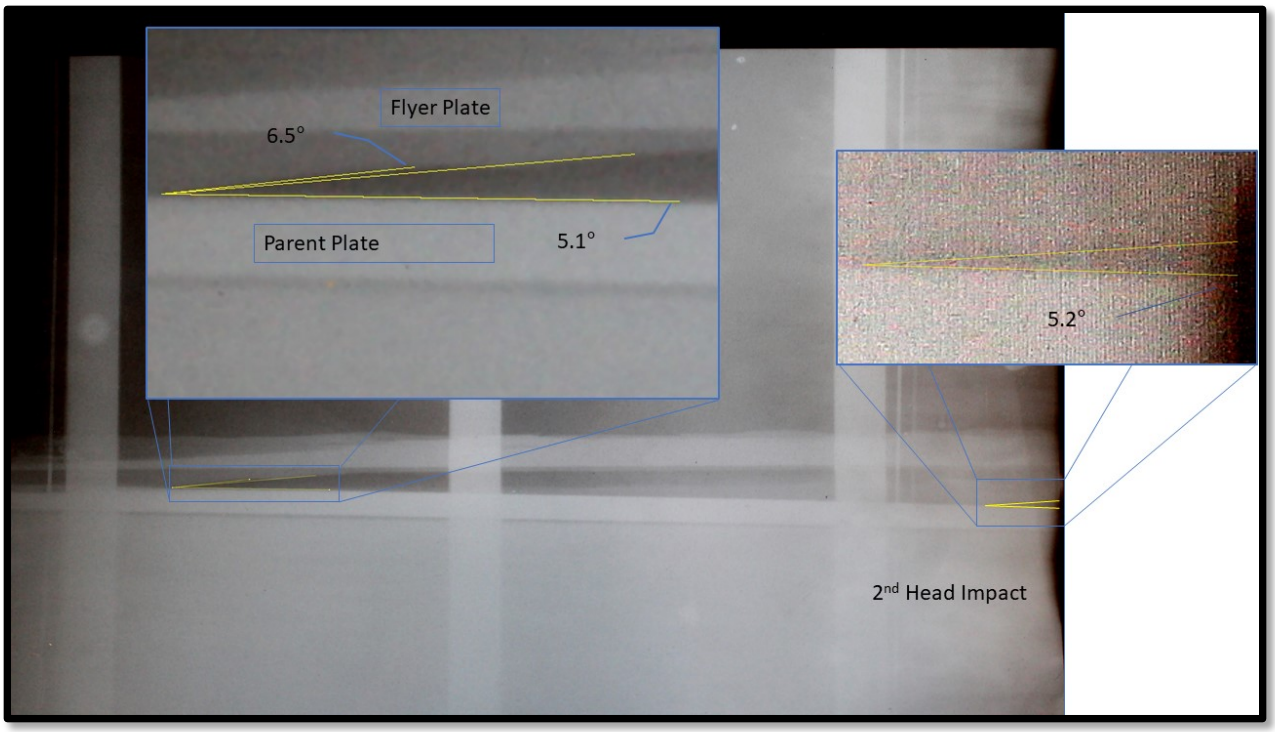

Figure 3-28: Full 1.5° X-Ray cassette image interpreted with X-Ray shadows from both X-Ray heads. Sub-figure (top-left) zooms in on the region showing the impact occurring when the first head fires. Sub-figure (top-right) shows the impact occurring when the second head functioned.

Using the reference marks that established the scale, the distance between the collision points was 11.734 inches. Based on the specified time delay of 65.1 μs, this corresponds to a weld velocity of 4.58 mm/μs.

Figure 3-29: 0.5° X-Ray image with images from both X-Ray heads

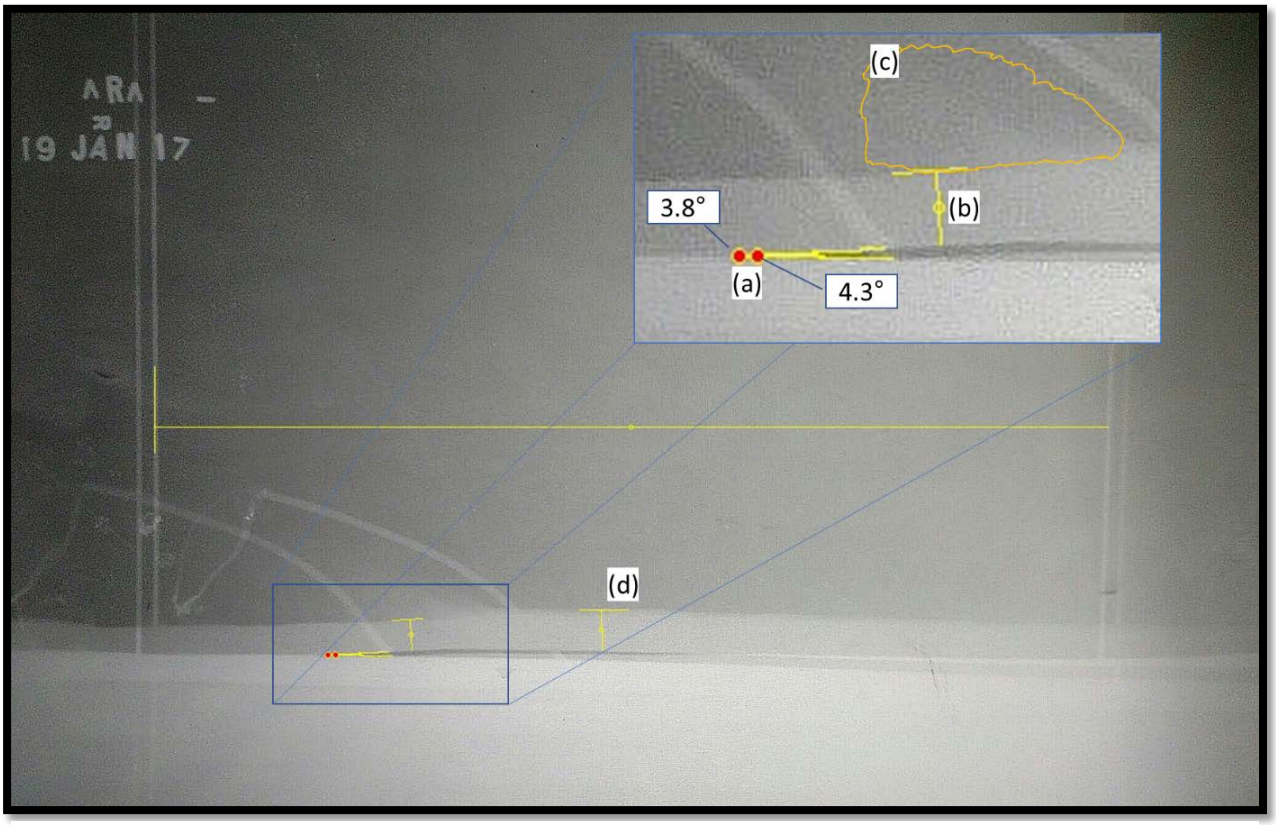

Figure 3-30: Annotated 0.5° X-Ray test. (a) marks the different vertices for listed angle measurements. (b) Measurement of in place flyer in flight at 0.392" projected thickness. (c) Region where dispersing explosive is visible. (d) Unperturbed flyer and C6 at 0.52".

3.3.2.2 0.5° Inclination Tests, January 19, 2018

Figure 3-29 above shows the X-Ray image captured for the 0.5°, subscale specimen. The image successfully captures the impact when the first X-Ray head fires, but missed the impact with the second head. Figure 3-30 annotates the image. In this image it is possible to make out the dissipating explosive (c), undisturbed flyer and explosive (d), and the in-motion flyer plate (b). Using the reference lines and the undisturbed flyer/explosive as a reference, it was possible to measure the projected thickness of the in-motion flyer plate to be 0.392 inches. This provides a measure of the amount of edge effects of the explosives.

For the weld velocity, missing the second impact limits our ability to quantify the average velocity. However, one can provide a lower bound. One can also estimate the impact point off the image using the slope of the top of the flyer plate at the edge of the image, the slope of the top of the parent plate, and the projected thickness shown in the first image. With a time delay of 50.5 μs and 11.881" from the first impact to the edge of the image, the lower bound is 5.97 mm/μs. The estimated distance off the image to impact is, 0.382", yielding an estimate of 6.17 mm/μs for the weld velocity.

3.3.2.3 2.5° Inclination Tests, January 19, 2018

The 2.5° subscale X-Ray image, Figure 3-31 below, is one of the clearest obtained. In

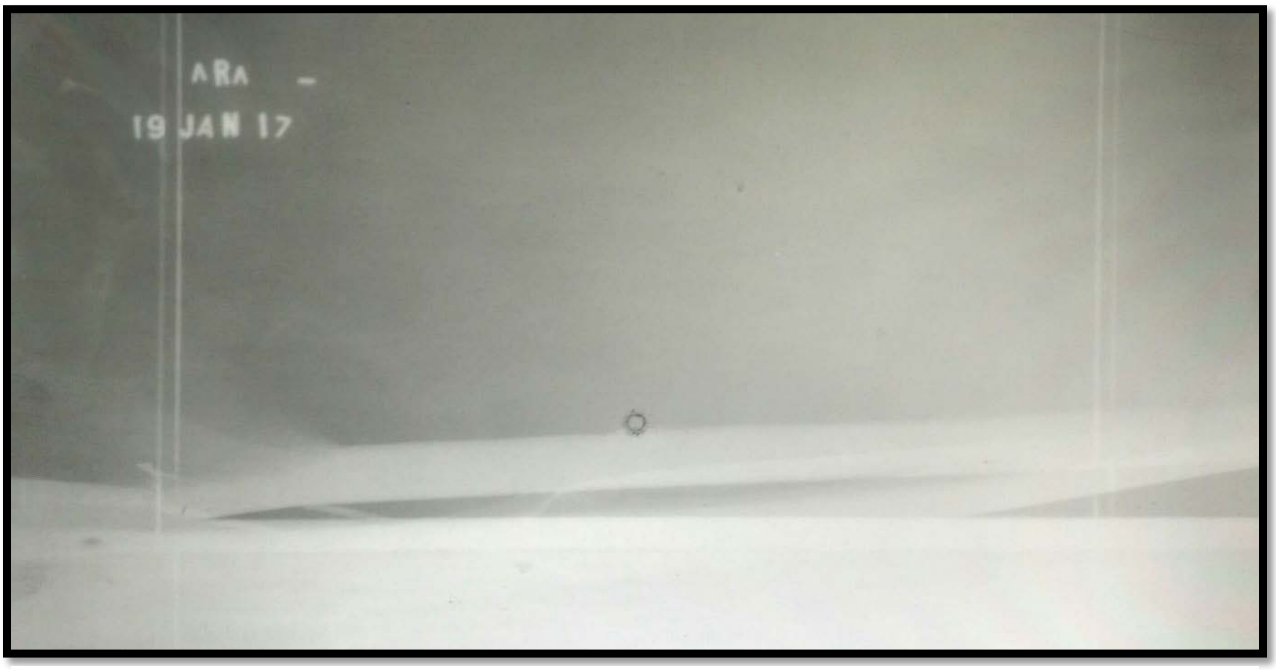

Figure 3-31: 2.5° subscale test X-Ray images.

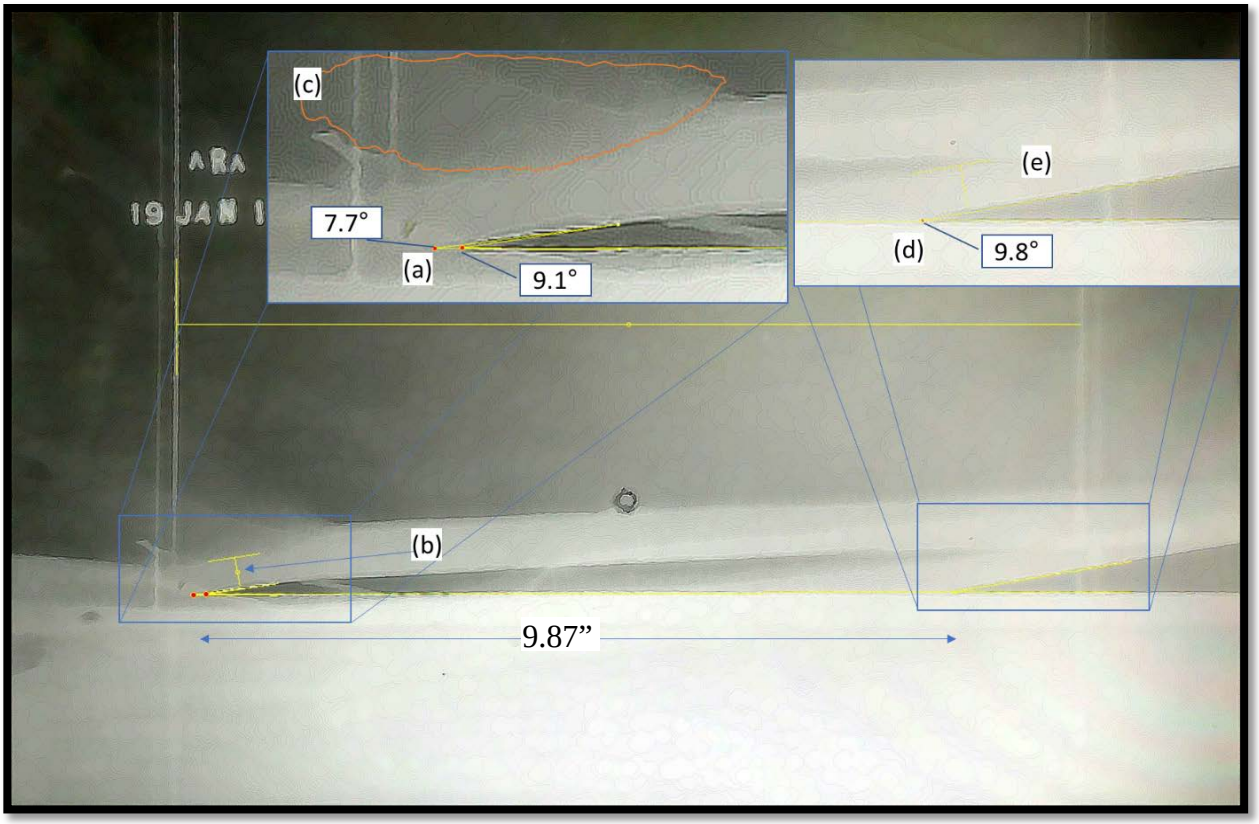

Figure 3-32: Annotated 2.5° test. (a) Angles based on different used angle vertices. (b) 1st image projected flyer thickness of 0.405". (c) Dispersing explosive. (d) 2nd impact angle; clearer image so only one vertex used. (e) 2nd measure of projected flyer thickness (0.420”) during flight from second X-Ray burst.

Figure 3-32, annotations list some of the measurements that were obtained. The first impact is shown by (a) and the second by (d). In this case the projected thickness of the in-motion flyer plate was able to be obtained in two locations ((b) & (e); 0.405” and 0.420” respectively). The distance between collision points is 9.87”, and the specified delay was 50.1 μs. This yields a 5.00 mm/μs average collision point velocity.

3.3.2.4 8° Inclination Test, February 23

The 8° subscale X-Ray image, Figure 3-33, clearly shows both impact points. The dark splotches are from the film impacting the film cassette/holder, which was unexpected, but just due to the violent nature of the event. In Figure 3-34, measured values are annotated. The

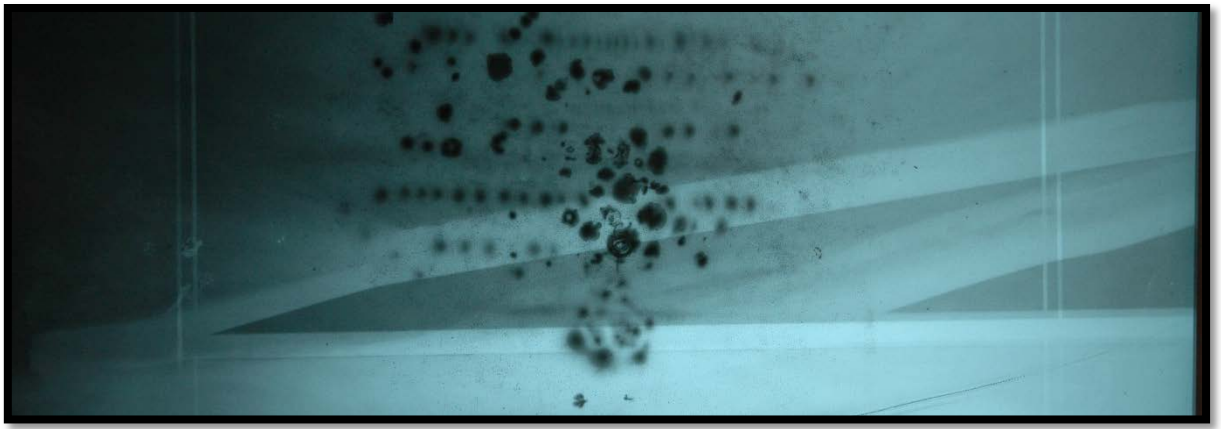

Figure 3-33: 8° subscale test X-Ray images.

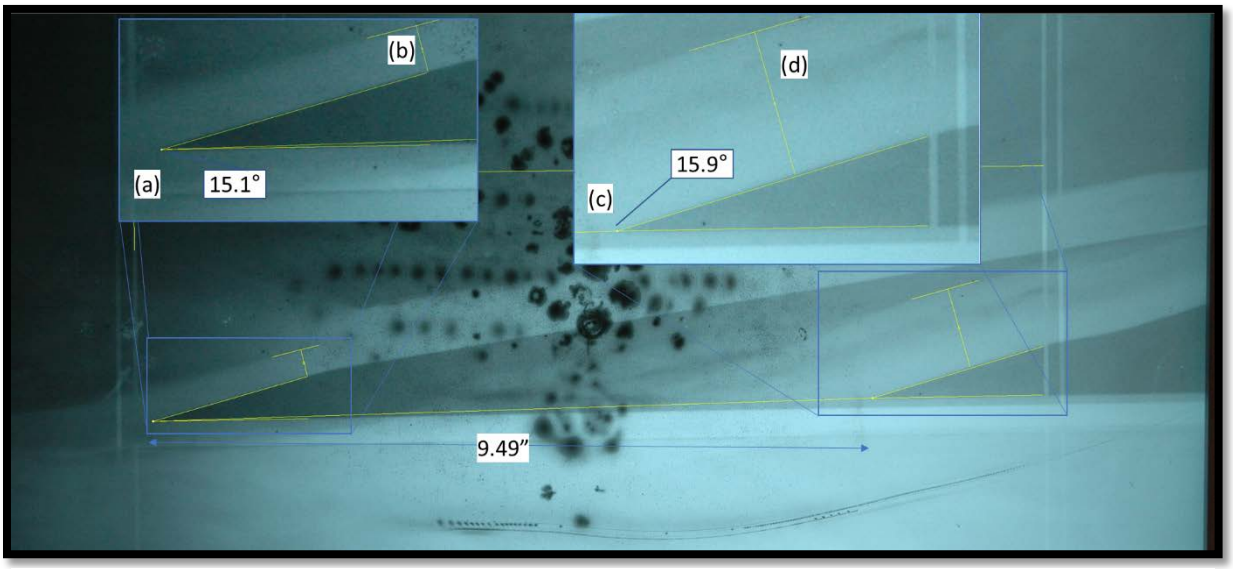

Figure 3-34: Annotated 8° test. (a) Impact angle from first head. (b) Projected thickness of 0.362” from the flyer plate. (c) 2nd Image of impact angle. (d) Projected flyer plate thickness of 1.1” in second image.

distance between collision points is 9.49”, and the specified time delay was 71.1 μs. This yields a 3.39 mm/μs average collision point velocity.

3.4 Analysis: Comparing Measured Results to Forecasted Values

3.4.1 Flyer Plate Velocities

The estimates of the flyer plate velocities did not go as smoothly as initially envisioned. The reported values in Table 3-9-Table 3-12 in Section 3.3.1 come from transversely arranged

pins (at the edges in the 1.5° and 2.5° tests, but also in the interior in the December 8° and 0.5° tests). In all cases but the 0.5° interior pins, the time of arrival data for these pins (using the difference in pin height divided by elapsed time for sequentially decreasing pin heights) generated flyer plate velocities that appear to be significantly too slow. Based on NMAP and other modeling, as well as predictions from the Gurney equation (see Equation (2-14)) [184], [185]), the values are anywhere from 10 to 2 times too small. The 8° test interior transverse arrays yield velocity estimates that are roughly ¼ of the expected value, while the 0.5° test actually gives velocity estimates that are in the correct order of magnitude. The hypothesis is (recalling that the 0.5° test that generated pin data did not weld) that the 0.5° test did not generate jetting, while the 8° test did and the jetting interfered with the measurement of the velocity in the 8° test. (This could occur if the jet completes the circuit for each pin earlier than it should have otherwise occurred). Interpretation of the oscilloscope data for the 0.5° make-up test was less noisy and more straightforward.

3.4.1.1 Edge Effect Correction

After reviewing the 1.5° and 2.5° tests, multiple attempts were made to estimate the time varying, deformed shape of the flyer plate and use that to correct velocity estimates. The plan for measuring the vertical plate velocity was based on time of arrival measurements in the top of the "T" shaped arrays at the edges of the setup. The assumption for calculating velocities was that a cross-sectional cut through the flyer plate (blue plane in Figure 3-35, noting that the flyer plate is not shown in order to reveal pin locations relative to the cut) could be assumed to be a rectangle oriented parallel to the parent plate.

What is clear from literature is that there are edge effects in explosive welding. Of significance at any edge, is the fact that that portion of explosive does not have the confining

effect of surrounding explosive in all directions, like explosive in the middle has. This lessens the impulse provided to accelerate the portion of the flyer underneath these edge regions. In reality, due to the extreme nature of this event, it has a non-uniform surface, that varies its shape with time.

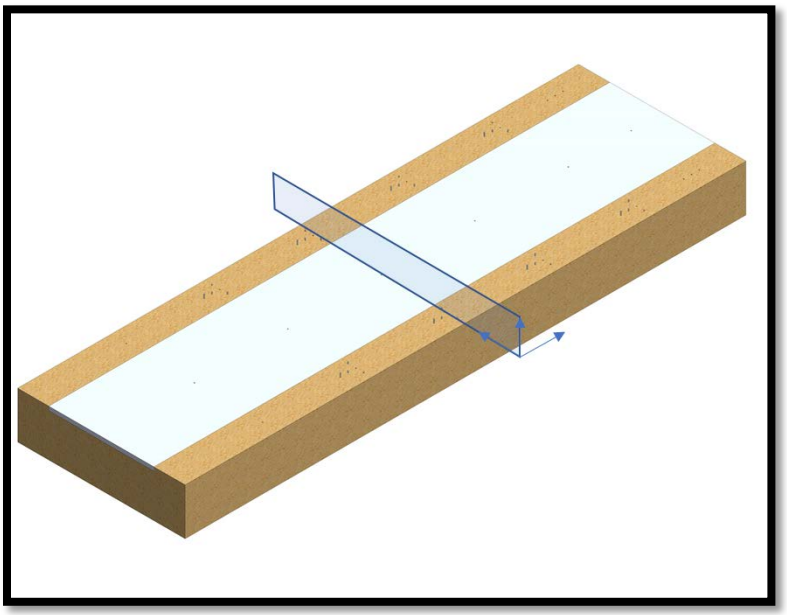

Figure 3-35: Cut plane referenced in subsequent figure. The flyer plate is not shown to highlight the spatial relation to the TOA pin arrays.

It was further identified that the TOA pin arrays used to measure the velocity of detonation during the actual welding events, provided additional confinement effects in the interior.[37] Figure 3-36 below shows the shape of the bottom edge of the cross-section, for discrete points in time. (The model is a plane strain model.) During the 1.5° and 2.5° tests, a VOD pin array (see Figure 3-19 (a) and 24 (a) above) was placed on top of the explosive to capture detonation velocity data. The confining effects of this array were not anticipated, and based on the modeling shown in Figure 3-36, it would have a significant effect. However, while

[37] It was later recognized that there was also a 6.35 mm difference between the explosive and plate width, which was unable to be captured.

this figure is dominated by the effect of this TOA pin array, the outside edges also show the effect of the lack of confinement, as they curve up away from the adjacent profile.

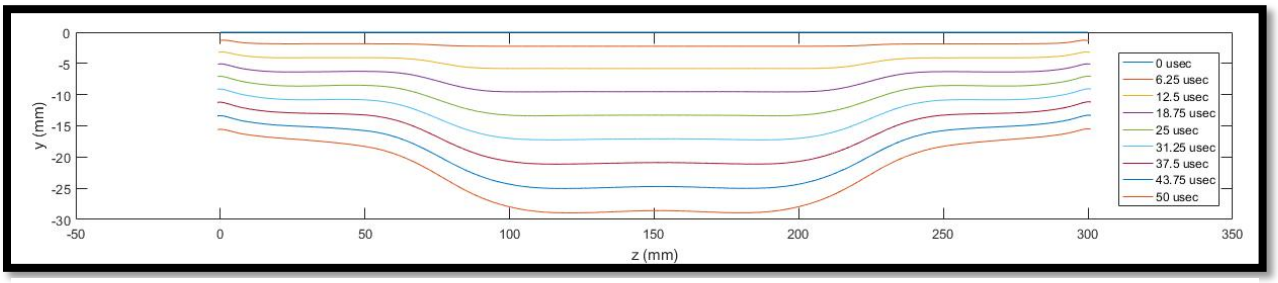

Figure 3-36: NMAP Cross-section modeling results.

Figure 3-37 below, helps illustrate the potential impact of this curvature. The calculation for the plate velocity was $V_p = \frac{\Delta h}{\Delta t}$. The time difference was measured, and it was assumed that the difference in pin heights was 1/16". However, with a more accurate profile, the true distance traveled is further. This results in our measurement for time difference being bigger, as the plate actually has to travel farther. This larger Δt, with our incorrect assumed Δh, makes the velocity approximation be much smaller than it was in reality.

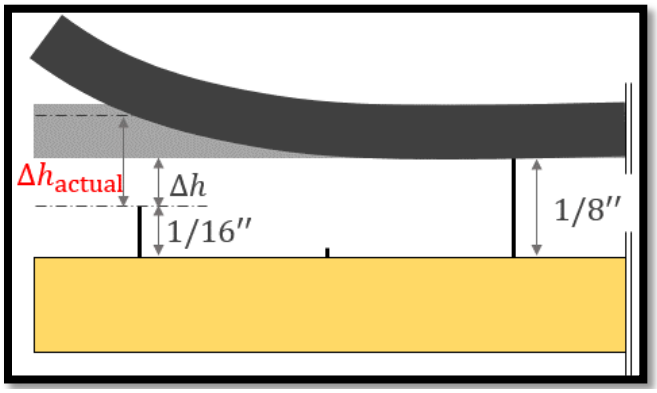

Figure 3-37: Edge effect on TOA pin measurements. A depiction of the instant in time that the 1/8" pin in a transverse array strikes the flyer plate, showing the assumed and the qualitatively more accurate profile.

In the first attempt to correct for edge effects, the profile in Figure 3-36 was used to estimate the true remaining height above the next sequential pin, and that distance was used in calculating the velocity estimate. The result of these attempts yielded estimates that were closer

to expected values in many cases, but did not adequately account for all issues. Both the wavy nature of the flyer plate deformations, and the possibility that the deformations were large enough to change the impact sequence (this did occur in certain tests), complicate the correction.

3.4.1.2 Estimate based upon longitudinal pins

Even in the 8° test with interior transverse pins, reliable data was not obtained in a welding specimen from the transverse arrays, and so it was attempted to identify other means to estimate the plate velocities. Figure 3-38 shows a longitudinal pin array in the moment when the plate arrives at Pin 1 (1/4" pin in T array; e.g. bottom pin in Figure 3-12 (b), Detail B). Since the plate has an angle β, the actual travel distance of the plate, h_{actual}, is larger than h. Thus, the plate velocity V_p was calculated by using the equation below.

$$V_p = \frac{h+\Delta h}{\Delta t}\frac{\cos(\beta)}{\cos\left((\beta-\alpha)/2\right)} = \frac{h+d\tan\beta}{\Delta t}\frac{\cos(\beta)}{\cos\left((\beta-\alpha)/2\right)} \quad (3\text{-}2)$$

where Δt is the difference of arrival times measured by the two pins. The vertical displacement $h+\Delta h$ is adjusted by the cosine terms because the direction of the plate velocity is not vertical. The angle β was calculated by using the average of measured weld velocities and the average of measured VOD's based on the Equation (3-3) below (derived from equations (2-1) and (2-2) above), where α, V_w, and V_d are the initial plate angle, weld velocity, and VOD, respectively.

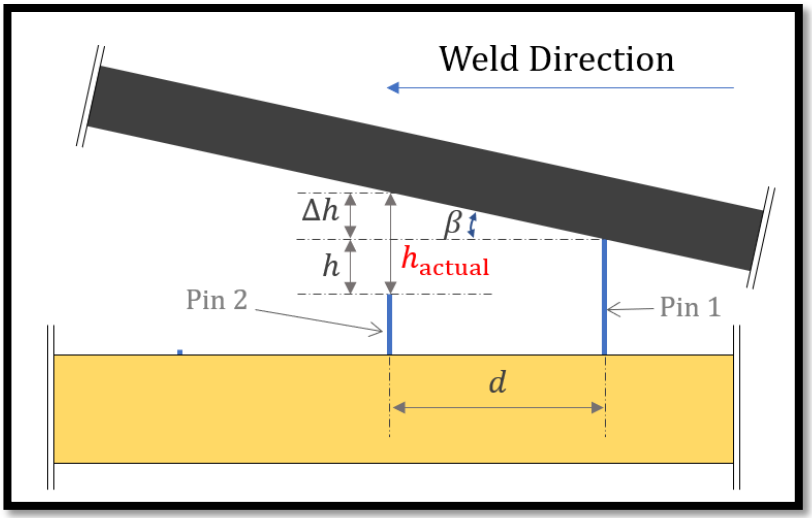

Figure 3-38: Longitudinal correction. Schematic two-dimensional view around a longitudinal pin array

$$\beta = \tan^{-1}\left(\frac{\sin\alpha}{\cos\alpha - V_w/V_d}\right) \tag{3-3}$$

Table 3-13: Flyer plate velocities cases based on longitudinal pin method (mm/μs)

Case	0.5°	1.5°	2.5°	8.0°
Average Arrival-Time-Differences (μs)	10.02	10.53	3.18	4.05
Plate Velocities (mm/μs)	0.40	0.40	2.82	1.88
Estimated Values (mm/μs)	0.380	0.380	0.920	0.920
Error ($\lvert 1 - V_{pM}/V_{pE} \rvert$) (%)	5.3%	5.3%	207%	104%

Table 3-13, above, shows the plate velocities obtained by the longitudinal pin methodology described above. The average arrival-time-difference is an average value of the arrival time differences between two adjacent longitudinal pins of pin groups B, C, and D. In Figure 3-38, a pairing of Pin 1 and Pin 2, as well as a pairing of pin 2 and the flush pin, are the two pairs of adjacent longitudinal pins used for generating the average plate velocity. The average plate velocities of 0.5° and 1.5° are close to the expected velocity of 0.38 km/sec calculated using NMAP. However, in the 2.5° and 8° cases, the obtained velocities are still much bigger than the expected plate velocity, which is 0.92 mm/μs by NMAP, 0.95 mm/μs by CTH, and 0.89 mm/μs by Gurney's equation. Upon receipt of the January 19, 2018 2.5° test X-Ray

images, substitution of measured impact angles (β) did not measurably improve the plate speed estimates.

Table 3-14 shows the plate velocity estimates back-calculated exclusively using average measured weld velocities (of pin groups B, C, and D) and detonation velocity, using geometric analysis Equation (3-3) and Equation (2-1) solved for V_p. These weld-velocity-based estimates are closer to the obtained velocities in Table 3-13 than the expected velocities. There is no clear reason identified for the discrepancy. However, it is clear that these issues occur with the more violent events. Although the 8° specimen fractured in two, it is possible that the 2.5° case was the most violent of all the tests, based on assumed activity at the collision point. This test had the MDF detonation velocity array providing explosive confinement, while the 8° had this confinement removed. The discrepancy in plate velocity measurements may have been associated with material jetting as well.

Table 3-14: Plate velocity estimates using geometric analysis based on measured V_w and V_d

Degree	Center	Left Side	Right Side	Avg.
2.5°	2.07	2.71	3.87	2.88
8.0°	2.00	1.87	1.55	1.81

3.4.2 WELD VELOCITIES

In general, the TOA pins showed a strong ability to capture the weld velocity of the specimen. The predicted weld velocities were reasonably close to the measured, especially when differences in model inputs are considered. For the 1.5° case where the C2 explosive detonated faster than expected, the mean measured weld velocity is less than 10% over the predicted value. In the case of the 2.5° test, the mean measured weld velocity is within 20% of the predicted when the detonation velocity was about 4% higher than expected. The flush mounted pins do not appear to be significantly affected by jetting or other action.

Table 3-15: Weld velocities from different sources

Source		0.5 Degrees	1.5 Degrees	2.5 Degrees	8.0 Degrees
Expected V_w (km/sec)		6.00	4.70	5.30	3.40
Pin Data	V_w (mm/μs)	5.83	5.07	6.13	4.62
	Error	2.83%	7.87%	15.66%	35.88%
X-Ray Images	V_w (mm/μs)	6.17	4.58	5.00	3.39
	Error	2.19%	2.55%	5.28%	0.29%

3.4.3 IMPACT ANGLES

The impact angles that were measured were reasonably close to the predictions.

Table 3-16: Measured impact angles for welding events tested.

Source	0.5 Degrees	1.5 Degrees	2.5 Degrees	8.0 Degrees
Expected Impact Angle, β (°)	3.6	4.6	10	15.5
Measured with X-Ray Image	4.1	5.2	9.8	15.9
% Error ($\lvert\beta_M/\beta_E$ -1$\rvert$ x 100)	10%	16%	2%	2.6%

3.4.3 SUMMARY

The experimental weld event program was a learning process, but overall very useful results were obtained. Triggering for flash radiography was resolved, and the subscale specimen results demonstrated a high level of capability. The potential exists for higher discharge levels and better resolution films to improve upon the X-Ray images. The TOA pins established a reasonably reliable ability to identify weld velocity, and even plate velocity for smaller events. However, perhaps due to jetting, the plate velocities were less reliable for the more violent events. The potential use of photon doppler velocimetry or other means could improve upon plate velocity measurements as well. In general though, the analysis based upon the design of welds proved rather effective in predicting outcomes, within the means of available data.

4. MECHANICAL VERIFICATION OF WELD QUALITY

4.1 INDUSTRY AND ACADEMIC STANDARDS FOR EVALUATION

Upon completing a series of welding tests, besides an apparent connection verified by manual means alone, it is critical to conduct an evaluation that more conclusively and quantitatively verifies the quality of the weld. This warrants a discussion of what properties identify a successful weld, which can really vary by intended purpose.

Within the cladding industry, there are a number of established standards for evaluating cladding. These primarily apply to pressure vessels and lay out a broad set of possible plating materials, as seen in ASTM A20 [186]. Not all of these plates are clad, but ASTM A263, A264, and A265, are all specifically for clad plate. They are, in order, steel clad with Chromium, Chromium-Nickel, and Nickel & Nickel-Base Alloy [158], [159], [187]. ASTM standard B432 is a similar standard for copper clad to steel, similarly for pressure vessel use, though not listed in A20. Additionally, ASTM B898 is a standard for Reactive and Refractory Metal Clad Plate, where one or both sides of an undesignated base metal has a layer of titanium, zirconium, tantalum, niobium, or one of their alloys applied [188] All of these, A263-5, B432, and B898, apply to cladding produced by explosive welding or by any other method. All five of these standards list a bond shear strength, shown in Figure 4-1, as a standard test. This test requires an average shear stress of 10,000-20,000 psi be achieved by the bonding. Other tests often specified are a tension requirement for the composite, as well as a bend test for ductility, which is shown in Figure 4-2. The tensile requirement isn't explicitly aimed at the bond, but the bend test is an alternative to the shear test, and serves to certify that the composite can tolerate a certain amount of bending without delamination.

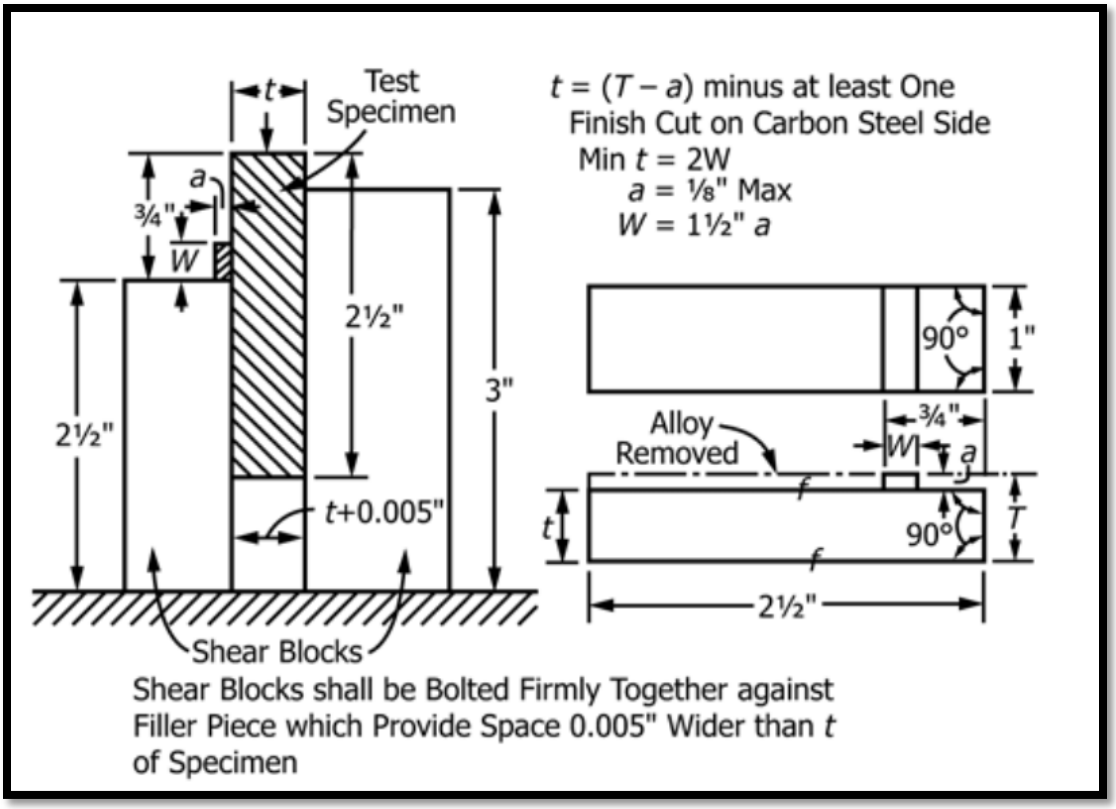

Figure 4-1: Standard cladding shear test from ASTM A263-5, B432, and B898. The cladding metal is milled away leaving a lug/stub that is sheared off in a jig made from the displayed shear blocks. [158]

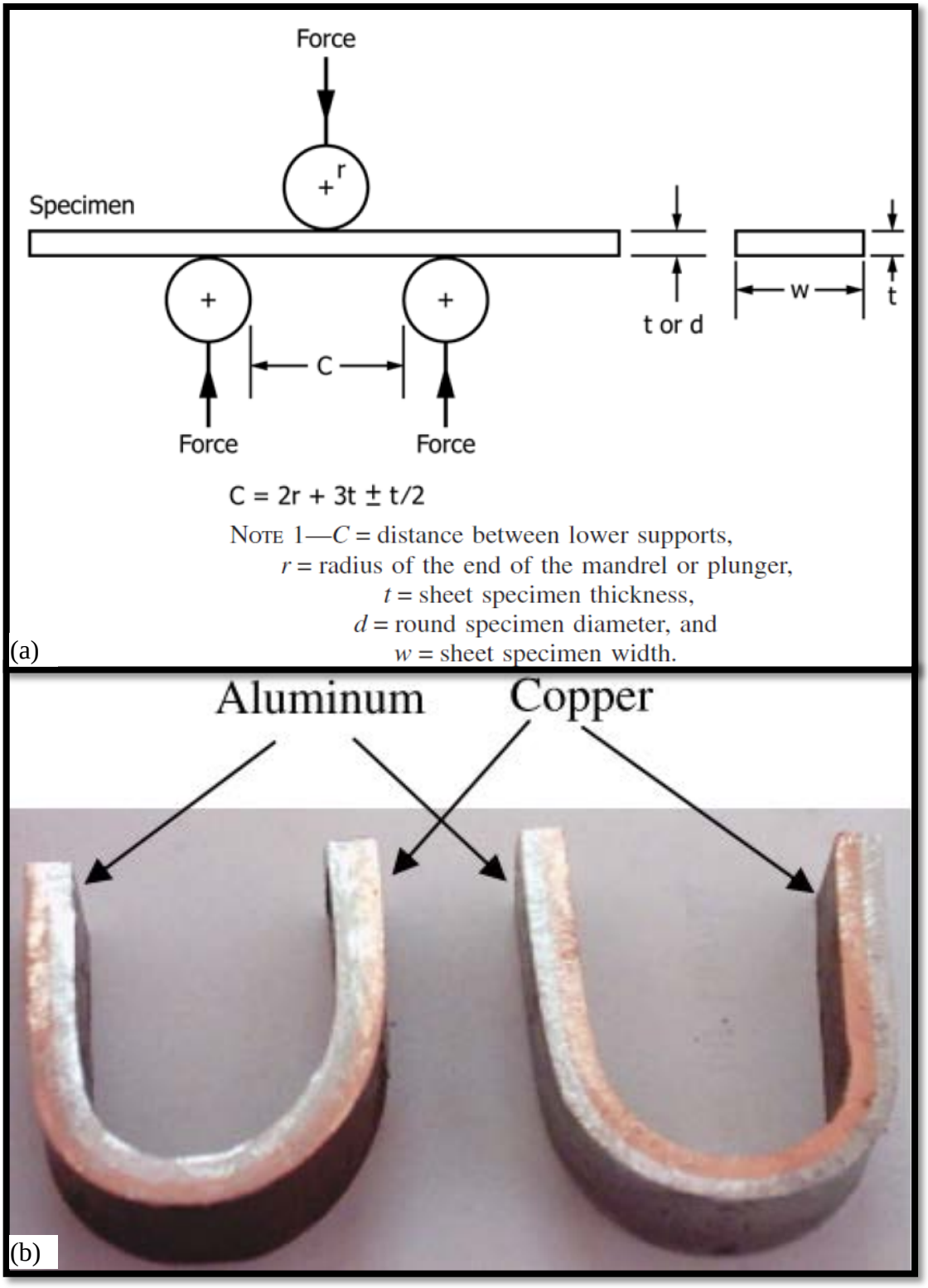

Figure 4-2: Bending ductility test of clad plates. (a) General schematic for a guided bend test establishing ductility in the bond. [244] (b) Example cladding test samples. [245]

While pressure vessel and boiler standards are more established, this doesn't cover the full scope of explosive welding purposes. Another segment of the market includes military applications. For maritime purposes, it is common to combine steel and aluminum components, relying on steel strengths where critical, but using aluminum to generally decrease the mass or for low temperature capabilities [189]. This illuminates the need for MIL Standard J-24445A, Joint, Bimetallic Bonded, Aluminum to Steel [190]. As the title suggests, it is for transition joints for steel to aluminum, with some of the applications having been discussed above. For these purposes, the tensile strength across the bond is of importance as well, so a purely tensile test without any other prying action, as shown in Figure 4-3, was included. The standard also includes a similar shear test to the one shown in Figure 4-1, but just including more shear tabs to break in one compression stroke. Other tests are listed as well in this standard.

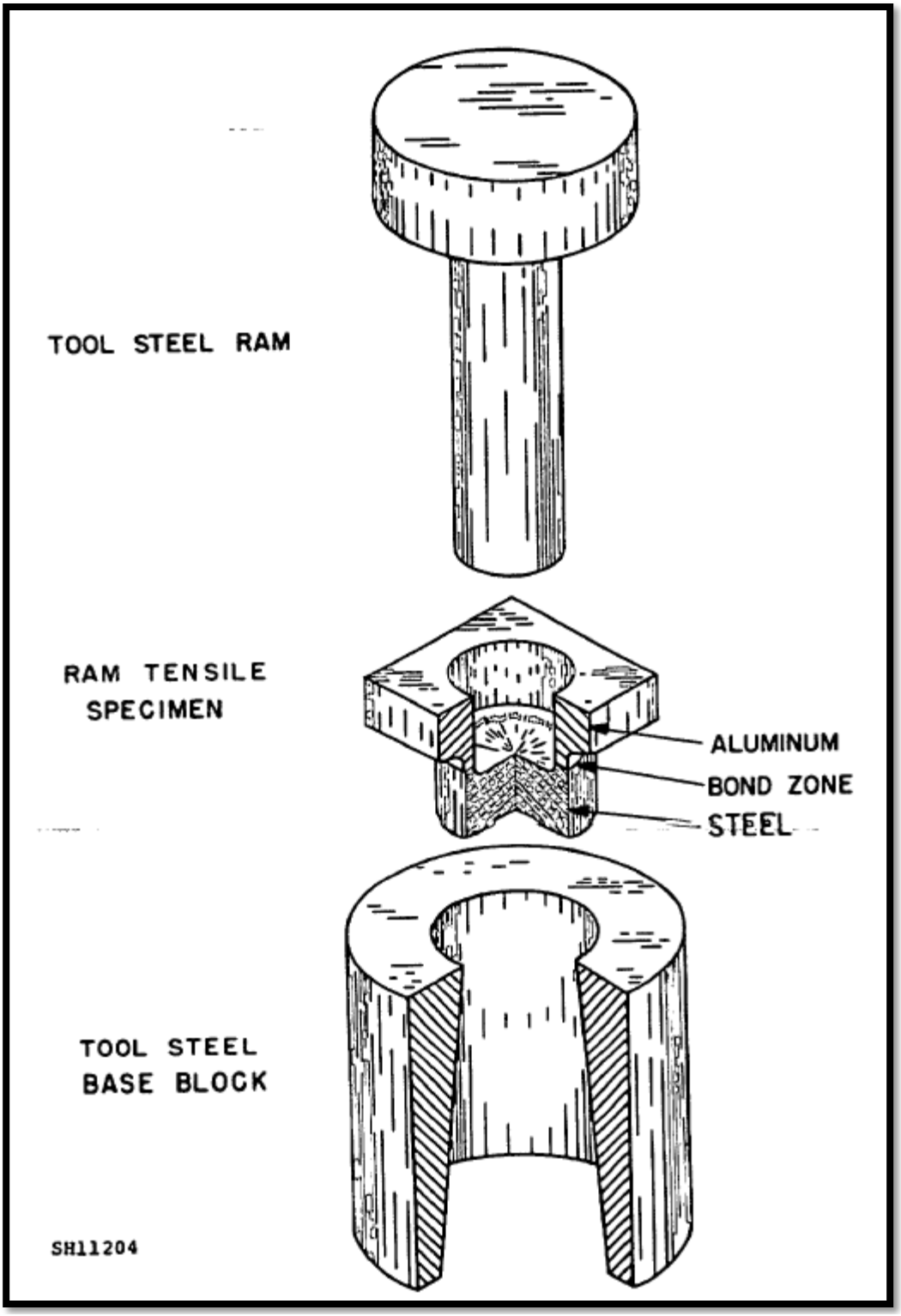

Figure 4-3: MIL Standard J-24445A ram tensile test, that stresses the bond layer in a purely tensile fashion.

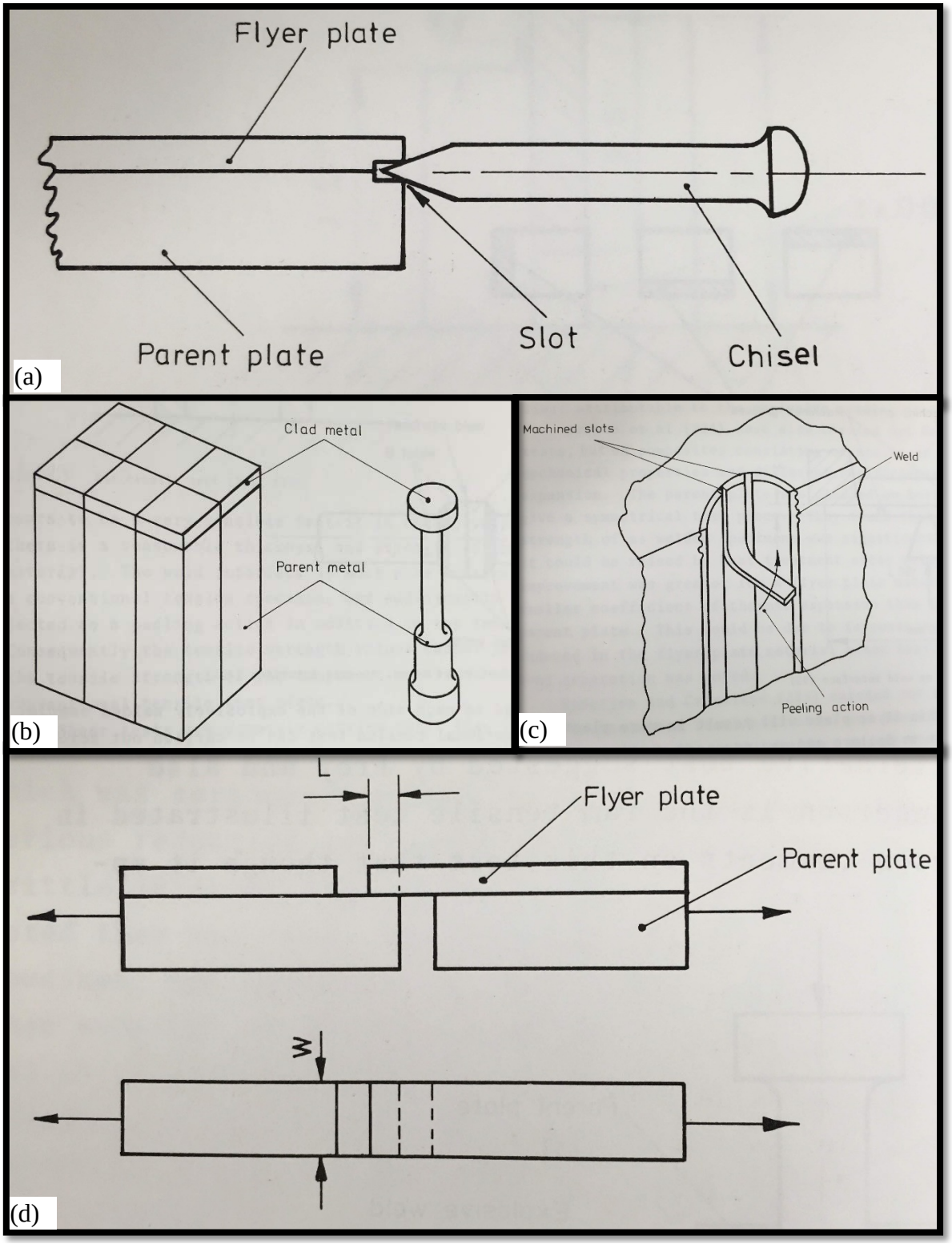

Figure 4-4: Alternative mechanical bond tests in research as shown by Crossland. In addition to these, Crossland shows a torsional test, an impact test, another tension test, and similar tests from above. (a) Chisel test that subjects the bond to a peeling action. (b) Tensile test requiring heavy milling. (c) Peel test for tubular weld. (d) Tensile shear test. [6, pp. 181–188]

While that exhausts the tests specifically for explosive welding available from standards agencies, researchers have developed other tests for use in evaluating the effectiveness of the bond. Figure 4-4 shows and briefly lists some additional tests as presented by Crossland [6, pp. 181–188]. Many of these tests have been used extensively. The strength of a bond in a peeling action, shown Figure 4-4 (a), has been evaluated frequently; just a small sampling includes [82], [191]–[195]. This obviously combines some indication of tensile strength with fracture characteristics along the bond. Another, common test is the tensile shear or lap-shear test shown in Figure 4-4 (d). This test, as opposed to the shear tests in the ASTM standards has a number of criticisms, as noted by both Crossland and Cannon [6, p. 183], [50, p. 108]. This specimen experiences a significant peeling action, and for thinner specimens or thinner individual layers, significant bending occurs during testing, which changes the inclination of the bond plane relative the macrolevel applied tensile forces. The difficulty in getting standardized shear tests, which are affected by the dimensions of the specimens and the length of bond in shear, is likely why the ASTM standards are as explicit as they are.

4.2 SELECTION OF TENSILE SHEAR TESTS FOR WELD EVALUATION

In this study, the decision was made to select the type of tensile shear test shown in Figure 4-4 (d) in order to mechanically evaluate the weld quality. It became clear upon evaluation of the varying definitions of weld success, the time required for different testing methods, and the costs associated with different methods that this was a sufficient test of weld quality, while still a feasible course to pursue in light of time and resource constraints.

As already noted, the intended use is critical in defining what makes successful welds. The needs (mechanical or otherwise) of weld bonds for pressure vessels, heat exchangers, or metallic transition joints are not all the same. As discussed in Section 2.2.4.1, there remains

dispute about whether a smooth or a wavy bond is a necessary criterion. As will be discussed in Section 4.6, the ASTM and MIL standards referenced above don't necessarily require what could be considered the full shear or tensile strength of the weakest material. Nor does the MIL standard require the full tensile strength of the aluminum. Further, all of those standards were for dissimilar metal bonds, which immediately separated them from the current experimental work. It became clear that the definition of success ultimately was in relation to its intended purpose, which in this case was an academic one that was inherently more flexible, as long as it was clearly articulated and reproducible.

Upon a review of prior studies, and evaluation of the goals of this study, it became clear that the tensile shear test would successfully meet the needs. Although it is not the most favored test, it has enjoyed significant use. Besides its noted mention in Crossland's text, numerous studies have used this method [4, pp. 181–183], [5, pp. 201–202], [23], [45], [50], [82], [196]–[202]. While this differs from published standards, there reason to accept deviation from them in this case. Since the published standards do not necessarily exactly relate to a specified base metal property (i.e. shear or tension strength), it is clear there is some other consideration at play, perhaps some sort of factor of safety for overall reliability of the entire plate or some other measure of required performance that is not explicitly articulated. The lack of the specific use associated with those standards, decreases the need to adhere to them. Alternatively, there is also a precedent for the use of an adhesive joint standard, ASTM D3165 [203], for justifying the use of this type of lap test, and examples are included in the list of references immediately above, although this seems more open to question based upon its specifications. With all of the reasoning laid out above, the tensile shear test was the best choice for the needs of this study.

4.3 SPECIMEN PREPARATION

4.3.1 DESIGN OF THE TEST STANDARD

Because the tensile shear test is not explicitly defined in any of the standards identified above, some deliberate work was required to choose the exact configuration, which is shown in Figure 4-5. Aspects of the test used by Cannon et. all were adopted [50, pp. 106–109]. Specifically, a width of 1 in (25.4 mm) was used, and that was adopted here. The overall length of the specimen was chosen primarily to accommodate standard tensile testing machines. Likewise, the width of the notches used, was based upon the size of smallest available milling bit, which was 1/8 in. Rather than extensively remove material, the as-clad final thicknesses of

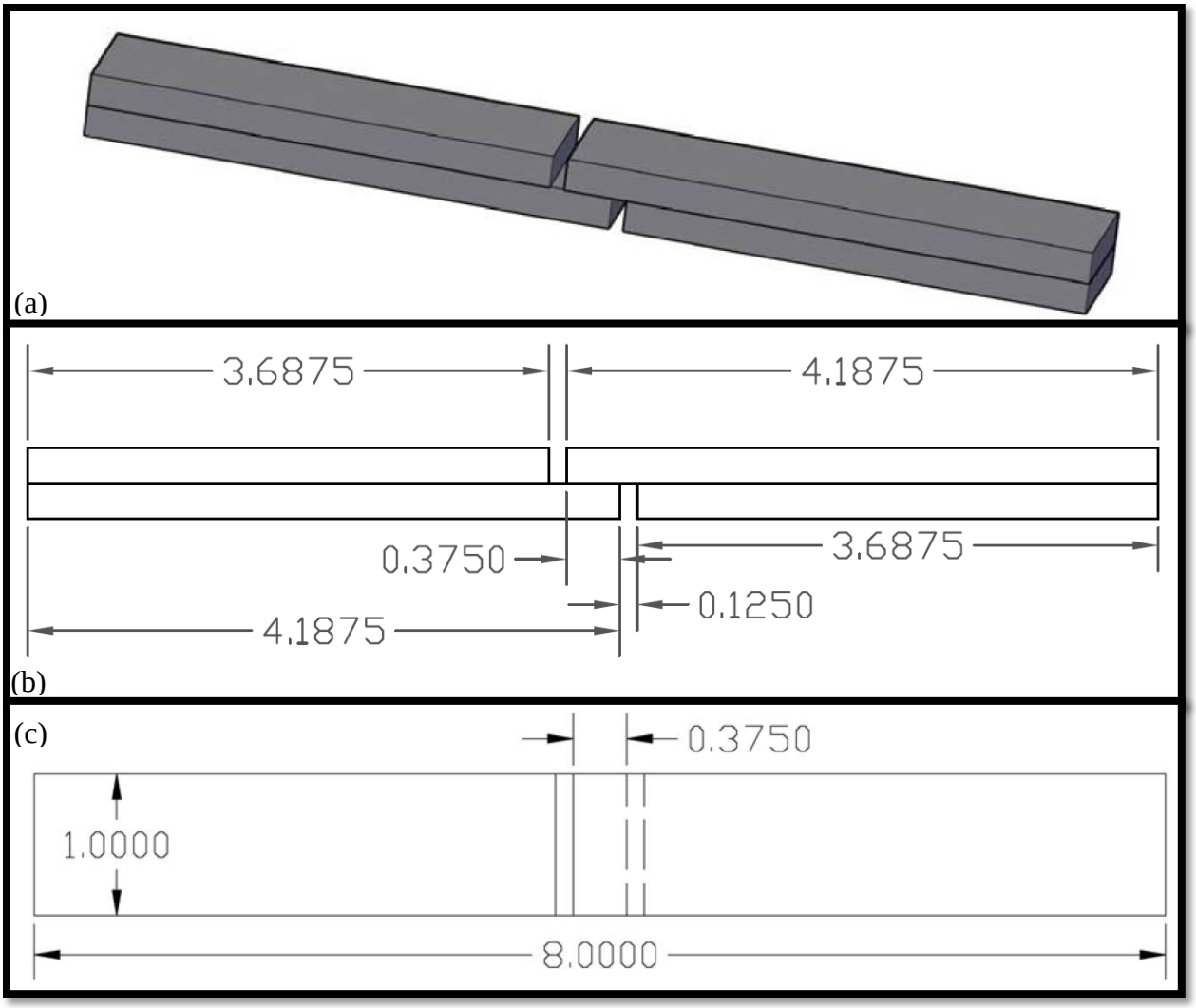

Figure 4-5: Tensile shear test specimen used in this study. All units in inches.

the materials were used. The last dimension to select was the length of the lap, *L*, which ended up being 3/8 in, as shown in Figure 4-5.

Figure 4-6 below, shows modeling that was done subsequent to initial design that illustrates a few key kinematic inevitabilities. Using the undeformed state as a starting point, and assuming that cuts in the reduced section result in a free body diagram as in Figure 4-6 (c), with a further cut on the weld plane, a limiting value of *L* can be proposed. The plane of the weld is assumed to only have an average shear stress acting on it, while the face of the reduced section cut has only an average tensile stress. A maximum length allowed to induce shear failure can be

derived, shown in Equation (4-1), labeling the thickness of the original plate as *t*, and using a von Mises relation to relate tensile strength, F_u, to shear strength. Using Equation (4-1) based on

$$t \cdot F_u > L \cdot \frac{F_u}{\sqrt{3}} \Rightarrow L < t\sqrt{3} \tag{4-1}$$

force equilibrium on a unit depth basis, as an estimate, with our original plate thickness, *t*=0.25 in, yields that *L* must be roughly kept below 7/16 in.

Taking this first estimate further, we allow for the obvious fact that the specimen will deform significantly before failure. The centroid of the applied tensile forces on the specimen were assumed, away from the notches, to act through the centroid of the cross section as in Figure 4-6 (b), which is not collinear with the resultants assumed in Figure 4-6 (c). It was assumed equilibrium would cause plastic hinging and align the centroids of the reduced sections with those of the bulk specimen. If that was indeed the scenario, then there was a fixed relative transverse displacement, and the longer the lap, *L*, the smaller the angle of rotation of the

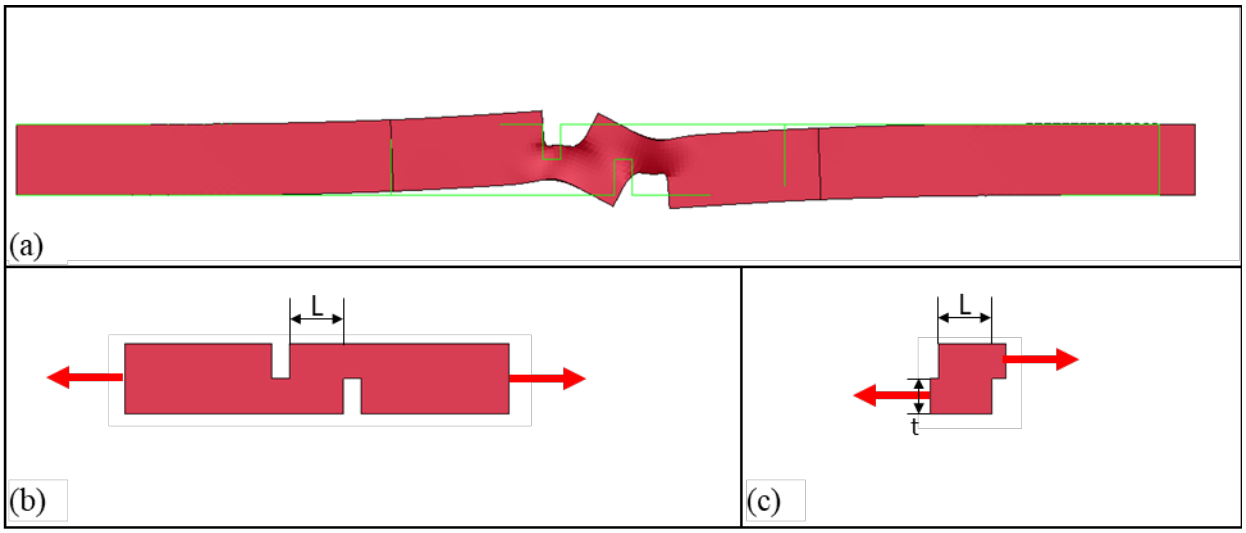

Figure 4-6: Anticipated deformed shape of the specimen. (a) The green lines show the original edge boundaries of the specimen, prior to deformation. Material to the left translates up, material to the right, translates down, and the material between the notches rotate, inclining the plane of welding that is being tested. (displacement exaggerated for clarity) (b) Force at centroid far from notches. (c) Forces shifted towards centroids of reduced sections, generating a couple.

welding plane. If the resultant acts at the centroid of the reduced section, each would shift by $\frac{t}{2}$. For these specimens that is 1/8" at each end, or ¼" total relative motion. Comparing that to the cap on *L*, the minimum angle was assumed to be approximately 30°. However, this deformed configuration, invalidates Equation (4-1), as the weld clearly will not have only a net shear acting on it. This is clear from the modeling result in Figure 4-6 (a).

So, assuming this 30° inclination, the relationship determining a limiting *L* was re-evaluated. With axes aligned such that direction 1 is normal to the inclined weld and direction 2 is parallel to it, with assumed average stresses, the second stress invariant, J_2, is $J_2 = \frac{1}{3}\sigma_{11}^2 + \sigma_{12}^2$. Next, σ_{11} and σ_{12} were related to the full tensile load, using an assumed 30° inclination. This was again compared to the limiting value in the von Mises relation resulting in Equation (4-2). This was evaluated for the initial plate thickness indicating that to ensure failure in the

$$L < t\sqrt{\frac{5}{2}} \tag{4-2}$$

weld plane, rather than the net section, the limiting value of L was approximately 3/8". This is slightly less than my original 7/16" value that generated the 30°, and so in this inclination, we would predict tensile failure in the net section, rather than failure on the weld plane. However, that would require the bond to handle both roughly 86% of the specimen's applied tension force in shear, plus a component equal to 50% of the specimen's applied tension force in tension.

Based upon this analysis, acknowledging the string of assumptions associated with it, and upon subsequent modeling shown in Figure 4-7, the value of *L* = 3/8" was selected. The modeling was executed in LS-DYNA R10.1 with Lagrangian finite elements, single integration points, default hourglass control, and an implicit analysis. The material model was MAT 003, plastic with isotropic hardening activated, and the parameters used are listed in Table 4-1 below.

The loading rate was selected in accordance with ASTM B557 for aluminum tests and 1 mm/min was used [204]. Welds that could develop failure of the net section in tension could be declared successful welds, while those that failed in the plane of the weld still could demonstrate

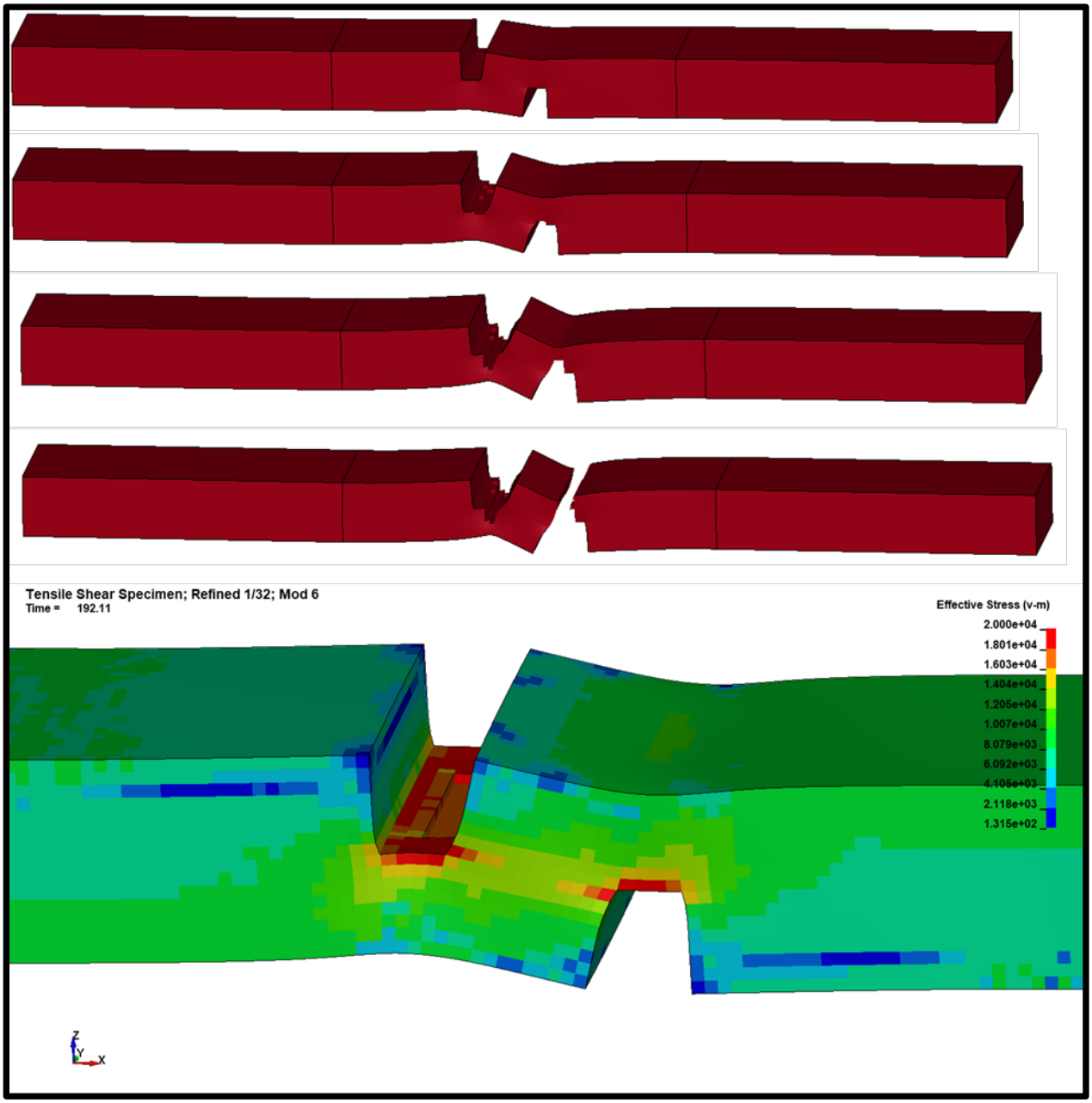

Figure 4-7: Modeling result for proposed configuration. Significant von Mises stress concentrated on the weld plane in this perfectly bonded scenario.

Table 4-1: Tensile Shear Test material model parameters

Young's Mod., E, (psi)	Poisson's Ratio	Yield Stress (psi)	Tangent Stiffness (psi)	Failure Strain
10^7	0.33	8000	50000	0.27

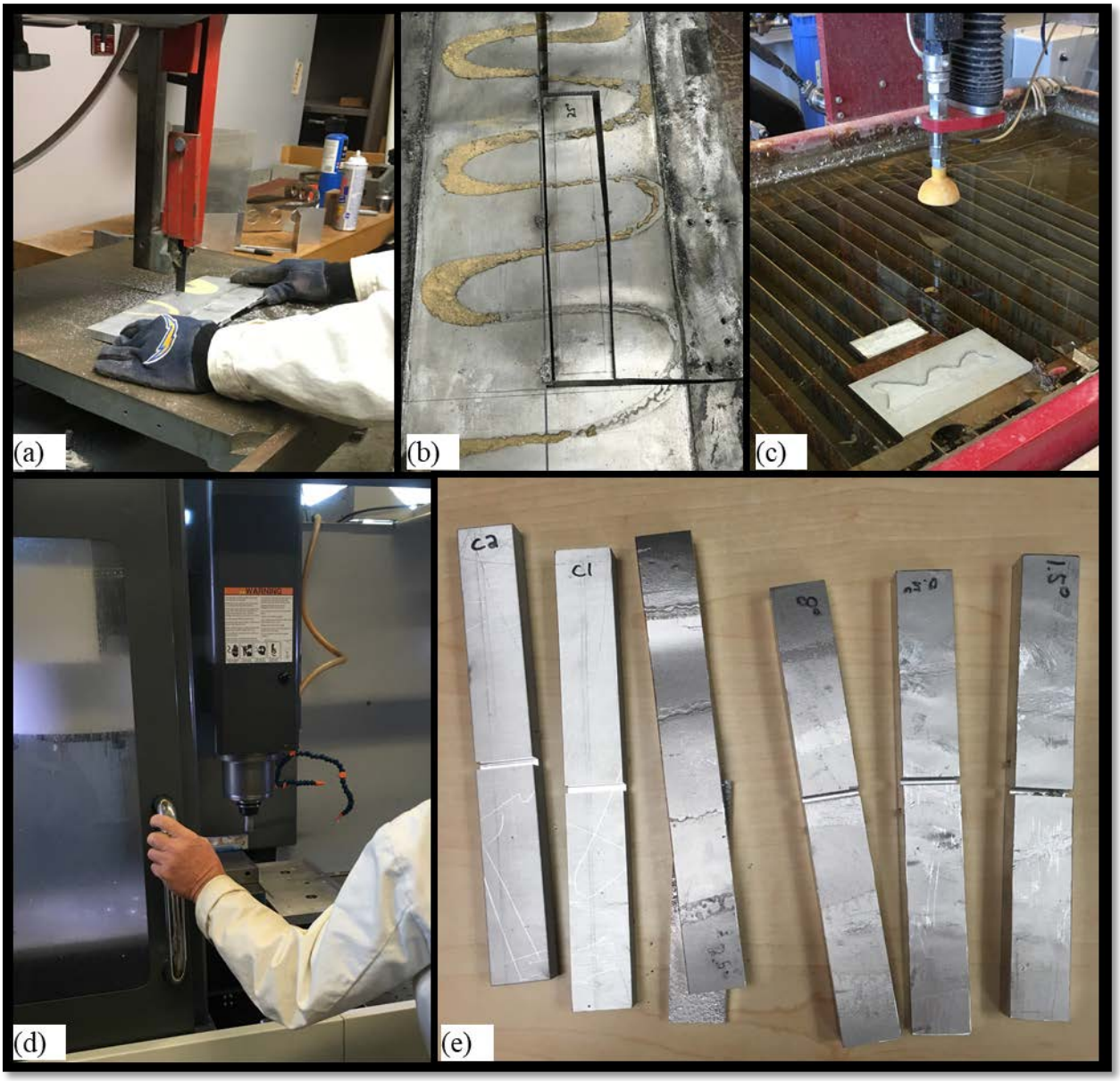

Figure 4-8: Fabrication of tensile shear specimens. (a) & (b) Band saw cuts to rough dimensions out of weld specimens. (c) Water jet cuts from control plate. (d) CNC milling to final dimensions. (e) Final specimens, showing one of the 2.5° specimens that failed during fabrication.

significant capacity, even if they became the weakest link. As a further control, it was determined to fabricate specimens of equal dimensions from 0.5" thick plate, which could be used as a comparison to see what load a pure 6061-O aluminum specimen could endure, inspired by Zabelka's work [23].

4.3.2 Fabrication of Specimens

The specimens were fabricated as shown in Figure 4-8. Rough cuts from the welded plates were made with a band saw, and then milled in the CNC machine using liquid cooling during the milling process. The control specimens, also Al 6061 aluminum were annealed, cut from plate using a water jet, and milled in the CNC as well. Although two separate test specimens were fabricated, both failed during or shortly after the process.

4.4 Effects of the As-Clad Condition on Testing

In many studies, testing is conducted in both the as-clad and further processed conditions. With different explosives, buffers, and further working, the final dimensions of the cladding can meet tolerances for the deviation from a flat planar surface that would be required for use. However, that kind of additional processing (with the exclusion of the buffers during the weld event) can potentially weaken the state of the bond. In this study, in order to assess the strength achieved in the bonding, no subsequent treatment or processing was executed. As a result, the weld specimens all had residual deformations to varying degrees.

It became clear as planning for the testing progressed, that the residual deformations would have a significant effect on the state of stress in the samples. Figure 4-9 below, shows each of the surviving weld samples. The residual deformations were essentially two dimensional in nature. Using a digital image and simple image analysis software, the sample geometries were traced and loaded into LS-DYNA models, also shown in Figure 4-9 with a 0.5" grid overlaid for

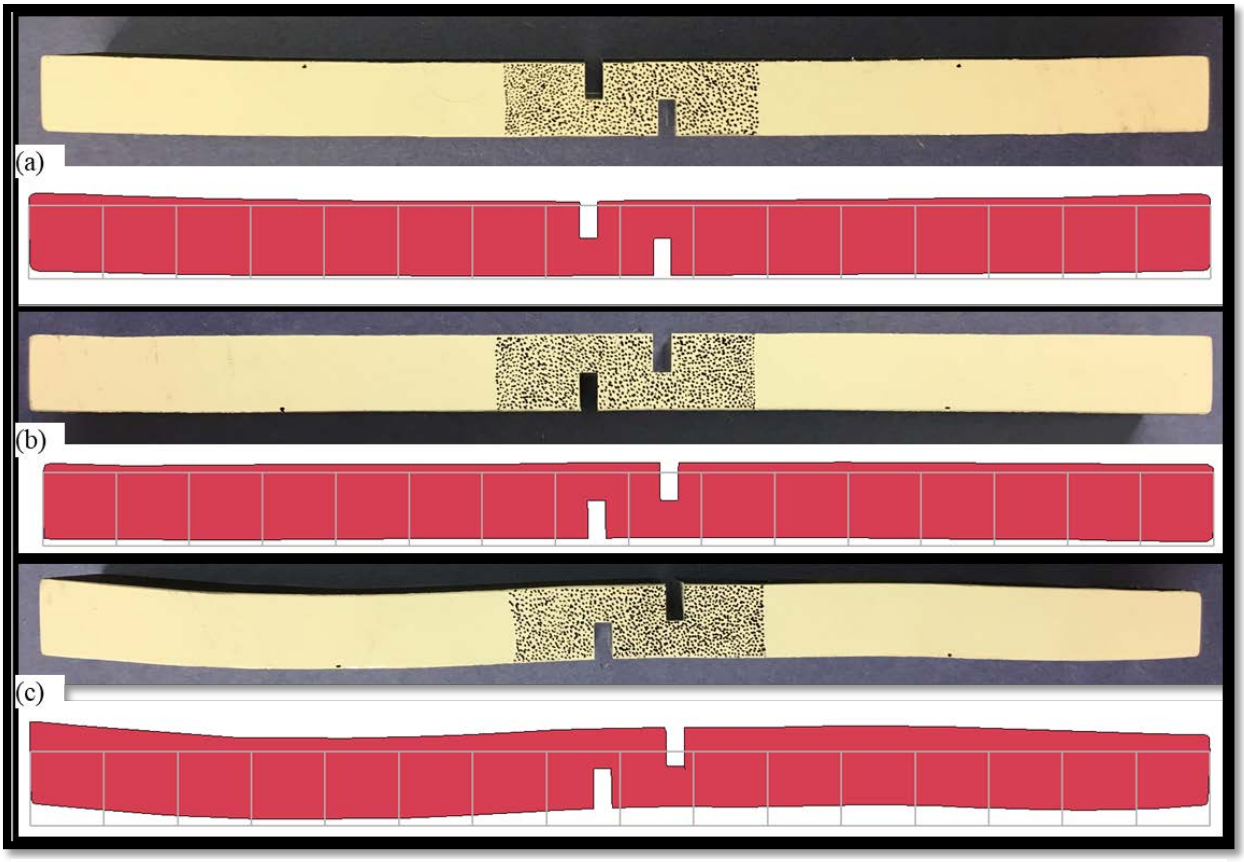

Figure 4-9: Residual deformations in tensile shear samples. In each sub-figure, the top is the sample prepared for testing, and the bottom is the geometry brought into an LS-DYNA model with an overlaid 0.5" grid. (a) 0.5° (b) 1.5° (c) 8°.

reference. These models were also implicit models using the same material model referenced above in Section 4.3.1 (also shown in Figure 4-7) with the same parameters in Table 4-1. Based on the estimate of the tensile load that could be achieved a grip force of 7 kip was required based on the grip manual [205, pp. 81–82]. A contact, surface-to-surface-mortar contact algorithm was applied with a static coefficient of friction of 0.61 and a dynamic coefficient of friction of 0.2. The models assumed a perfect bond across the weld. The results from the final gripping iteration was output as a dynain[38] file for use as a starting point for the tensile test. In all three tests, regions near the notches experienced plastic strains solely due to gripping. Hence at the start of

[38] This is an LS-DYNA output file that describes the state of a model in a format for use as a keyword starting point for another model.

testing, the specimens were already experiencing internal loads. Since the plan was to use digital image correlation to observe the strain field during testing and prior to failure, it was clear that our image collection had to begin prior to gripping the specimens in order to capture the actual strains experienced in the material. However, in spite of these effects from gripping, they all still predicted the same failure mode as the original model, which was a failure in the reduced section by the notches. It was anticipated the effects could become significant for the welds, which may not achieve that ideal condition.

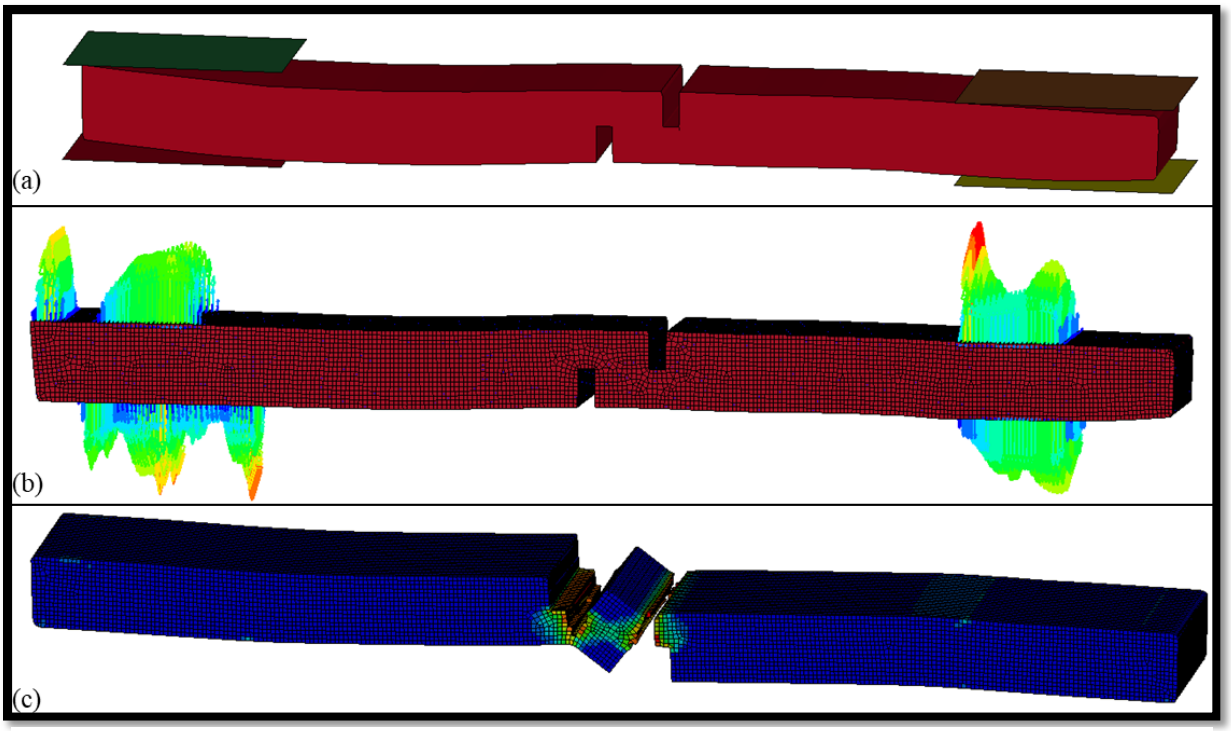

Figure 4-10: Modeling of weld samples. The 8° sample as an example of the process. (a) Model with rigid shell elements simulating machine grips. (b) Reaction pressures after gripping. Prescribed displacements until a roughly 7 kip grip force at each end. (c) The end point of (b) used as a start point to simulate the tension test. (Plastic strains plotted)

4.5 TESTING

4.5.1 TESTING SYSTEMS AND PROCESS

4.5.1.1 Overview of systems and Data Collection Plan

As shown in (a), an MTS Model 370.25 load frame system with a 100 kN capacity was used for loading the specimens. The data collection was through a few different means. First the data collection streams native to the load frame system were used, including time, head displacement, and load measurements at a roughly 10 HZ sampling rate. Second, as a more precise displacement measurement and over a smaller length, a laser extensometer was used, shown in Figure 4-11 (b) & (c). However, due to the nature of this specimen with specific localized behavior, the third technique was necessary. The third data collection stream was to use digital image correlation to identify the surface strain field on the specimen, to gain a better understanding of the behavior and state of stress near the weld surface. Figure 4-11 (c) above, shows the software used, VIC 2D, by Correlated Solutions [206]. Figure 4-11 (a) and (c) show the lighting and camera system used to capture images.

Figure 4-11: Test systems used during mechanical evaluation. (a) An MTS system with Model 370.25 (100 kN) load frame, Series 647 hydraulic wedge grips, and Series 793 software for loading and data. Also, a high-resolution digital camera for image data. (b) A model LE-05 EIR laser extensometer for an additional displacement measure. (c) Specimen with laser and reflective tape in place. (d) VIC-2D software by Correlated Solutions used for digital image correlation.

4.5.1.2 Digital Image Correlation Data Collection and Details

In digital image correlation, the specimens are prepared, as shown in the tops of each sub-figure in Figure 4-9. A white background is applied with paint, and then a speckle pattern is

added over the region of interest. The speckle pattern was applied manually using a fine point sharpie, in accordance with [207]. Then during the course of the event, a series of images must be captured. These images are the raw data of the process. In this study, special care was taken during image collection due to the residual deformations of the specimens. In order to capture strains imposed during clamping, image collection had to begin before the main test started.

In the case of both the 0.5° and 8° specimens, clamping just the first end caused strains. This was due to the fact that the wedge grips, vertically aligned for testing, had a limiting opening width of 0.75 in (19.1 mm), and due to the roughly 0.5 in specimen thickness, there was very little room for the opposite end to traverse before it either bore against the opposite grip (if already inserted) or passed the point where it could later be inserted into the top grip.

In the process used then, the first end was gripped as lightly as possible. The image collection system was focused, readied, and then initiated prior to tightening the grip to the required clamping force. Collection continued during gripping of the other end as well, and the transition to the main test was made as quickly as possible. In the case of the 1.5° specimen, gripping the first end did not cause an impact with the opposite side wedge grip, and so this process was slightly simpler, allowing a normal first grip before collecting images. The control specimens, flat to factory tolerances, did not require these steps, and image collection started immediately prior to loading.

The images during the tests were collected by a high-resolution digital camera, using a continuous movie file that started during gripping (in the case of the weld samples), and ran through the completion of the test. The movie files were then read into Matlab and selected frames were extracted and written to tiff files for direct use in Vic-2D. In the case of the control specimens, 301 images were taken each at an even interval after the start of testing. However,

for the weld specimens extra steps were taken. In order not to sample a series of frames where no movement occurred (i.e. after gripping, but before loading), the video images were analyzed using the function “imabsdiff” in Matlab to determine when the specimens were being strained. Then frame sampling was only taken during the application of forces to the specimen.

The colors of a white background with black speckles is selected to allow use of a grey scale image. In a simplified manner guided by [208], Figure 4-12 below will be referred to, which could correspond to black and white results for an idealized pattern. Figure 4-12 (a) & (b) show a part of an image and high level of zoom in data and in visual representation. Within this part of the image, a “subset” is specified at a given size, as shown in Figure 4-12 (a), which becomes a finger print of sorts for that part of the image. Then Figure 4-12 (c) and (d) represent the data and visual representation of a subsequent image. Essentially, an algorithm tries to find the original subset, in the new image, (which in this case has shifted up and right). In practical use the initial image could the first image, or could be the immediately preceding image, depending upon the degree of deformation.

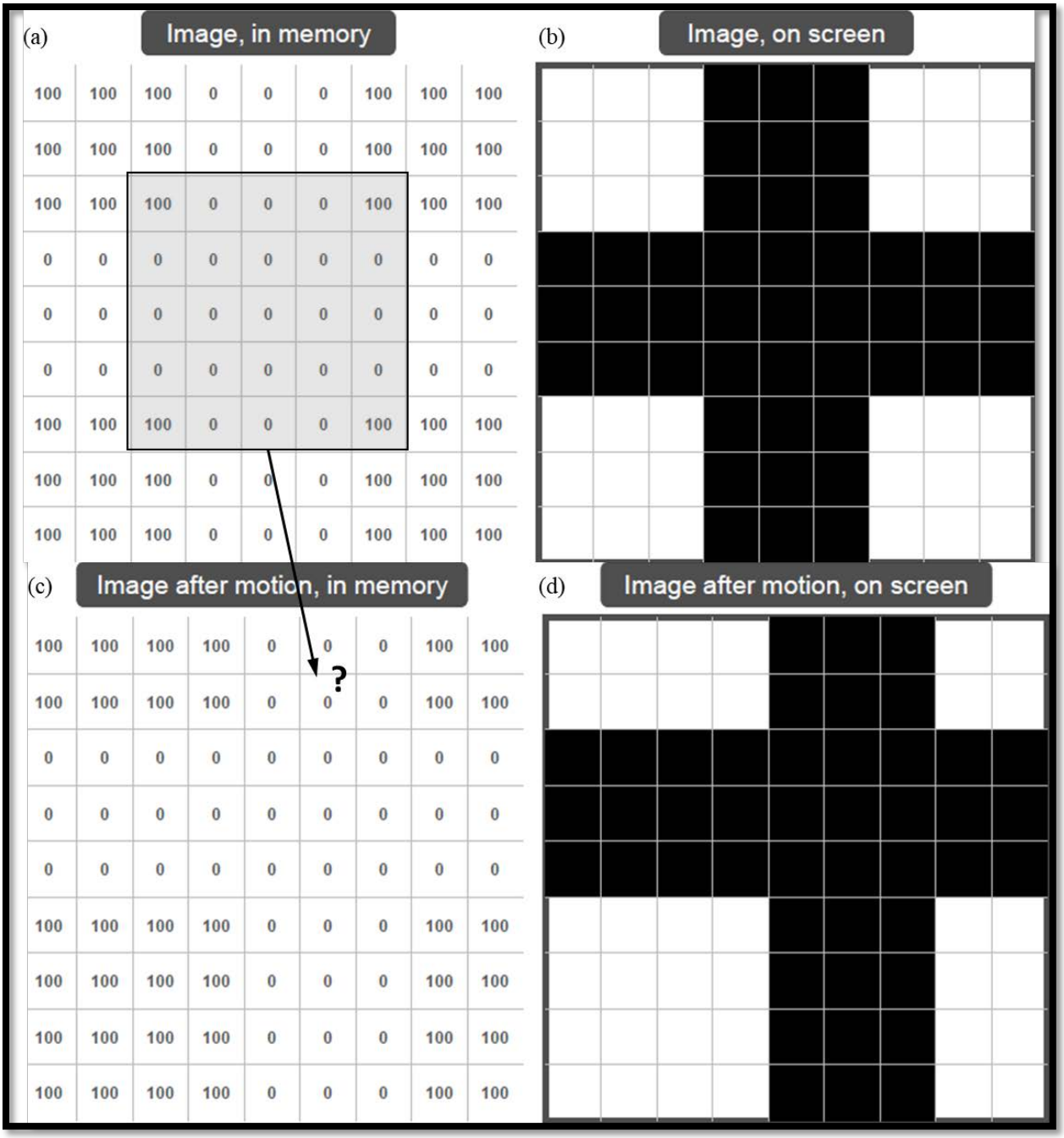

Figure 4-12: Image pixel, subset, and motion basics. (a) Example black & white image part in imagery. (b) Corresponding image part shown in pixels. (c) Subsequent image part at same location in memory. (d) Subsequent image part at same location visually. Images from [208].

With the entire image broken down into subsets, a correlation function of some type is applied in order to locate the new locations of the subsets after motion and deformation. Shown below is an example correlation equation, Equation (4-3), which is a sum of squared differences

$$C(x,y,u,v) = \sum_{i,j=-n/2}^{n/2} \left(I(x+i,y+j) - I^*(x+u+i,y+v+j)\right)^2 \quad (4\text{-}3)$$

correlation function that is used where *x* & *y* are original pixel locations, *u* & *v* are corresponding horizontal and vertical displacements, *i* & *j* are horizontal and vertical indices for referencing pixels adjacent to pixel(x,y), *n* is the size of the subset and *I* and *I** correspond to the initial and subsequent images. Subsets need to contain enough pixels, relative to speckle size, to be reliably identified, and some rules of thumb can be found in [206]–[208]. For further detail the reader can refer to [209]. The result is after a region is identified for analysis and a series of images are analyzed, a set of displacement data results is generated along with a local error measure that was globally minimized in the correlation.

Two additional settings that can be applied in the analysis are the step size and strain window or filter size. The step size relates to the pixel spacing (one value in horizontal and vertical directions) that is used for generating approximation functions used in the correlation. The strain window or filter size relates to how far in each direction the approximation function is smoothed. Increasing the step size and strain window size can increase the smoothness of the result. In this study, the subset size, step size, filter window, and whether a single reference image vs. a moving reference image (*I* in Equation (4-3)) is used will be listed for all results.

4.5.2 Macro-Level Results

The control and weld specimens were tested as indicated above. The control specimens were tested first, followed by the weld specimens. The control specimens both generated failures

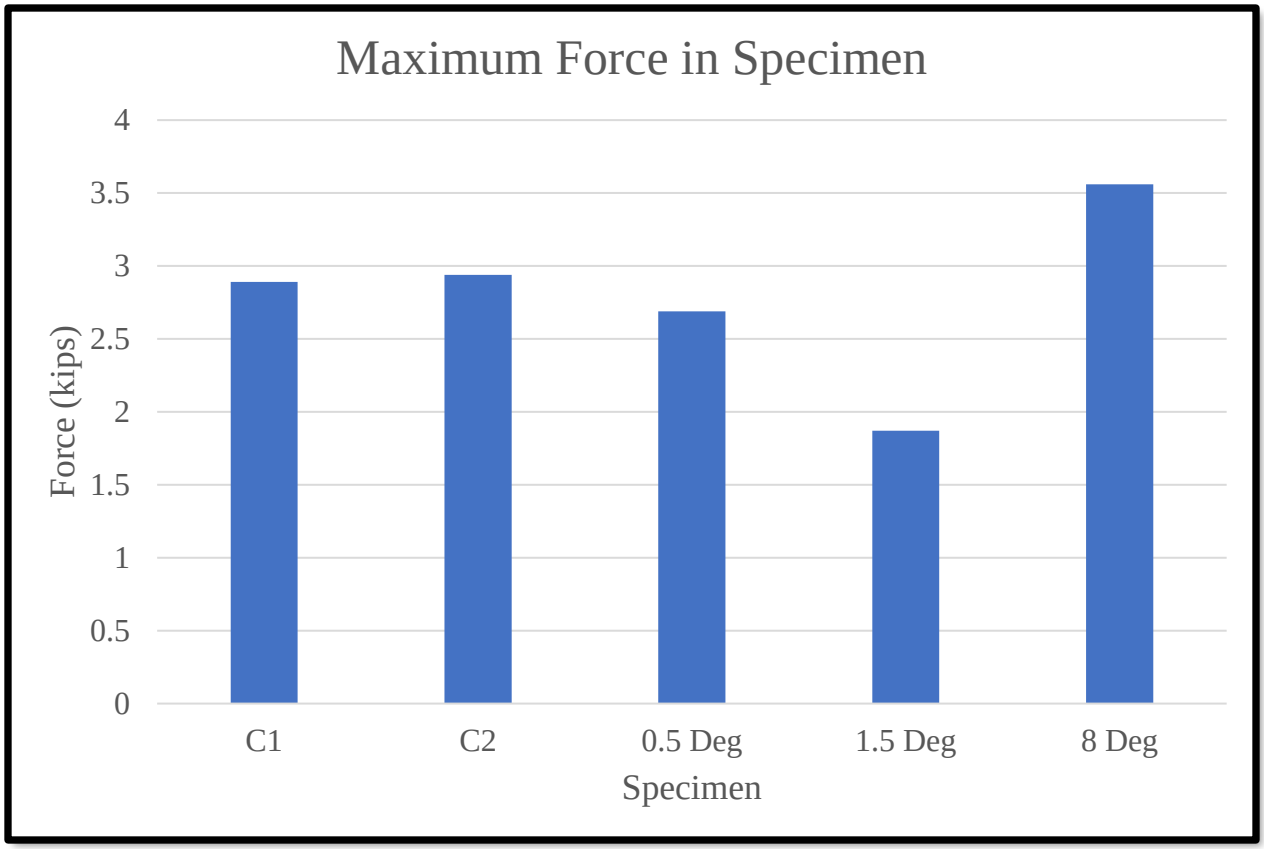

Figure 4-13: Maximum forces in specimens. (2.5° scenario had no testable specimens)

Table 4-2: Average Stress Results

	C1[39]	C2	0.5°	1.5°	8°
Max Force (kips)	2.89	2.94	2.69	1.87	3.56
Normalized Result (% of Control Avg.)	Avg. Force = 2.92 kip		92.3%	64.1%	122%
Rotation of Weld Plane at Max Load	X[40]	15.1°	2.32°	0.30°	1.57°
Average Shear Stress (ksi)	7.45	7.58	7.18	4.99	9.49
Average Normal Stress (ksi)	2.01	2.04	0.29	0.03	0.26
Average von Mises Stress	8.22	8.37	7.2	4.99	9.5
Normalized Result (% of Control Avg.)	Avg. VM Stress 8.29 ksi		86.8%	60.2%	115%

[39] For the first control specimen, a math error resulted in a loading rate that was too slow. Image data ended roughly 55% of the way through the test because its duration was so long. Stresses calculated using the C2 rotation.

[40] By the test ended at 82% or the time required to reach the maximum loading, at which point 11.5° of rotation had occurred in the plane corresponding to welding.

in the reduced section after showing signs of significant deformation along the plane that would correspond to the faying surface in the weld samples. This was consistent with the modeling and analysis conducted. Only the 8° achieved a result similar to the controls, with the 1.5° and 0.5° failing along the weld boundary. Both the 0.5° and 1.5° specimens exhibited behavior indicating internal brittle or cracking behavior associated with a part of their load displacement curves as shown in Figure 4-14 & Figure 4-15 above and below. However, as shown above in Figure 4-13 and Table 4-2, the 1.5° and 0.5° specimens still carried substantial loads. While the control specimen C2, did not get image data up to the max load, it was clear that both control specimens

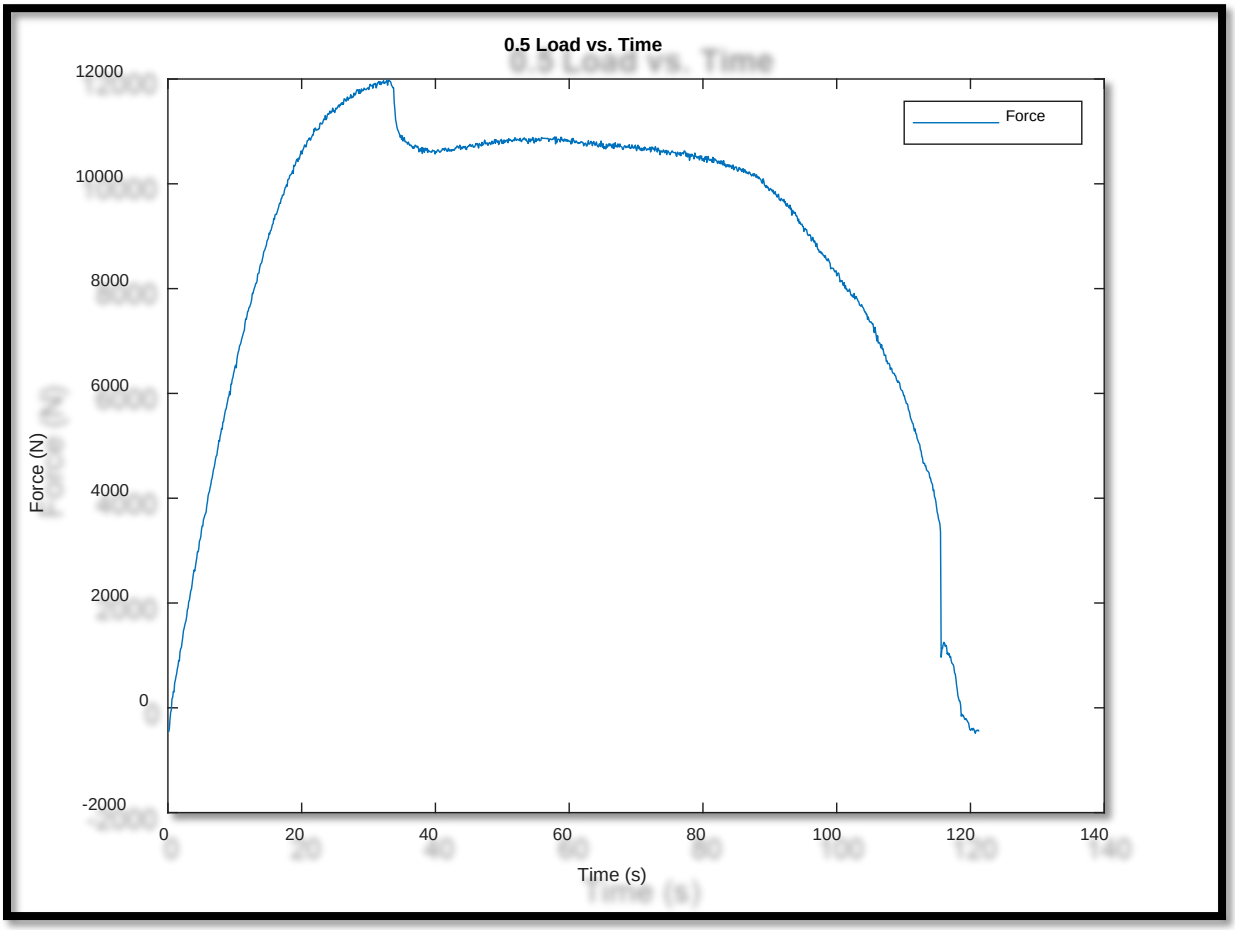

Figure 4-14: 0.5° load versus time plot exhibiting signs of some sort of brittle loss of capacity at around 35 seconds of loading, but with otherwise ductile behavior. Displacement rate at 1 mm/min

reached much larger rotations at their maximum loading. All tested samples achieved over 60% of the reference control values in both absolute load and average von Mises stress.

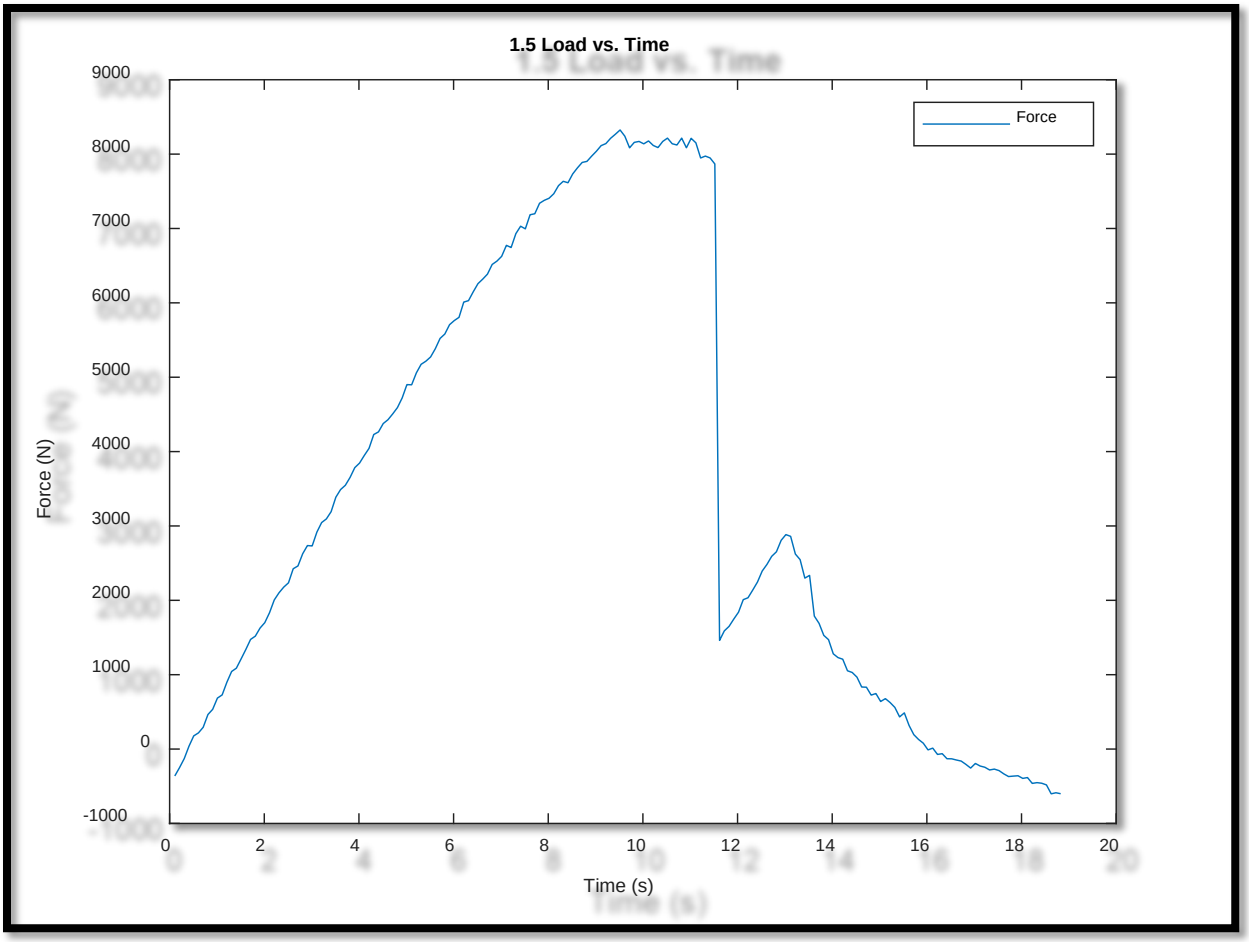

Figure 4-15: 1.5° load versus time plot exhibiting a sharp drop in capacity at just under 12 seconds.

4.5.3 Digital Image Correlation Results

4.5.3.1 Digital Image Correlation Software Specific Settings

VIC-2D offers many capabilities. Full displacement fields are found for the regions of interest, based upon the chosen analysis specifications. Here they will be used to identify the regions of yielding, based upon a two dimensional von Mises based yielding strain. Figure 4-16 below, shows how the region to be tracked is selected by the user, identifying the region with the speckle pattern. Figure 4-17 shows how the subsets overlay onto the region selected, as well as

the selection of the step size. Within the analysis windows consistency, confidence, and matchability parameters, as well as the filter size are selected. Lastly, the choice of whether to use a single reference image or incremental references is made, and the type of strain to be calculated is selected. In this analysis, Lagrangian strains were generated.

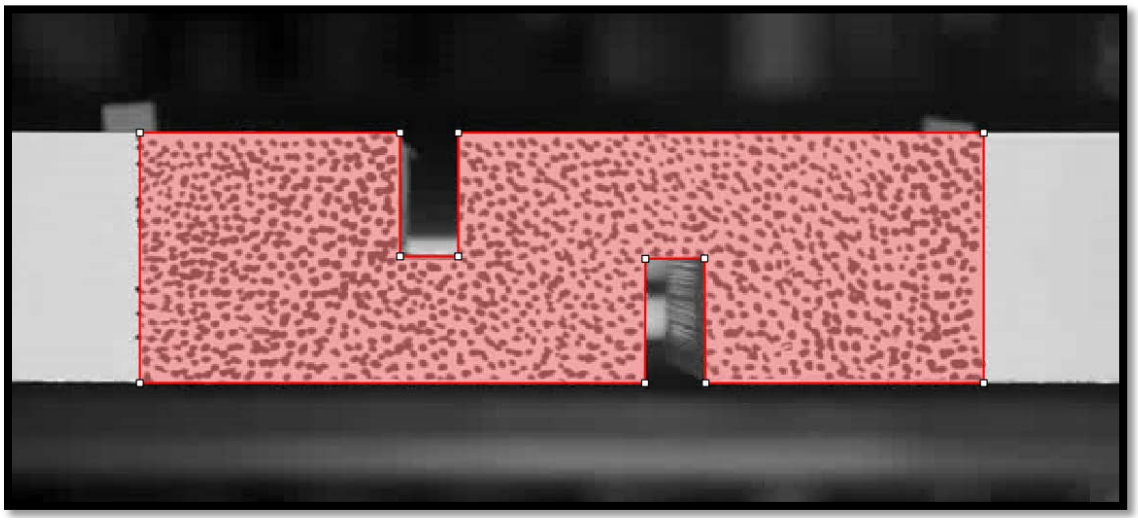

Figure 4-16: VIC-2D region of interest selection identifies the region to track.

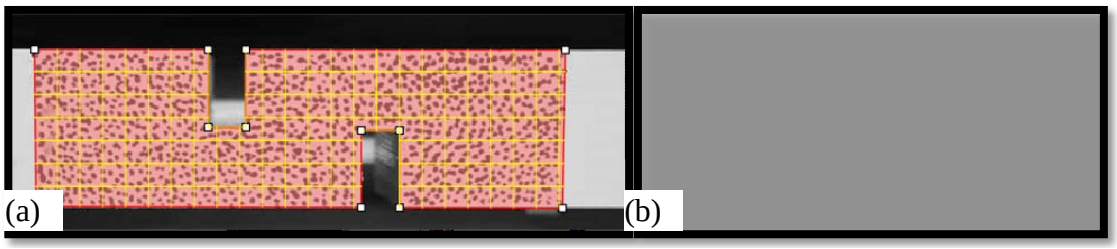

Figure 4-17: Subset and step selection shown in an example. (a) Overlay of subsets selected in (b).

In generating the Lagrangian strains, an added selection allows the calculation of principle strains, the angle from horizontal to the first principle strain, and also a von Mises strain. This last term will be used to present the state of strain at the maximum loading for the samples. Equation (4-4) below, shows the equation used to evaluate the von Mises strain, ε_{vm}. In this formulation, ε_1 and ε_2 are the principle strains from a standard 3D eigenvalue analysis of the

$$\varepsilon_{vm} = \sqrt{{\varepsilon_1}^2 - \varepsilon_1\varepsilon_2 + {\varepsilon_2}^2} = \sqrt{3J_2^{\varepsilon\prime}} \quad (4\text{-}4)$$

strain tensor, where the out of plane component is assumed to be zero. This is done since VIC-2D has no measure of that value, as what it does have is only a surface measurement. As shown in the latter part of the equation, this is equal to the $\sqrt{3}$ times $\sqrt{J_2^{\varepsilon\prime}}$, where $J_2^{\varepsilon\prime}$ is the second invariant of the deviatoric strains. This strain measure, different from some other strains such as the effective strain, is of direct use when attempting to calculate the von Mises stress up to the point of yielding. Just as it can be shown that $\sigma_{vm} \equiv \sqrt{3J_2} = \sigma_Y$ is the initial yield criteria, (where J_2 is the second invariant of the deviatoric stresses and σ_Y is the uniaxial yield stress), that relation can be expanded to relate to the yield criteria to von Mises strain in the elastic range using the definition of J_2 and the relation between deviatoric stress and strain. This results in Equation (4-5), for direct comparison to the uniaxial yield stress criteria, σ_Y. Equation (4-5) will

$$\sigma_{vm} = 2\mu\, \varepsilon_{vm} \quad (4\text{-}5)$$

be applied using the limiting value of σ_Y.= 8,000 psi and μ = 3770 ksi for Al 6061-O. This results in the identification of the limiting von Mises strain before the material has yielded. This value is ε_{vm} =1.06x10^{-3}.

4.5.3.2 Digital Image Correlation Data

The view in Figure 4-18 highlights the rotation of the control specimen under load. In that figure, the test time is 216 seconds. At the loading in Figure 4-19, test time of 345 sec, the control specimen 2 still exhibited greater than 50% of its max capacity and was at a greater loading than the overall ultimate load for the specimen. Next, the net section failed with prying in the notches. The specimen achieved substantial amount of yielding along the analogous weld plane prior to achieving maximum resistance as shown in Figure 4-20. The specimen achieved significant additional strains along the analogous weld plane, greater than 100% of the yield

strain, as shown in Figure 4-21. However, strains were concentrated near the notches, consistent with the hinging that was occurring, and eventually led to notch failure.

In Figure 4-22, the 0.5° specimen shows some delamination in certain locations at maximum load, but these cracks did not propagate out of control. A substantial strain concentration appears along the weld surface and hinging appears to a degree in the right notch, related to the crack. Figure 4-23 shows the specimen at its last significant loading. At this state, it still held >85% of its maximum capacity. Based on modeling, after gripping there was pressure along the weld plane, and when it failed it still maintained contact on that surface.

In Figure 4-26, the 1.5° specimen is shown after max loading, and immediately before failure. Despite the noise, an accumulation of strain appears in the left part of the weld surface. As can be seen in Figure 4-15, the 1.5° test exhibited a brittle loss of capacity at around 11 s of loading. This captured in subsequent images in Figure 4-26 and Figure 4-27. Upon full failure, the specimens separated indicating a tensile stress component. As seen in the load curve, there was some ductility prior to failure, and roughly 4-5 times the yield strain was achieved as shown in Figure 4-28. However, the loss of capacity and spike in strains within the 1 sec event was significant.

Figure 4-29 shows the 8° test at 135 seconds of loading; the time of maximum loading. Hinging is apparent based on the concentration of strains near the left notch especially. At the loading in Figure 4-30, the 8° specimen retained >50% of its maximum resistance, which equates to a rough average stress just above yield stress for the base metal (ignoring normal components). Figure 4-31, corresponding to Figure 4-29, shows the maximum load occurred at greater than 5 times the von Mises strain required for yielding along the entire length of the surface. Significant strains, on the order of four times the yield strain occurred in the left notch

due to gripping. In Figure 4-32, the concentration of strains and eventual cracking in the left notch and portion of weld is apparent, relieving significant further strains along the center of the weld.

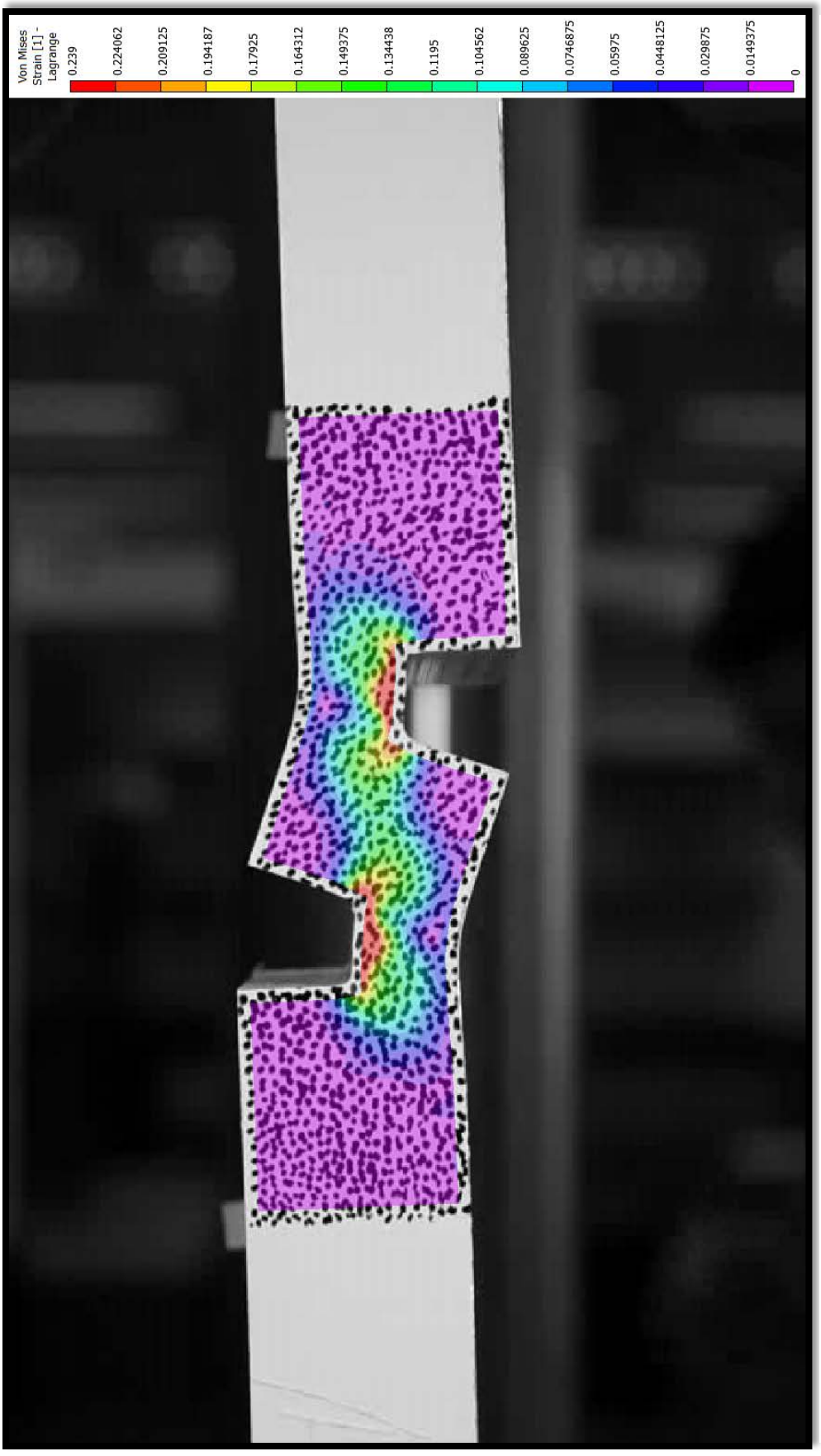

Figure 4-18: Control 2 specimen at maximum load, showing the von Mises strain. Incremental reference, Subset: 17, Step: 1, Filter: 15.

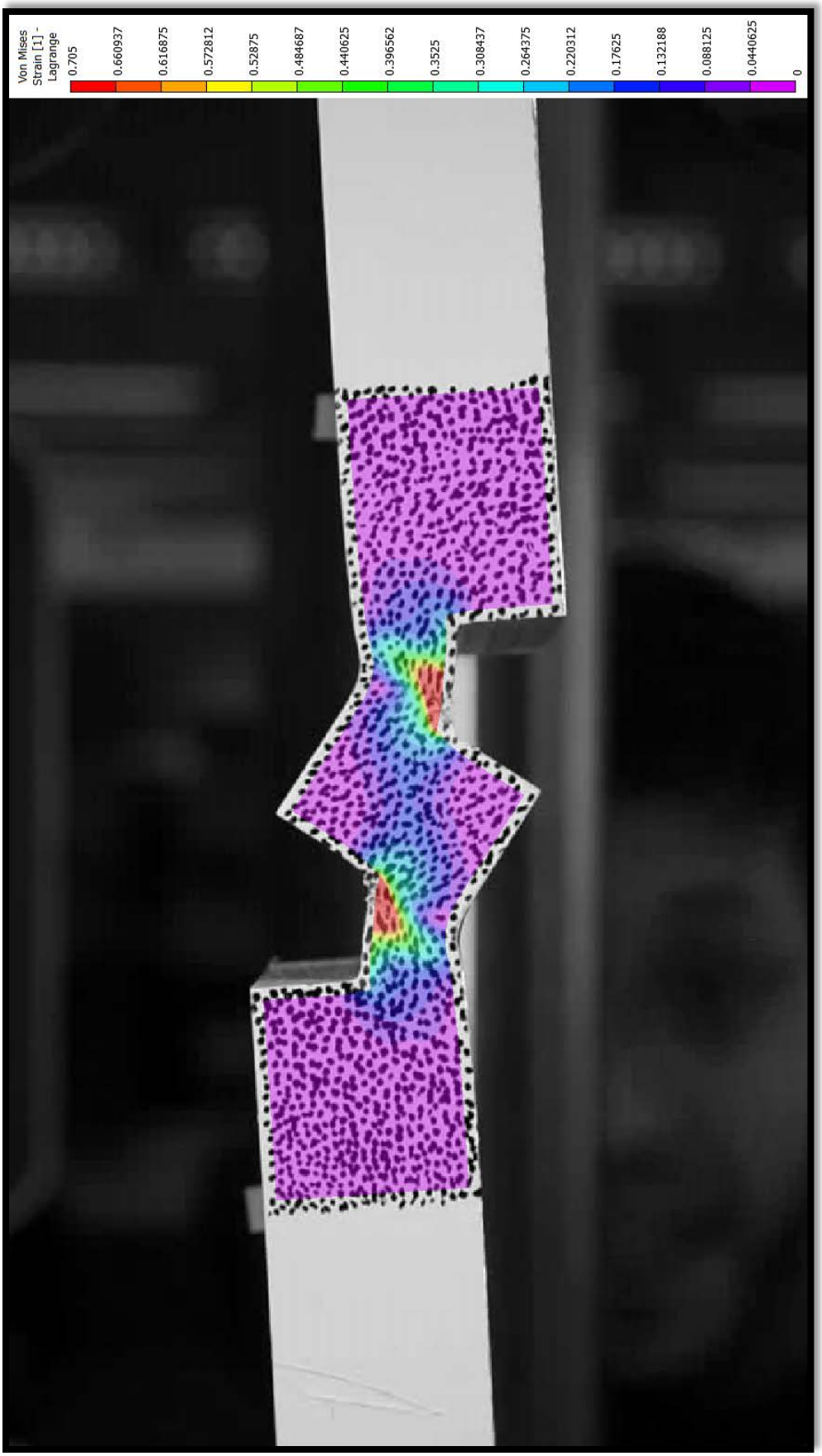

Figure 4-19: Control specimen 2 at last significant capacity.

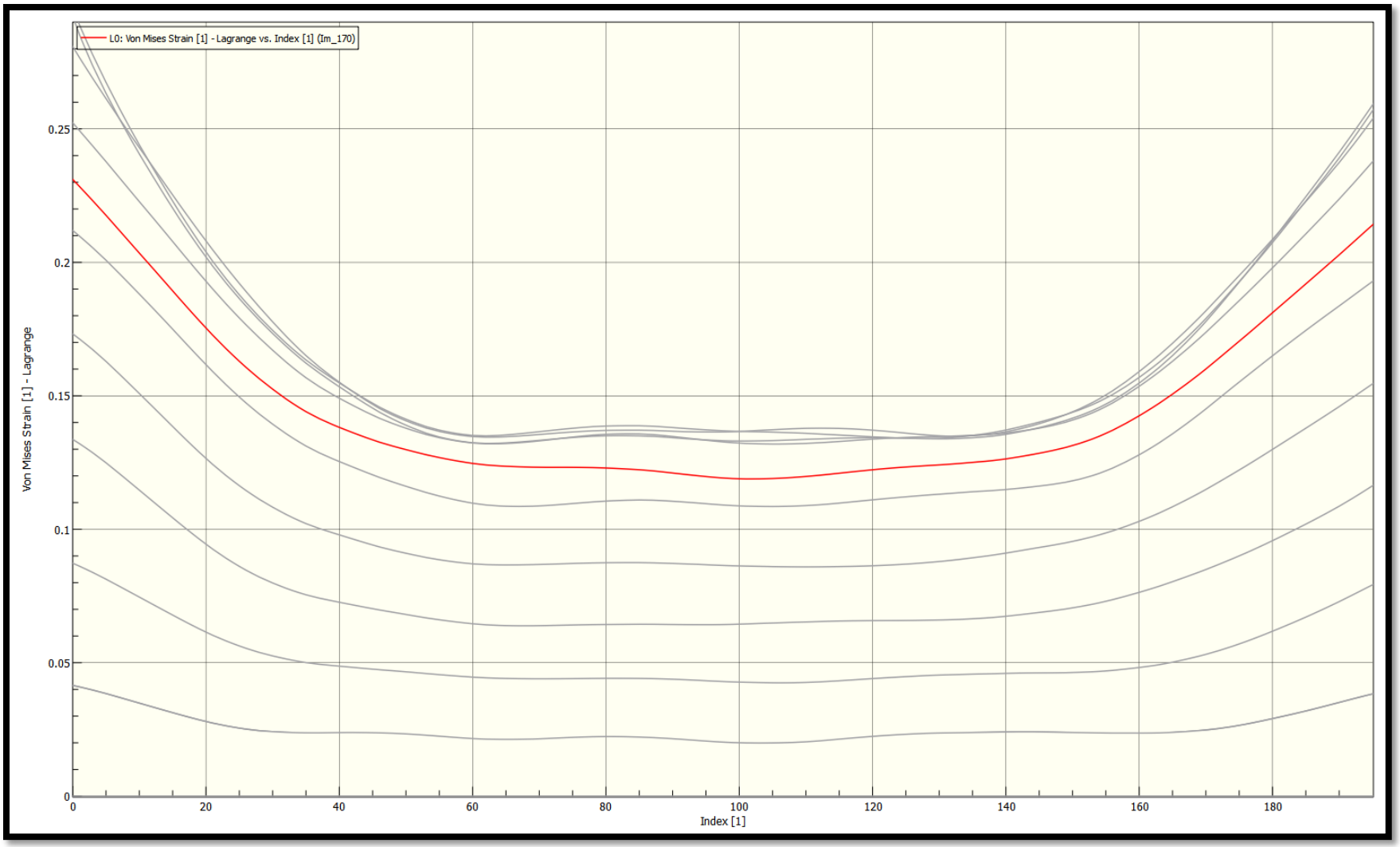

Figure 4-20: Control 2 von Mises strain profile at maximum loading in red. Other time profiles in grey, starting at 26 sec, after some yielding. Profiles are plotted versus an index of their relative position along the bonding surface (1-200).

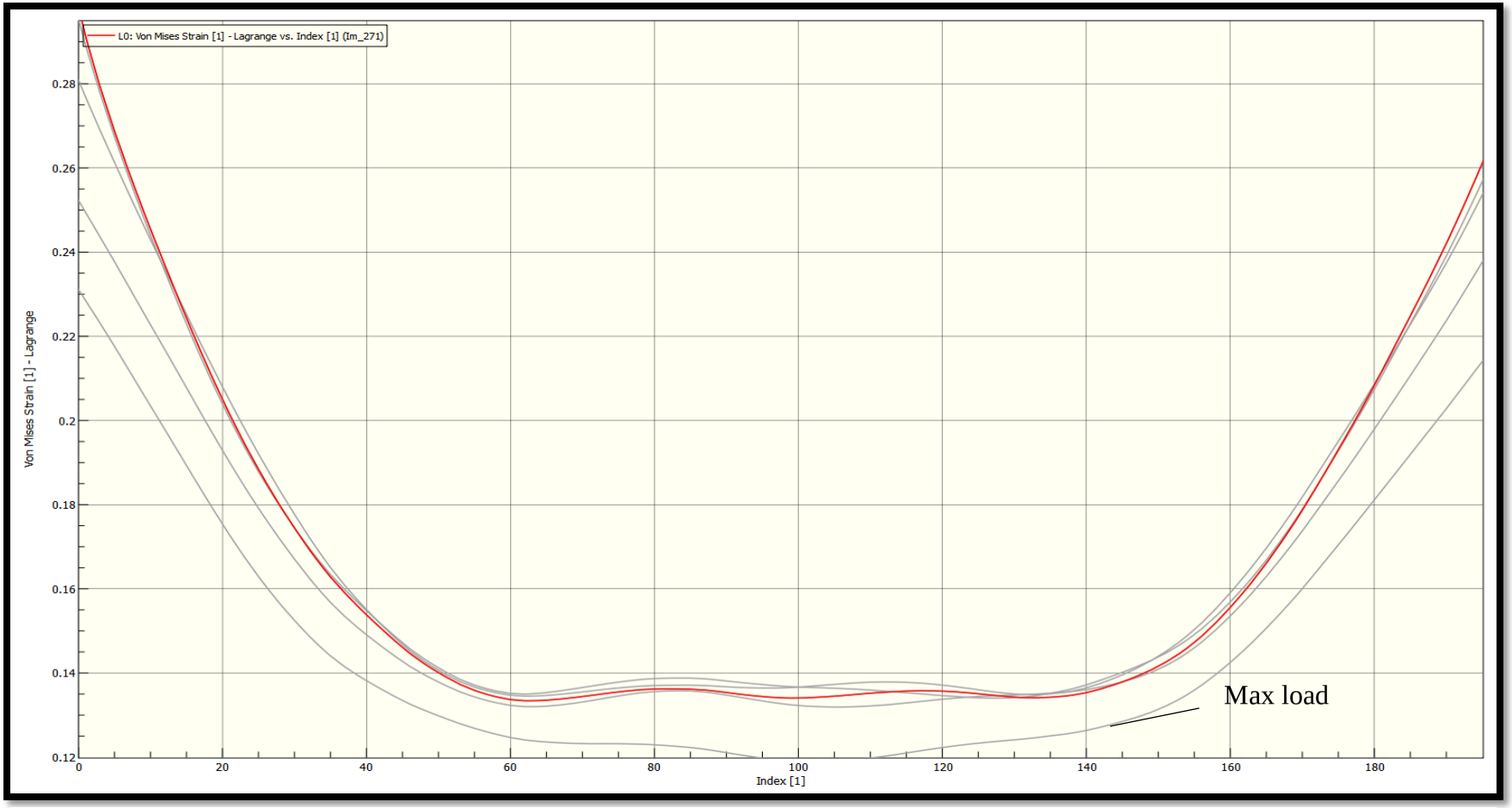

Figure 4-21: Control 2 showing von Mises strains after max load and up to last significant capacity (line in red). Max load line is annotated. Profiles are plotted versus an index of their relative position along the bonding surface (1-200).

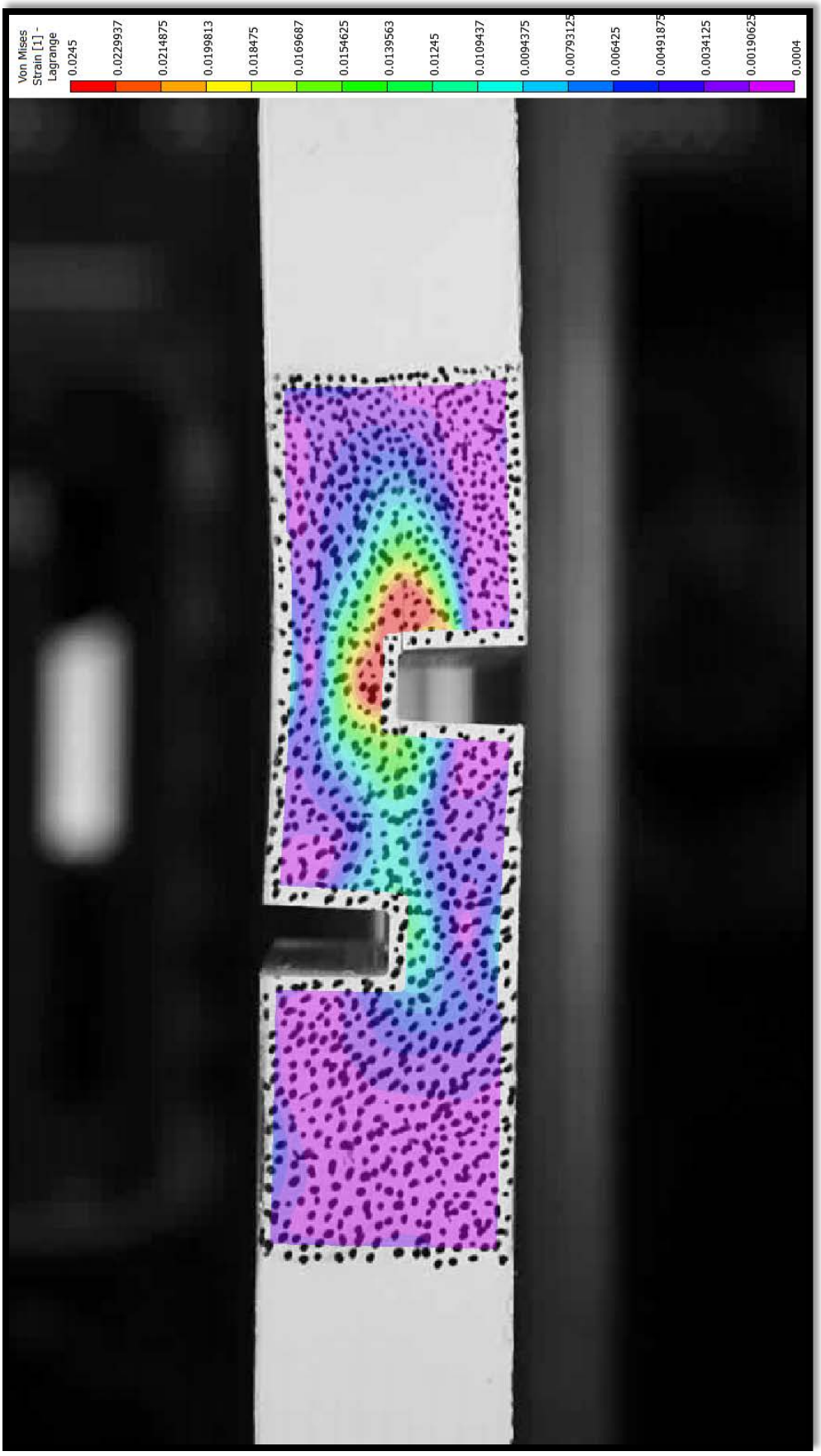

Figure 4-22: 0.5° specimen von Mises strains at max load. Test time is 33 seconds. Incremental reference, Subset: 21, Step: 3, Filter: 25.

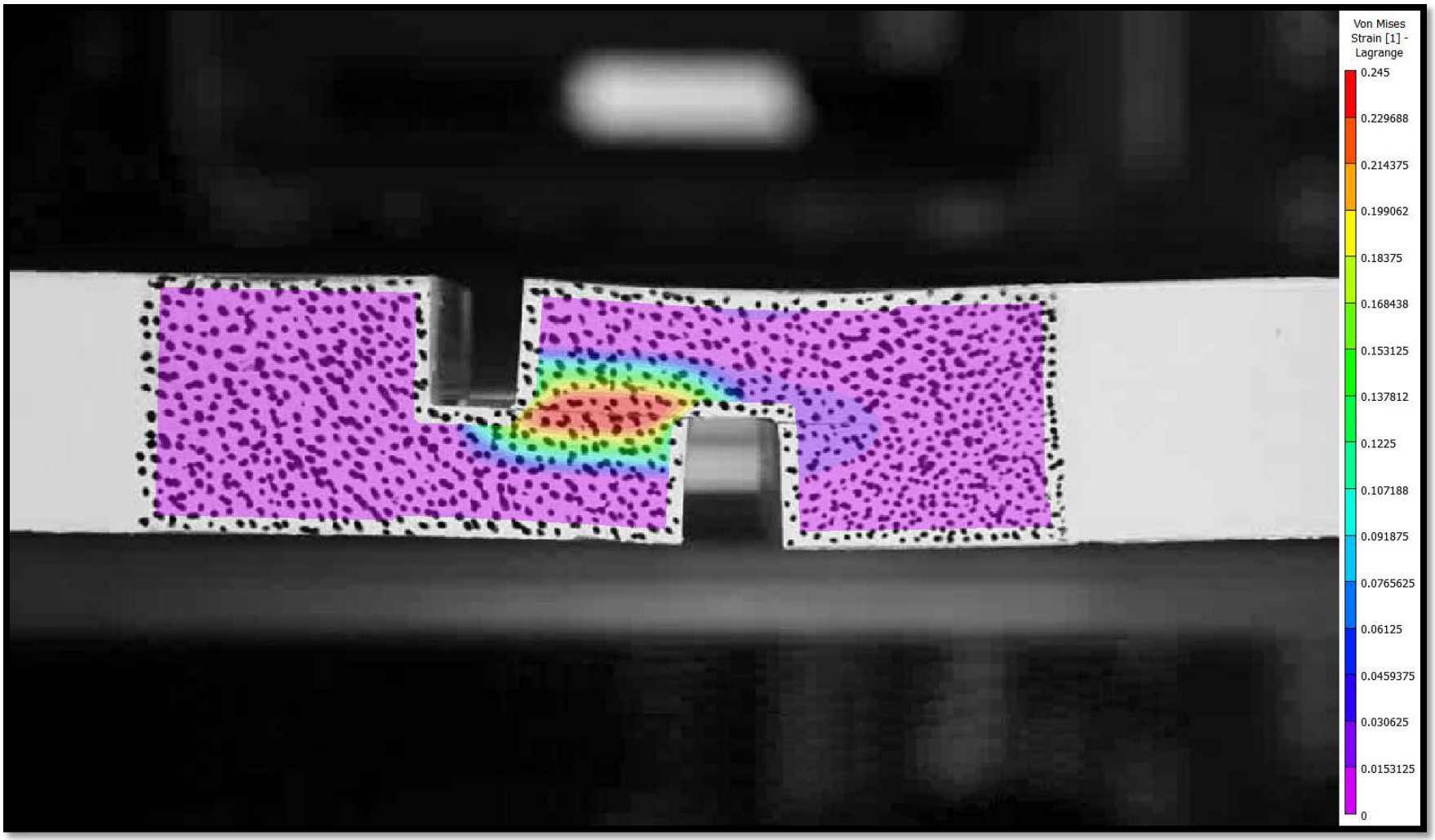

Figure 4-23: 0.5° von Mises strain at last significant loading at t = 87 sec. Slight hinging from the crack at right. Significant straining on the weld.

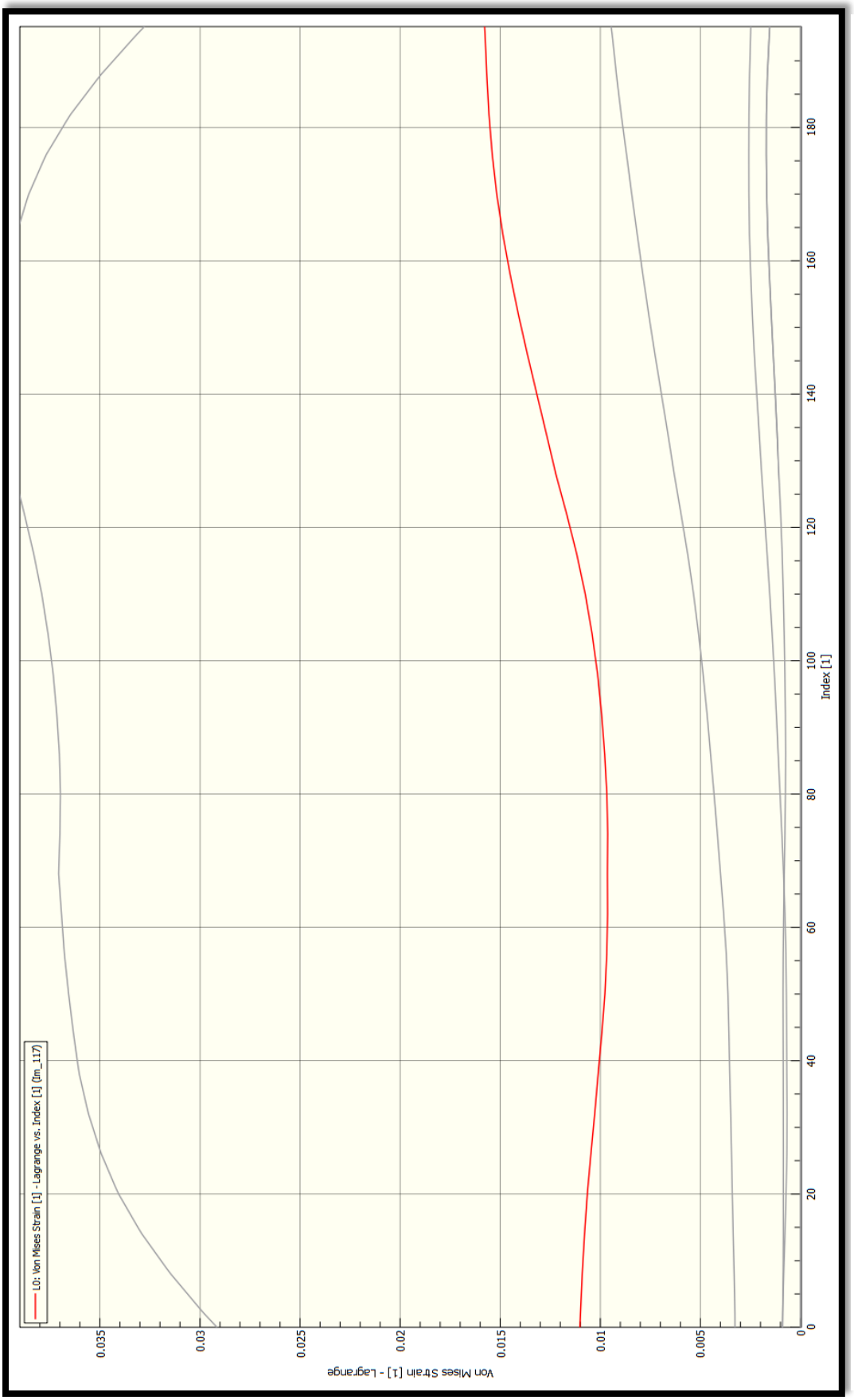

Figure 4-24: 0.5° weld surface von Mises strains at maximum loading in red. The lowest nonzero plot is during gripping, showing yielding. Profiles are plotted versus an index of their relative position along the bonding surface (1-200).

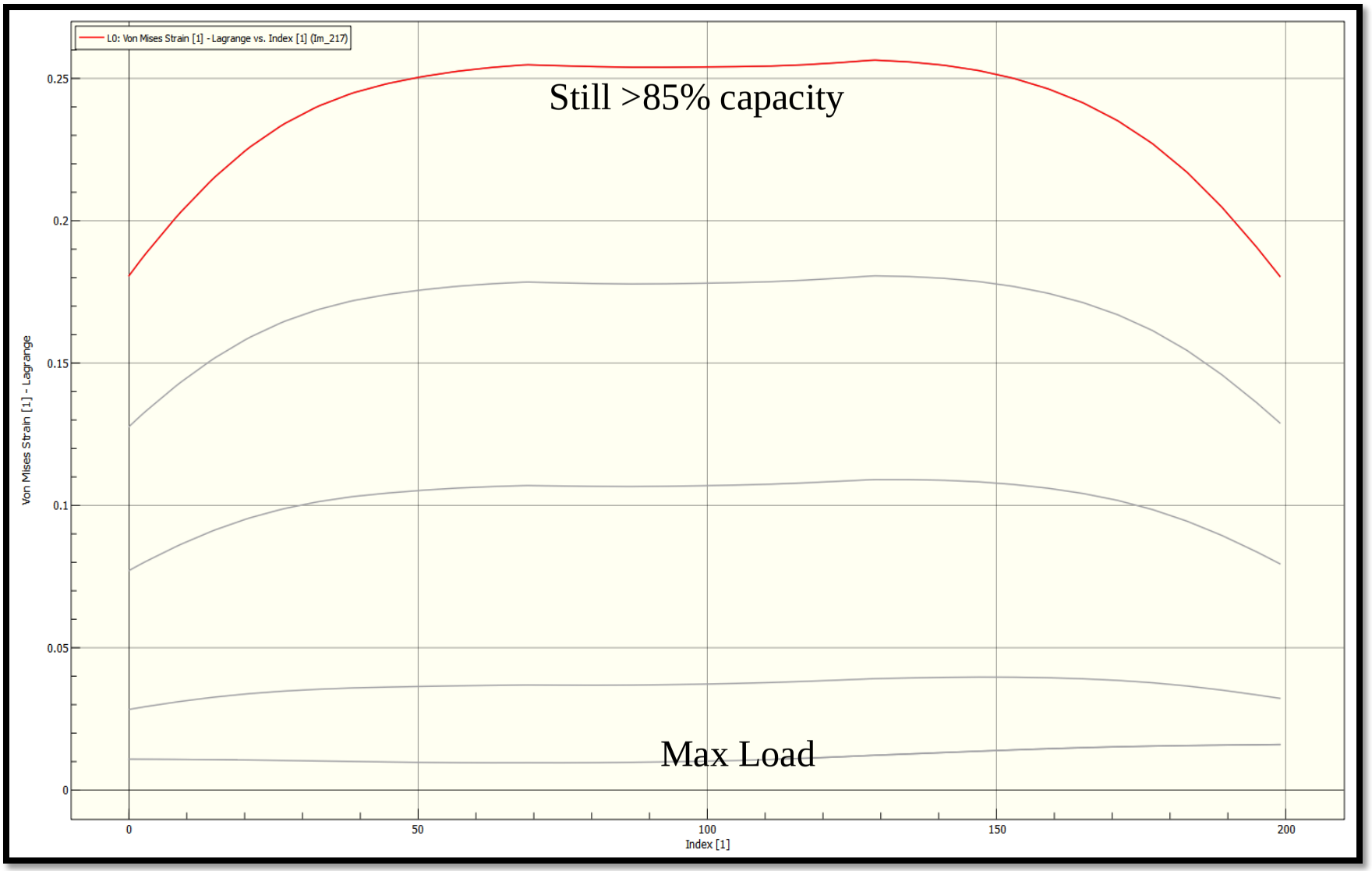

Figure 4-25: 0.5° von Mises strains at the weld surface at last significant loading. A substantial degree of straining occurred; ≈ 200% of ε_y. Profiles are plotted versus an index of their relative position along the bonding surface (1-200).

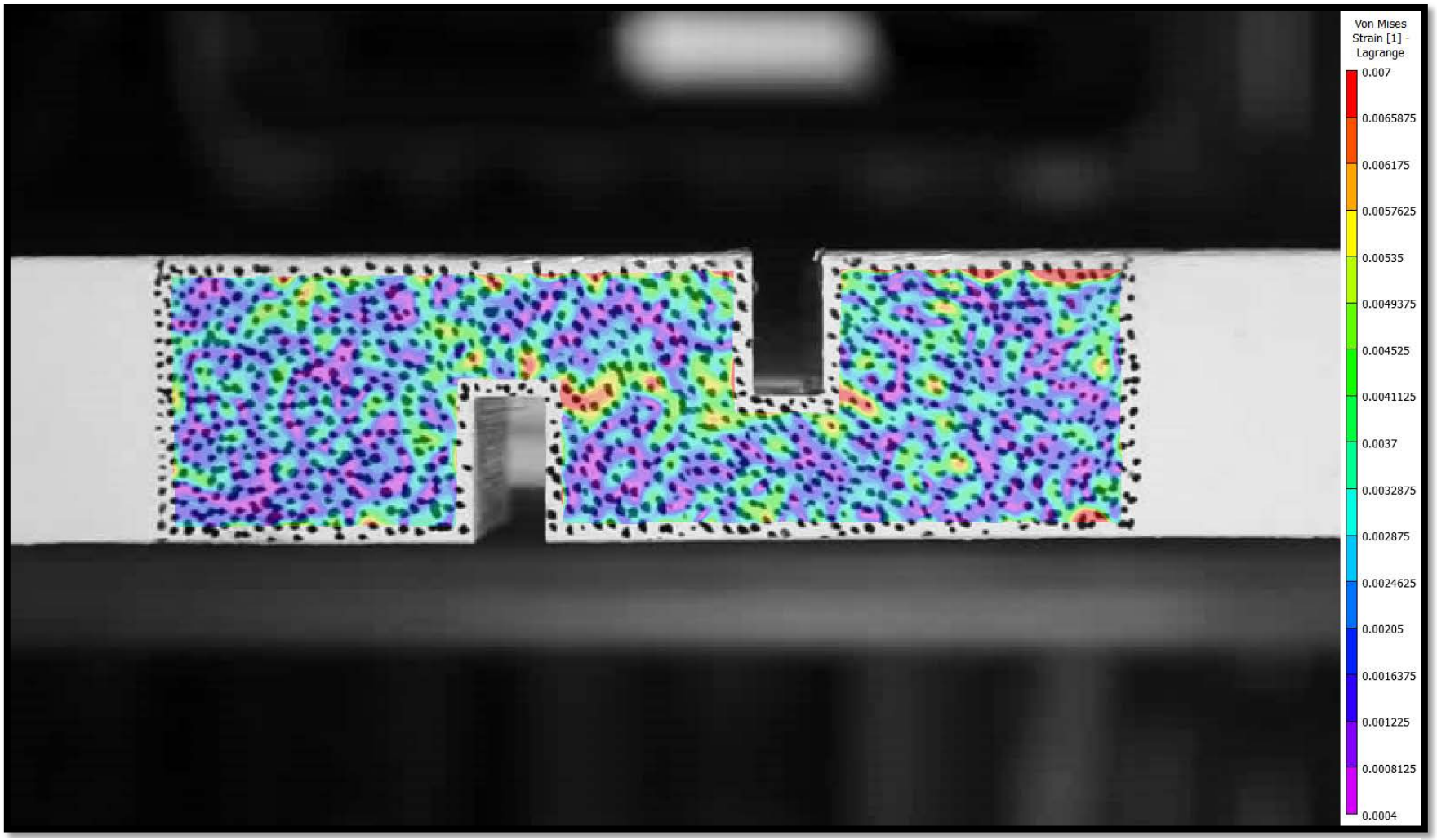

Figure 4-26: 1.5° von Mises strain before loss of capacity; t = 305 s since gripping; 11 s of loading. Initial reference, Subset: 21, Step: 1, Filter: 25.

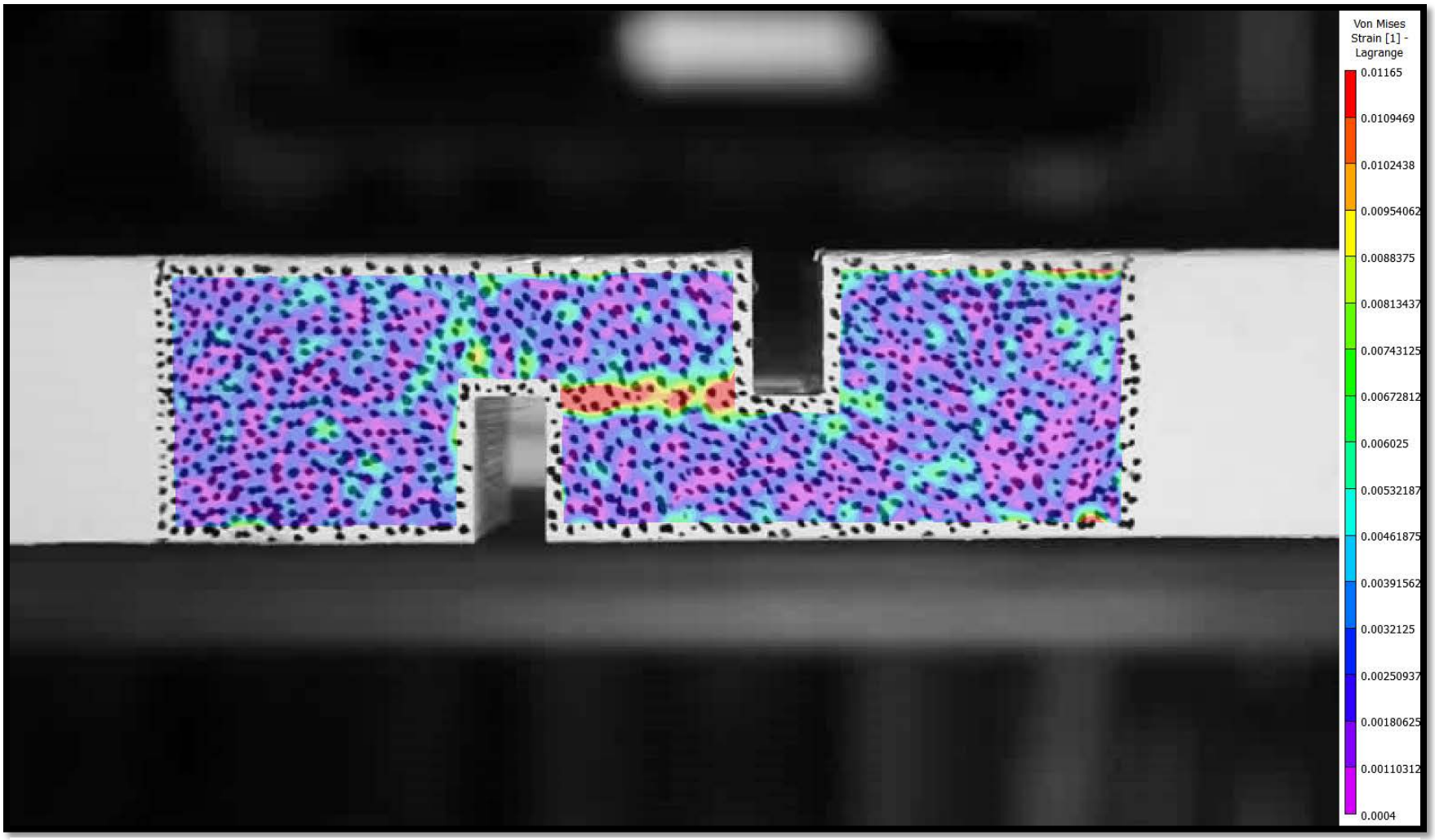

Figure 4-27: 1.5° test von Mises strains after capacity loss. Within one second of Figure 4-27, a roughly 300% increase in strain on the weld.

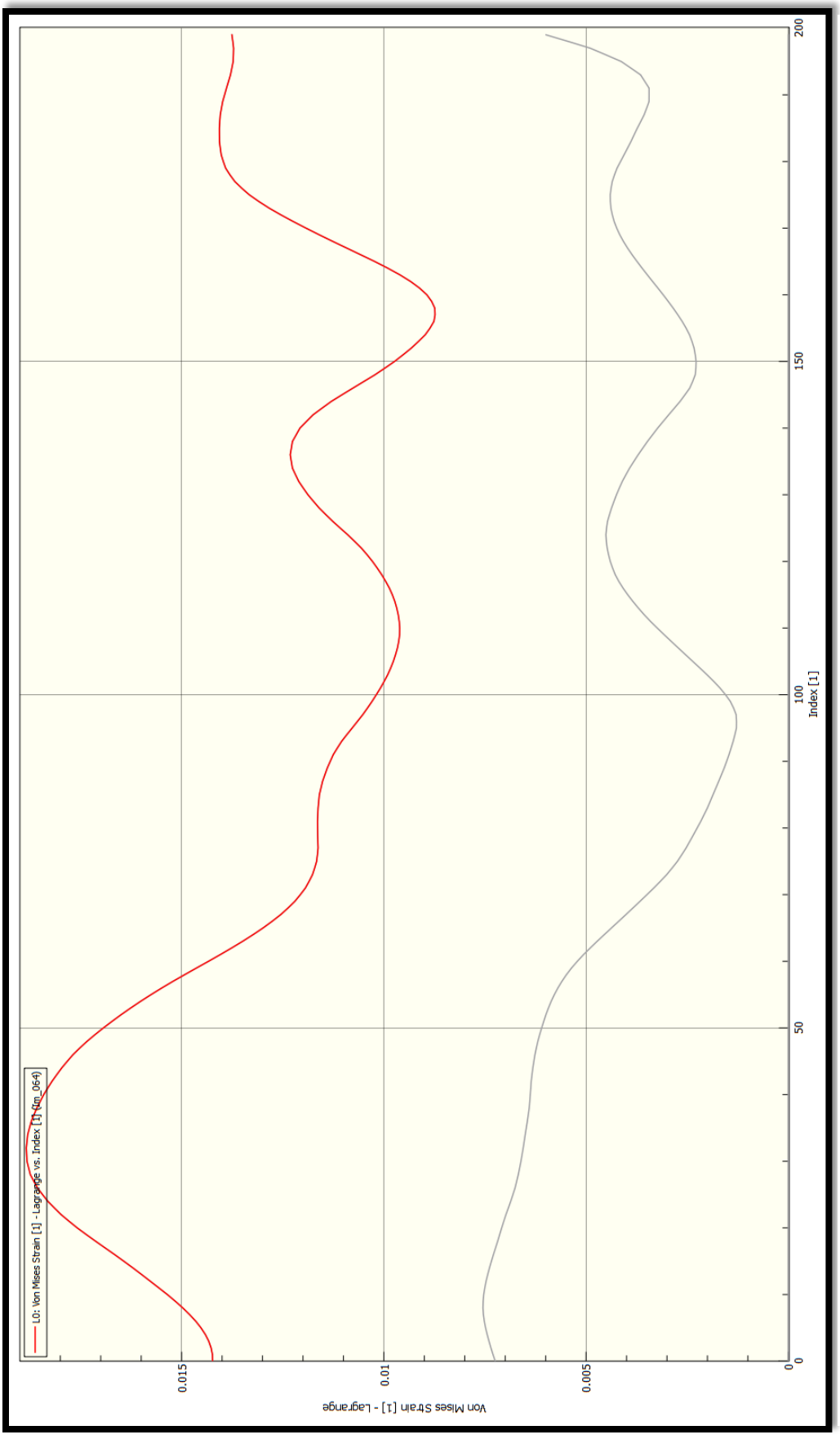

Figure 4-28: 1.5° test weld surface strains before and after failing. Grey line is von Mises strain before, while red is after failing. Profiles are plotted versus an index of their relative position along the bonding surface (1-200).

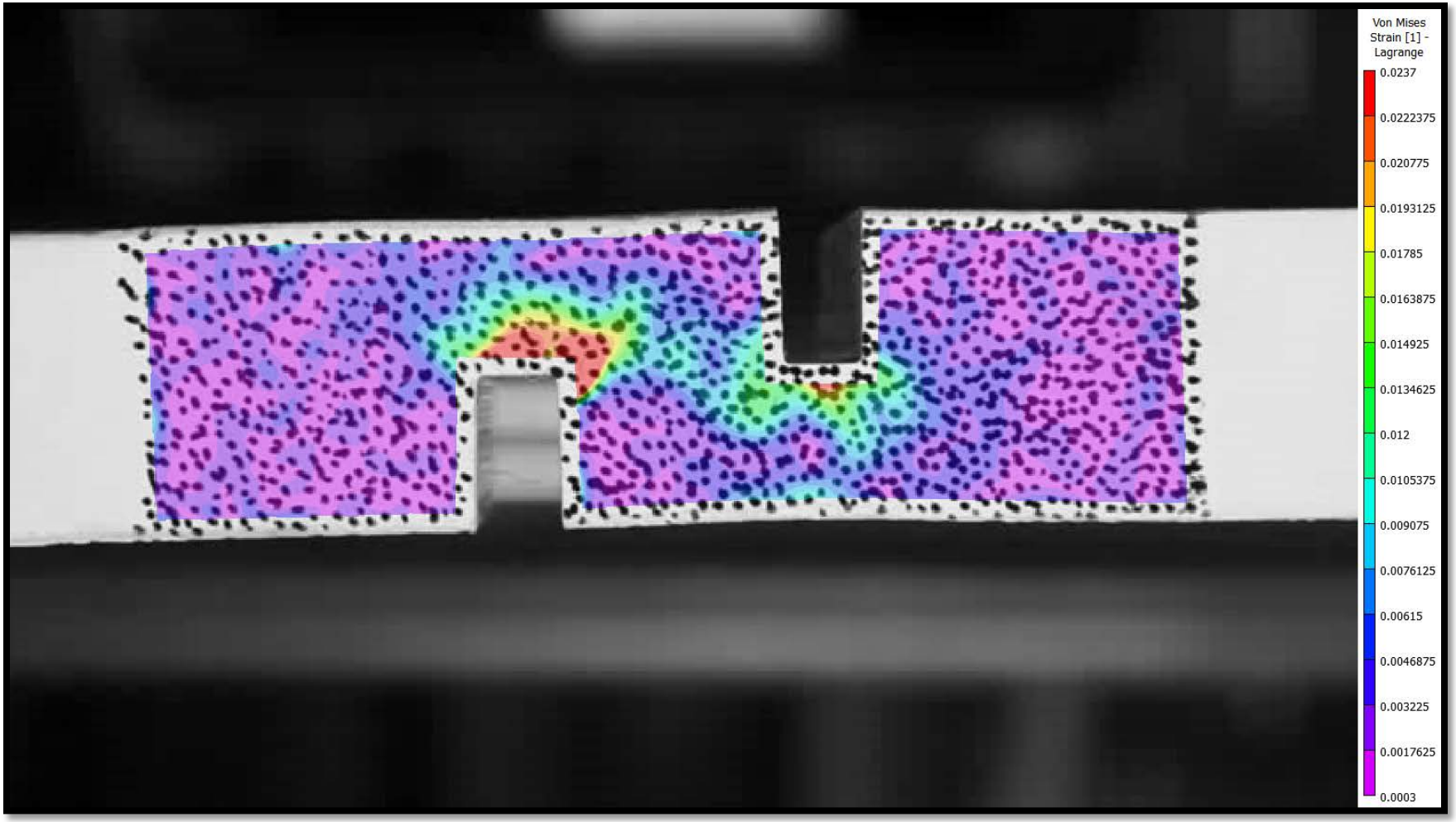

Figure 4-29: 8° test showing von Mises strains at maximum loading. Time = 135 s of loading. Initial reference, Subset: 21, Step: 1, Filter: 25

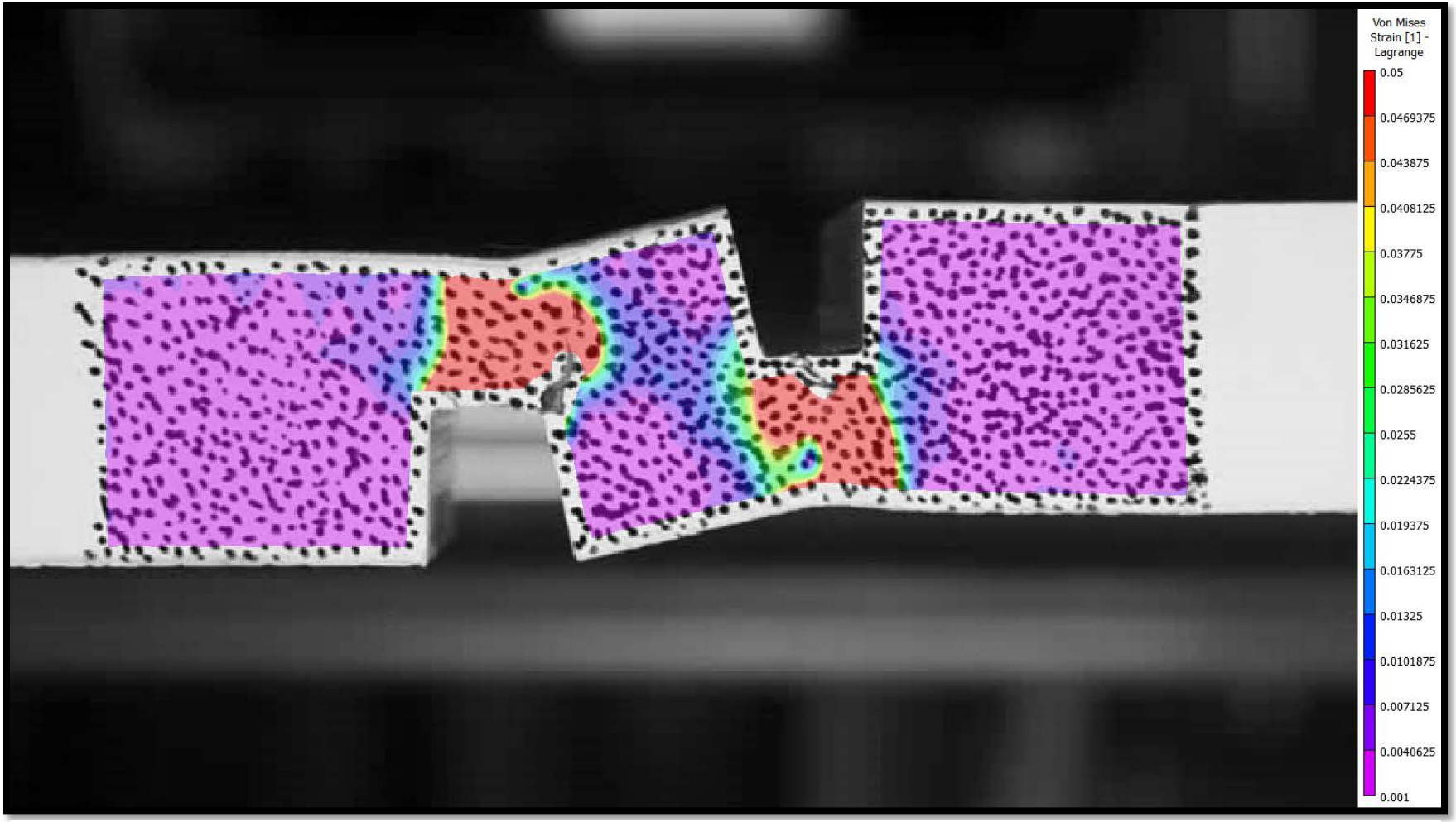

Figure 4-30: 8° test at point of last significant resistance. Despite large cracks, still sustaining 50% of its max resistance. T = 384 s of loading.

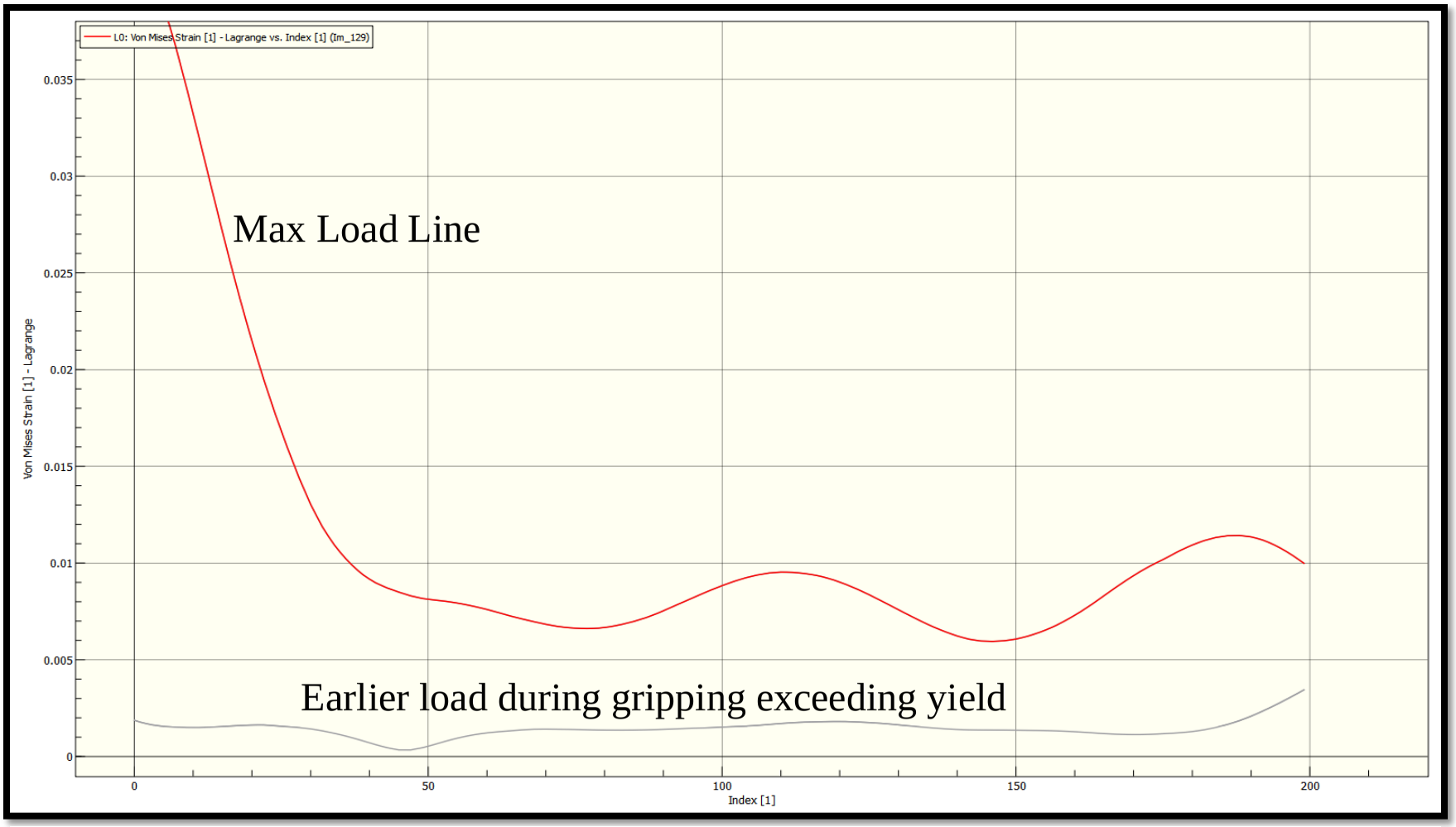

Figure 4-31: 8° test von Mises strains along the weld surface, at max loading in red at t = 135 sec of loading. Strains from partial gripping already generating strains greater than the yield strain along nearly the entire surface, 4/5 of the way through the gripping period. Profiles are plotted versus an index of their relative position along the bonding surface (1-200).

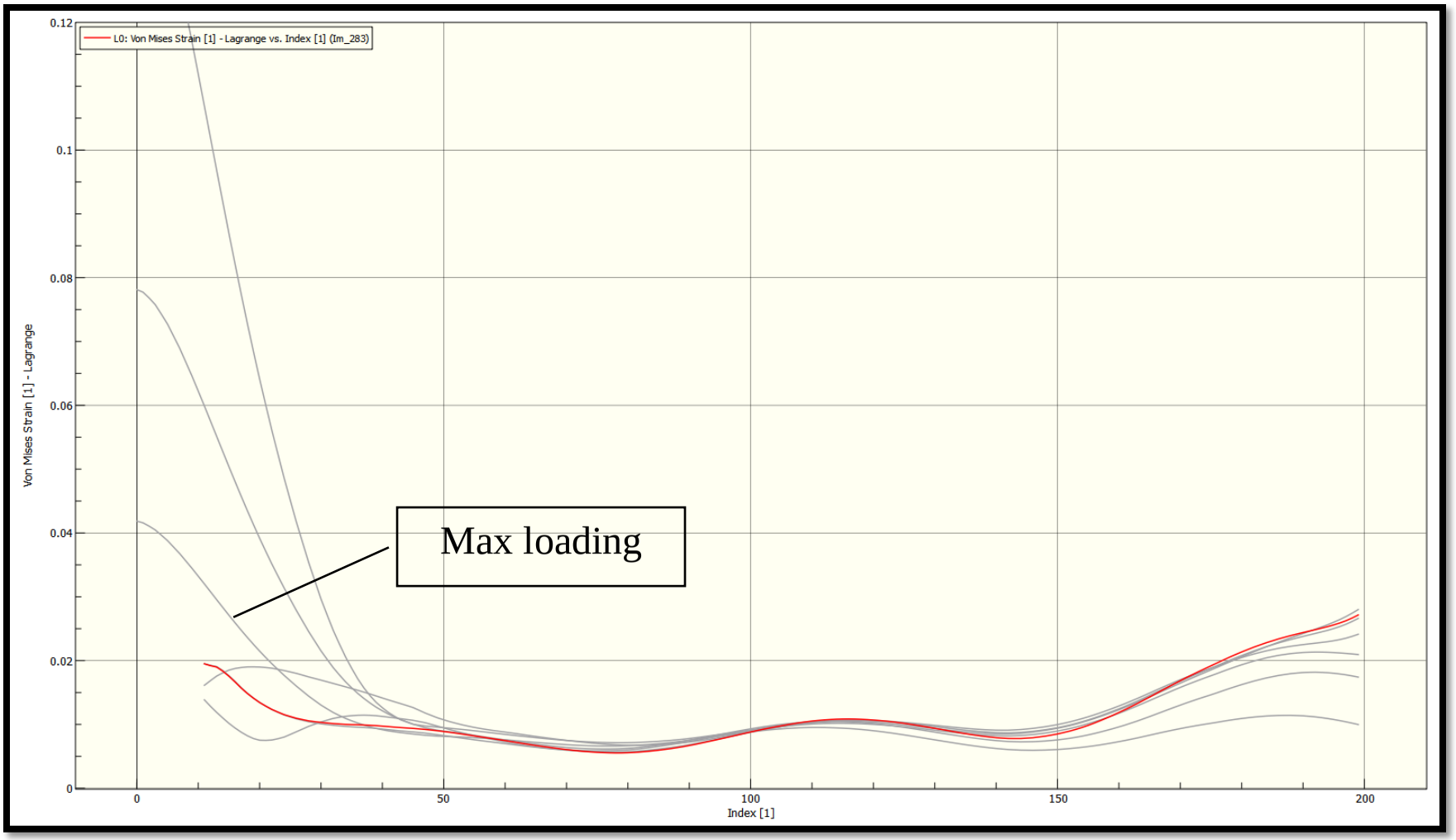

Figure 4-32: 8° test at last significant resistance. After 384 sec of loading, the effects of cracking at either end concentrates deformations. Profiles are plotted versus an index of their relative position along the bonding surface (1-200).

4.6 DISCUSSION OF TEST RESULTS

Although limited in sample size, the mechanical tests were successful in general. Clearly the 2.5° specimen, which failed to survive two attempts at fabrication cannot qualify as a good weld, but on the other end of the spectrum, the 8°specimen outperformed both of the control specimens. Somewhere in the middle there is a cutoff for what is a minimally successfully weld. As discussed above in Section 4.1 and 4.2, the definition of a successful weld partly depends on the use. The ASTM standards for clad chromium in boiler plates[159] ends up requiring roughly 20% of the capacity of the weaker metal be carried by the bond. Alternatively, the bimetallic aluminum to steel joints require roughly 80% of the capacity of aluminum, but these are in more direct structural applications in many cases. If the less restrictive comparison is used, referring to Table 4-2, the least performing weld, the 1.5°, achieved over 60% of the control capacity, and would seem to meet the criteria. Additional ductility measures could restrict the use of a similar weld, as Figure 4-15, Figure 4-26, and Figure 4-27 show the 1.5° case's brittle nature. However, it would depend on the degree of required ductility. Figure 4-28 shows von Mises strains exceeding roughly 4 times the strain required for yielding, which is potentially significant. The 1.5° weld is somewhat marginal in quality.

The 0.5° specimen has a much stronger case to be considered a good weld. Although there was some drop in capacity, as shown in Figure 4-14, it was much slighter, and then followed by a long yield plateau. Its strength capacity relative to the controls was over 85% of that of the solid base metal. It seems to clearly represent a good weld.

For the 8° sample, the discussion is not centered on whether it is good enough, but rather upon superlatives. This weld outperformed both control specimens significantly. This is likely due to work hardening introduced by the impact. In fact, all samples demonstrated that the inner

faying surfaces were likely carrying higher tensile stresses, decreasing the resulting couple under the notches, which is borne out by the rotations found in Table 4-2. Using the criteria initially envisioned when designing the tensile shear tests (i.e. will the weld transfer enough force to fail the net section), the 8° is the only one to meet the stricter standard.

5. METALLURGICAL OBSERVATIONS

In this chapter, the results of a metallurgical evaluation of the welded samples will be presented. Starting with the composition and chemistry of the samples, it will then cover macro and mesoscale observations of the weld samples, and finally microscopic evaluations will be presented.

5.1 METAL COMPOSITION AND CHEMISTRY

The material used in this study, as previously noted, was wrought 6061-O Aluminum. The material was commercially procured in the T6 state as a 0.25 in. plate, and then annealed to the O state. Although 6061-O is available straight from the manufacturer, it is not available in thicknesses desired for the conduct of this test series.

Table 5-1: Al 6061 elemental composition [210].

Material Designation	Composition (wt%) (max unless a range)							
	Si	Fe	Cu	Mn	Mg	Cr	Zn	Ti
Al 6061	0.4-0.8	0.7	0.15-0.40	0.15	0.8-1.2	0.04-0.35	0.25	0.15

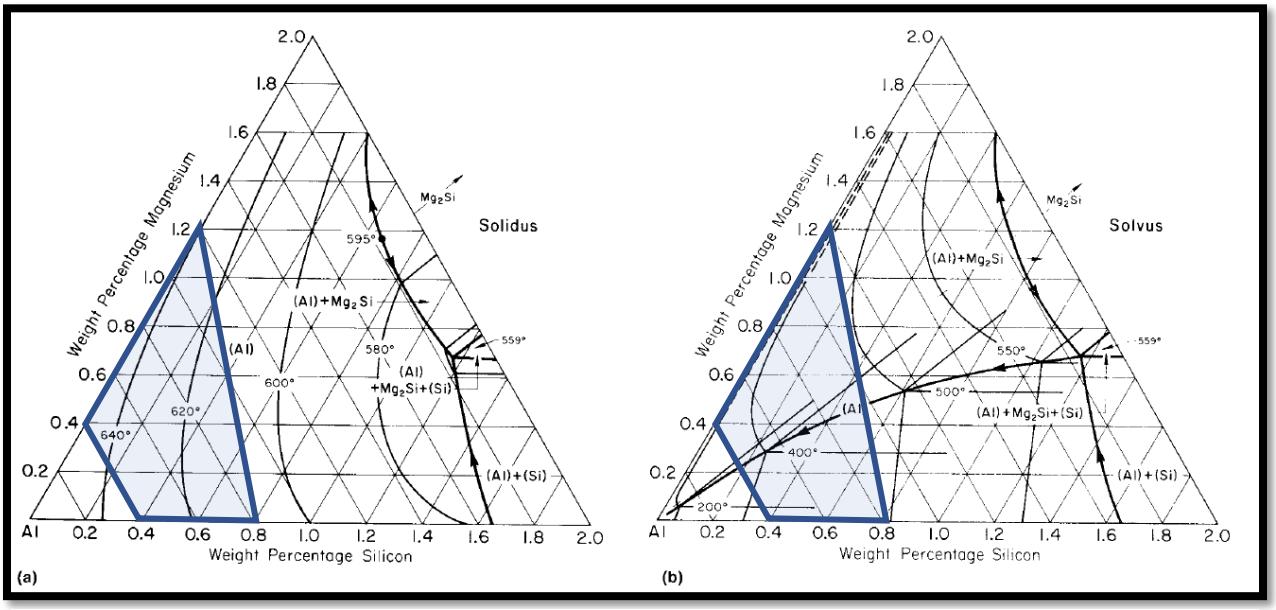

Figure 5-1: Al 6xxx Solidus and Solvus ternary diagrams in the aluminum corner, with the ranges of silicon and magnesium for 6061 highlighted and bounded in blue, assuming no other impurities. [213]

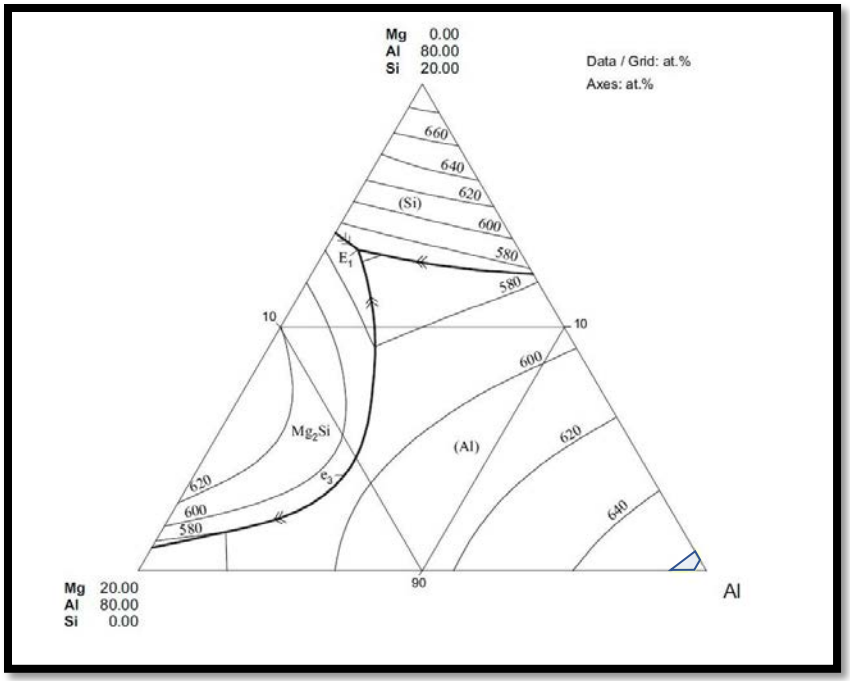

Figure 5-2: Liquidus ternary diagram for the Al-Mg-Si system, again with the bounds for the 6061 composition shown bounded by blue and shaded (bottom right corner). [211]

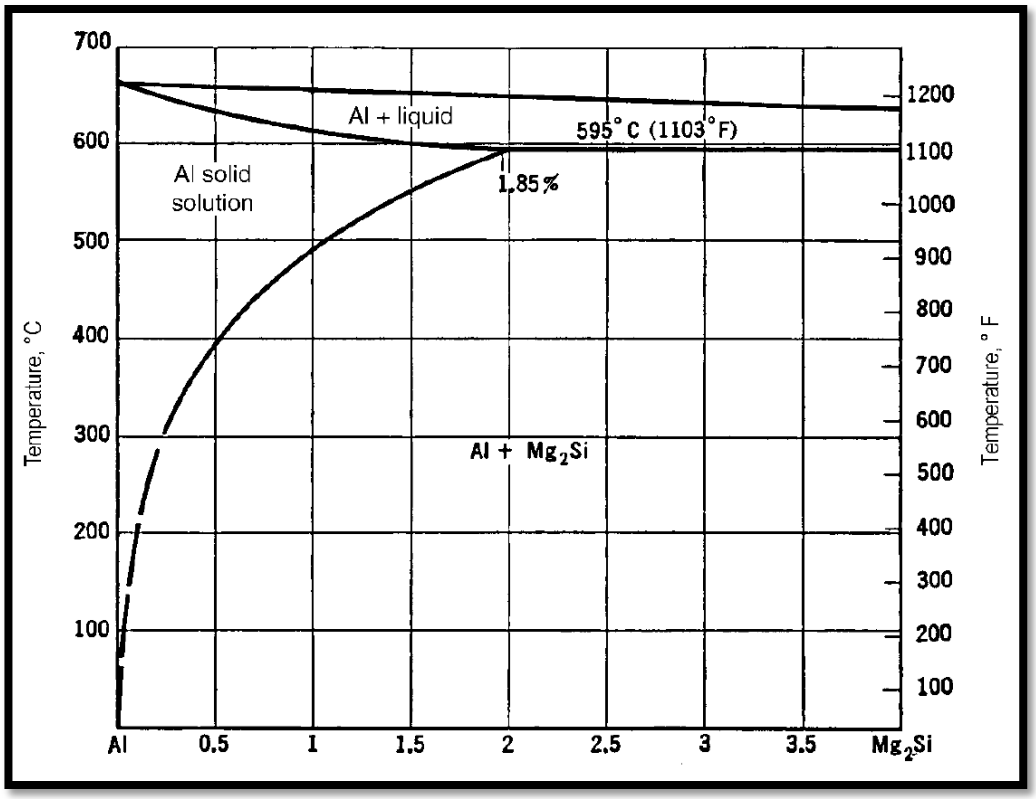

Figure 5-3: Quasi-binary phase diagram for aluminum and magnesium silicide, Mg_2Si, at the aluminum end showing the binary eutectic temperature. [213]

The different series of Aluminum are categorized due to the predominant alloying elements. For the 6000 series, the primary alloying elements are Silicon and Magnesium, which makes this series a subset of the age hardening aluminum alloys. The specific composition specification is listed in Table 5-1 above. Figure 5-1 above, shows the 6xxx series ternary diagram in the aluminum corner for the solvus and solidus characteristics, and Figure 5-2 shows the ternary diagram with the liquidus bounds. Additionally, although the 6000 series is listed as having Silicon and Magnesium as the two separate alloying elements, what typically occurs is that the compound Mg_2Si, magnesium silicide, is formed and a pseudo-binary composition is generated with aluminum, shown in Figure 5-3.

Comparing all three figures to one another provides a view of the possible variation of melt/solidification behavior, which is clearly complex. In contrast, the constitutive model used primarily in this study, as shown in Table 3-3, only includes a single melt temperature of 653 °C. While this is like a good estimate of the liquidus surface over the region of permissible alloying contents, the behavior is more complex. Obviously, the Johnson-Cook approach is a power law curve fit, which does not instantly turn to "melt" and is effective for its purpose. But the review of the phase diagrams provides the "why" for the thermal softening and some other key temperature points of interest. E_1 is a ternary eutectic between Al-Mg_2Si-Si at 557 °C and e_3 is the peak of the binary eutectic valley between Al and Mg_2Si at 594 °C, both on Figure 5-2. Heading the opposite direction from e_3 to E_1, leads to the ternary eutectic E_2 between the β phase (Mg_2Al_3), Al, and Mg_2Si, which occurs at 450 °C. [211] Depending upon the exact composition within the allowable window, as well as the local variation in as-solidified composition, earlier temperatures start to hint at possible mechanisms for softening with the possibility of localized melt in a heterogenous manner. In fact eutectic melting is a reason that overheating can be a

problem in heat treating alloys [210, p. 292]. The other complicating consideration is that phase diagrams represent equilibrium conditions, and the behavior in explosive welding does not stay within an equilibrium-like process. A finite time is required for phase change in order to rearrange structure, and conceivably the material could remain in a superheated, non-equilibrium state until the rapid quenching returns it back below a melting temperature.

The main point of the paragraph above in discussing the eutectic temperatures (even while only hinting at the kinetics of phase change) was to highlight that although much of the discussion in explosive welding attempts a binary classification of fusion versus solid state, especially in the very fine bond discussed in Section 2.2.4.3, there is room for variation at the hyper-local level. It was also to highlight that at non-eutectic compositions, there is room for solid and melted phases together at the same time, which seems important when Paul references a melt layer as small as 20 nm[41] [154].

5.2 MACRO & MESO SCALE OBSERVATIONS OF WELDED SPECIMENS

5.2.1 MACRO OBSERVATIONS

In Section 3.4.1.1, a discussion of the edge effects generated in explosive welding illuminated the behavior of the transverse cross-section during welding. Although the exact setup had the edge effect exacerbated by the board on top of the explosive, the results in Figure 3-36, also show the effect solely due to the less confined explosive on the edge. This effect would also be apparent in a longitudinal cross-section, at the end of detonation, as can be seen in Crossland [6, p. 116]. The edge effects of less explosive confinement were exhibited in the welding samples shown in Figures 3-15, 3-19, 3-21, & 3-23. In all of these cases, it is clear the

[41] For aluminum, 20 nm would be equivalent to only 50 unit cells thick.

specimens have a curvature that is generally concave up on the surface where the explosive was placed.

Additionally, in the Design of Welds portion of Section 2.2.2.3, it was noted that the corners and edge corners of the plates are vulnerable to spalling at times, and the placement of spall bars can prevent edge spalling. Again, Figures 3-15, 3-19, 3-21, & 3-23, show evidence that rarefaction effects spalled off corner edges. Especially in Figures 3-15 & 3-19, where the explosives were thinner, the edges show spalling action, but in these cases it was not quite enough to throw away the fractured material, which is still attached at points.

5.2.2 MACRO/MESO SCALE OBSERVATIONS

5.2.2.1 Hardness Distribution

In Section 4.5.2, based upon the lack of rotation of the notched specimen, it was inferred that there was a hardness increase in the region of the weld. As the stresses near the weld surface increased, in the welded samples, the yield strength was not reached as quickly (due to cold working), developing a larger resultant force in that region. In normal circumstances, as noted in Section 2.2.4.1, a common practice is to take microhardness measurements of some sort along the cross-section, through the thickness of the welded plates. In this study, the author was unable to include hardness evaluation using micro-indentation, and the observations from Section 4.5.2 are all that illuminates these properties.

5.2.2.2 Optical Microscopy of the Weld Bonds

- Preparation

The specimens were cut from the plates in the locations roughly shown in Figure 5-4. Based upon the limiting suggested standoff of 25 mm as referenced in Section 2.2.2.2 and shown

in Table 3-7, the weld samples were taken within regions of welding where the flyer plate standoff did not exceed this limit, just as for the selection of the tensile shear samples.

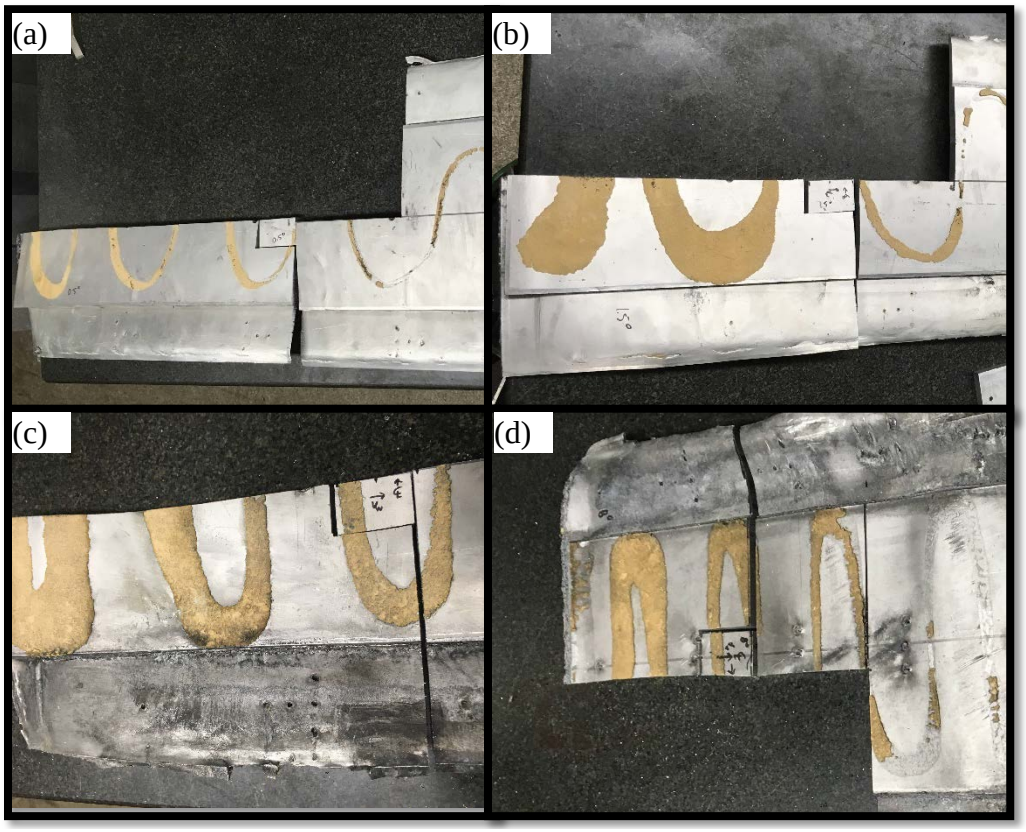

Figure 5-4: Specimen sample locations relative to the full plate. (a) 0.5° (b) 1.5° (c) 2.5° (d) 8°

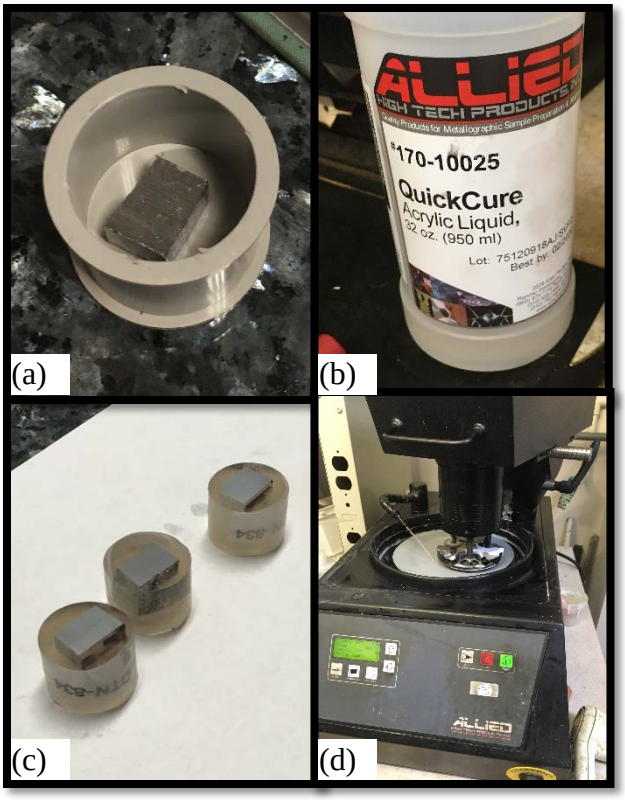

Figure 5-5: Sample preparation. (a) Samples were further cut to a final size to fit the mold. (b) Acrylic hardening liquid added to secure the specimen. (c) 3 of 4 final mounted specimens. (c) Liquid cooled polishing machine for grinding and final polishing.

The samples were further prepared as illustrated in Figure 5-5. After cutting to a final size and embedding in acrylic material, they were prepared in accordance with standard grinding and polishing practices in a liquid cooled machine to preserve grain structure. A succession of fine grit grinding/sanding discs were used, followed by a polishing cloth, using suspended finer grit solutions. The samples were then chemically etched using Keller's reagent, which has its components listed in Table 5-2 [212].

Table 5-2: Composition of Keller's reagent. [213]

Keller's Reagent	2 mL HF (40%)	3 mL HCl (38%)	5 mL HNO_3 (70%)	190 mL Distilled water

- Optical Image Results

Figure 5-6: Optical image of the 0.5° bond. Defects (cracks & voids) are visible. Frequent and sometimes relatively thicker melting, as much as roughly 100 µm, appear along the bond. However, some regions of thin, abrupt bonding appear.

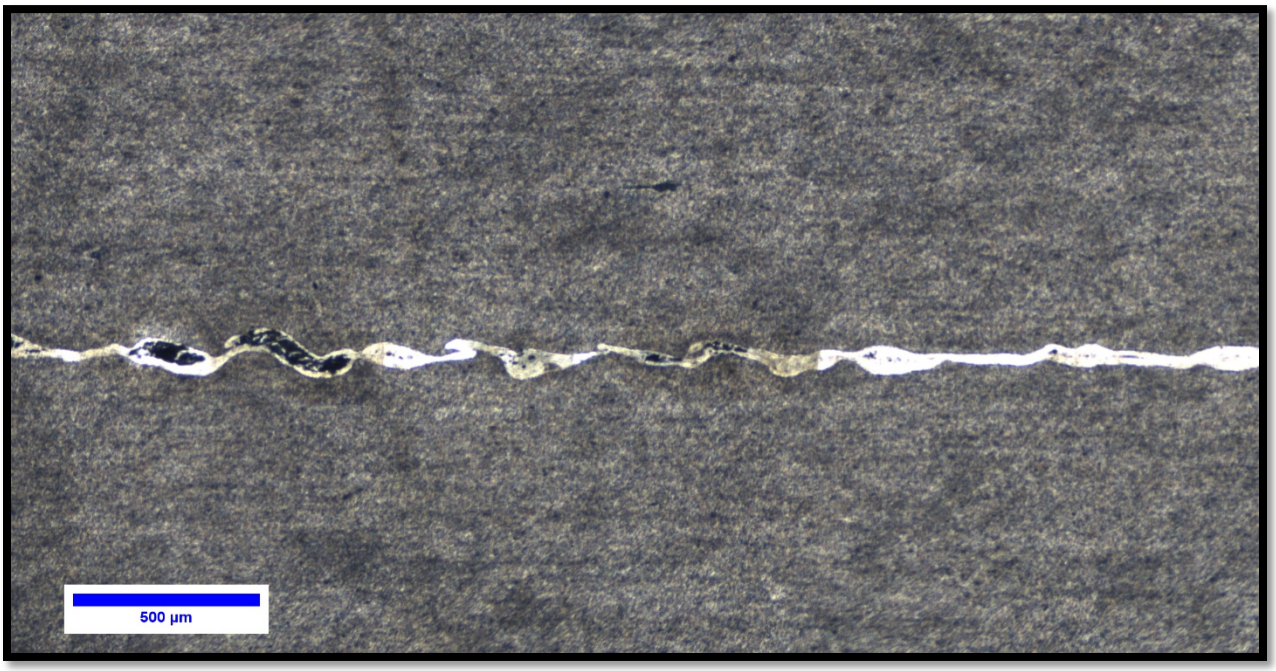

Figure 5-7: Optical image of 1.5° weld. Larger degree of consistent melt with a few discrete and larger voids that the 0.5° case. Hints of waves at roughly a wavelength of 180 µm and peak-to-peak amplitude of 140 µm, but this is not consistent or significant throughout. Other waves as long as 440 µm shown.

For both the 0.5° and the 1.5° specimens, some regions, typical of what is shown in Figure 5-6 & 5-7, had melt regions 20-40 μm thick with more frequent voids. Other areas in both were 100-150 μm thick. The 2.5° showed a variation of behavior; initially significantly melted, with the portion in Figure 5-8 showing waves. Waves were consistent in the 8° specimen.

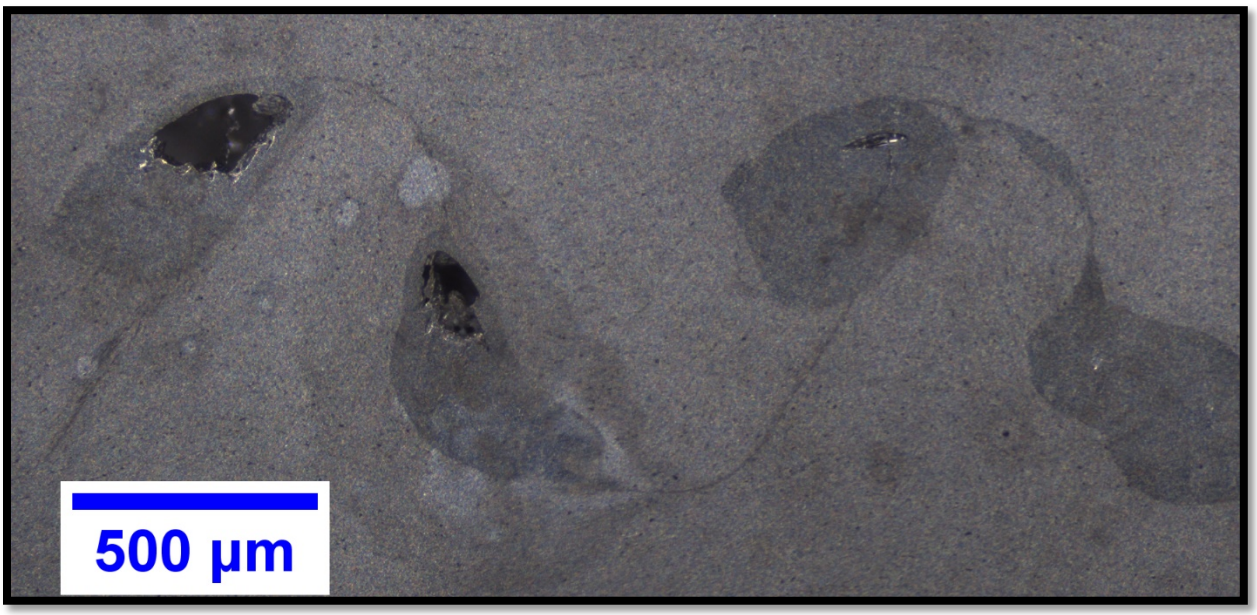

Figure 5-8: Optical image of 2.5° specimen. Shown are the largest waves on the sample, which were not steady throughout. Wavelength approximate 1.3 mm, with peak-to-peak amplitude of 0.8 mm. Some reagent wicking remains.

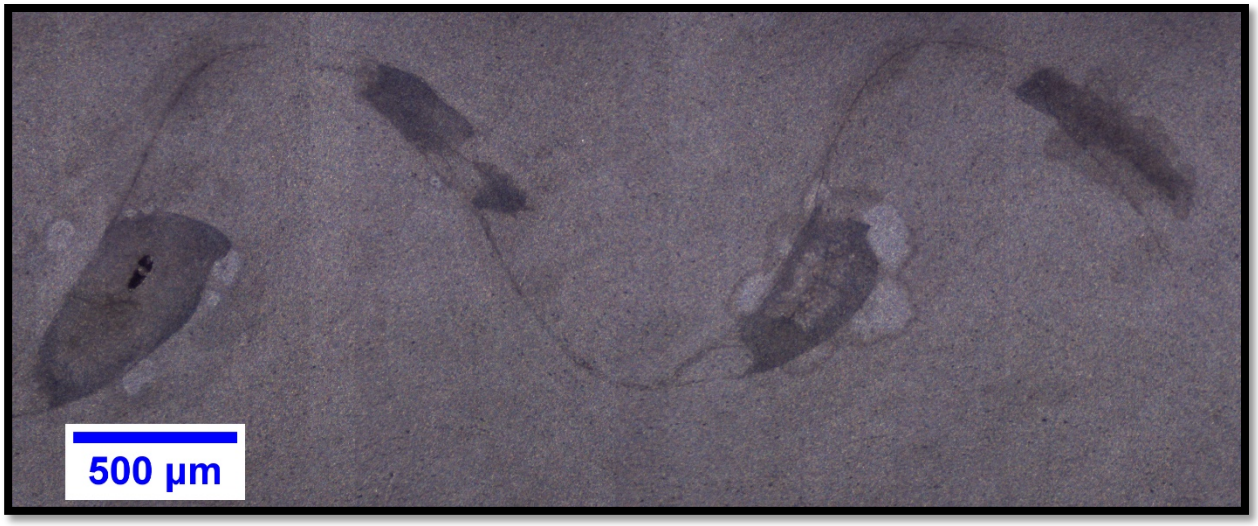

Figure 5-9: Optical image of 8° specimen. Waves were consistent across the whole specimen with an average wavelength of 2.0 mm and an average amplitude of 1.1 mm. Some wicking of reagent remains.

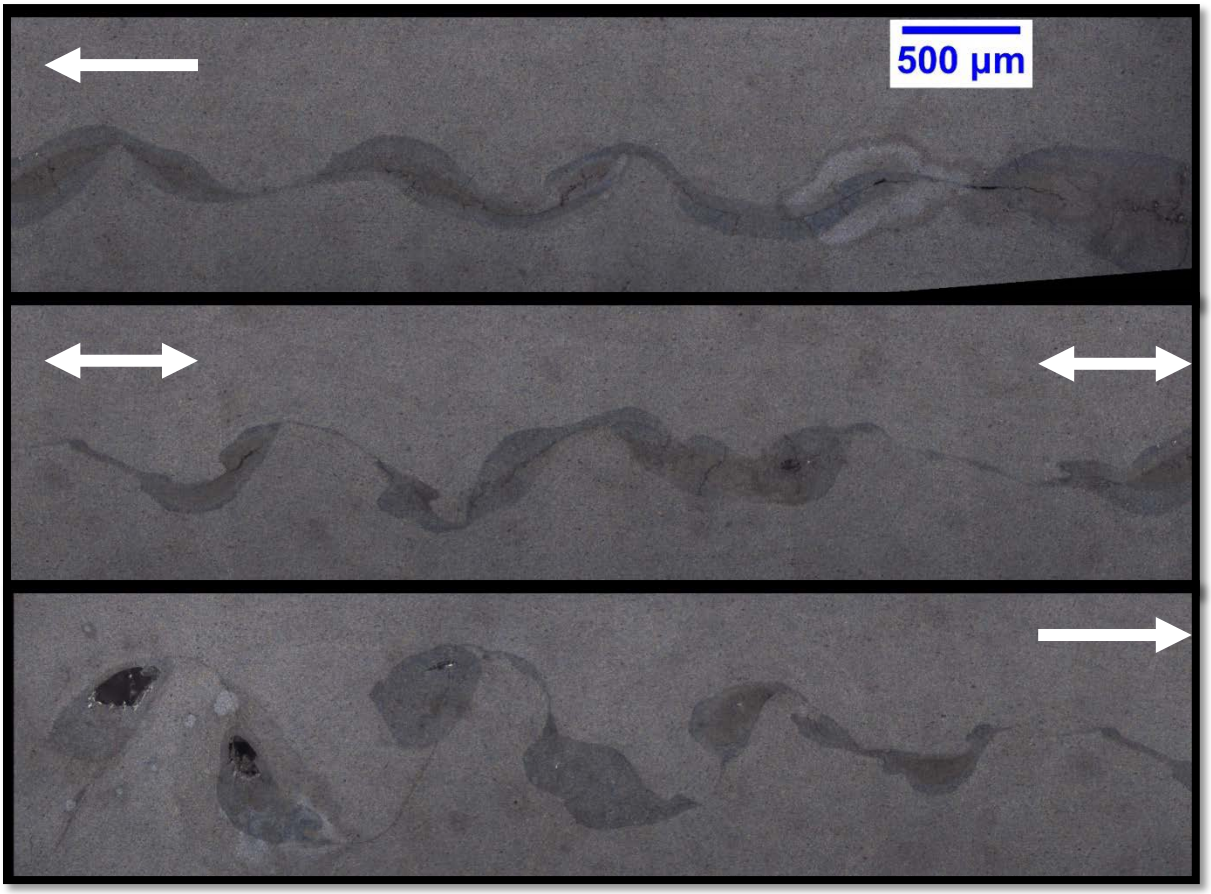

Figure 5-10: Full length of the 2.5° weld. Arrows solely to note connections, not weld direction. Top figure is rightmost while bottom is leftmost portion of the full sampled length of the 2.5° weld. The evolving nature is clear as well as significant melting, especially in the rightmost portion.

Figure 5-10 above, shows the full length of the weld in the 2.5°sample that was taken. It is clear that an evolving portion of the weld was captured. Also, the figure shows the prevalence of the amount of melt, even in portions of muted interfacial waves. Interestingly, it appears the 2.5° specimen had waves and they were lost, with significant melt occurring in their place. This may have been due to changes in the weld velocity and impact angle. It was initially assumed that the upper bound of the weld window would not be significant, as alluded to in Section 3.1.1. Many figures depicting the upper boundary imply it is roughly the same shape as the lower boundary, but simply shifted upward and to the right to some degree. This can be seen in Figure 2-23 a), and it is juxtaposed with Wittman's upper boundary in sub figure b). Wittman seemed to suggest that the upper boundary could in fact differ in shape from the lower boundary, such that at higher weld speeds, it narrows or even closes the gap of allowable welding before the right limit can be reached. This may also have been at play in the 2.5° sample.

- Comparisons to Literature-based Predictions

Shown below in Table 5-3, the observed wavelengths in the optical images were compared to the results predicted by Equation (2-19) from Section 2.2.3.2. While the wavelengths for the 1.5° are somewhat subtle/questionable, they still agree with predicted values actually fairly well. Similarly, the agreement for the 2.5° case is quite close, and even the 8° wavelength is in the neighborhood of the prediction.

Table 5-3: Comparison of measured wavelength and amplitude to Equation (18) and set ratio predictions.

Specimen	0.5°	1.5°	2.5°	8°
λ Predicted by Equation (2-19) (μm)	210	340	1200	3000
Measured λ (μm)	N/A	≈ 310	1300	2000
% Difference to Prediction	N/A	8.8%	8.3%	33%
Measured Peak-to-Peak Amplitude (2a) (μm)	N/A	140	800	1100
Measured Ratio (a/λ)	N/A	0.23	0.31	0.28
% Difference to 0.25 [131]	N/A	8%	24%	12%

What is also striking in reviewing Table 5-3 is the agreement of the observed wavelengths to the expected ratio. As discussed in the Bond Interfacial Amplitude portion of Section 2.2.3.2, there is a lot of agreement by independent researchers on the relative value of this ratio. Acknowledging that there is reasonable statistical deviation, the results in Table 5-3 agree quite well with this prediction, even in the case of the 8° specimen that deviates more from the wavelength prediction.

5.3 MICROSCALE OBSERVATIONS VIA SCANNING ELECTRON MICROSCOPE

Several distinctive details are revealed upon closer examination. While the 0.5° was difficult to resolve, as shown in Figure 5-11, the 1.5° specimen revealed additional details about the nature of the bond layer. Figure 5-12 shows another image identifying the thickness of the broader melt layer, while also showing the inner parts of a shrinkage void. The prevalence of these kind of cracks explain the bonds brittle mechanical behavior. The 2.5° specimen clearly experienced a violent shock. The image in Figure 5-14 shows evidence of refined grain structure. Figure 5-15 uses the 2.5° specimen to show a view of the interior of a shrinkage crack inside a vortex region. The images in Figure 5-16 & 5-17 are the most detailed view of regions of high-quality bonding in the 8° specimen. In both images, regions of good bond are referenced

to the surrounding material. A concentration of sliver like surface voids from etching are the only indication of the bond. They clearly highlight the intense shearing at the surface, but it is clear a very intimate bond has been produced.

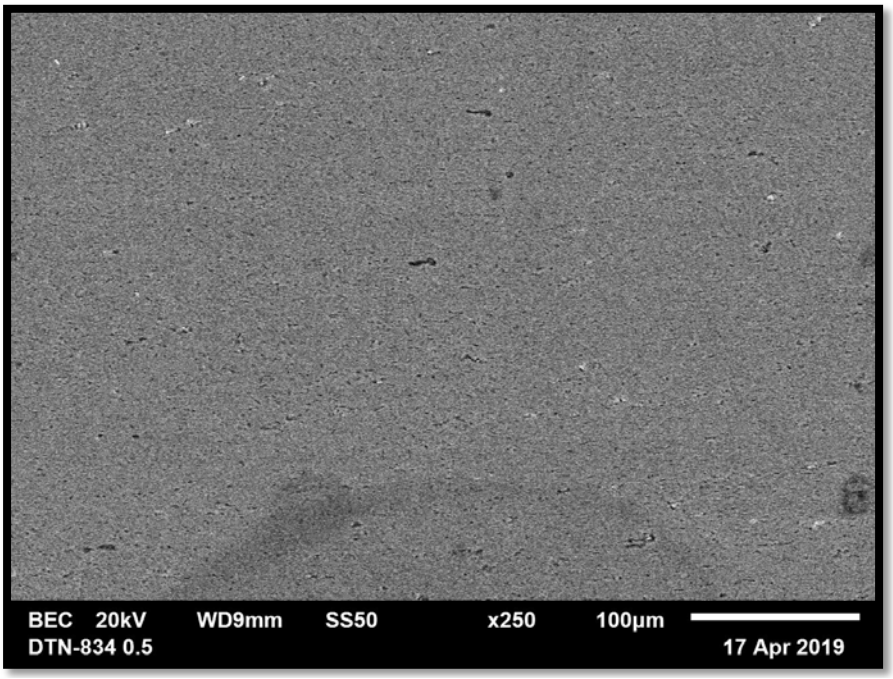

Figure 5-11: 0.5° specimen SEM image. Defining features were difficult to resolve on this specimen.

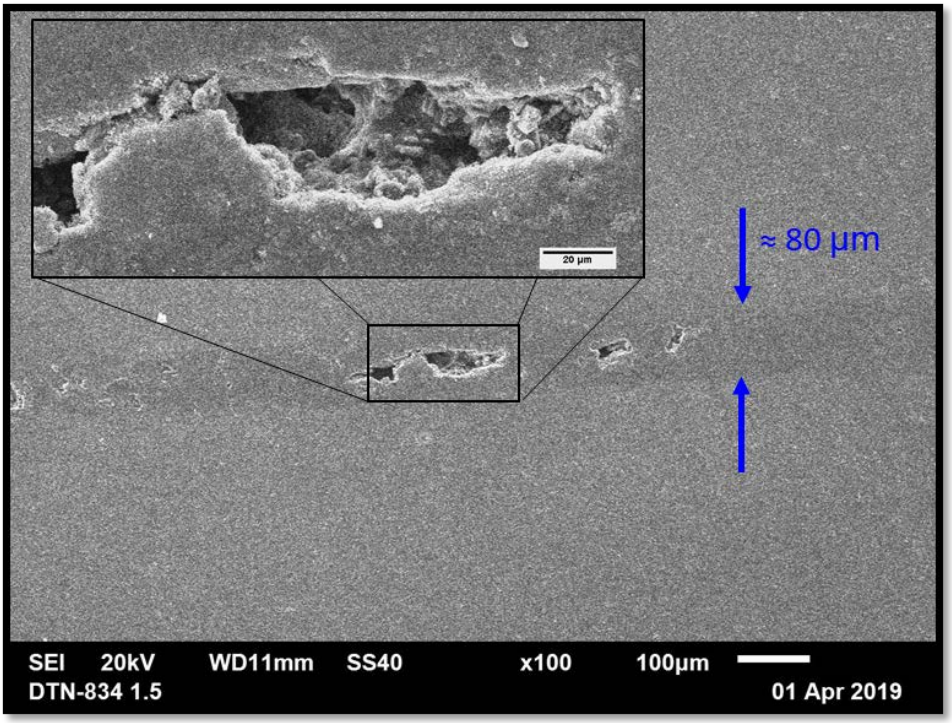

Figure 5-12: 1.5° specimen melt and void. Image of voids formed in melt area, with rough melt thickness annotated in blue.

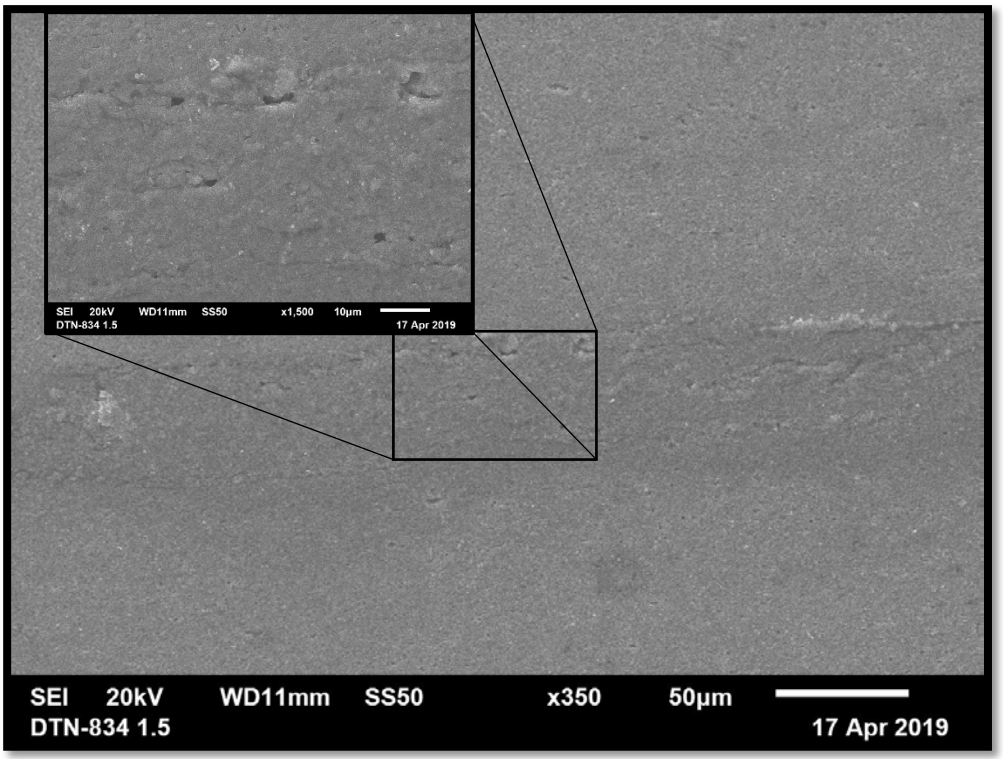

Figure 5-13: 1.5° specimen microcracks and melt layer.

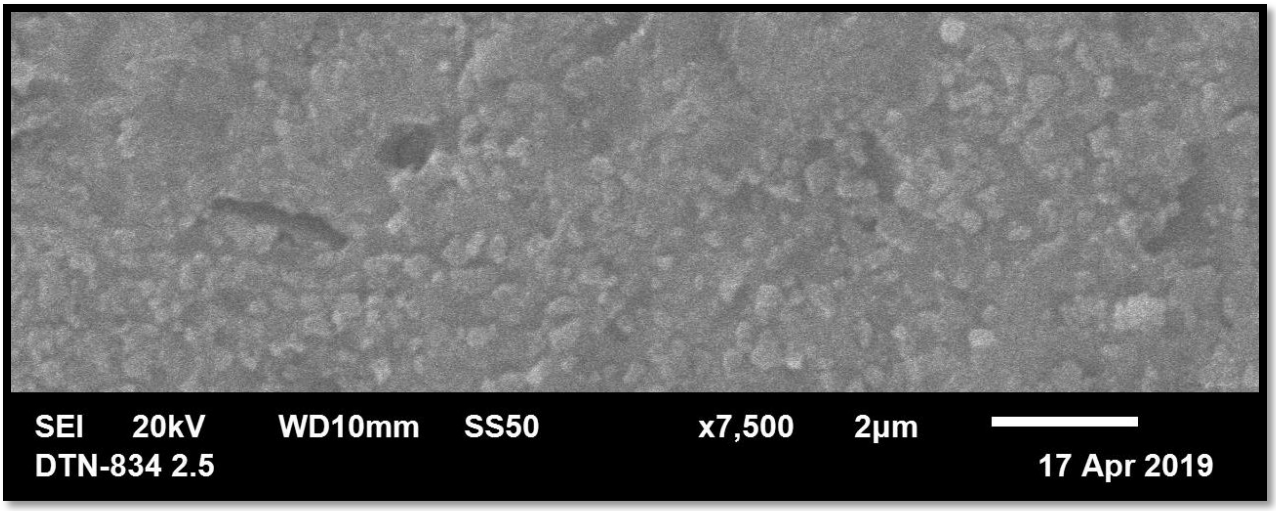

Figure 5-14: 2.5° specimen in the vicinity of the weld. Small grain size is visible in this image.

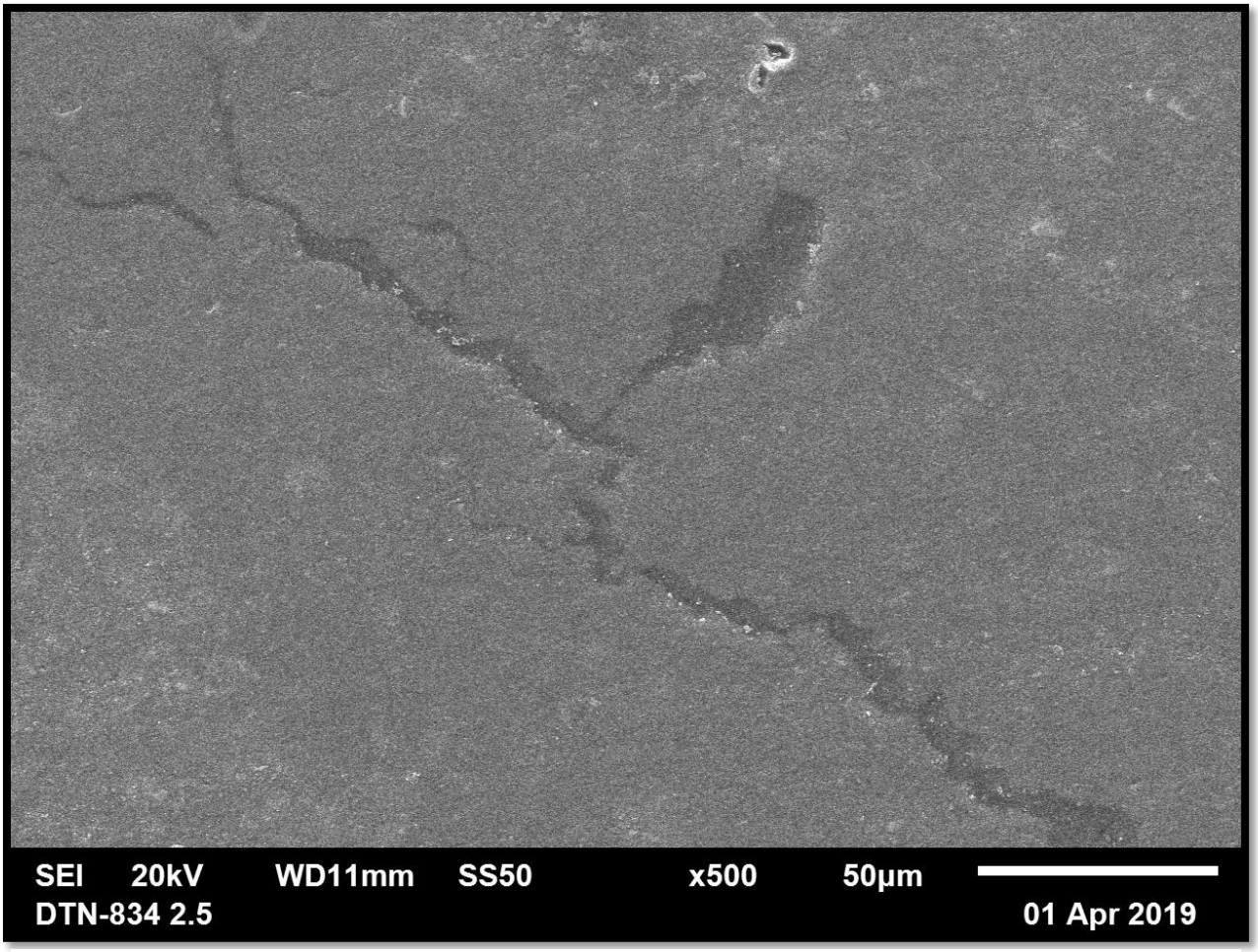

Figure 5-15: 2.5° specimen melt pocket. Shrinkage cracking after liquid in the lower pressure vortex solidifies and cools. The edge of the melt is visible at the upper left and lower right, in lighter grey.

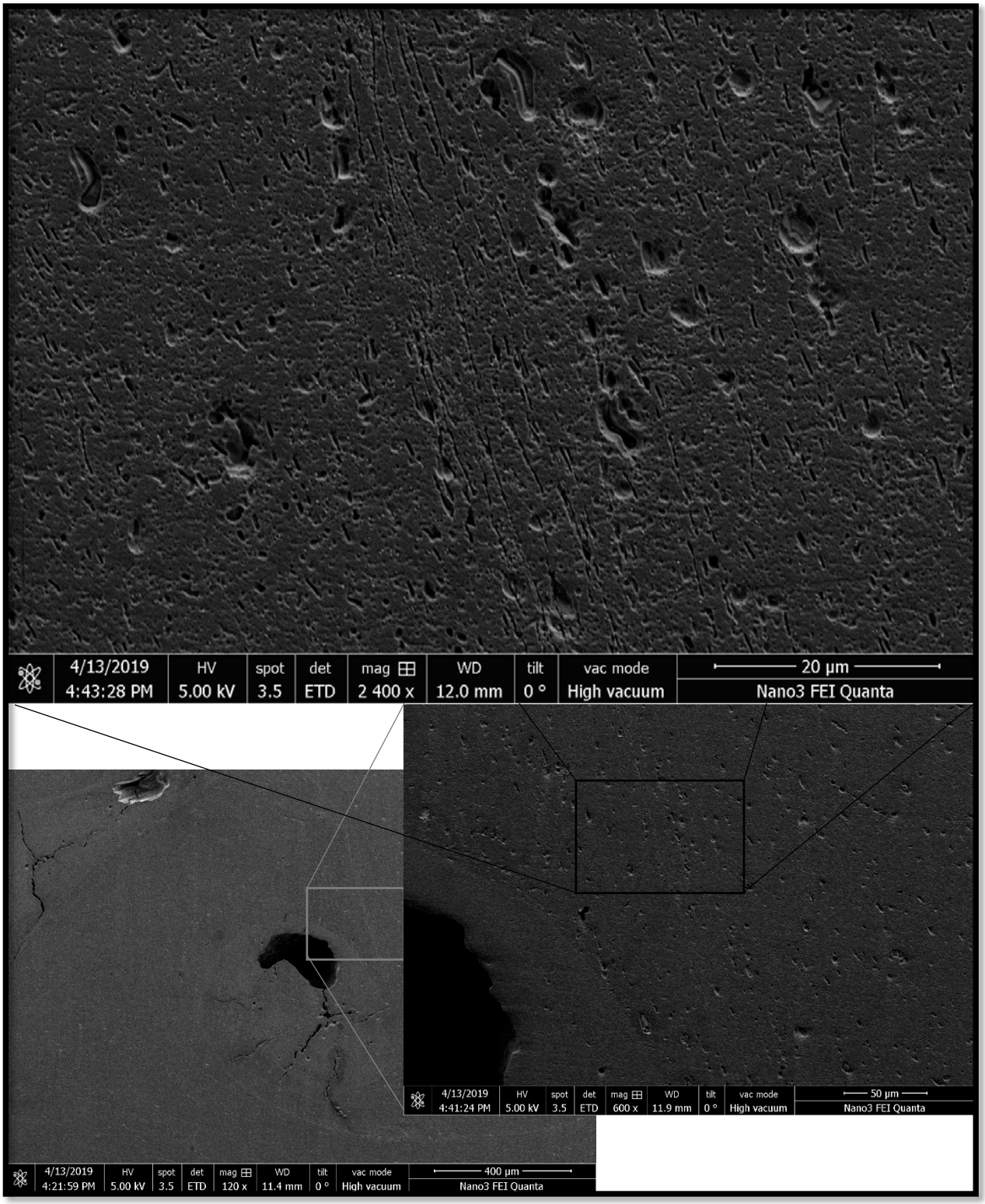

Figure 5-16: 8° specimen near good bond by a vortex. Melt pockets on either side of a wave crest are visible in the lower left, as well as the light grey line of good bond connecting the top. This is zoomed in on successively in the lower right, and then upper image.

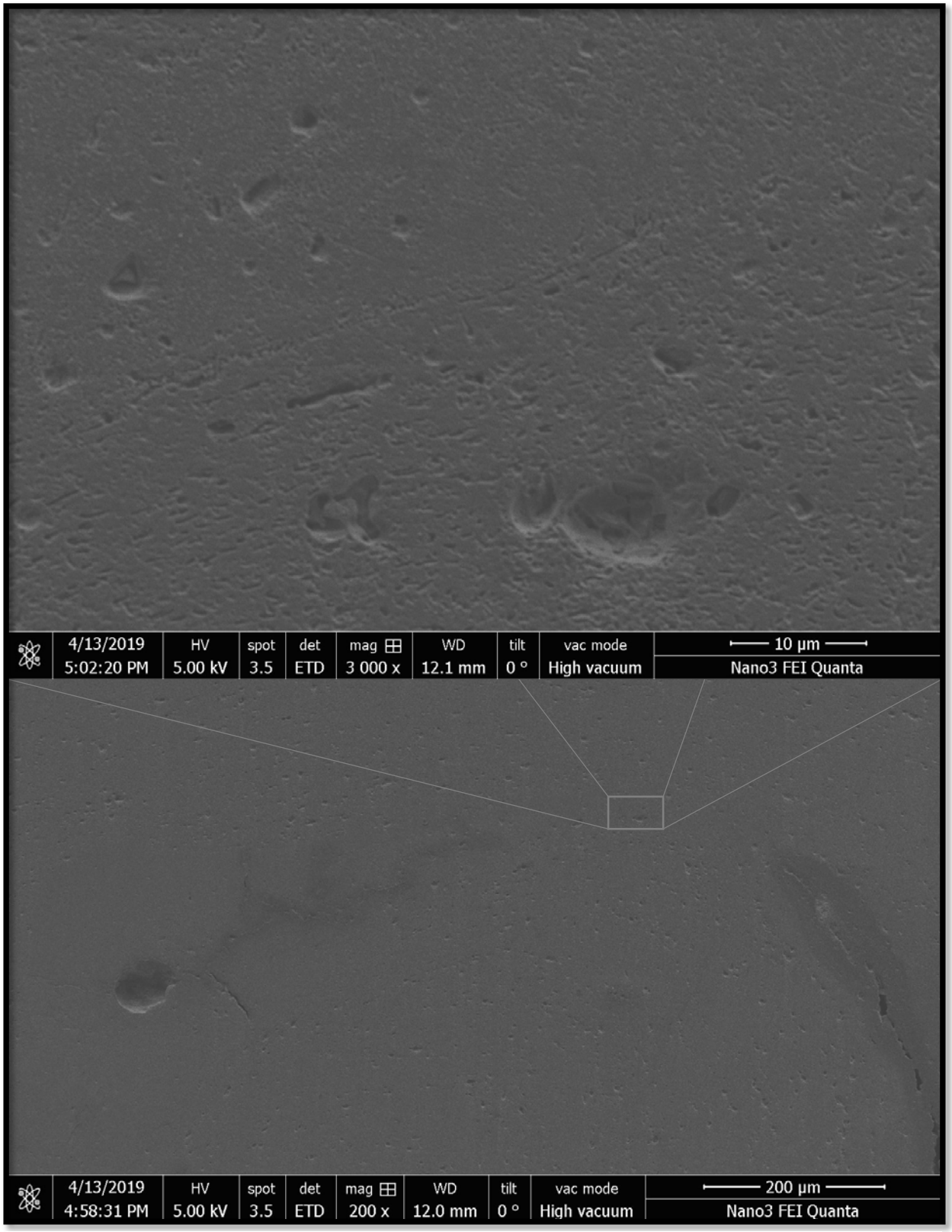

Figure 5-17: 8° images nearer the top of a wave crest. Melt from vortices visible on either side in the lower image, showing the region of the upper image. Very few indicators of the boundary remain.

5.4 NANO-SCALE OBSERVATION OF THE 8° SAMPLE

The 8° specimen clearly performed the best during testing. As opposed to the 0.5° and 1.5° cases, which in mechanical testing and under observation showed less desirable bonding, this specimen achieved high strength and ductility. The 2.5° specimen clearly generated too much melting and was inconsistent in its bonding. Based on this, the 8° was chosen for additional inspection.

The 8° specimen had several locations selected for evaluation. Attempts were made to location the regions of the best, most characteristically "solid state" bonding of the separate plates. Figure 5-18 shows images of a sample location before, during, and after initial milling for extraction. Figure 5-19 shows the specimen after further preparation and just prior to attachment to the extraction needle. The specimen was then mounted and thinned down to 100 nm, as shown in Figure 5-20. The mounted specimen was taken to the UC Irvine Materials Research Institute for examination by TEM.

The specimen was imaged on a JEM-2800 Transmission Electron Microscope. A stitched result is shown in Figure 5-21. This appears to show a very fine-grained region transition to a region with much larger grains. Figure 5-22 shows that fine grain region more clearly. Here many of the grains are ~80 nm, with some as small as 20 nm. The grains appear to be beginning to change characteristics after getting larger, but the sample width was not large enough to capture whether another fine grain region exists. This is consistent with the ~6 μm wide sample not appearing to totally traverse the surface area with apparent disturbance in the middle resolution image of Figure 5-18. This progression appears as though it could fit within the pattern described in the right side of Figure 2-42 in Section 2.2.4.3. However, additional samples would help to more firmly establish a corroborating case for that model.

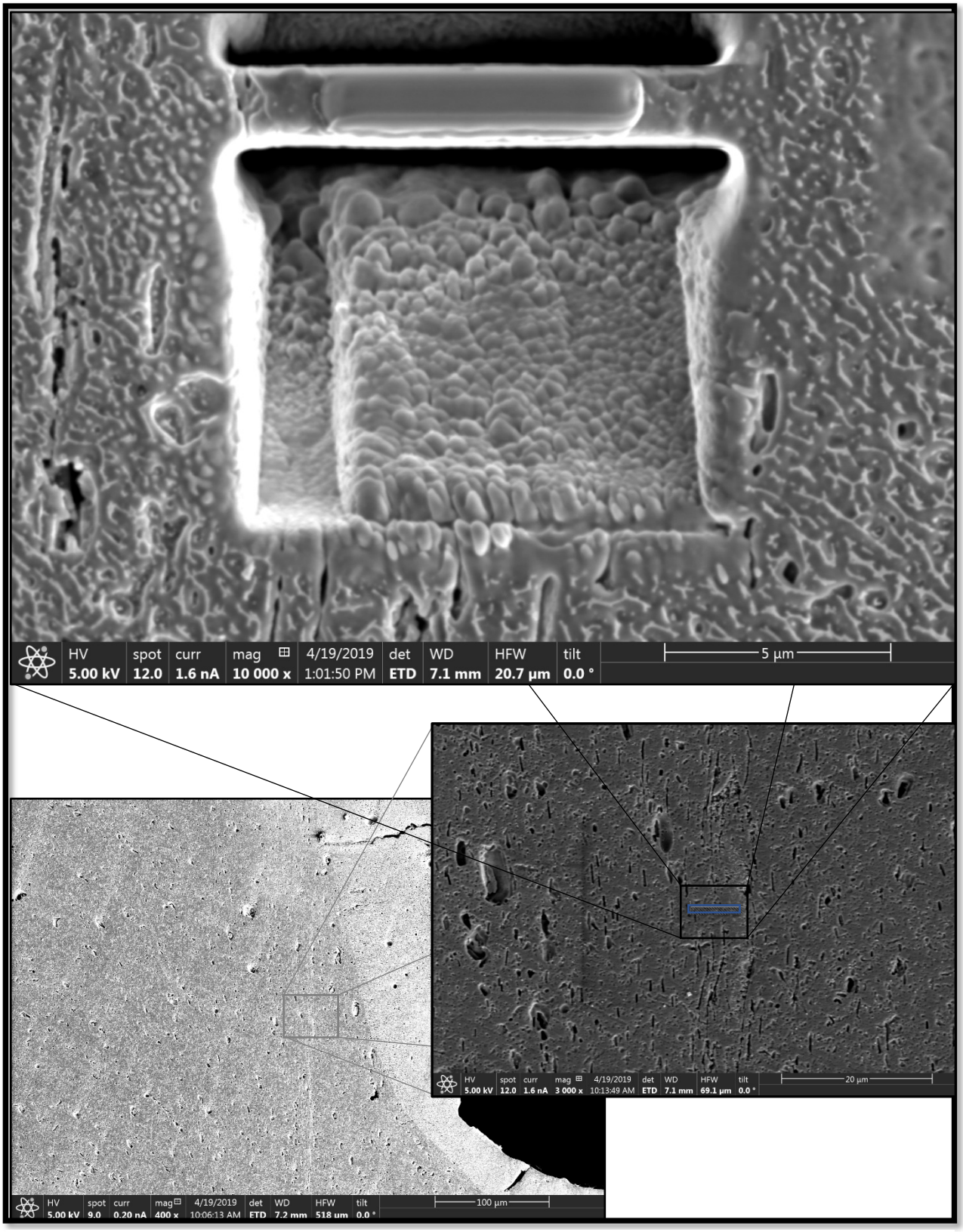

Figure 5-18: 8° Focused Ion Beam preparation. This sample is from the same location in Figure 5-17. In the lower left, the image has rotated 180° from that of the prior figure. The middle right shows the planned material deposition location for extracting, and the upper figure shows the result after both deposition and micro-milling was executed.

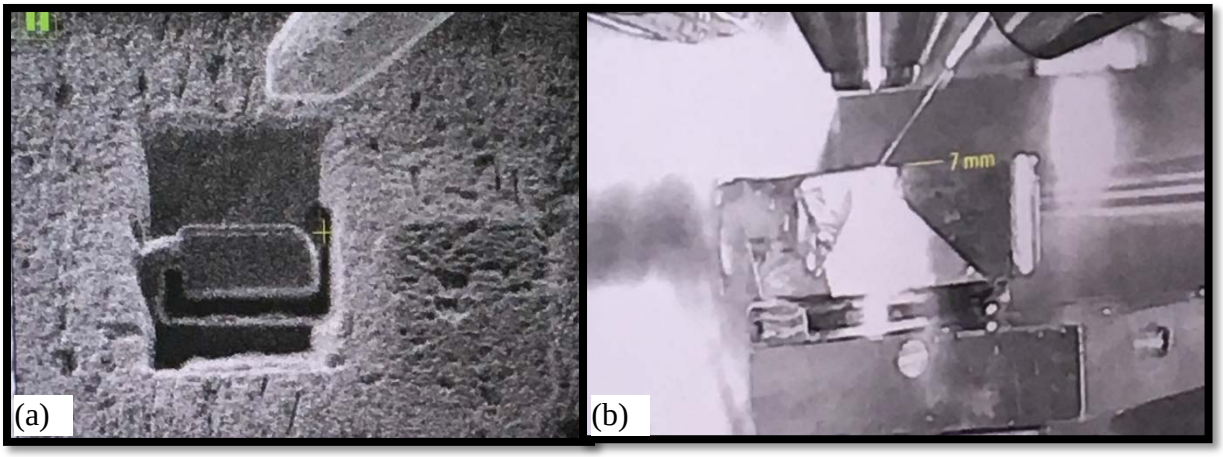

Figure 5-19: TEM sample extraction preparation. (a) The milled specimen further separated on the right, bottom, and a portion of its left side. The extraction needle is shown prior to deposition of joining material. (b) Chamber view of the full-size specimen with the extraction needle.

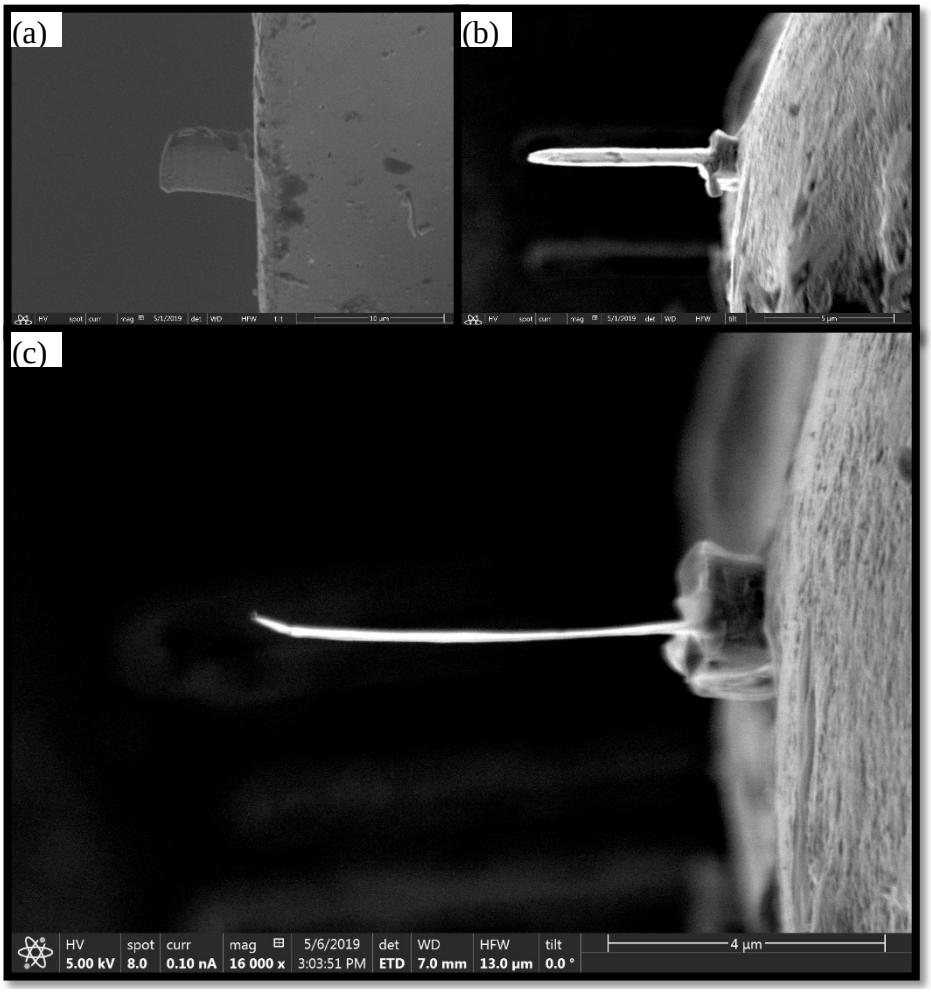

Figure 5-20: Mounted TEM sample. (a) Side view after initial mounting, showing protective material on top, and mount to the right. (b) Top view after initial mounting and some thinning. (c) Top view after complete thinning to less than 100 nm thick.

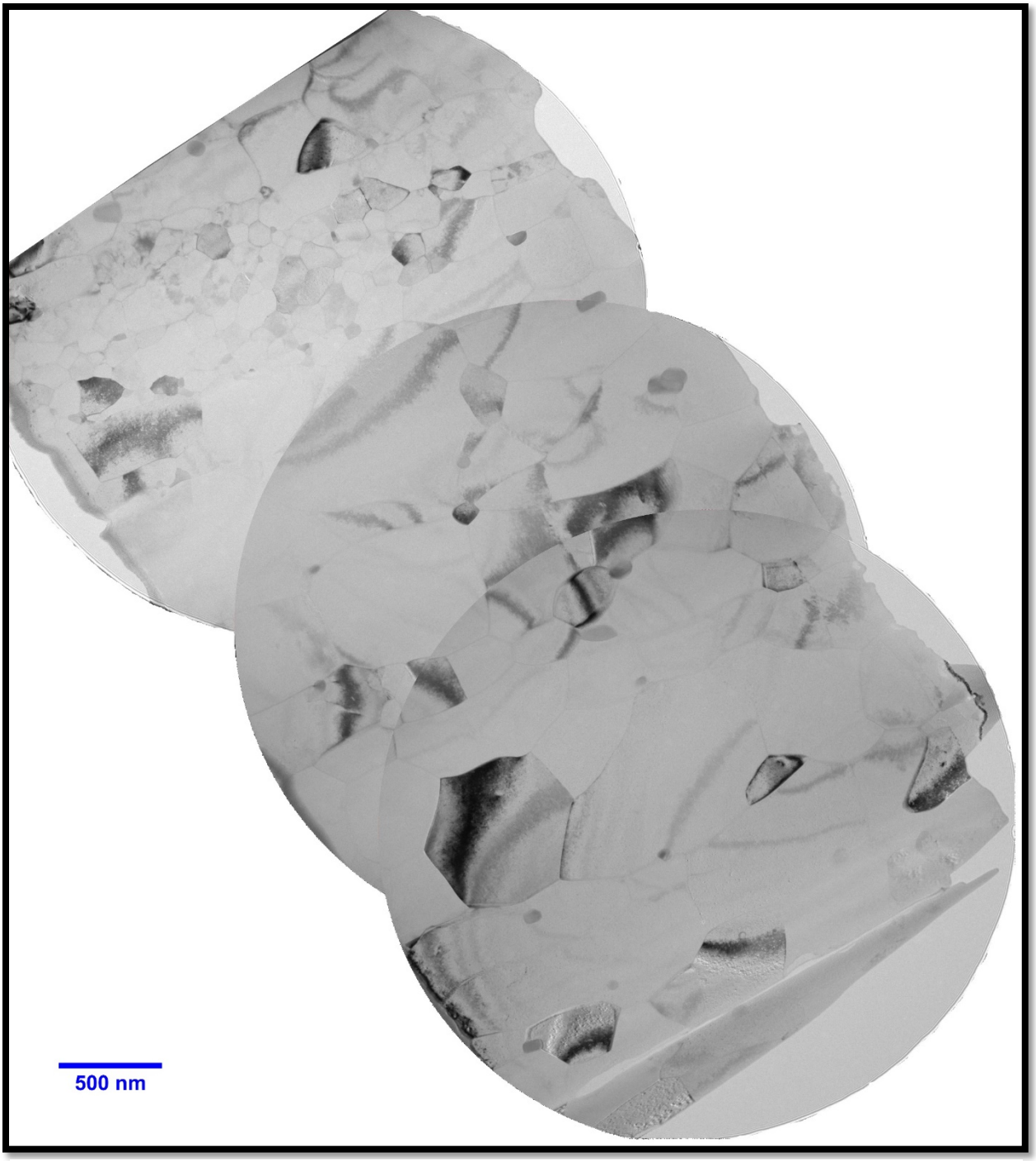

Figure 5-21: Stitched TEM image of the bond zone. The upper left edge in this image is the right side of the sample in Figure 5-19 (a), and the upper right side of here, is the top there. Nearly all deposition on top has been removed in the thinning process.

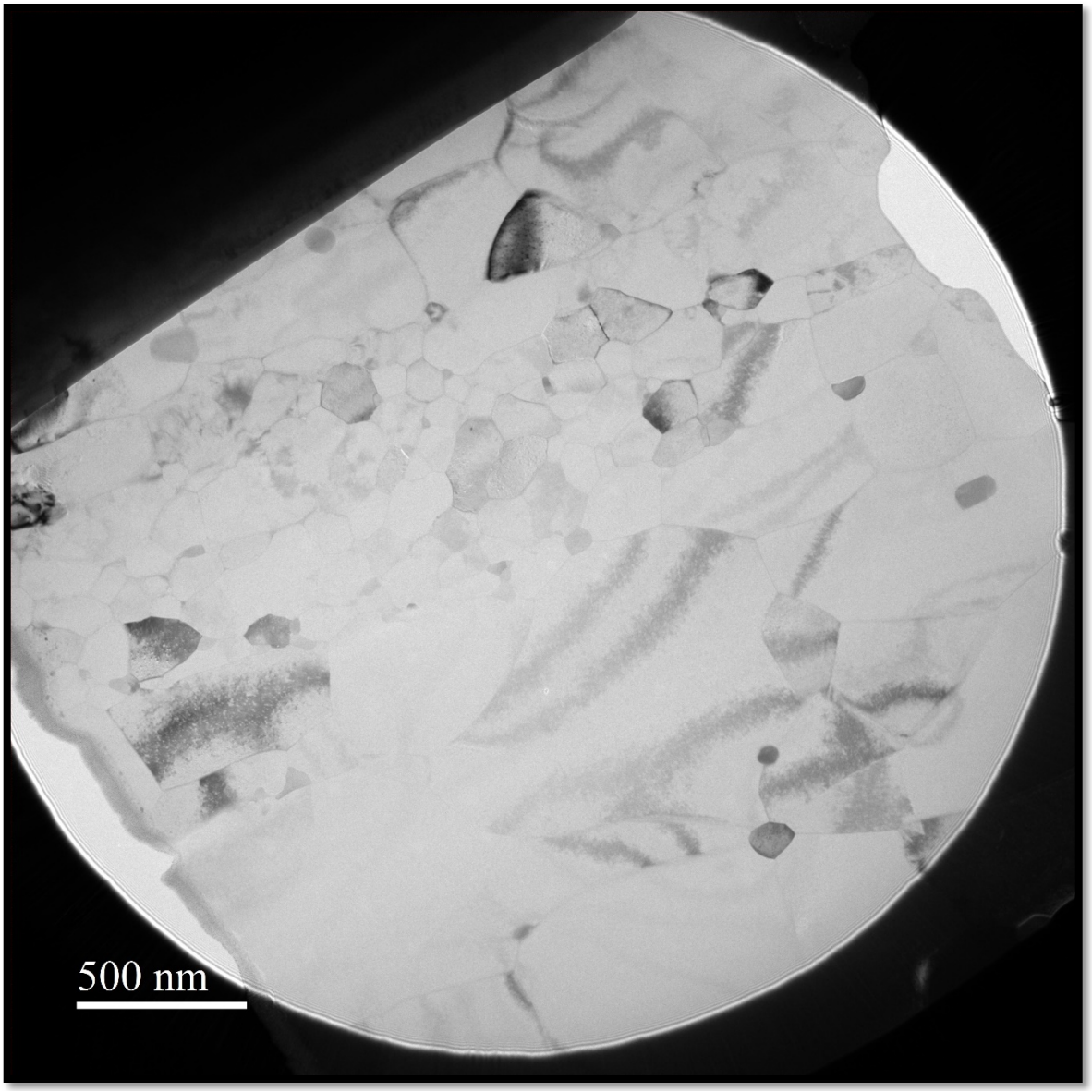

Figure 5-22: Band of fine grains in the bonding zone.

6. NUMERICAL METHODS FOR EXPLOSIVE WELDING

The commercial software LS-DYNA[214], [215] was used for numerical modeling of explosive welding events. Undoubtedly, the use of a research code provides advanced users the most control and insight into computational modeling, but there is also a place, at times, for the use of a commercial platform to allow those without the time or other means to develop code to generate useful analysis. A significant aim was to evaluate what could be achieved with this platform.

The modeling in LS-DYNA was conducted using the Multi-Material Arbitrary Lagrangian-Eulerian (MM-ALE) formulation in an adiabatic application. An overview of the relevant theory for the modeling will be presented, as well as the details of implemented parameters, then significant results will be presented relative to theoretical and measured criteria, and the usefulness of this approach will be discussed.

6.1 THEORETICAL BACKGROUND FOR LS-DYNA MULTI-MATERIAL ALE

The intent of this section is not to provide a comprehensive presentation of the theory involved in all aspects of the multi-material ALE formulation. However, in reviews of literature, the description of "ALE" modeling has appeared to have different meanings, and so the purpose of this review is to clarify high level concepts involved in the modeling, and to differentiate them from other cases of "ALE" modeling. For the interested reader the following are suggested general references for this material, all of which have been relied upon in the preparation of this section [216]–[220]. For an LS-DYNA specific presentation, readers are referred to [221].

6.1.1 KINEMATICS, MATERIAL DERIVATIVES, AND CONSERVATION LAWS IN ALE

6.1.1.1 Kinematics

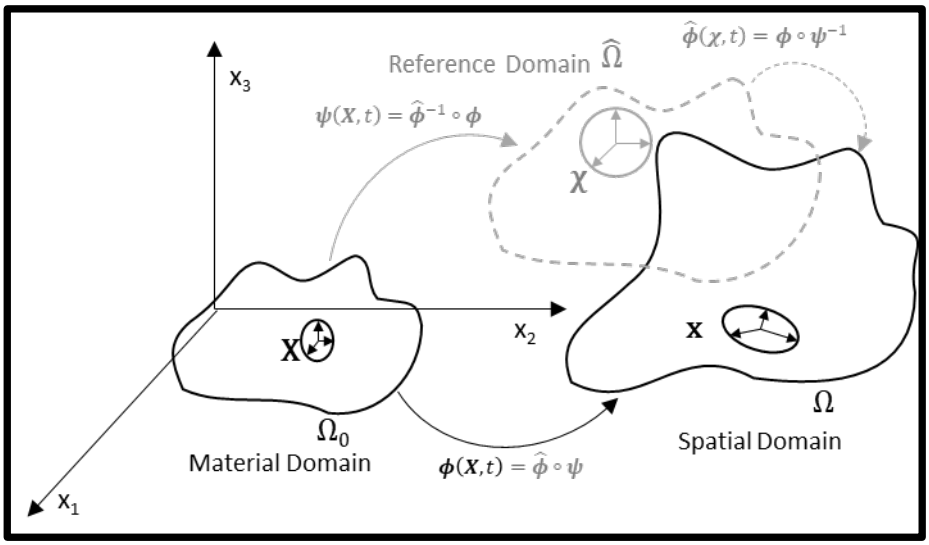

Figure 6-1: Mapping between ALE domains.

In the standard Lagrangian formulation, material points are denoted by their initial spatial location $\boldsymbol{X}$ at time $t = 0$ in the domain Ω_0 and are related to their current spatial location $\boldsymbol{x}(\boldsymbol{X},t)$ at time t in the spatial domain Ω. This is represented by the mapping $\boldsymbol{\phi}(\boldsymbol{X},t)$, as shown in Figure 6-1, in the black lines and text. In this frame, mathematical nodes for computation are assigned in the start of modeling in Ω_0 and travel with material points. The other bounding modeling formulation is the Eulerian scenario, where material points are not explicitly tracked by nodes, but rather control volumes are used. In this sort of modeling, the mathematical nodes for computation are fixed in spatial coordinates x_1, x_2, & x_3 in the tracked spatial domain, while the material (within subset Ω) flows through the mesh over time. Pictorially, it would be as though the material domain Ω_0 and mapping $\boldsymbol{\phi}$ was removed from Figure 6-1, in addition to the grey portions. Mathematically, as an alternative, you could state the material points can be mapped with the inverse map as in $\boldsymbol{X} = \boldsymbol{\phi}^{-1}(\boldsymbol{x},t)$. In the Eulerian model, material advects between and can (in certain methods) mix within finite elements, as well as can exit or enter the full modeled

domain depending on boundary conditions. A main disadvantage for Lagrangian formulations in finite elements is that with severe deformations, elements become ineffective at relating nodal displacements to internal continuum effects, while the main disadvantages for the Eulerian case are that material point data is harder to track and larger computational domains must be defined to model large movements, even for small amounts of material.

In the Arbitrary Lagrangian-Eulerian formulation, a balance is struck where computational mathematical nodes are neither aligned with material points (Lagrangian), nor fixed in space (Eulerian), but rather are allowed to move arbitrarily in space. This attempts to take the best of both alternatives, and is represented in Figure 6-1 by the added domain and annotations in grey. Moving the reference domain $\widehat{\Omega}$ can limit the advection between elements (a potential source of accumulated error) and can limit the overall size required for the set of computational nodes for modeling by best placing the referential coordinates, χ.

6.1.1.2 Material Derivatives and Conservation Laws via Density Example

As a starting point, it is clear that Newton's laws, especially the 2nd, expressed as conservation of momentum, applies to discrete masses. For the purpose of applying this type of physical law, a material derivative is defined as a derivative with respect to time following a discrete mass, and is denoted as $\frac{D[\cdot]}{Dt}$ where the dot is the quantity in question. In a continuum, the smallest discrete mass, a differential volume, is referred to by its initial coordinates $\boldsymbol{X}$. The material derivative of density, referred to its material coordinate in a Lagrangian formulation, $\rho(\boldsymbol{X}, t)$, then is $\frac{D}{Dt}\rho(\boldsymbol{X}, t) = \frac{\partial}{\partial \boldsymbol{X}}\rho(\boldsymbol{X}, t) \cdot \frac{\partial \boldsymbol{X}}{\partial t} + \frac{\partial}{\partial \boldsymbol{t}}\rho(\boldsymbol{X}, t)$. But as the reference positions of material points do not change with time, $\frac{\partial \boldsymbol{X}}{\partial t} = 0$ and so $\frac{D}{Dt}\rho(\boldsymbol{X}, t) = \frac{\partial}{\partial \boldsymbol{t}}\rho(\boldsymbol{X}, t)$, which is nearly trivial. However, it denotes the time rate of change of the material particle, which is what we want.

In contrast, the Eulerian representation of a material derivative is more involved. In this representation, the density of a material particle is referred to its current spatial coordinates, not its original point, i.e. $\rho(\boldsymbol{x}, t)$, where the indirect mapping $\boldsymbol{x} = \boldsymbol{\phi}(\boldsymbol{X}, t)$ is not relied upon. Here the material derivative becomes $\frac{D}{Dt}\rho(\boldsymbol{x}, t) = \frac{\partial}{\partial \boldsymbol{x}}\rho(\boldsymbol{x}, t) \cdot \frac{\partial \boldsymbol{x}}{\partial t} + \frac{\partial}{\partial \boldsymbol{t}}\rho(\boldsymbol{x}, t)$. The value $\frac{\partial \boldsymbol{x}}{\partial t}$ is not necessarily zero, but is rather the instantaneous velocity at that point, **v**. So, in the Eulerian case, $\frac{D}{Dt}\rho(\boldsymbol{x}, t) = \frac{\partial}{\partial \boldsymbol{t}}\rho(\boldsymbol{x}, t) + \boldsymbol{v}\frac{\partial}{\partial \boldsymbol{x}}\rho(\boldsymbol{x}, t)$. By analogy, $\frac{D}{Dt}[\cdot(\boldsymbol{x}, t)] = \frac{\partial}{\partial \boldsymbol{t}}[\cdot(\boldsymbol{x}, t)] + \boldsymbol{v}\frac{\partial}{\partial \boldsymbol{x}}[\cdot(\boldsymbol{x}, t)]$ for other parameters, when referring to current spatial coordinates.

Taking the material derivative in an ALE formulation is even more involved, but it starts in the same manner. In the ALE case, the reference coordinates are from $\widehat{\Omega}$ and expressed as χ. So density, referred to the ALE reference domain, is $\rho(\boldsymbol{\chi}, t)$. With the same logic as above, $\frac{D}{Dt}\rho(\boldsymbol{\chi}, t) = \frac{\partial}{\partial \boldsymbol{t}}\rho(\boldsymbol{\chi}, t) + \frac{\partial}{\partial \boldsymbol{\chi}}\rho(\boldsymbol{\chi}, t) \cdot \frac{\partial \boldsymbol{\chi}}{\partial t}$. The second term on the righthand side is equivalent to $\boldsymbol{c}\frac{\boldsymbol{\partial}}{\boldsymbol{\partial x}}\rho(\boldsymbol{x}, t)$, where $\boldsymbol{c} \equiv \boldsymbol{v} - \widehat{\boldsymbol{v}}$, $\boldsymbol{v}$ is material velocity as above, and $\widehat{\boldsymbol{v}}$ is the reference mesh velocity. For more detail, refer to [217, pp. 419–422]. Material derivatives of density using the ALE formulation would then be shown in Equation (6-1), below. This can be employed for generic quantities, substituting the desired value for ρ.

$$\frac{D}{Dt}\rho = \frac{\partial}{\partial \boldsymbol{t}}\rho(\boldsymbol{\chi}, t) + \boldsymbol{c}\frac{\boldsymbol{\partial}}{\boldsymbol{\partial x}}\rho(\boldsymbol{x}, t) \tag{6-1}$$

Moving to the conservation of mass, as an example, some similar processes will be followed. A conservation expression that is a mix of density as a function of $\boldsymbol{x}$ and density as a function of $\boldsymbol{\chi}$ is used, where each is more convenient computationally. The Eulerian expression can be used as a starting point to arrive at the final employed conservation expression. The Eulerian expression for conservation of mass is $\frac{D}{Dt}\rho(\boldsymbol{x}, t) + \rho(\boldsymbol{x}, t)\boldsymbol{\nabla} \cdot \boldsymbol{v} = 0$. The single step of

substituting in the material derivative from the ALE reference system (Equation (6-1)) produces the commonly employed form of conservation of mass. This is shown in Equation (6-2), below.

$$\frac{\partial}{\partial \boldsymbol{t}}\rho(\boldsymbol{\chi}, t) + \boldsymbol{c}\frac{\boldsymbol{\partial}}{\boldsymbol{\partial x}}\rho(\boldsymbol{x}, t) + \rho(\boldsymbol{x}, t)\boldsymbol{\nabla}\cdot\boldsymbol{v} = 0 \tag{6-2}$$

Similar derived formulations for conservation of linear momentum and conservation of energy are among the strong form requirements applied in modeling. What is critical to note, is that this heart of the ALE formulation is not a complete method and is largely based on kinematics and reference configuration selection.

6.1.2 Numerical Algorithms for Evaluation

Upon formulating the strong form of the ALE equations that will be used, different methods for evaluation can be used. Two methods, the Petrov Galerkin and the Streamline Upwinding Petrov-Galerkin (SUPG) formulation are used, after deriving the weak form of the applicable equations. See [217, Secs. 7.5-7.8] for details. In LS-DYNA however, operator splitting is used. For details and equations the reader is referred to [216], [219], but the process will be conceptually highlighted here. This process essentially takes a governing equation and separates it into two parts. A Lagrangian step includes the source term and then an Eulerian step contains the convective term. The solution is advanced in time in a Lagrangian step, and then in the Eulerian (or ALE) step, the material and other solution variables, such as equivalent plastic strain, temperature, or damage, are advected onto the reference mesh. This method has theoretical limitations on accuracy, but can be comparatively fast and the theoretical limitations don't turn up strongly in practice.

6.1.3 The Multi-Material Formulation

6.1.3.1 Contrast to Other Common ALE Formulations

In the introduction to Section 6.1, it was alluded to that "ALE" modeling is a term that is not always precisely used. The essence of an ALE formulation means a model follows and applies the kinematic formulations of Section 6.1.1, as noted at that section's end. This is just the same as saying you used Lagrangian modeling or Eulerian modeling; more detail is required. However, even when you specify the use of finite elements, there is a major break in possibilities for what can be ALE modeling.

The version of ALE that appears to have the most common recognition is what Benson refers to as "simplified ALE" in [216, p. 325]. This formulation restricts the arbitrary nature of the background mesh formulation in a couple key ways. First, it does not allow the background mesh and computational nodes to move outside of the spatial domain occupied by the material in question. This directly means that nodes initially on the boundary of the material stay on that boundary, while the only arbitrary variation allowed for node placement is within the space enclosed by that boundary. Second, a direct result and intended purpose of the first, is that within finite elements composed of these nodes, there will only be one material of any type. This allows adjustment of the computational nodes to create more regularly shaped elements in modeling events that would otherwise have severely distorted Lagrangian meshes. This formulation is implemented in LS-DYNA, element formulation 5, 1 point ALE, and is also in Abaqus as an adaptivity technique [222, Sec. 12.2]. In both of these software the naming simply specifies ALE, which has clearly become a standard way to refer to this technique.

However, the technique above is referenced in order to specifically contrast the alternative that is used here, as it is easy for the first two letters of "MM-ALE" to be dropped in

an imprecise reference. There is a significant difference in terms of the details of implementation. While the simplified ALE finite element formulation above limits mesh motion and only allows one material within a single element, that is not a requirement of the description in Section 6.1.1. Some Eulerian formulations allow multiple materials within a single element and that is the formulation to be used, with implications to be discussed.

6.1.3.2 Mixed Elements

The term mixed elements is applied when multiple materials are included within one finite element, as in Figure 6-2 below. This is not an example of multi-field methods, which are sometimes referred to as mixed methods and can be referenced for contrast in [217, Sec. 8.5]. In the context of the LS-DYNA multi-material formulation, mixed elements are covered by Benson in [216], [219] in sections on mixture theory. In this theory, thermodynamic assumptions are required about the pressure, temperature, and strain rates of the materials within the mixed element. The mean strain of the element must be partitioned to the materials in the element, then the stress is updated in each material in the element, and finally the mean stress of the element is assembled. Only the first step varies in different methods [219, p. 22].

The implementation used in LS-DYNA uses mean strain rate mixture theory, where the mean strain is assumed to apply to each material. This means that in an element containing steel and air, clearly different mechanically, both materials individually undergo the same internal strains as the bulk element is strained. In the case of the welding studies of this effort, there is an immediate “numerical weld” when two material groups enter the same element. Sharing the same strain rates, there must be a convection outside the same element until their strain rates can differ. However, with the right element size, there are ample opportunities for this to occur and implementation of newer failure models also alleviate this. This strain rate assumption is clearly

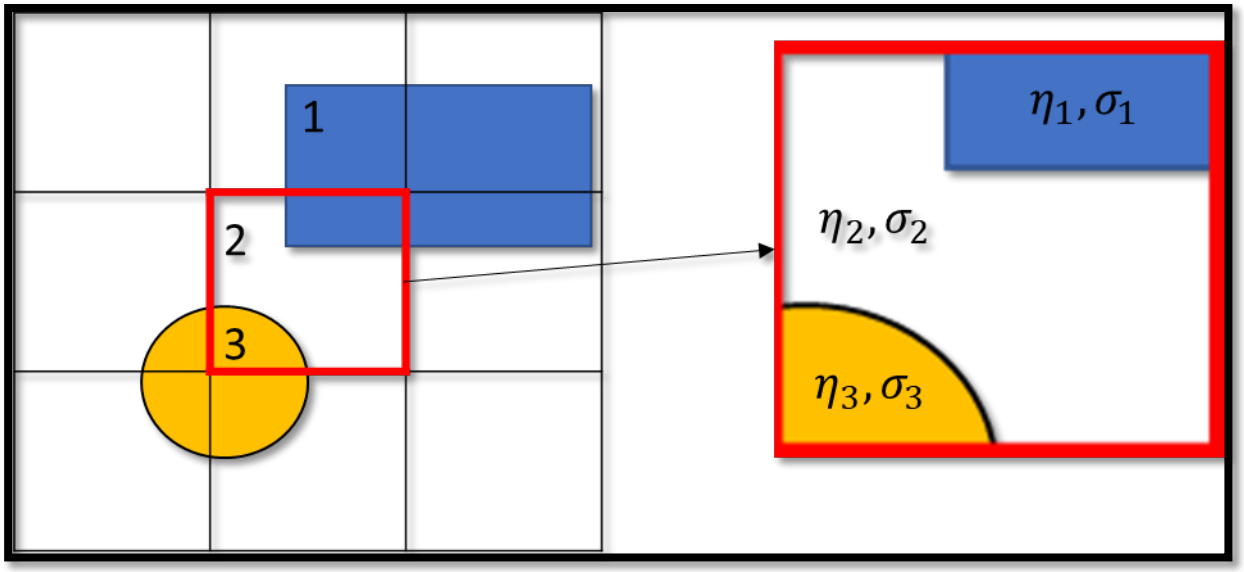

Figure 6-2: Multiple materials in an ALE/Eulerian element, labeling material stresses, σ_k, and volume fractions, η_k, in the expanded image to the right side of the figure. k=1..3 designates each material.

physically wrong in an exact manner, but as an approximation it is simple, effective, and conserves energy [219, p. 22]

In the scenario for the red element in Figure 6-2 above, the entire element has the same mean strain rate. Then via mechanical/thermodynamic relations (constitutive relation and equation of state), each material within the element has its stress, σ_k, calculated. Finally, the composite element stress is calculated via Equation (6-3) below, where nmat is the total number of materials in the element and η_k is the fraction of the total element volume that is material k; volume fraction for short. This allows the numerical solution of the mathematical model in the Lagrangian step with additional stability algorithms included.

$$\bar{\sigma} = \sum_{k=1}^{nmat} \eta_k \sigma_k \tag{6-3}$$

With the Lagrangian step completed, the advection/remap is required to occur. The material that moves beyond the element's domain must be reassigned to an appropriate neighbor element. A part of this, in multiple dimensions especially, requires appropriate material interface

information, so that the correct material is advected. Equation (6-3) above, applies without any reference to the material interfaces. However, if the calculation for the time step following the state shown in Figure 6-2 shows that all material flows one half an element upward, it is important that it is material 1's volume that exits the red element. This control is accomplished by material interface reconstruction algorithms. Amongst the different options for interface reconstruction, LS-DYNA uses the volume of fluids method that looks at the volume fraction of the material in the element and its adjacent elements to identify the correct interface. These surfaces are not necessarily connective between elements, as they are calculated independently, but work approximately. With that established, the advection algorithms can be selected. LS-DYNA offers multiple, but the van Leer 2nd order accurate with half-index-shift method was used [223], [224].

6.1.4 COUPLED EULERIAN-LAGRANGIAN

In an effort to limit the size of the ALE domain, portions of the physical domain were modeled using standard Lagrangian finite elements.[42] This enabled two smaller background meshes to be employed, with interaction between ALE and Lagrangian FEM materials connecting things together, rather than using one large continuously connected and purely ALE mesh. In LS-DYNA, the coupling method used was a penalty-based coupling mechanism. The Lagrangian surface and selected ALE materials are identified for coupling, with a specified number of coupling points per Lagrangian segment. The locations of the coupling points are searched relative to the ALE materials, and a standard penalty formulation is applied to prevent overlap. The coupling essentially applies surface tractions to the Lagrangian segments, while applying velocity boundary conditions to the ALE domain.

[42] The use of this capability has only been found once by the author in literature on impact welding, but the capability was used to different effect in that instance.[237]

6.2 MODEL DETAILS AND PARAMETERS

The explosive welding event models that will be presented used all the different modeling techniques discussed above in Section 6.1, as implemented in LS-DYNA R10.1 [214], [215]. Multi-Material ALE elements modeled explosives and the highly deformed inner layers of the welding surface. The bulk of the aluminum plates were modeled using standard Lagrangian finite elements, and they were coupled to the MM-ALE materials. The model was completely adiabatic, with no heat transfer modeling into/out of the domain or in between elements, and was completed on a Linux CentOS cluster. Compute nodes had 32 processors each, with roughly 250 GB of memory, and OpenMPI MPP communications were used for runs of up to 3 nodes with up to 75 processors. LS-DYNA does not independently account for units, so a consistent unit system is required. In these models, units of cm, μs, Mbar, °K, grams, and 10^7 Newtons are used.

6.2.1 MATERIAL MODELS AND PROPERTIES

As discussed in Section 3.1.2.1, separate modeling was conducted early on in the study, and some material parameters were presented there. Those tables will be referenced as appropriate or supplemented here, as required. Material models and properties will be presented in order for the explosive, aluminum, and void space.

The PETN explosive was modeled using the MAT_HIGH_EXPLOSIVE_BURN formulation in LS-DYNA. This material, as used, requires explosive density, ρ_0, detonation velocity, D_{CJ}, and Chapman-Jouget pressure, P_{CJ}, with values as shown in Table 3-2. Based upon specified ignition points and times, the model ignites the explosive at a linear rate set by the detonation velocity, D_{CJ}. The material model also requires an associated explosive equation of state to define the pressure, volume, energy relation after detonation. The equation of state used

is the Jones-Wilkins-Lee model from [225]. All parameters are shown in Table 3-2, other than V_0, initial relative volume, which was set to 1.[43]

$$p = A\left(1 - \frac{\omega}{R_1 V}\right)e^{-R_1 V} + B\left(1 - \frac{\omega}{R_2 V}\right)e^{-R_2 V} + \frac{\omega E}{V} \tag{6-4}$$

The Aluminum 6061-O was modeled using the Johnson-Cook constitutive relation[182], the Gruneisen Equation of State[226]–[228], and the added Johnson-Cook fracture model [183]. The Johnson-Cook constitutive and fracture model are implemented in LS-DYNA in keyword MAT_JOHNSON_COOK. Equation (6-5a) & (6-5b) identify the expression for the flow

$$\sigma_y = (A + B\bar{\varepsilon}^{p\,n})(1 + c\ln\dot{\varepsilon}^*)(1 - T^{*m}) \tag{6-5a}$$

$$T^* = \frac{T - T_{room}}{T_{melt} - T_{room}} \tag{6-5b}$$

$$\varepsilon^f = max\left(\left[D_1 + D_2 e^{D_3\sigma^*}\right][1 + D_4\ln\dot{\varepsilon}^*][1 + D_5 T^*], EFMIN\right) \tag{6-6a}$$

$$\sigma^* = \frac{p}{\sigma_{eff}} \tag{6-6b}$$

$$D = \sum \frac{\Delta\bar{\varepsilon}^p}{\varepsilon^f} = 1\ at\ failure \tag{6-6c}$$

stress and Table 3-3 above lists the relevant parameters. Here $\bar{\varepsilon}^p$ is effective plastic strain and $\dot{\varepsilon}^*$ is the normalized log-linear, effective total strain rate divided by a reference rate that was set to the value of $10^{-1}s^{-1}$. The strain at fracture is specified by Equation (6-6a) and (6-6b) where the parameters are in Table 3-3; p is pressure, σ_{eff} is effective stress, and EFMIN is the minimum required strain for fracture. For the failure of the ALE Johnson-Cook aluminum, the card ALE_FAIL_SWITCH_MMG was included to switch failed aluminum to void.[44]

[43] The coefficient c in Table 4, is only used in calculating the isentrope P-V relation, which is not directly implemented in this model.[225]

[44] This was included only in the latter models as it was learned it became necessary for stability in the finer mesh. It was considered to switch the material to another JC aluminum fluid group modified for compression only,

The Mie-Gruneisen equation of state is implemented in LS-DYNA using a cubic shock-velocity as a function of particle-velocity using keyword EOS_GRUNEISEN. In the limited review by the author, there appears to be some variation in the exact implementations for this equation of state model by different authors, but early works referenced above identify a term

$$p = \frac{\rho_0 c^2 \mu \left[1 + \left(1 - \frac{\gamma_0}{2}\right)\mu - \frac{a}{2}\mu^2\right]}{\left[1 - (S_1 - 1)\mu - S_2 \frac{\mu^2}{\mu + 1} - S_3 \frac{\mu^3}{(\mu + 1)^2}\right]^2} + (\gamma_0 + a\mu)E \tag{6-7}$$

relating the change in potential energy with respect to volume and a term related to the Gruneisen parameter, internal energy, and volume [227]. That is clearly visible in the compressed matter relation in LS-DYNA shown in Equation (6-7) above. For expanded matter

$$p = \rho_0 c^2 \mu + (\gamma_0 + a\mu)E \tag{6-8}$$

(in tension), the relation in Equation (6-8) above applies. In all equations, ρ_0 is initial density, c is the intercept of the shock velocity/particle velocity (v_s/v_p) relation, γ_0 is the unitless Gruneisen

$$\mu = \frac{\rho}{\rho_0} - 1 \tag{6-9}$$

gamma, a is the unitless first order correction to γ_0, E is internal energy, and μ is defined in Equation (6-9) above. For Equation (6-7), S_1, S_2, and S_3 are unitless coefficients of the slope of the v_s/v_p curve. The values of the Mie-Gruneisen parameters used are shown in Table 3-4 above.

The void space was modeled as a vacuum using keyword MAT_VACUUM with density 1.225 gm/m^3. This formulation is primarily for providing a void space, and the mass is not intended as a physical mass, but rather to avoid numerical instabilities [221].

which would conserve mass, but was not implemented due to time. The default is to switch to a vacuum, but use of this command this appeared to work better than allowing the default to take effect.

6.2.2 Geometry, Elements, and Boundary Conditions

Figure 6-3, below, shows the geometry that was modeled in 2D. Though this was a 2D model, and there are some 2D formulations in LS-DYNA, in this case a 3D formulation was

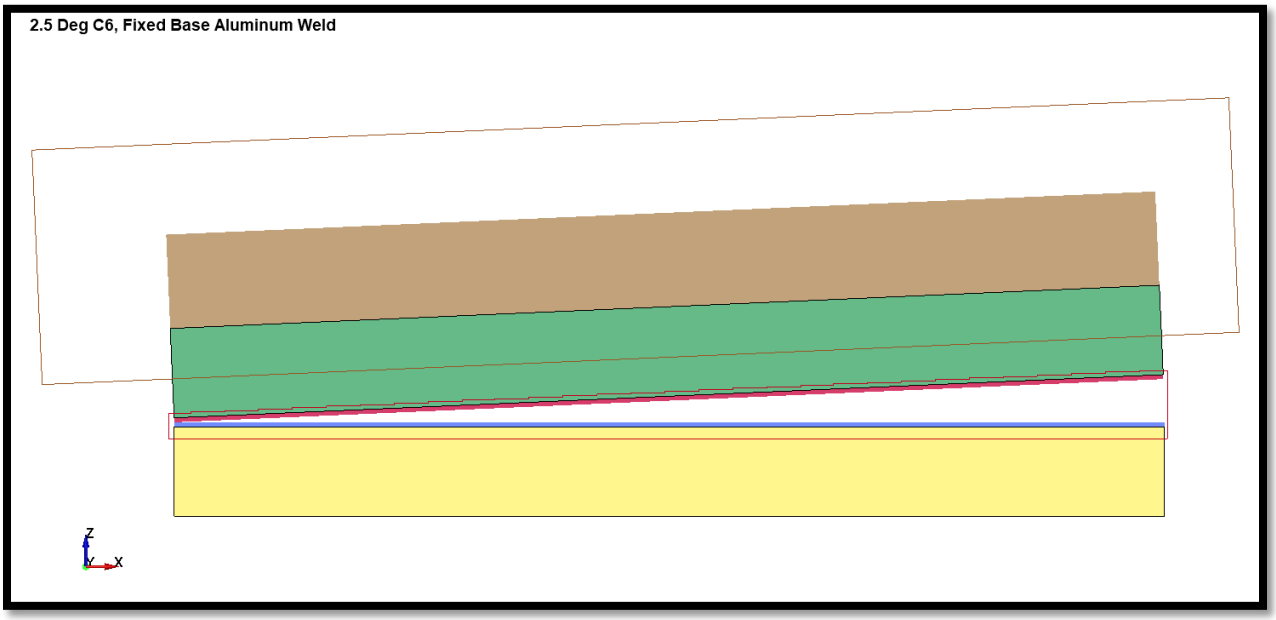

Figure 6-3: Example weld 2D modeling geometry shown for the 2.5° inclination. The solid brown is the explosive. Green and red are the flyer plate, while the yellow and blue are the parent. Red and blue portions of the plates were MM-ALE layers of aluminum. Two MM-ALE background meshes are outlined in brown (explosive) and impact zone (red). 6.7 cm of plate was modeled, initiated on the left.

used. To simulate 2D plane strain, all nodes had a fixed translation condition applied in the *y* direction (for the ALE this generates zero velocity condition in that direction). For the MM-ALE regions, element form 11 (single integration point MM-ALE) was used, and for the Lagrangian FEM regions (green and yellow in Figure 6-3) single point, constant stress elements were used. The full thickness of specimens and explosives were modeled, as if they were 6.7 cm specimens. The bottom nodes for the parent plate were fixed in all directions. For the MM-ALE no boundary conditions were applied in the X & Z directions, so material was allowed to advect out of the domain. Additionally, no pressure boundary conditions were applied.

In order to generate the MM-ALE explosive and aluminum, the two background meshes shown were used. These were meshed with rectangular hexahedron elements parallel to the brown and red outlines respectively, shown in Figure 6-3. This background mesh was initially set to be entirely the void material. The solid brown, red, and blue portions of Figure 6-3 representing explosive and aluminum MM-ALE layers, are actually shell element containers used to identify the geometry. After initialization, the INITIAL_VOLUME_FRACTION_GEOMETRY keyword was used to fill those elements with the appropriate volume fraction of explosive and aluminum respectively. The aluminum MM-ALE material for the flyer and parent plates were listed as separate fluid groups (AMMGs) in order to track their interface and prevent automatic welding. Detonation points were placed down the left side of the explosive at the spacing of the elements in the background mesh.

6.2.3 Euler-Lagrange Coupling, Mesh Motion, and Hourglass Control

6.2.3.1 Euler-Lagrange Coupling

The general theoretical details of Euler-Lagrange coupling were outlined in Section 6.1.4. This is implemented in the CONSTRAINED_LAGRANGE_IN_SOLID card. Specific MM-ALE parts were coupled to specific Lagrangian meshes (e.g. explosive only to the parent plate). The number of coupling points were adjusted to try to keep two coupling points per ALE element (not counting the y direction). The coupling types were either type 4 or 5, which apply as described for elements without or with erosion, respectively. Leakage, where the MM-ALE material passes the boundary, was a problem at times (for the explosive). The parameter ileak=2 was commonly used for the most robust leakage control possible. For the explosive to plate coupling, only pressure was coupled, but for the aluminum to aluminum couples, direc=3 was specified, coupling shear and tensile tractions as well.

Significant effort was spent to identify optimal numbering of coupling points. More coupling points per Lagrangian segment can eventually cause instability. This became evident, as the *y* dimension did not change, even though the number of coupling points was expanded (NQUAD expands simultaneously in both normal directions on the segment face). In certain cases, hourglassing in the *y* direction was visible and large NQUAD values generated the instability more frequently. Ultimately, the LS-DYNA user's manual and other sources recommend keeping the ratio of the Lagrangian and Eulerian element sizes close to unity. As stated, the model's elements were roughly at a ratio of 2:1. This was done to try to limit the number of elements in regions of less interest, but in the end, limits on the size for NQUAD before instability prevented further enlarging explosive mesh and Lagrangian mesh sizes.

6.2.3.2 Background Mesh Motion

The motion of the background mesh is one of the more important aspects of the modeling. Several options are available. In general, the option to use curves prescribing the motion and deformation of the mesh was selected. However, for the initial coarse mesh models, the option for the impact mesh to automatically follow the mass center of the ALE material was used. This allowed the opportunity to identify what mesh motion was necessary spatially before prescribing a set motion. In general, the explosive background mesh was made twice the size of the flyer Lagrangian mesh, and was prescribed to translate down and to the right to follow the path of the flyer plate. No mesh distortion, expansion, or contraction was applied for the explosive, but the motion kept the explosive applying pressure to the plate throughout motion.

For the impact background mesh, the size would generally be ½ the size of the Lagrangian FEM part meshes. In nearly all models, it was expanded, horizontally to the left, as the start of the bond zone was forced that direction. In many models, it expanded vertically (z

direction), as well. This was necessary to keep the leftmost portion of the weld ALE material in the domain as the parent plate compressed downward, while simultaneously keeping in a portion of the flyer plate that had yet to move down on the right side. After a period of time, all of the flyer would be moving downward, and then the domain just translated vertically.

In the more refined models, the vertical expansion of the impact mesh did start to generate some instabilities. In some cases, it may have been due to advection, but in other cases, it appeared to be due to numerical roundoff for the element z coordinate, which would artificially contract the z directed size of certain elements. This would result in microbursts of pressure in the affected elements and generally led to instability. For the finest meshes evaluated in the 2.5° inclination, vertical expansion had to be removed to get successful runs. For the 1.5° and 0.5° models, likely due to the narrow gaps in those setups, the finest mesh runs were only successful when the initial spatial domain modeled was expanded and switched to be Eulerian (a simple adjustment that only applies to mesh motion). For those inclinations, the added memory requirement from the expanded mesh's initial dimensions were easily offset by a reduced requirement following from the decreased standoff relative to the 2.5° or 8° cases.

6.2.3.3 Hourglass Control

A comparison of the different available hourglass control options was conducted. LS-DYNA offers a default viscous LSTC formulation, the Flanagan-Belytschko viscous and stiffness forms, Quintessential Bending Incompressible (QBI) control, as well as others. In certain cases, it was believed to be observed that excessive hourglassing was eroding Lagrangian elements before it was totally appropriate (this was partly associated with the number of coupling points discussed above). Due to high velocity deformations, it was expected that viscous forms would be preferable. This proved true, although there was some success with the Flanagan-

Belytschko stiffness method. In the end, the LS-DYNA default viscous formulation with the default values proved the most effective at controlling extreme hourglassing, while not overly stressing elements causing earlier erosion.

6.3 CHALLENGES IN MODELING

Using the formulation above was not without challenges. Some were discussed above already. The ones referenced above include uncovering the recommended use of ALE_FAIL_SWITCH_MMG, the stability issues discussed with mesh motion, the leakage in the Euler-Lagrange coupling, and the instabilities associated with element sizes and coupling points (NQUAD). Additionally, in arriving at the decision to use the ALE_FAIL_SWITCH_MMG card, it became clear that in older versions of LS-DYNA, element erosion for MM-ALE literally deleted the background element, which inserted a gap in the domain [229]. Correspondence with the author of [229] confirmed that newer versions have a default switch-to-vacuum formulation instead, but the keyword puts the modeler in explicit control.

There were also further challenges. The use of the penalty coupling formulation that accounts for erosion proved critical, as Lagrangian element erosion under the explosive proved inevitable. Without that formulation, the model vented explosive through the flyer plate, affecting the validity of the result even in the cases where it did not cause complete instability or run failure.

For initially filling the inclined ALE plates with material, an alternative to volume filling into a uniform mesh is to make separate part meshes that are connected on their boundary nodes. This was the method for generating the geometry that was initially pursued. This resulted in very thin, pentahedral elements that appeared to cause tremendous stability issues. The use of regular rectangular or cubic hexahedrons is strongly recommended.

Many favorable results were obtained. Additionally, many of the lessons learned boiled down to following recommendations that can be found in literature or internet searches from LS-DYNA or other sources, which ought to be deviated from only when time is available for experimentation.

6.4 MODELING RESULTS

6.4.1 MACRO-LEVEL COMPARISONS TO EXPERIMENTS

In Section 5.2.1, large-scale deformation and damage observations were discussed in light of the recommended practices for their control from literature. Figures 3-15, 3-19, 3-21, & 3-23, all showed failures of the flyer plate edges. This was consistent and related to edge effects from spalling and to lack of confinement, which was discussed in the Design of Welds portion of Section 2.2.2.3. Figure 6-4 below, predicts this behavior at the edges of the modeled domain. However, in this case, the results indicate that this is primarily associated with shearing towards the unconfined material edges, rather than any tensile/spalling behavior.

Figure 6-4: Prediction of edge failure based on modeling. Shown is the explosive ALE in blue and the Lagrangian FEM flyer plate in green. (a) shows the left end of the model, and (b) shows the far end. In both cases, and consistent among all models, these edges without material and explosive confinement predicted spalling.

6.4.2 Modeled Result for Welding Parameters

The measurements of modeling weld parameters were taken in an average manner in all cases. The pressure distribution in the event was viewed over several timesteps until a steady state was achieved relative to the collision point, before any data point extraction was attempted. For the plate velocity, a point on the leading edge of the flyer plate was identified and related to a Lagrangian node nearest it after the MM-ALE layer. Then the solution was advanced in time, similar to the representation in Figure 2-17 b), until the material underneath the Lagrangian point had traversed a significant amount of its travel toward the collision point. The spatial coordinate was then identified relative to the Lagrangian node, for the new leading edge of the flyer plate. The distance was calculated, and then the average velocity was generated by dividing by the time elapsed. Initial points were selected just after the peak pressure in the bottom face of the flyer (i.e. under the detonation point and already primarily accelerated). The final points were selected before getting too close to the collision point where rapid deceleration is occurring due to flow stagnation.

The state (point in time) used to begin plate velocity tracking was also used for the measurement of the impact angle. Spatial points (away from any localized curving from initial bending or collision effects) along the flyer were used to calculate an angle relative to the horizontal parent plate.

For the measurement of the plate velocity, the same starting state was used to identify the location of the collision point. Then the model was advanced in time as much as possible, where another point was identified to allow for an average velocity calculation.

Table 6-1 below, summarizes the results from modeling in LS-DYNA with comparisons to measured and NMAP modeling values. As discussed in Section 6.2.3.2, in the most refined runs, some adjustments to the background mesh were required to get stable runs. Some runs had

Table 6-1: Weld parameter modeling results compared to other modeling and measurements. Plate velocities from TOA pins are likely inaccurate. LS-DYNA mesh size refers to initial size of impact zone background mesh. Nonlinear Meshfree Analysis Program, as discussed in Ch. 3 results included for comparison. [180], [230]

			0.5°	1.5°	2.5°	8°
Plate Velocity (mm/μs)	TOA Pin		0.40	0.40	*2.82*	*1.88*
	NMAP*		0.38	0.38	0.92	0.92
	LS-DYNA (by mesh size)	100 μm	0.61	0.62	0.74	0.80
		50 μm	0.61	0.61	0.81	0.84
		20 μm	0.61†	0.65†	0.77‡	0.83
Weld Velocity (mm/μs)	TOA Pin		5.83	5.07	*6.13*	*4.62*
	X-Ray		6.17	4.58	5.00	3.39
	NMAP		6.30	4.80	5.30	3.60
	LS-DYNA (by mesh size)	100 μm	6.21	5.46	5.46	3.82
		50 μm	6.30	5.43	5.47	3.90
		20 μm	6.33†	5.53†	5.50‡	3.87
Impact Angle (°)	X-Ray		4.1	5.2	9.8	15.9
	NMAP		3.7	4.6	9.8	15.6
	LS-DYNA (by mesh size)	100 μm	5.5	6.3	8.5	14.4
		50 μm	5.2	6.7	9.0	14.3
		20 μm	5.2†	6.9†	8.9‡	14.0

* NMAP plate velocity values from modeling of flyer and explosive only
† 0.5° and 1.5° 20 μm meshes were converted to Eulerian with added domain expanse
‡ 2.5° 20 μm mesh model results were based on an adjusted background mesh motion, relative to earlier runs (vertical expansion eliminated & extra domain expanse added).

differing degrees of leakage of ALE explosive through the Lagrangian coupling surfaces, but all leakages in final runs were deemed insignificant in the modeled result, especially for the parameters of interest. Given those differences and the non-monotonic nature of some of the parameters extracted, it did not seem appropriate to try to describe convergence properties based upon the mesh refinements conducted.

In general, the modeling is quite close. The results for the 0.5° and 1.5° predict higher velocities and angles compared to other measurements and modeling, while the results for the

thicker explosive predict lower velocities and angles. For the welding window parameters of weld velocity, V_w, and impact angle, β, all of the predictions are within 30% of the measured values. This could be improved if a more detailed parametric study could be taken, including the opportunity to measure exact material parameters; if certain other parameters within the MM-ALE and Lagrangian model were calibrated; and if time for other model adjustments was available. This level of capability would certainly serve to facilitate weld design.

6.4.3 PREDICTION OF JETTING

The modeling formulation predicted jetting in two of the four cases as shown in Figure 6-6, 6-7, 6-8, & 6-9. The 2.5° and 8° models had jetting predictions at all three mesh resolutions, while the 0.5° and 1.5° models did not have jetting at any resolution. This was consistent with what was found using NMAP by another modeler [180], [230]. This is a very practical and critical result, as jetting is a precondition for the best quality welds. The modeling even provides good detail on the jets. Material from both the parent the flyer plates are shown entering the jet, as shown in Figure 6-5. For the 2.5° and 8° cases, the thicknesses of the jets were less than that predicted by the first order, inviscid & incompressible approximation as shown in Table 6-2. Interestingly, the 2.5° case, which appears to be the most accurate model, is 26% less than the incompressible/inviscid fluid analogy, just as was identified above in Section 2.2.2.2 and mentioned [88].

Table 6-2: Modeled jet thickness versus prediction from Equation (2-9)

Case	Prediction	LS-DYNA	LS-DYNA/Prediction
0.5°	54 μm	None	N/A
1.5°	84 μm	None	N/A
2.5°	148 μm	107 μm	73%
8°	380 μm	152 μm	40%

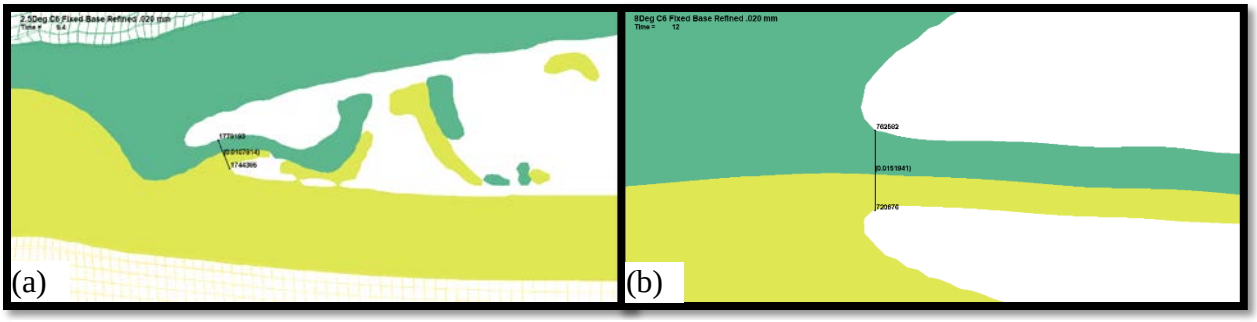

Figure 6-5: Jet thickness from modeling. Distances labeled inside of the parentheses are in cm. (a) 2.5° case. (b) 8° case.

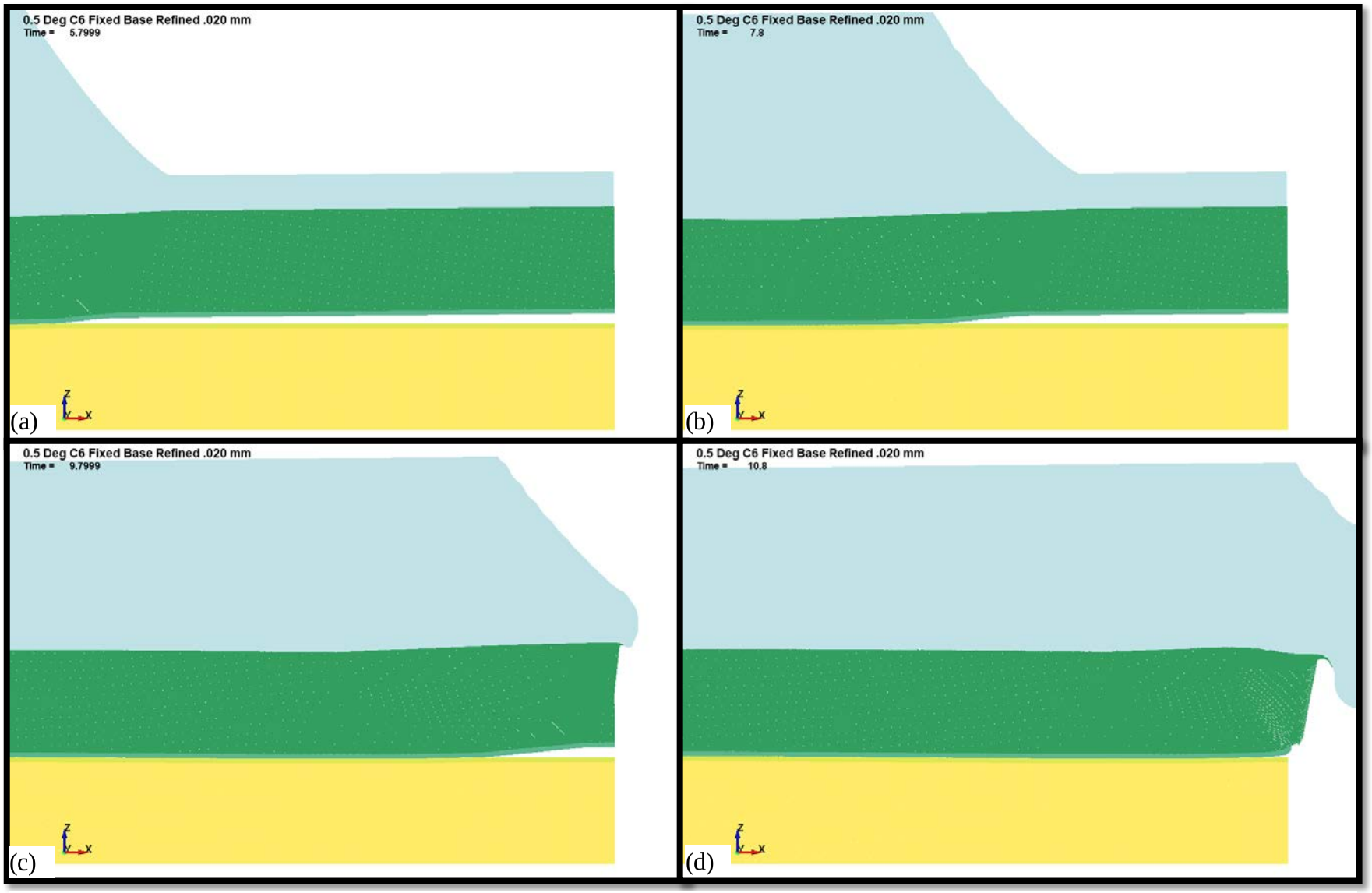

Figure 6-6: Modeling of 0.5° case showing snapshots of the result. No jetting predicted by this model.

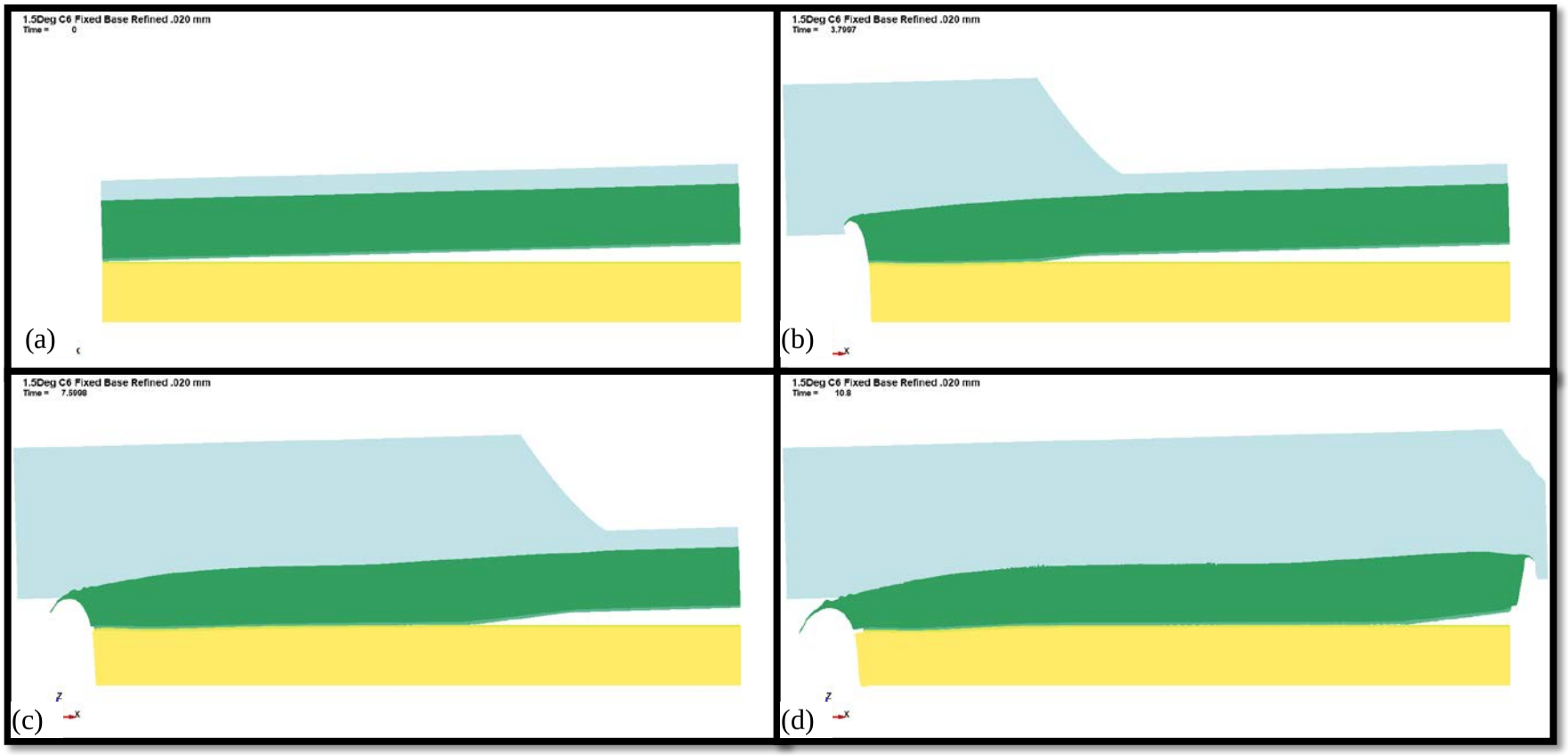

Figure 6-7: Modeling of the 1.5° case. No jetting is visible in this model.

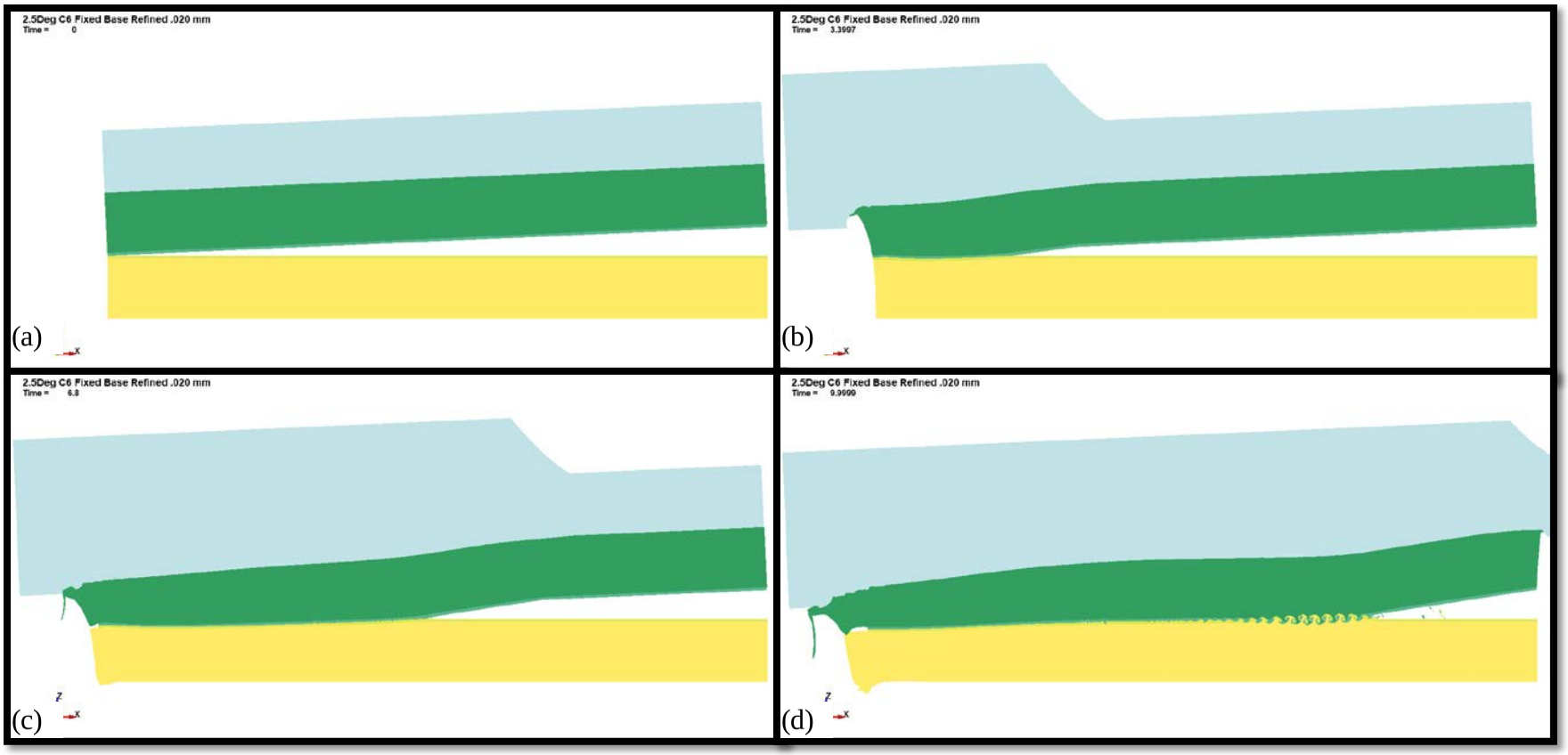

Figure 6-8: Modeling of 2.5° case. Jetting is visible in (c) and (d). Also in (d) a wavy interface with vortices is clearly produced by the model.

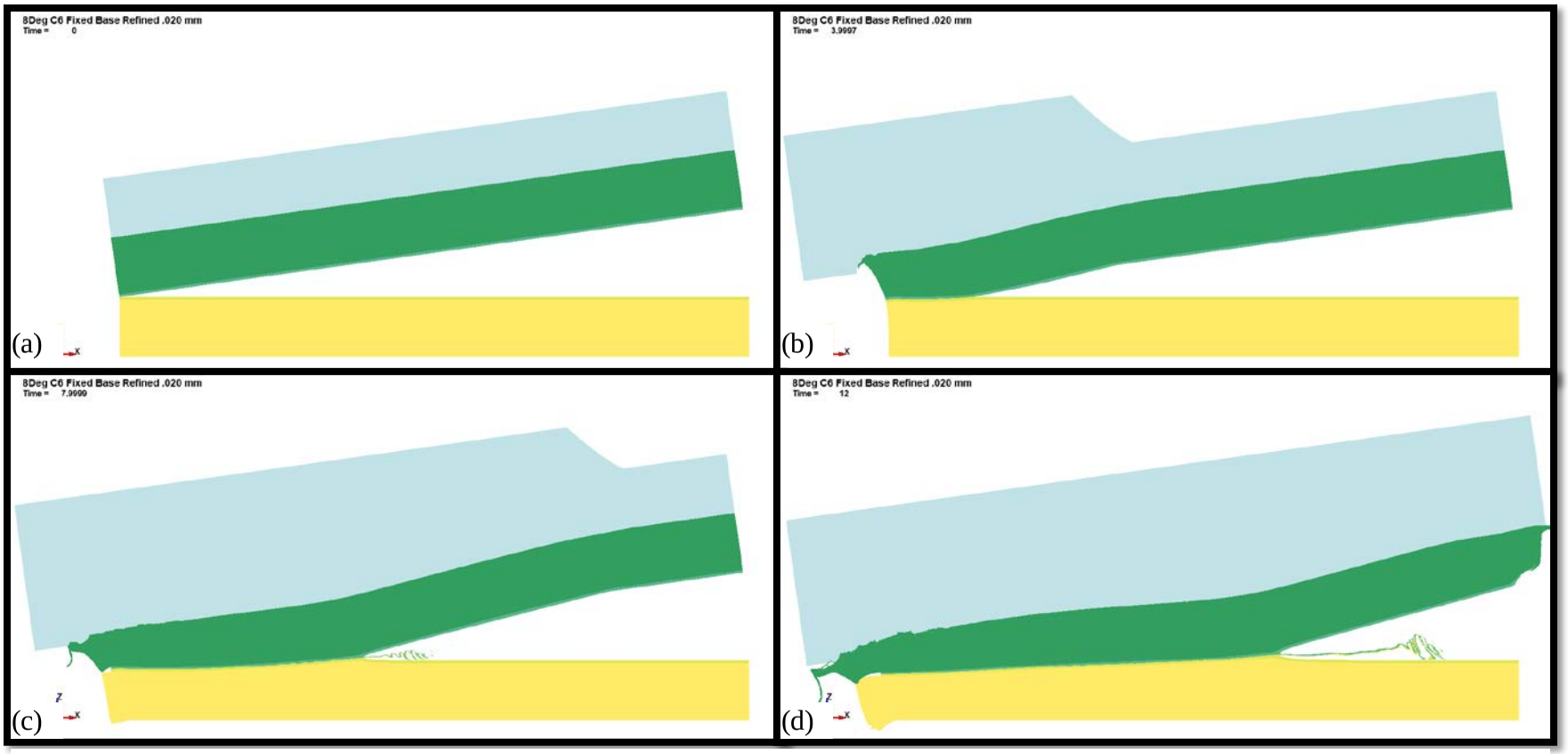

Figure 6-9: Modeling result for the 8° case. Jetting appears in (c) and (d).

6.4.4 WAVELENGTH AND AMPLITUDE PREDICTION

Figure 6-10 and Figure 6-11 below, show the positions and nodes used for identifying the wavelength and amplitudes generated in the models. The 2.5° case in Figure 6-10, has general

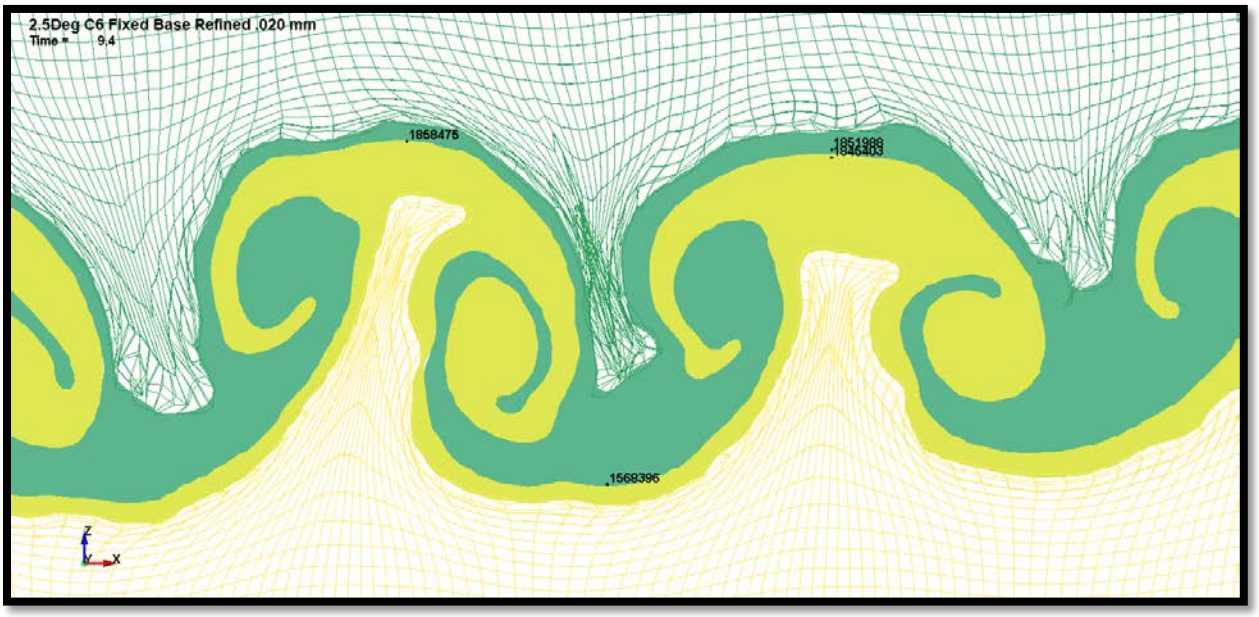

Figure 6-10: 2.5° wave and amplitude measurement positions. Wavelength, λ = 1.07 mm. Peak-to-peak amplitude, 2a = 846 μm measured from bottom node to line connecting top nodes. a/λ = 0.396

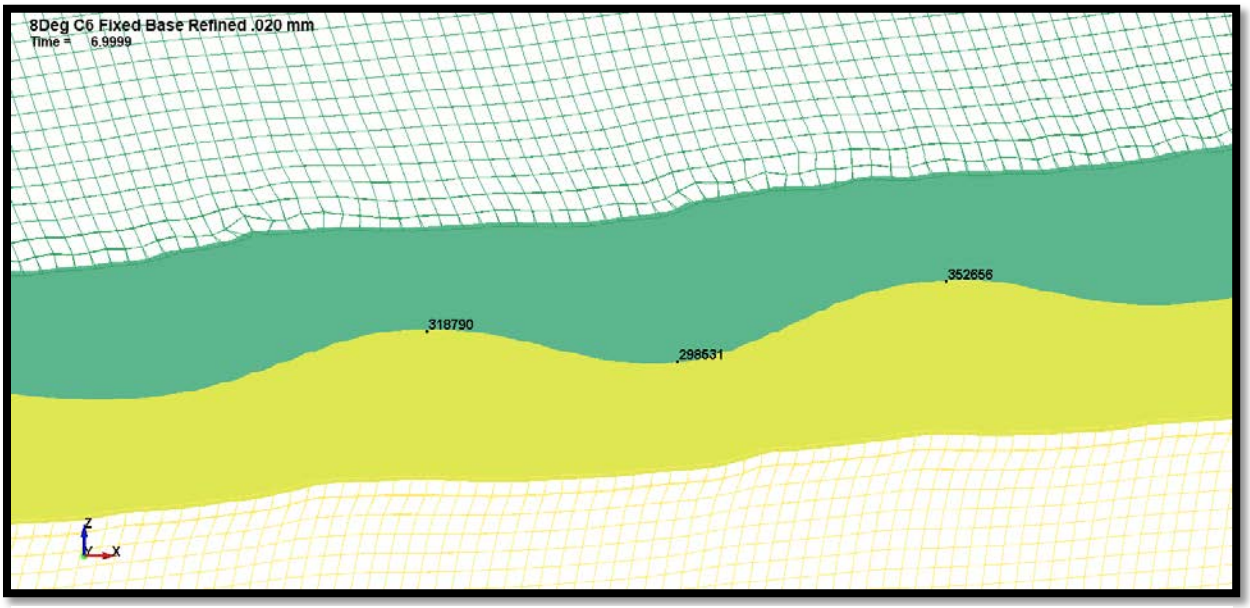

Figure 6-11: 8° wave and amplitude measurement positions. Wavelength, λ = 1.13 mm. Peak-to-peak amplitude, 2a = 117 μm. a/λ = 0.052.

agreement with the measured and predicted values in Table 5-3 from Chapter 5. For the 2.5° case, the modeled value of 1.1 mm is within about 15% of the measured value. The peak-to-peak amplitude is within 6% of the measured value. However, the 8°case is less accurate. The modeled wavelength of 1.1 mm is 45% less than the measured value of 2 mm, and the modeled peak-to-peak amplitude is 89% lower than the measured value of 1.1 mm.

As noted above, in order to get the models to run with the more refined impact meshes, it was necessary to make adjustments to the modeling technique for all but the 8° case. For the 2.5° case, the vertical mesh expansion that had been in place (and that was in place still for the 8° 20 μm mesh) was removed, leaving only translation for the vertical motion in the background mesh. This was the model run that resulted in the more accurate wavelength and vortex results.

It is interesting to note that the waves began to appear in the 8° case, reached a peak intensity, and then suddenly stopped being generated. The rough time in the model where the waves stopped being generated coincides with the time shown in Figure 6-11, t = 7 μs. Additionally, between 6.5 and 7 μs (the spacing of results recorded), the model's background mesh experienced significant change in its motion. At 6.8 μs, the horizontal expansion, keeping the left end of the weld largely within the domain was halted. At 6.6 μs the vertical mesh coordinate control went from an expanding mesh to a purely translating mesh. Both transitions were abrupt and may have been related to the disappearance of wave formation. However, similar transitions for the horizontal mesh motion remained in the 2.5° model. In the 8° model, the mesh motion transition from simultaneous vertical expansion and translation, to only vertical translation is the salient difference with the mesh motion in the 2.5° model.

6.4.5 Other Modeling Connections to Theory

6.4.5.1 Evidence Supporting Kelvin-Helmholtz Wake Instability Behind the Collision

While the jetting that occurred in the models of the 2.5° and 8° cases was physically separated from the flyer plate and shows no support for Hunt's Kelvin-Helmholtz instability in front of the collision point [53], there is support for the "Kelvin Helmholtz" wake instability behind the collision point. As noted in Section 2.2.3.1, in fluid mechanics this type of instability, caused by a continuously varying velocity profile is still commonly referred to by the "Kelvin Helmholtz" name, even though it is not the classical case, nor was it studied by either Kelvin or Helmholtz. The velocity profile in question for the steady state coordinate system, is a wake behind an interior obstruction, similar to that shown in Figure 2-32. This consists of a profile with a slower velocity at a central elevation, and then, on both sides of the slower layer, an inflection followed by an asymptotic, faster velocity. Figure 6-12 below, shows two examples of the jet wake velocity found in modeling. Figure 6-12 (a) is at the point in time immediately prior to the start of interfacial wave generation, and (b) shows how the velocity profile persists in a disturbed state after the waves have begun forming. Note that the modeling coordinate system is not the traveling, steady flow coordinate system, but that the inner layer jetting towards the right relative to material above and below it is a similar relative profile.

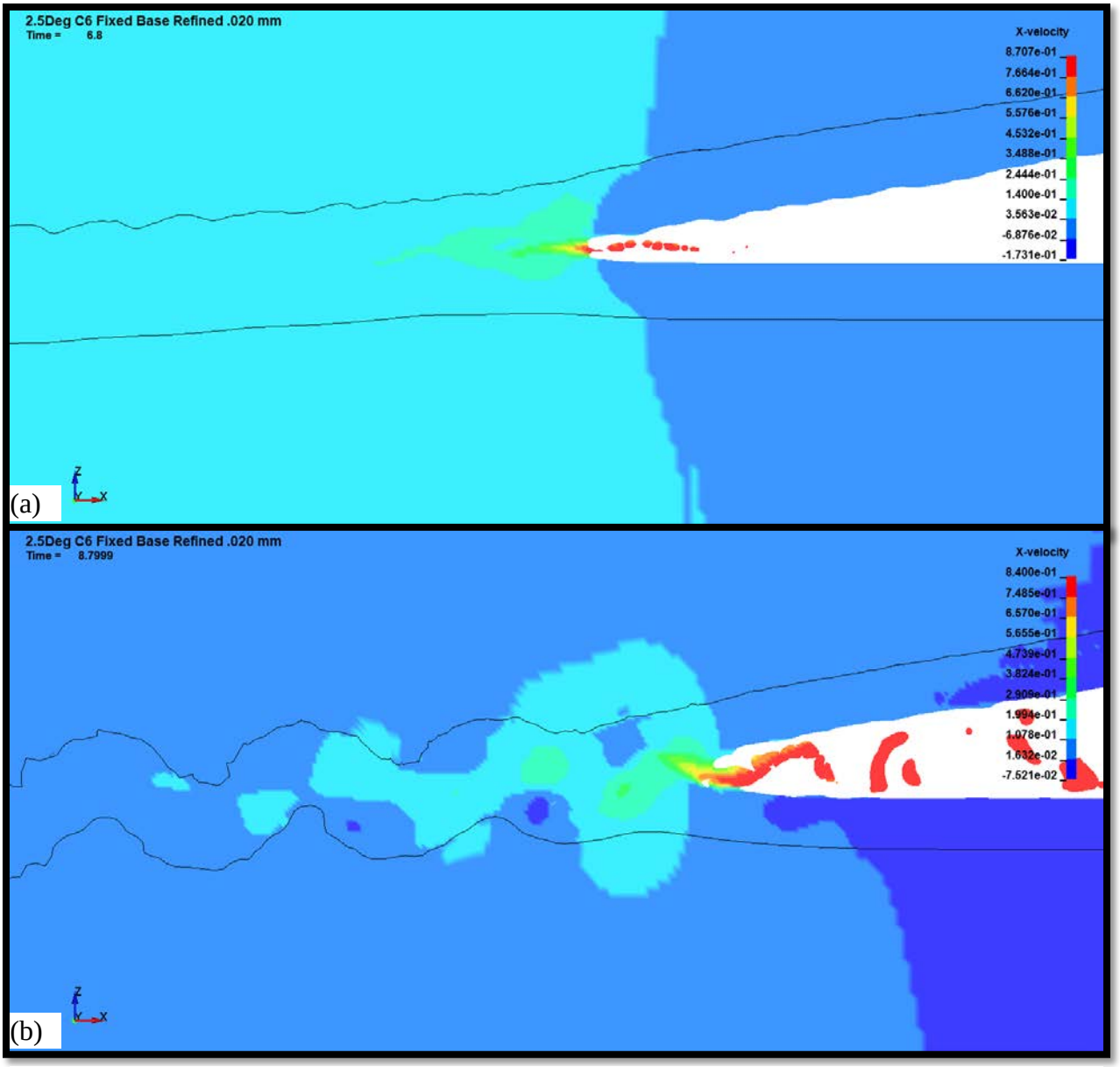

Figure 6-12: Velocity wakes behind the collision point shown as modeled in the 2.5° case at two times.

6.4.5.2 Modeling Support for the "Hump"

In Section 2.2.3.1 and Section 2.2.3.4, humps near the collision point were discussed. The indentation mechanism, proposed by Bahrani, Black and Crossland as a modification of Abrahamson's model suggests that a hump is formed, and that it is accompanied by an associated indentation, as shown in Figure 2-25. Prior modeling work shown in Figure 2-36 & 39, among

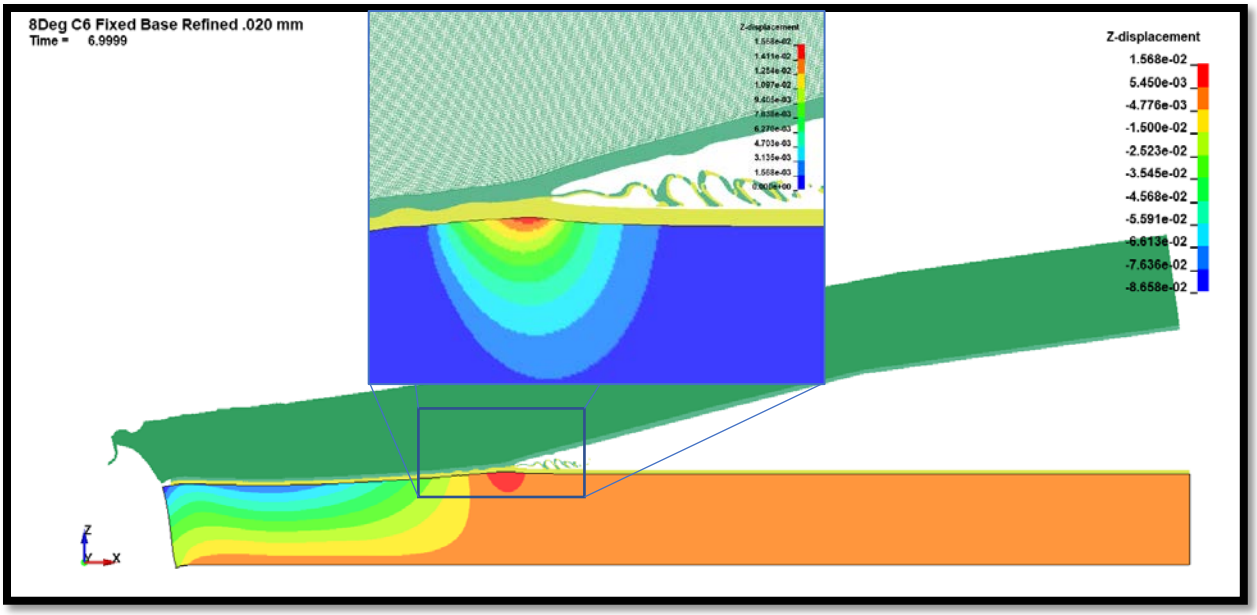

Figure 6-13: Support for the "hump" associated with the indentation mechanism is shown.

other works, supported the idea that a hump is indeed formed. The modeling in this study further adds to the numerical support for the formation of a hump, as shown in Figure 6-13. However, the hump that is predicted does not appear to be similar to the indentation hump of Figure 2-25. In Figure 6-13, only vertical displacement of the parent plate is fringed to identify positive vertical displacements. It is clear that near the hump, which clearly forms, there is not an immediately following penetration or indentation that could be associated with the fluid jet. The indentation does appear in Abrahamson's fluid/grease model [32] and some depression is visible in the images in Blazynski's liquid analogue experiment [142], but in both cases it is formed much closer to the collision point than this model supports. Those early analogues, while illustrative use materials of significantly differing properties with no ability to replicate the elastic-plastic transition required to truly replicate the behavior of metals.

However, this model does seem to support the formation of a hump, but just one that raises uniformly underneath and adjacent to the collision point. Within the model, it was possible to follow through time as the individual hump forms underneath the collision point, and

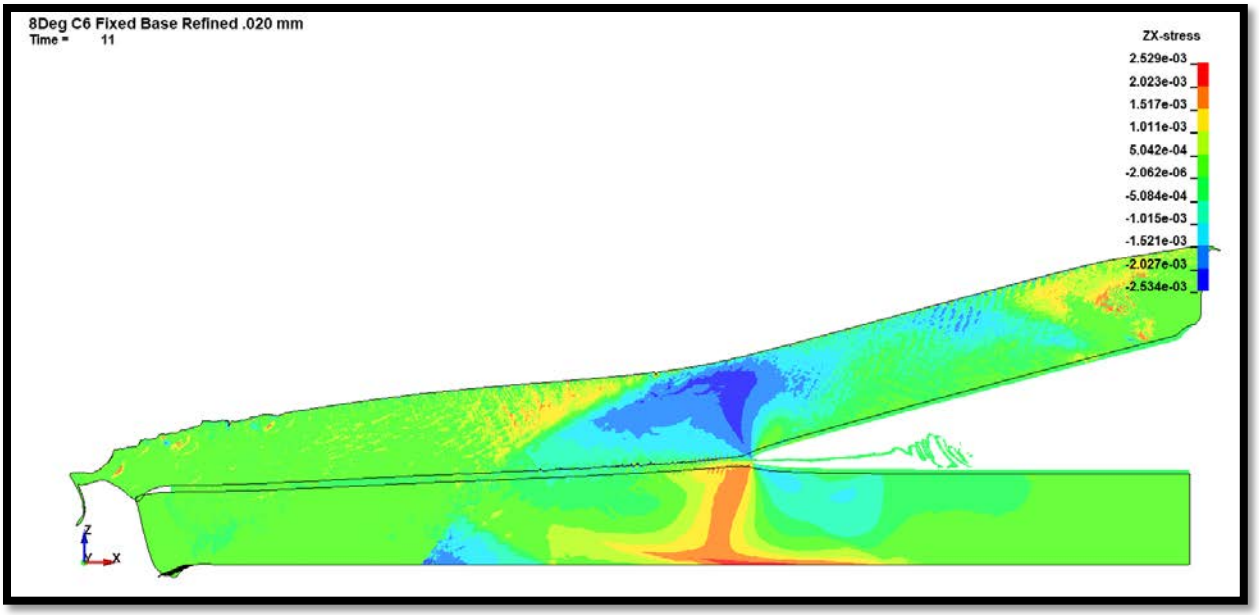

Figure 6-14: Shear shock front traveling just ahead of the collision point in the 8° model.

progresses across the parent plate in step with the collision. This is supportive of a traveling Rayleigh-type surface shock wave. If this mechanism is true, there could be an associated shear shock wave front that is also traveling with the collision point. Figure 6-14 shows the presence of a shear shock front that is visible in LS-DYNA model, when viewing shear stresses. As the top of the parent plate is struck, a positive XZ shear is induced. The elastic shear wave velocity would be about 3.1 mm/μs, but the collision point travels at ≈ 3.9 mm/μs in this model.[45] The strain rate sensitivity of the Johnson-Cook constitutive model supports the formation of this shock, and its presence is what would be expected if the "hump" were consistent with a traveling Rayleigh-type surface shock wave.

6.4.5.3 Evaluation of Acoustic Criteria for Wave Initiation

Although the intent for the 2.5° case was to select a weld velocity that was just below the acoustic speed of the material, it is actually just above that speed. That makes the 8° case the

[45] At this point of time in the model, the elastic dilatational waves are just ahead of the jet.

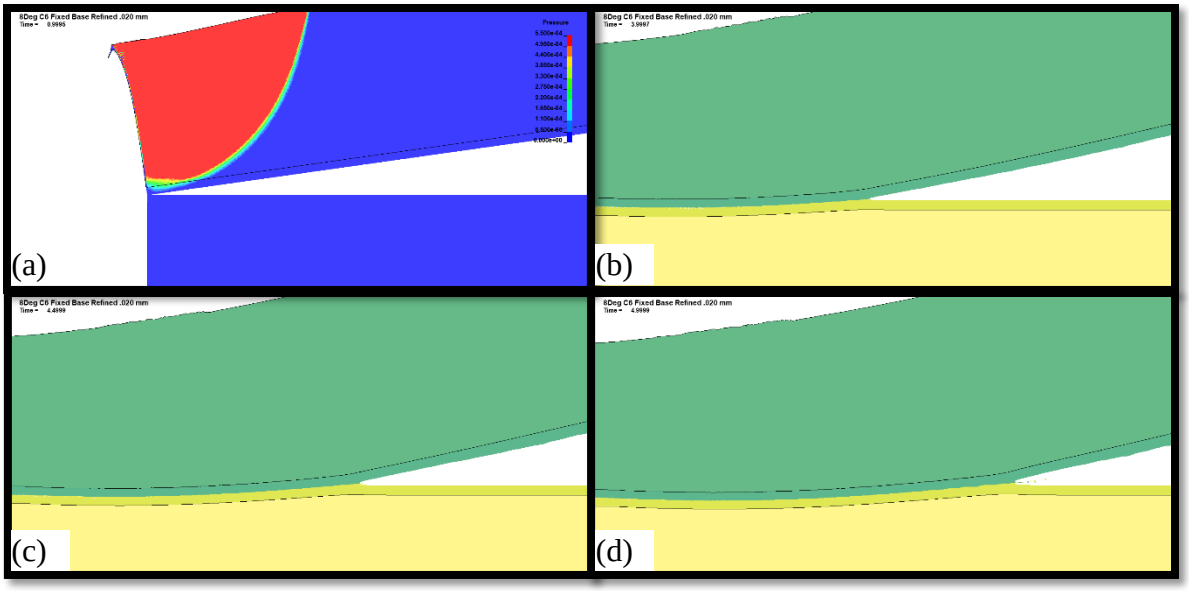

Figure 6-15: Acoustic wave theory assessment. Time for rarefaction arrival ≈ 3.5 μs. [101] (a) Plot showing the arrival of the first stresses to the parent plate as roughly 1 μs. (b), (c), & (d) Consecutively recorded resultant states in the vicinity of when rarefaction would arrive according to the theory. Subtle waves can be seen in (d).

only one where the timing of the arrival of the rarefaction wave from first contact could be compared to the formation of waves. This comparison is shown in Figure 6-15. Subfigure (a) shows that the flyer plate first impacts the parent plate at roughly 1 μs. The expression suggested by Godunov et al is used to estimate the arrival of the rarefaction wave back to the surface of the impact. This time was calculated in accordance with Equation (2-15) from [101] to be ≈ 3.5 μs. The next three subfigures show the bond interface at intervals before and after that arrival timing. In the last, small boundary interfacial waves are seen to begin to appear.

As discussed in Section 2.2.3.3, the author believes that the primary instability is generated at the interface due to the wake velocity profile, which Section 6.4.5.1 supports. Once unstable, any number of triggers would conceivably suffice to initiate an instability. The conditions of the unstable velocity profile were present by the state shown in Figure 6-15, and so this model could conceivably evaluate whether this mechanism could be a part of a trigger.

Based on the initiation of waves at this point, though small, there appears to be reason at least to consider the theory not disproven.

6.4.5.4 Lack of Stress-Wave Mechanism Support

The author is skeptical of the stress wave mechanism. As covered in Section 2.2.3.1, it suggests that waves will form on the surface of the flyer plate prior to it impacting the surface of the parent plate. While there is some measure of graininess and resolution that limits the X-Ray image's ability to corroborate this idea, however some of the images, especially the 1.5° case shown in Figure 3-27, do show some measure of surface waviness. However, this is not consistently shown in the X-Ray images. Some waviness can be seen in the 2.5° flyer plate edge as it closes with the collision point, but it occurs on a wavelength that is too small to make sense. The acoustic speed at roughly 5.3 mm/μs, would require over 2 μs to traverse a direction normal to the plate surface, while the waves shown in the flyer are much smaller than that. Figure 6-16 shows the progress of the acoustic wave front, and it is clear it is not associated with the visible waves in the flyer surface. All variations of fringe range fail to recover any other wave fronts.

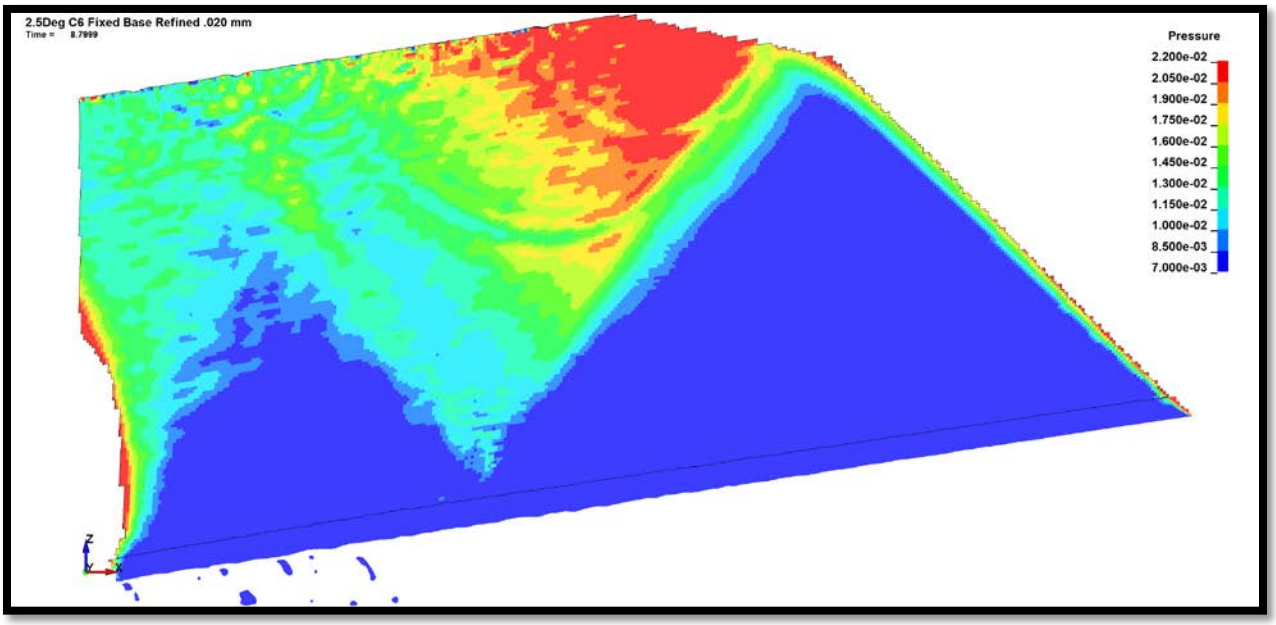

Figure 6-16: Flyer acoustic wave front for the in-flight portion of the plate shown in the 2.5° model.

6.4.6 TEMPERATURE PREDICTIONS

With the use of the Johnson-Cook and Gruneisen models, adiabatic temperature effects are included in the model. Either the implementation, some part of the MPI related plotting, or the post processing does appear to have mixed some data, but in general some interesting results were found.[46] While this is based on only adiabatic effects, the modeling does predict melting in certain areas. Figure 6-17 – 6-20 show the homologous temperature $T - T_{room}$ for selected states. The homologous melt temperature would be 632°C, which is the red limit of the fringe plot. Interestingly, the 2.5° case which had the worst weld, has the largest region with temperatures exceeding the melt temperature.

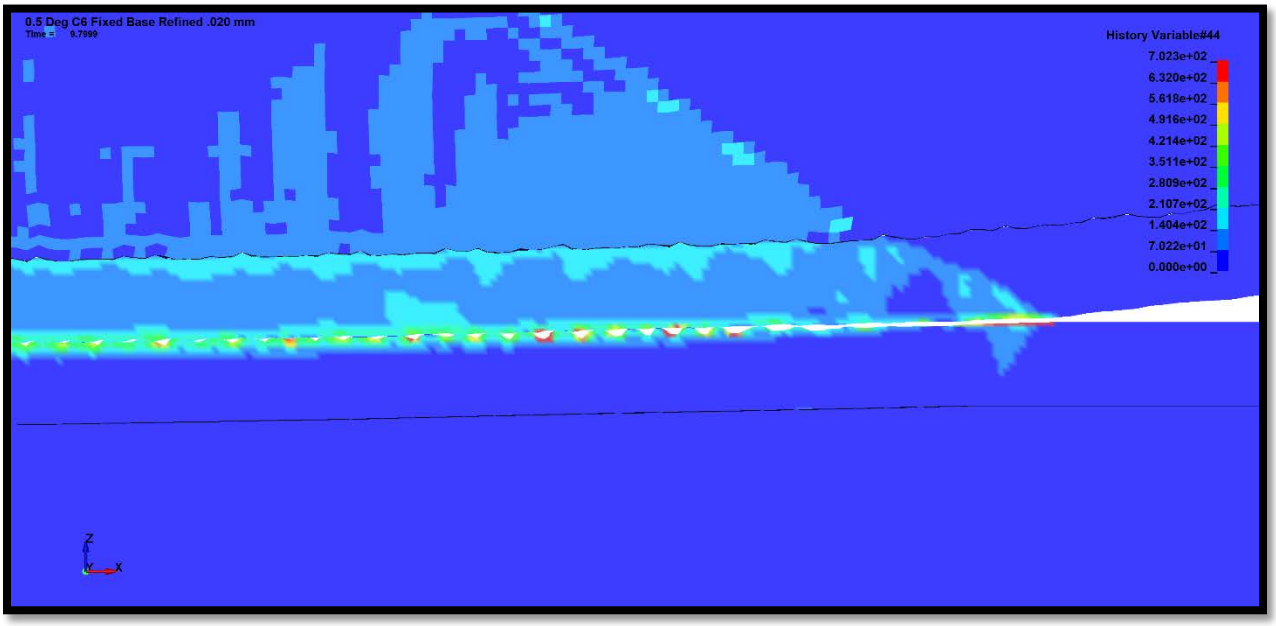

Figure 6-17: 0.5° temperature distribution at t = 9.8 μs.

[46] For the 8° case, the temperature data for the MM-ALE layer in the parent plate was unable to be recovered in time for inclusion.

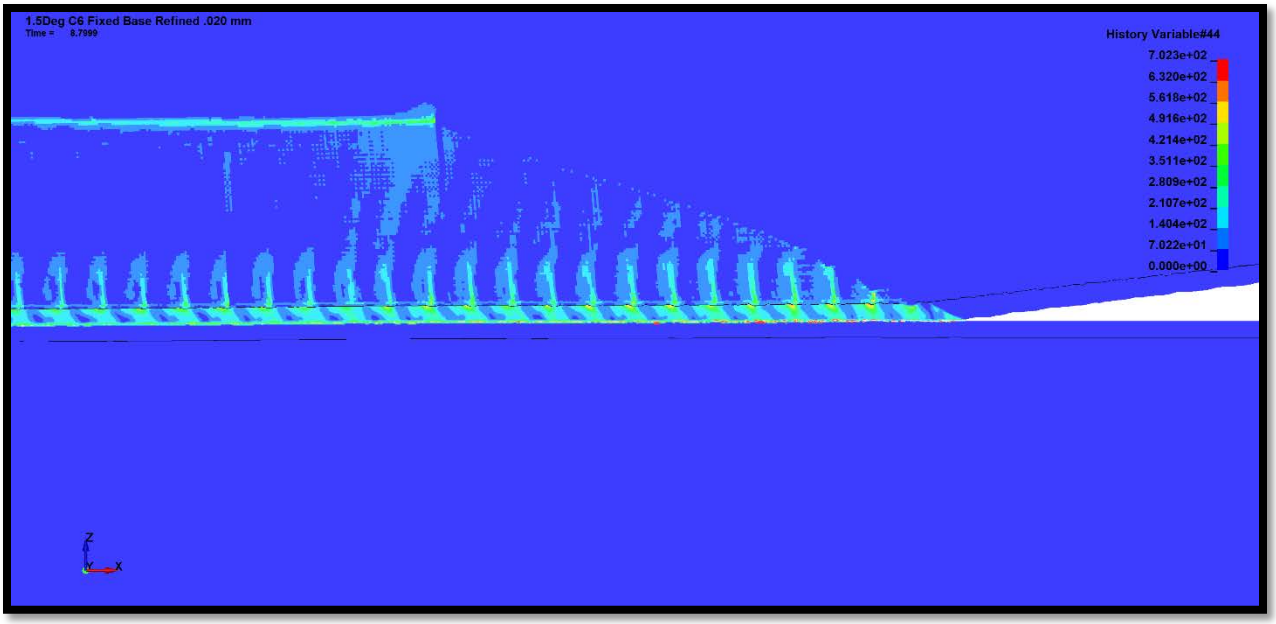

Figure 6-18: 1.5° temperature distribution at t = 8.8 μs

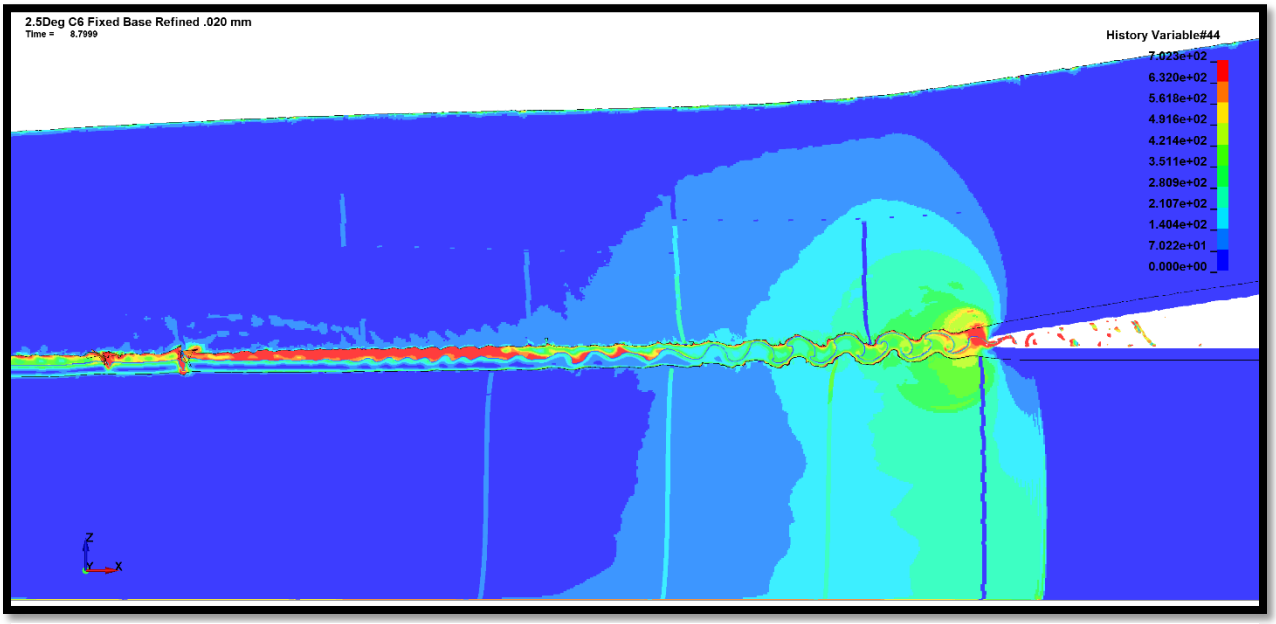

Figure 6-19: 2.5° temperature distribution at t = 8.8 μs

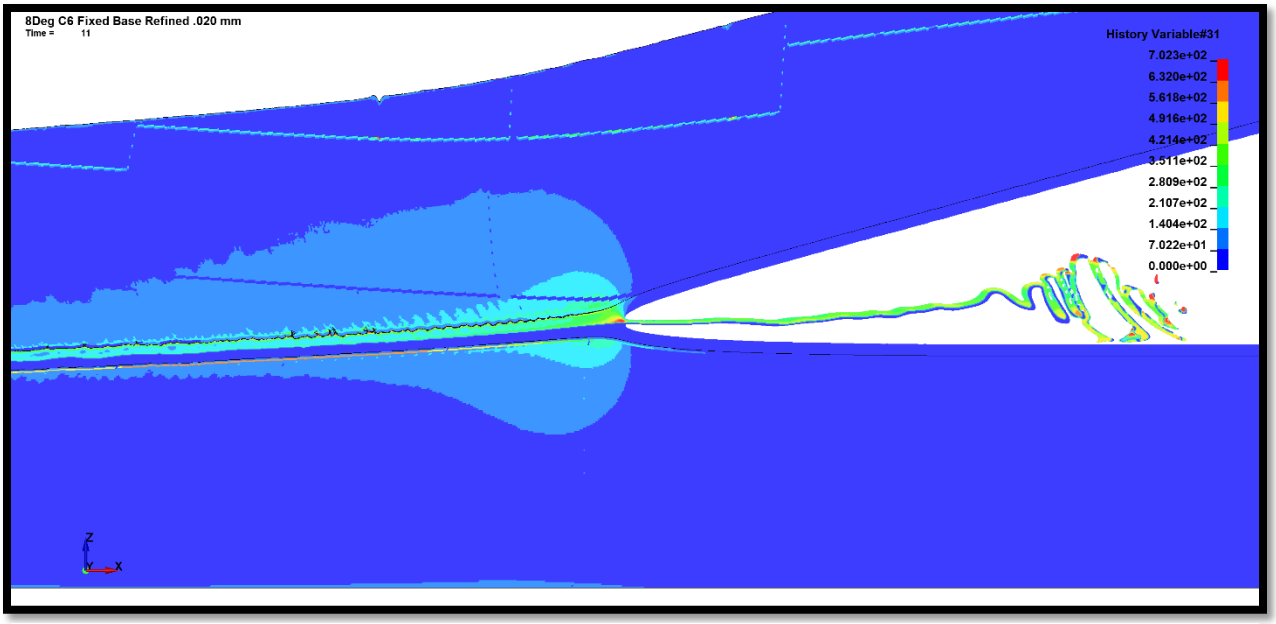

Figure 6-20: 8° temperature distribution at t = 11 μs.

6.5 Discussion of Explosive Welding Modeling

The use of LS-DYNA's multi-material formulation is one of the available and feasible options for commercial modeling of this process. It is conceivably desirable to use modeling as a means to evaluate welding configurations in order to predict welding. Although there are certain challenges associated with the use of this formulation, it also has many benefits and has demonstrated the capability to predict the salient behaviors of impact welding.

There were certainly a number of challenges. A number of stability issues were encountered along the way in conducting this modeling. For the MM-ALE formulation, during the modeling associated with this effort, only the modeling that exclusively used rectangular shaped hexahedral elements proved stable. Although LS-DYNA provides the opportunity to use independent parts to generate the full background mesh and initial the positions of the respective MM-ALE materials, unless that could be accomplished with rectangular prismatic elements, the author would recommend volume filling instead. The author also experienced unusual issues associated with background mesh movements. While they present an opportunity to limit the

domain expanse for the mesh, some of the movements or changes of movements may have lost details that would otherwise generate interfacial waves, as the contrast between the 2.5° and 8° show. As noted in [219, p. 35], the advection algorithms are not capable of conserving both momentum and kinetic energy, and momentum is what is typically conserved in implementation. Energy dissipation is potentially an issue, and extra mesh movements could complicate the calculation. Additionally, although a small domain of material was modeled using MM-ALE, it is still a very expensive formulation. Also, in comparison to a research code, where an experienced analyst can see all details of implementation, errors that occur can sometimes be difficult to troubleshoot due to the opaque nature of using the commercial code.

However, the drawbacks mentioned above are in contrast to the benefits. As shown in the 2.5°, the modeling possesses the capability to generate much of the behavior that could establish whether welding will occur. Very reasonable values for welding parameters were generated. Wavy interface prediction is possible, as well as the prediction of jetting. All of this is possible, without requiring the level of knowledge and detail to implement a custom code. A relatively large specimen can be modeled. Plus, temperature predictions are possible, and LS-DYNA can combine thermal modeling, or multi-physics modeling for magnetic pulse welding as well. In a parallel configuration, memory can be saved with Euler-Lagrange coupling.

7. CONCLUSION

7.1 SUMMARY AND CONCLUSIONS

The research in this dissertation has been a substantive and in-depth study of the explosive welding of aluminum plates. In addition to the great deal of personal growth it represents for the author and the benefit that growth accrues for his professional service, significant contributions for the practice of explosive welding have been made. These are composed of individual additions, augmentations, and reinforcements of the existing state of knowledge for the objectives discussed at the start of this document.

For the goal of furthering the understanding of the process, mechanism, and effects of explosive welding, significant work has been concluded. One major subcategory that supports this objective was addition of data that highlights the value of existing empirical relations, adding additional reaffirming data or that reinforces existing theories that have not been wholly accepted in literature.

In reaffirming existing empirical relations, several specific contributions have been made. In Chapter 5, the results associated with some of the metallurgical observations, the measured result from the welding experiments described in this work were compared to the value from literature based predictive empirical relations. A 1968 relationship between the flyer plate thickness and impact angle shown in Equation (2-19) proposed by Deribas, Kudinov, Matveenkov, and Simonov was tested versus the experimental conditions with very favorable results. Also, in Chapter 5, the observation that the wavelength to amplitude ratio of bond interfacial waves is relatively constant was also tested. A comparison to the proposed ratio of 0.25 proposed by Godunov, Deribas, and Kozin proved similarly reaffirmed. A wealth of studies referenced and available show that the hardness profile of explosively welded plates is typically

increased, as long as effective bonding has occurred, and this result was indirectly reaffirmed with the difference in rotation between the control samples and the 8° specimen recounted in Chapter 4.

The information that was corroborated also included some evidence about the nature of good bonds in Chapter 5 and information corroborating process theory based upon the numerical simulations in Chapter 6. In Chapter 5, the TEM imaging sample shows some support for the structure shown by Berlin and discussed in Section 2.2.4.3. Much literature discusses a "hump" associated with explosive welding. This is sometimes inadvisably conflated with the indentation mechanism of wave formation discussed Section 2.2.3.1, but the form that was supported in Chapter 6 is specifically outlined in Section 2.2.3.4. The goal of the discussion in Section 6.4.5.2 was to distinguish the "hump" from the indentation mechanism and relate it to a potential Rayleigh surface shock wave traveling in the affected plates with the collision.

Additionally in Chapter 6, independent modeling evidence in support of a continuously varying wake, Kelvin-Helmholtz-type instability originally proposed by Robinson was provided. Modeling showed that a continuously varying vertical profile of the jet wake velocity exists behind the collision point. This was argued in Section 2.2.3.3 to be the requisite condition for bond interfacial wave formation, which can be subsequently triggered by many varying causes including acoustic excitations. One such trigger, the arrival of a rarefaction wave at the bond surface was consistent with the Chapter 6 modeling, as discussed in Section 6.4.5.3.

Another objective of this dissertation was to answer questions and provide data on the welding of Aluminum 6061-O alloy to itself. One set of such questions were proposed during the formation of the test series that was presented in Chapter 3.

In Section 3.1 the weld window for this alloy was developed, hypotheses were made, and questions posed about the effects of selecting different inclination angles for the test series. In Section 3.1.2.2, the selection of the 0.5° and 1.5° inclination angles were chosen to evaluate whether literature suggestions of staying below the acoustic speed of metals was a critical consideration. Results in Chapters 4 and 5, which show that the 0.5° welding was actually superior, demonstrated that crossing that threshold is acceptable, and was one instance where the 25% bound proved an acceptable substitute to the more deliberate approach of identifying the minimum critical impact angle for jetting in the supersonic regime.

The other test proposed in Section 3.1 was of the usefulness of the 2024 smooth to wavy transition zone in predicting this transition for 6061-O aluminum. The 2.5° and 8° inclinations were selected to test weld states on either side of this boundary. As the results in Chapter 5 show, this transition does not seem to wholly align with the transition for 6061-O. While the 8° did have a wavy bonding interface, so did the 2.5° in portions of the sample tested. Consistent with other theory basing this transition on the hardness of the metals involved, the transition is different for 6061-O. The results in Chapter 5 further hint that perhaps the qualitative shape of the upper boundary for welding narrows with the lower bound, similar to the originally present window by Wittman shown in Figure 2-23.

Tremendous progress was made in evaluating LS-DYNA's MM-ALE formulation as a tool for the design of welds. In Chapter 6, the modeling results for welding parameters at different resolutions were gathered and compared to both other modeling and to physical measurements from Chapter 3. The LS-DYNA modeling demonstrated a good capability to predict these parameters. The comparisons made for wavelength, amplitude, and their ratio in Chapter 5 were used to test the modeling results and showed a favorable comparison, especially

for the 2.5° model result. Also, the modeling also proved capable of predicting jetting, and was its prediction was consistent with other research level predictions (at comparable resolutions) in identifying the 2.5° and 8° cases as the ones that would jet. Jetting being often considered a necessary, but not fully sufficient condition for good welding, this metric was prescient in highlight the less substantial bond in the 0.5° and 1.5° inclinations. In addition, the 2.5° case shows the capability to predict complicated bonding interface morphologies, as well as highlight cases where melting may be an issue.

7.2 RECOMMENDATIONS FOR FUTURE WORK

The test series in this dissertation was intended to be the first part of a more in-depth study. The foremost recommendation would be to expand the test and modeling series to generate a statistically significant and qualified set of data. In that expanded series lessons learned in the first study would further refine the results obtained. The use of photon doppler velocimetry or other means could be incorporated for velocity measurements. Further research on available means may result an ability to measure temperature in a meaningful way. Measurement of the jet speed could be attempted either with Argon flash backlighting or perhaps with video, if the shielding approach in Cannon et. al could prove effective [50, Sec. II. B.]. A production explosive could be used, microhardness measurements included, and electron backscatter diffraction added for grain identification.

The kinetics of phase change and bond formation are certainly an interesting process that is not completely explained. Using modeling and with additional research, the design of a test series that attempts to produce and measure the states and results for the purposes of illuminating this process would be a very significant contribution.

Additionally, recent works have emphasized acoustic vibrations as a key trigger and influencer of the bond interfacial waves that are formed. Using modeling, it could be possible to identify tests which ought to generate specific results based upon input of differing acoustic input. This could corroborate this mechanism as an influencing trigger of the waves, and provide new detail in how they could be used for controlling bond wave formation.6.4.5.3

REFERENCES

[1] J. S. Rinehart and J. Pearson, *Behavior of Metals Under Impulsive Loads*. New York, NY: American Society of Metals, 1954.

[2] C. Munroe, "Modern Explosives," *Scribner's Magazine*, vol. 3, pp. 563–576, 1888.

[3] W. P. Walters, "The Shaped Charge Concept Part II. The History of Shaped Charges," Aberdeen Proving Ground, MD, 1990.

[4] T. Z. Blazynski, *Explosive welding, forming, and compaction*. New York, NY: Elsevier Science Pub. Co, 1983.

[5] A. A. Ezra, *Principles and Practice of Explosive Metalworking*. London: Industrial Newspapers Limited, 1973.

[6] B. Crossland, *Explosive welding of metals and its application*. New York: Oxford: Clarendon Press; New York: Oxford University Press, 1982.

[7] J. S. Rinehart and J. Pearson, *Explosive Working of Metals*. New York: Pergamon Press Inc., 1963.

[8] G. Birkhoff, D. MacDougal, E. Pugh, and G. Taylor, "Explosives with Lined Cavities," *Journal of Applied Physics*, vol. 19, pp. 563–582, 1948.

[9] J. S. Rinehart, "Some quantitative data bearing on the scabbing of metals under explosive attack," *Journal of Applied Physics*, vol. 22, no. 5, pp. 555–560, 1951.

[10] J. S. Rinehart, "Some Quantitative Data Bearing on the Scabbing of Metals under Explosive Attack," *Journal of Applied Physics*, vol. 22, no. 5, pp. 555–560, May 1951.

[11] J. Pearson and J. S. Rinehart, "Deformation and fracturing of thick-walled steel cylinders under explosive attack," *Journal of Applied Physics*, vol. 23, no. 4, pp. 434–441, 1952.

[12] J. S. Rinehart and J. Pearson, "Conical Surfaces of Fracture Produced by Asymmetrical Impulsive Loading," *Journal of Applied Physics*, vol. 23, no. 6, pp. 685–687, 1952.

[13] J. S. Rinehart and J. Pearson, "Engravement of transient stress wave particle velocities," *Journal of Applied Physics*, vol. 24, no. 4, pp. 462–469, 1953.

[14] J. Pearson and J. S. Rinehart, "Hardness plateaus and twinning in explosively loaded mild steel," *Journal of Applied Physics*, vol. 25, no. 6, pp. 778–781, 1954.

[15] J. S. Rinehart, "Deformation of an explosively loaded aluminum single crystal," *Journal of Applied Physics*, vol. 26, no. 11, pp. 1315–1317, 1955.

[16] J. Pearson and J. S. Rinehart, "Application of the engravement method to the study of particle velocity distribution in explosively loaded cylinders," *Journal of Applied Physics*,

vol. 26, no. 12, pp. 1431–1435, 1955.

[17] J. Pearson and J. S. Rinehart, “Surface Motion Associated with Obliquely Incident Elastic Waves,” *The Journal of the Acoustical Society of America*, vol. 25, no. 2, pp. 217–219, 1953.

[18] J. Roth, “The Forming of Metals By Explosives,” *The Explosives Engineer*, no. March-April, pp. 52–55, 1959.

[19] L. R. Carl, “Brass Welds Made by Detonation Impulse,” *Metal Progress*, vol. 46, no. July to December, pp. 102–103, 1944.

[20] A. A. Deribas, V. M. Kudinov, F. I. Matveenkov, and V. A. Simonov, “Explosive welding,” *Combustion, Explosion, and Shock Waves*, vol. 3, no. 1, pp. 69–72, 1967.

[21] A. A. Deribas, “The Work of Academician M. A. Lavrent’ev in the Field of the Physics of Exposion,” *Combustion, Explosion, and Shock Waves*, vol. 11, no. 6, pp. 815–818, 1975.

[22] E. W. LaRocca and J. Pearson, “Explosive Press for Use in Impulsive Loading Studies,” *Review of Scientific Instruments*, vol. 29, no. 10, pp. 848–851, 1958.

[23] R. J. Zabelka, “Explosive Welding of Metals,” University of California Los Angeles, 1960.

[24] “Explosive welding is on the way,” *Steel*, vol. 145, no. 18, pp. 83–85, 1959.

[25] S. V. Jones, “EXPLOSIVES USED TO JOIN METALS; Du Pont Receives Patent for Cladding Process,” *New York Times*, New York, NY, p. 29,31, 20-Jun-1964.

[26] A. A. Deribas, “Explosive Welding and Its Application,” in *14th International Symposium on Explosive Production of New Materials: Science, Technology, Business, and Innovations*, Moscow: Torus Press, 2018.

[27] V. S. Sedykh, A. A. Deribas, Y. I. Bichenkov, and Y. A. Trishin, “Explosion Welding,” *Svarochnoye Proizvodstvo*, vol. 5, no. NASA Technical Translation F-140, pp. 3–6, 1962.

[28] J. Pearson, V. Philipchuk, and J. S. Rinehart, “Why Explosive Forming Works,” *Steel*, vol. 144, no. Jan 19. Penton Publishing, Cleveland, pp. 62–65, 1959.

[29] J. Fairlie, “Explosive welding and forming open another door for industry,” *Welding Engineer*, vol. 44, no. 4, pp. 61–62, 64, 1959.

[30] J. Pearson, “Metal working with explosives,” *Journal of Metals*, vol. 12, no. 9, September, pp. 673–681, 1960.

[31] J. M. Walsh, R. G. Shreffler, and F. J. Willig, “Limiting conditions for jet formation in high velocity collisions,” *Journal of Applied Physics*, vol. 24, no. 3, pp. 349–359, 1953.

[32] G. Abrahamson, “Permanent periodic surface deformations due to a traveling jet,” *Journal*

of Applied Mechanics, pp. 519–528, 1961.

[33] V. Philipchuk and F. Le Roy Bois, “Explosive Welding,” 3,024,526, 1962.

[34] G. R. Cowan, J. J. Douglass, and A. H. Holtzman, “Explosive Bonding,” 3,137,937, 1964.

[35] A. A. Popoff, “Explosive Welding Process,” 3,140,537, 1964.

[36] J. G. Banker, “Evolution of the Global Explosion Metalworking Industry Past-Present-Future.” Presentation at 14th International Symposium on Explosive Production of New Materials: Science, Technology, Business, and Innovations, 2018.

[37] P. Watson, N. Janet, D. Rohr, D. Newquist, C. Crawford, and L. Bragg, “Clad Steel Plate from Japan,” Washington, D.C., 1995.

[38] D. Freeman, “Exploding Business Growth - Boulder-Based Firm Has Iron-Clad Grip On Worldwide Industry,” *Rocky Mountain News*, Denver, CO, p. 7C, 10-Sep-2005.

[39] Wikipedia, “Coinage Act of 1965,” 2019. [Online]. Available: https://en.wikipedia.org/wiki/Coinage_Act_of_1965#cite_note-FOOTNOTE1964_House_hearings156–158-39. [Accessed: 15-Feb-2019].

[40] N. Ida and J. Snyder, “Method and Apparatus for Explosive Forming of Metal Articles,” 3206963, 1965.

[41] J. Neal and H. Kling, “Method and Apparatus for Explosively Bonding a Plurality of Metal Laminae to Uranium Alloy,” 3182392, 1965.

[42] “History of Dynamic Materials Corporation,” 2019. [Online]. Available: https://www.referenceforbusiness.com/history2/32/Dynamic-Materials-Corporation.html. [Accessed: 15-Feb-2019].

[43] G. R. Cowan and A. H. Holtzman, “Flow configurations in colliding plates: Explosive bonding,” *Journal of Applied Physics*, vol. 34, no. 4, pp. 928–939, 1963.

[44] A. A. Deribas, *The Physics of Explosive Hardening and Welding*. Novosibirsk, Russia: Nauka, 1972.

[45] A. S. Bahrani and B. Crossland, “Explosive welding and cladding: an introductory survey and preliminary results,” *Proceedings of the Institution of Mechanical Engineers*, vol. 179, no. 1964, pp. 264–305, 1964.

[46] M. R. Sewailem and T. Z. Blazynski, “Underwater Explosive Forming of Rectangular Metal Sheet,” in *8th International M.T.D.R. Conference (Incorporating the 2nd International CIRP Production Engineering Research Conference)*, 1967, pp. 1301–1318.

[47] Y. Ishii, “Explosive Welding,” *Journal of the Japanese Welding Society*, vol. 36–1300, no. 12, p. 1287, 1967.

[48] S. H. (Denver R. I. Carpenter, “Center for High Energy Forming,” Denver, CO, 1974.

[49] V. D. Linse and R. H. Wittman, “Explosive Bonding,” 1967.

[50] G. E. Cannon, C. Lindbergh, D. H. Merkle, R. H. Wittman, J. Workman, R. D. Potter, and W. O. Carter, “Explosive Impulse Welding Vol. I,” USAF Academy, CO, 1977.

[51] S. H. Carpenter and R. H. Wittman, “Explosion Welding,” *Annual Review of Materials Science*, vol. 6, pp. 177–200, 1975.

[52] A. A. Deribas and I. D. Zakharenko, “Determination of Limiting Collision Conditions Ensuring the Welding of Metals by Explosion,” *Combustion, Explosion, and Shock Waves*, vol. 11, no. 1, pp. 151–153, 1975.

[53] J. N. Hunt, “Wave formation in explosive welding,” *Philosophical Magazine*, vol. 17, no. 148, pp. 669–680, 1968.

[54] G. R. Cowan, O. R. Bergmann, and A. H. Holtzman, “Mechanism of bond zone wave formation in explosion-clad metals,” *Metallurgical and Materials Transactions B*, vol. 2, no. 11, pp. 3145–3155, 1971.

[55] A. S. Bahrani, T. J. Black, and B. Crossland, “The Mechanics of Wave Formation in Explosive Welding,” *Proceedings of the Royal Society A: Mathematical, Physical and Engineering Sciences*, vol. 296, no. 1445, pp. 123–136, 1967.

[56] A. A. Deribas, V. M. Kudinov, F. I. Matveenkov, and V. A. Simonov, “Simulation of the Process of Wave Formation in Explosive Welding,” *Fizika Goreniya i Vzryva*, vol. 4, no. 1, pp. 100–107, 1968.

[57] J. F. Kowalick and D. R. Hay, “A mechanism of explosive bonding,” *Metallurgical Transactions*, vol. 2, no. 7, pp. 1953–1958, 1971.

[58] S. R. Reid, “A discussion of the mechanism of interface wave generation in explosive welding,” *International Journal of Mechanical Sciences*, vol. 16, no. 6, pp. 399–400, 1974.

[59] S. R. Reid and N. H. S. Sherif, “Prediction of the Wavelength of Interface Waves in Symmetric Explosive Welding.,” *J Mech Eng Sci*, vol. 18, no. 2, pp. 87–94, 1976.

[60] S. R. Reid, “Wake instability mechanism for wave formation in explosive welding,” *International Journal of Mechanical Sciences*, vol. 20, no. 4, pp. 247–253, 1978.

[61] T. Onzawa and Y. Ishii, “Fundamental Studies on Explosive Welding : Observations of Metal jet and wavy pattern,” *Transactions of the Japan Welding Society*, vol. 6, no. 2. pp. 98–104, 1975.

[62] H. El-Sobky and T. Blazynski, “Experimental investigation of the mechanics of explosive welding by means of a liquid analogue,” in *5th International Conference on “High Energy*

Rate fabrication," 1975, pp. 1–21.

[63] J. L. Robinson, "The mechanics of wave formation in impact welding," *Philosophical Magazine*, vol. 31, no. 3, pp. 587–597, 1975.

[64] A. A. Deribas, V. M. Kudinov, and F. I. Matveenkov, "Effect of the Initial Parameters in Explosive Welding Process Formation in Explosive Welding," *Fizika Goreniya i Vzryva*, vol. 3, no. 4, pp. 344–348, 1967.

[65] A. A. Deribas, V. F. Nesterenko, and V. A. Simonov, "Chronicles: Third International Symposium on the Use of Explosive Energy in Manufacturing Metallic Materials of New Properties," *Combustion, Explosion, and Shock Waves*, vol. 13, no. 3, pp. 417–423, 1977.

[66] F. A. McKee and B. Crossland, "Further Experiments on the Mechanism of Explosive Welding," in *5th International Conference on "High Energy Rate fabrication" Vol. 2*, 1975, pp. 4.11.1-4.11.24.

[67] R. A. Weber and V. D. Linse, "Evaluation of Explosive Bonding for Patching Aluminum With Aluminum," Champaign, IL, 1988.

[68] M. Hammerschmidt and H. Kreye, "Microstructure and Bonding Mechanism in Explosive Welding," in *Shock Waves and High-Strain-Rate Phenomena in Metals: Proceedings of an International Conference on Metallurgical Effects of High-Strain-Rate Deformation and Fabrication*, M. A. Meyers, Ed. Albequerque, NM: Plenum Press, New York, 1981, pp. 961–973.

[69] A. Szecket, D. J. Vigueras, and O. T. Inal, "The Cyclic Presure Distribution of Explosively Welded Interfaces," in *Metallurgical Applications of Shock-Wave and High-Strain-Rate Phenomena*, L. E. Murr, K. P. Staudhammer, and M. A. Meyers, Eds. New York, NY: Marcel Dekker, INC., 1986, pp. 887–903.

[70] D. V Jaramillo, O. T. Inal, and A. Szecket, "Effect of base plate thickness on wave size and wave morphology in explosively welded couples," *Journal of Materials Science*, vol. 22, no. 9, pp. 3143–3147, 1987.

[71] D. V Jaramillo, A. Szecket, and O. T. Inal, "On the Transition from a Waveless to a Wavy Interface in Explosive Welding," *Materials Science and Engineering*, vol. 91, pp. 217–222, 1987.

[72] M. A. Meyers, L. E. Murr, and K. Staudhammer, "Support for Organizing and Hosting Explomet 90: International Conference on Shock-Wave and High-Strain-Rate Phenomena in Materials," La Jolla, CA, 1992.

[73] R. Dormeval, "On the history of DYMAT," 2013. [Online]. Available: https://www.dymat.org/aboutDYMAT/history_of_dymat.html. [Accessed: 18-Feb-2019].

[74] "Clad Steel Plate from Japan, Inv. 731-TA-739 (First Review)," Washington, D.C., 2001.

[75] D. Pearson, S. Aranoff, D. Okun, C. Lane, I. Williamson, and D. Pinkert, “Clad Steel Plate from Japan, Inv. 731-TA-739 (Second Review),” Washington, D.C., 2007.

[76] A. Newell, G. Houck, A. Preece, R. Hughes, and D. Corkran, “Clad Steel Plate from Japan U . S . International Trade Commission, Investigation 731-TA-739 (Third Review),” Washington, D.C., 2013.

[77] D. Johanson, I. Williamson, M. Broadbent, R. Schmidtlein, and J. Kearns, “Clad Steel Plate from Japan U . S . International Trade Commission, Investigation 731-TA-739 (Fourth Review),” Washington, D.C., 2018.

[78] “Asahi-Kasaei Corporate Profile,” 2018. [Online]. Available: https://www.asahi-kasei.co.jp/asahi/en/aboutasahi/corporate_pdf/pdf/profile.pdf. [Accessed: 14-Nov-2018].

[79] D. J. (High E. M. I. Butler, “Private Phone Call,” San Diego, CA, 22-Mar-2019.

[80] “Benefits of Explosively Welded Metals,” *Pacific Aerospace and Electronics, Inc. Webpage*. [Online]. Available: http://pacaero.com/products/explosive-bonded-metals/benefits-explosively-welded-metals/. [Accessed: 18-Feb-2019].

[81] G. K. Fenton and G. S. Daehn, “Modeling of electromagnetically formed sheet metal,” *Journal of Materials Processing Technology*, vol. 75, no. 1–3, pp. 6–16, 1998.

[82] A. Vivek, S. R. Hansen, B. C. Liu, and G. S. Daehn, “Vaporizing foil actuator: A tool for collision welding,” *Journal of Materials Processing Technology*, vol. 213, no. 12, pp. 2304–2311, 2013.

[83] A. Kapil and A. Sharma, “Magnetic pulse welding: An efficient and environmentally friendly multi-material joining technique,” *Journal of Cleaner Production*, vol. 100, pp. 35–58, 2015.

[84] I. D. Zakharenko, *Explosion Welding of Metals*. Minsk: Mauka i Tekhnika, 1990.

[85] S. Liu, J. G. Banker, and C. Prothe, “Explosion Welding,” *ASM Handbook: Welding Fundamentals and Process*, vol. 6, no. A, pp. 690–700, 2011.

[86] W. D. Callister, *Materials Science and Engineering: An Introduction*, 7th ed. New York, NY: John Wiley & Sons, 2007.

[87] R. W. Messler, “An Overview of Joining Processes,” in *ASM Handbook, ASM*, vol. 6A, no. Fundamentals and Processes, 2011, pp. 3–12.

[88] S. K. Godunov, A. A. Deribas, and V. I. Mali, “Influence of material viscosity on the jet formation process during collisions of metal plates,” *Combustion, Explosion, and Shock Waves*, vol. 11, no. 1, pp. 1–13, 1975.

[89] A. V. S. A. STERN, O. BECHER, M. NAHMANY, D. ASHKENAZI, “Jet Composition in Magnetic Pulse Welding : Al-Al and Al-Mg Couples,” *Welding research*, no. August,

pp. 257–264, 2015.

[90] S. Kakizaki, M. Watanabe, and S. Kumai, “Simulation and experimental analysis of metal jet emission and weld interface morphology in impact welding,” *Journal of Japan Institute of Light Metals*, vol. 61, no. 7, pp. 328–333, 2011.

[91] I. D. Zakharenko, “Critical Conditions in Detonation Welding,” *Combustion, Explosion, and Shock Waves*, vol. 8, no. 3, pp. 341–345, 1972.

[92] R. H. Wittman, “The Influence of Collision Parameters on the Strength and Microstructure of an Explosion Welded Aluminium Alloy,” in *Proceedings of the 2nd Symposium on Use of Explosive Energy in Manufacturing Metallic Materials of New Properties and Possibilities of Application thereof in the Chemical Industry*, 1973, pp. 153-167 [English version].

[93] A. A. Deribas, V. A. Simonov, and I. D. Zakharenko, “Investigation of Explosive Welding Parameters for Arbritrary Combinations of Metals and Alloys,” in *5th International Conference on “High Energy Rate Fabrication,”* 1975, pp. 4.1.1-4.1.24.

[94] J. B. Ribeiro, R. Mendes, and A. Loureiro, “Review of the weldability window concept and equations for explosive welding,” *Journal of Physics: Conference Series*, vol. 500, no. 5, 2014.

[95] Q. Zhou, J. Feng, and P. Chen, “Numerical and experimental studies on the explosive welding of tungsten foil to copper,” *Materials*, vol. 10, no. 9, 2017.

[96] A. A. Deribas, “The explosive working of materials in the USSR,” *High Pressure Research*, vol. 1, no. 5–6, pp. 365–376, 1989.

[97] S. A. Salem, L. G. Lazari, and S. T. S. Al-Hassani, “Explosive Welding of Flat Plates in Free Flight,” *International Journal of Impact Engineering*, vol. 2, no. 1, pp. 85–101, 1984.

[98] M. R. Khanzadeh, S. A. A. Akbari Mousavi, A. Amadeh, and G. H. Liaghat, “Correlation between numerical finite element simulation and experiments for explosive cladding of nickel base super alloy on hot tool steel,” *Strain*, vol. 48, no. 4, pp. 342–355, 2012.

[99] W. A. Allen, J. M. Mapes, and W. G. Wilson, “An effect produced by oblique impact of a cylinder on a thin target,” *Journal of Applied Physics*, vol. 25, no. 5, pp. 675–676, 1954.

[100] A. Loureiro, R. Mendes, J. B. Ribeiro, R. M. Leal, and I. Galvão, “Effect of explosive mixture on quality of explosive welds of copper to aluminium,” *Materials and Design*, vol. 95, pp. 256–267, 2016.

[101] S. K. Godunov, A. A. Deribas, A. V. Zabrodin, and N. S. Kozin, “Hydrodynamic Effects in Colliding Solids,” *Journal of Computational Physics*, vol. 5, no. 3, pp. 517–539, 1970.

[102] R. C. Gupta and G. S. Kainth, “Swinging Wake Mechanism for Interface Wave Generation in Explosive Welding of Metals,” *Journal of Applied Mechanics*, vol. 57, no.

3, p. 514, 1990.

[103] Q. Chu, M. Zhang, J. Li, and C. Yan, “Experimental and numerical investigation of microstructure and mechanical behavior of titanium/steel interfaces prepared by explosive welding,” *Materials Science and Engineering A*, vol. 689, no. December 2016, pp. 323–331, 2017.

[104] T. Zhang, W. Wang, W. Zhang, Y. Wei, X. Cao, Z. Yan, and J. Zhou, “Microstructure evolution and mechanical properties of an AA6061/AZ31B alloy plate fabricated by explosive welding,” *Journal of Alloys and Compounds*, vol. 735, pp. 1759–1768, 2018.

[105] T. von Karman, “Über den Mechanismus des Widerstandes, den ein bewegter Körper in einer Flüssigkeit erfährt,” *Nachrichten von der Gesellschaft der Wissenschaften zu Göttingen, Mathematisch-Physikalische Klasse*, vol. 5, pp. 509–517, 1911.

[106] N. J. Zabusky and G. S. Deem, “Dynamical evolution of two-dimensional unstable shear flows,” *Journal of Fluid Mechanics*, vol. 47, no. 2, pp. 353–379, 1971.

[107] P. K. Kundu, I. M. Cohen, and D. R. Dowling, *Fluid Mechanics*, Sixth. Elsevier Inc., 2016.

[108] A. Nassiri, G. Chini, and B. Kinsey, “Spatial stability analysis of emergent wavy interfacial patterns in magnetic pulsed welding,” *CIRP Annals - Manufacturing Technology*, vol. 63, no. 1, pp. 245–248, 2014.

[109] A. Nassiri, “Investigation of Wavy Interfacial Morphology in Magnetic Pulsed Welding: Mathematical Modeling, Numberical Simulations, and Experimental Tests,” University of New Hampshire, 2015.

[110] A. Nassiri, B. Kinsey, and G. Chini, “Shear instability of plastically-deforming metals in high-velocity impact welding,” *Journal of the Mechanics and Physics of Solids*, vol. 95, pp. 351–373, 2016.

[111] K. K. Botros and T. K. Groves, “Characteristics of the wavy interface and the mechanism of its formation in high-velocity impact welding,” *Journal of Applied Physics*, vol. 51, no. 7, pp. 3715–3721, 1980.

[112] R. Mendes, J. B. Ribeiro, and A. Loureiro, “Effect of explosive characteristics on the explosive welding of stainless steel to carbon steel in cylindrical configuration,” *Materials and Design*, vol. 51, pp. 182–192, 2013.

[113] C. C. Merriman, “MICROSTRUCTURE EVOLUTION OF FCC METALS DURING THE EXPLOSIVE WELDING PROCESS,” Washington State University, 2015.

[114] P. V. Vaidyanathan and A. Ramanathan, “Computer-aided design of explosive welding systems,” *Journal of Materials Processing Tech.*, vol. 38, no. 3, pp. 501–516, 1993.

[115] B. Zlobin, V. Sil’Vestrov, A. Shtertser, A. Plastinin, and V. Kiselev, “Enhancement of

Explosive Welding Possibilities by the Use of Emulsion Explosive," *Archives of Metallurgy and Materials*, vol. 59, no. 4, p. 1587, 2014.

[116] S. A. A. Akbari Mousavi and P. Farhadi Sartangi, "Experimental investigation of explosive welding of cp-titanium/AISI 304 stainless steel," *Materials and Design*, vol. 30, no. 3, pp. 459–468, 2009.

[117] K. K. Botros and T. K. Groves, "Fundamental impact-welding parameters - An experimental investigation using a 76-mm powder cannon," *Journal of Applied Physics*, vol. 51, no. 7, pp. 3706–3714, 1980.

[118] M. M. Hoseini Athar and B. Tolaminejad, "Weldability window and the effect of interface morphology on the properties of Al/Cu/Al laminated composites fabricated by explosive welding," *Materials and Design*, vol. 86, pp. 516–525, 2015.

[119] X. Li, H. Ma, and Z. Shen, "Research on explosive welding of aluminum alloy to steel with dovetail grooves," *Materials and Design*, vol. 87, pp. 815–824, 2015.

[120] A. Szecket, "An experimental study of the explosure welding window using a gas gun," Queen's University, Belfast, 1979.

[121] V. I. Lysak and S. V. Kuzmin, "Lower boundary in metal explosive welding. Evolution of ideas," *Journal of Materials Processing Technology*, vol. 212, no. 1, pp. 150–156, 2012.

[122] Y. Matsui, M. Otsuka, T. Hinata, E. Carton, and S. Itoh, "Explosive welding of light weight metal sheets," *Proc. of the 8th International LS-DYNA User's Conference*, pp. 59–66, 2004.

[123] A. Vivek, B. C. Liu, S. R. Hansen, and G. S. Daehn, "Accessing collision welding process window for titanium/copper welds with vaporizing foil actuators and grooved targets," *Journal of Materials Processing Technology*, vol. 214, no. 8, pp. 1583–1589, 2014.

[124] T. Lee, S. Zhang, A. Vivek, B. Kinsey, and G. S. Daehn, "Flyer Thickness Effect in the Impact Welding of Aluminum to Steel," *Journal of Manufacturing Science and Engineering*, vol. 140, no. 12, p. 121002, 2018.

[125] E. Zamani and G. H. Liaghat, "Explosive welding of stainless steel-carbon steel coaxial pipes," *Journal of Materials Science*, vol. 47, no. 2, pp. 685–695, 2012.

[126] G. H. S. F. L. Carvalho, R. Mendes, R. M. Leal, I. Galvão, and A. Loureiro, "Effect of the flyer material on the interface phenomena in aluminium and copper explosive welds," *Materials and Design*, vol. 122, pp. 172–183, 2017.

[127] G. H. S. F. L. Carvalho, I. Galvão, R. Mendes, R. M. Leal, and A. Loureiro, "Explosive welding of aluminium to stainless steel," *Journal of Materials Processing Technology*, vol. 262, no. March, pp. 340–349, 2018.

[128] A. A. Deribas, "Phenomena with High-Speed Collisions Between Solids," *Combustion*,

Explosion, and Shock Waves, vol. 9, no. 2, pp. 229–240, 1973.

[129] C. Cheng and Q. Tan, "MECHANISM OF WAVE FORMATION AT THE INTERFACE IN EXPLOSIVE WELDING," *Acta Mechanica Sinica*, vol. 5, no. 2, pp. 97–108, 1989.

[130] B. Wronka, "Testing of explosive welding and welded joints. Wavy character of the process and joint quality," *International Journal of Impact Engineering*, vol. 38, no. 5, pp. 309–313, 2011.

[131] S. K. Godunov, A. A. Deribas, and N. S. Kozin, "Wave Formation in Explosive Welding," *Journal of Applied Mechanics and Technical Physics*, vol. 12, no. 3, pp. 398–406, 1971.

[132] W. Klein, "GEFUGEANDERUNGEN BEIM EXPLOSIVPLATTIEREN VON STAHL MIT STAHL UND EINIGEN NICHTEISENMETALLEN.," *TECHNISCHE MITTEILUNGEN KRUPP FORSCHUNGSBERICHTE*, vol. 23, no. 1, p. 14, 1965.

[133] T. von Karman, "Über den Mechanismus des Widerstandes, den ein bewegter Körper in einer Flüssigkeit erfährt," *Nachrichten von der Gesellschaft der Wissenschaften zu Göttingen, Mathematisch-Physikalische Klasse*, pp. 547–556, 1912.

[134] A. Abe, "Numerical simulation of the plastic flow field near the bonding surface of explosive welding," *Journal of Materials Processing Technology*, vol. 85, no. 1–3, pp. 162–165, 1999.

[135] B. Wronka, "Testing of explosive welding and welded joints. The microstructure of explosive welded joints and their mechanical properties," *Journal of Materials Science*, vol. 45, no. 13, pp. 3465–3469, 2010.

[136] I. Plaksin, J. Campos, J. Ribeiro, R. Mendes, J. Direito, D. Braga, and R. Pruemmer, "Novelties in physics of explosive welding and powder compaction," *Jounal de Physique IV*, vol. 110, pp. 797–802, 2003.

[137] A. Szecket and M. Mayseless, "The triggering and controlling of stable interfacial conditions in explosive welding," *Materials Science and Engineering*, vol. 57, no. 2, pp. 149–154, 1983.

[138] B. Wronka, "The influence of base plate thickness and anvil on the characterics of explosive welded joints," *Insight*, vol. 41, no. 6, pp. 383–387, 1999.

[139] E. V. Kuz'min, A. N. Dorodnikov, A. P. Peev, V. I. Lysak, and S. V. Kuz'min, "Structure and properties of joints produced by ultrasound-assisted explosive welding," *The Physics of Metals and Metallography*, vol. 116, no. 8, pp. 817–822, 2015.

[140] E. V. Kuz'Min, S. V. Kuz'Min, V. I. Lysak, and A. N. Lata, "Plastic deformation and wave formation on the interface of metals welded by ultrasound-assisted explosive welding," *Journal of Physics: Conference Series*, vol. 894, no. 1, 2017.

[141] H. El-Sobky and T. Z. Blazynski, "Experimental Investigation of the Mechanics of

Explosive Welding by Means of a Liquid Analogue," in *5th International Conference on "High Energy Rate Fabrication,"* 1975, pp. 4.5.1-4.5.21.

[142] T. Z. Blazynski, "Simulation of Explosive Welding Parameters by means of a liquid analogue," *Materialwissenschaft und Werkstofftechnik*, vol. 21, no. 1, pp. 16–27, 1990.

[143] A. Oberg, J. A. Schweitz, and H. Olofsson, "Computer Modeling of the Explosive Welding Process," in *8th International Conference of High Energy Rate Fabrication*, 1984, pp. 75–84.

[144] A. A. A. Mousavi and S. T. S. Al-Hassani, "Numerical and experimental studies of the mechanism of the wavy interface formations in explosive/impact welding," *Journal of the Mechanics and Physics of Solids*, vol. 53, no. 11, pp. 2501–2528, 2005.

[145] V. A. Simonov, "Binding criterion for metals with explosive welding," *Combustion, Explosion, and Shock Waves*, vol. 27, no. 1, pp. 121–123, 1991.

[146] M. A. Meyers, "Dynamic Behavior of Materials.," *Dynamic Behavior of Materials*, 1994.

[147] R. V. Tamhankar and J. Ramesam, "Metallography of explosive welds," *Materials Science and Engineering*, vol. 13, no. 3, pp. 245–254, 1974.

[148] I. A. Bataev, A. A. Bataev, V. I. Mali, V. A. Bataev, and I. A. Balaganskii, "Structural changes of surface layers of steel plates in the process of explosive welding," *Metal Science and Heat Treatment*, vol. 55, no. 9–10, pp. 509–513, 2014.

[149] J. Song, A. Kostka, M. Veehmayer, and D. Raabe, "Hierarchical microstructure of explosive joints: Example of titanium to steel cladding," *Materials Science and Engineering A*, vol. 528, no. 6, pp. 2641–2647, 2011.

[150] C. Borchers, M. Lenz, M. Deutges, H. Klein, F. Gärtner, M. Hammerschmidt, and H. Kreye, "Microstructure and mechanical properties of medium-carbon steel bonded on low-carbon steel by explosive welding," *Materials and Design*, vol. 89, pp. 369–376, 2016.

[151] I. A. Bataev, A. A. Bataev, V. I. Mali, and D. V. Pavliukova, "Structural and mechanical properties of metallic-intermetallic laminate composites produced by explosive welding and annealing," *Materials and Design*, vol. 35, pp. 225–234, 2012.

[152] S. Patra, K. S. Arora, M. Shome, and S. Bysakh, "Interface characteristics and performance of magnetic pulse welded copper-Steel tubes," *Journal of Materials Processing Technology*, vol. 245, pp. 278–286, 2017.

[153] S. Narayan, S. Tanaka, A. Mori, and K. Hokamoto, "Welding of Sn and Cu plates using controlled underwater shock wave," *Journal of Materials Processing Technology*, vol. 245, pp. 300–308, 2017.

[154] H. Paul, M. M. Miszczyk, R. Chulist, M. Prażmowski, J. Morgiel, A. Gałka, M. Faryna,

and F. Brisset, “Microstructure and phase constitution in the bonding zone of explosively welded tantalum and stainless steel sheets,” *Materials and Design*, vol. 153, pp. 177–189, 2018.

[155] H. R. Zareie Rajani and S. A. A. Akbari Mousavi, “The effect of explosive welding parameters on metallurgical and mechanical interfacial features of Inconel 625/plain carbon steel bimetal plate,” *Materials Science and Engineering A*, vol. 556, pp. 454–464, 2012.

[156] I. N. Maliutina, V. I. Mali, I. A. Bataev, A. A. Bataev, M. A. Esikov, A. I. Smirnov, and K. A. Skorokhod, “Structure and microhardness of Cu-Ta joints produced by explosive welding,” *The Scientific World Journal*, vol. 2013, 2013.

[157] M. Acarer and B. Demir, “An investigation of mechanical and metallurgical properties of explosive welded aluminum-dual phase steel,” *Materials Letters*, vol. 62, no. 25, pp. 4158–4160, 2008.

[158] ASTM International, “A263 Standard Specification for Stainless Chromium Steel-Clad Plate 1,” ASTM A263-12, 2012.

[159] ASTM International, “A264 Standard Specification for Stainless Chromium-Nickel Steel-Clad Plate,” ASTM A264-12, 2012.

[160] A. Szecket, O. T. Inal, D. J. Vigueras, and J. Rocco, “A wavy versus straight interface in the explosive welding of aluminum to steel,” *Journal of Vacuum Science & Technology A: Vacuum, Surfaces, and Films*, vol. 3, no. 6, pp. 2588–2593, 1985.

[161] F. Fehim, Y. Ramazan, and S. Tolga, “The effects of heat treatment on the microstructure and microhardness of explosive welding,” *Scientific Research and Essays*, vol. 6, no. 19, pp. 4141–4151, 2011.

[162] I. A. Bataev, A. Bataev, V. I. Mali, V. Burov, E. Golovin, A. Smirnov, and E. Prikhodko, “Structure and Fatigue Crack Resistance of Multilayer Materials Produced by Explosive Welding,” *Advanced Materials Research*, vol. 287–290, pp. 108–111, 2011.

[163] I. Bataev, A. Bataev, V. I. Mali, M. Esikov, and V. Bataev, “Peculiarities of Weld Seams and Adjacent Zones Structures Formed in Process of Explosive Welding of Sheet Steel Plates,” *Materials Science Forum*, vol. 673, pp. 95–100, 2011.

[164] M. P. Bondar and V. F. Nesterenko, “Contact Deformation and Bonding Criteria under Impulsive Loading,” *Combustion, Explosion, and Shock Waves*, vol. 27, no. 3, pp. 364–376, 1991.

[165] M. P. Bondar, “Localization Of Plastic Deformation On Contacts, Determining The Formation Of A Strong Joint,” *Combustion, Explosion, and Shock Waves*, vol. 31, no. 5, pp. 612–616, 1995.

[166] U. Andrade, M. A. Meyers, K. S. Vecchio, and A. H. Chokshi, “Dynamic

Recrystallization in High-Strain-Rate Plastic Deformation of Copper," *Acta Metallurgica et Materialia*, vol. 42, no. 9, pp. 3183–3195, 1994.

[167] M. A. Meyers, V. F. Nesterenko, J. C. LaSalvia, Y. B. Xu, and Q. Xue, "Observation and modeling of dynamic recrystallization in high-strain, high-strain rate deformation of metal," in *Journal de Physique IV: Proceedings EuroDymat 2000. 6th International Conference on Mechanical and Physical Behaviour of Materials under Dynamic Loading*, 2000, pp. 51–56.

[168] S. Chen, G. S. Daehn, A. Vivek, B. Liu, S. R. Hansen, J. Huang, and S. Lin, "Interfacial microstructures and mechanical property of vaporizing foil actuator welding of aluminum alloy to steel," *Materials Science and Engineering A*, vol. 659, pp. 12–21, 2016.

[169] A. A. A. Mousavi, S. J. Burley, and S. T. S. Al-Hassani, "Simulation of explosive welding using the Williamsburg equation of state to model low detonation velocity explosives," *International Journal of Impact Engineering*, vol. 31, no. 6, pp. 719–734, 2005.

[170] Z. Fan, H. Yu, and C. Li, "Interface and grain-boundary amorphization in the Al/Fe bimetallic system during pulsed-magnetic-driven impact," *Scripta Materialia*, vol. 110, pp. 14–18, 2016.

[171] B. Liu, A. Vivek, M. Presley, and G. S. Daehn, "Dissimilar Impact Welding of 6111-T4, 5052-H32 Aluminum Alloys to 22MnB5, DP980 Steels and the Structure–Property Relationship of a Strongly Bonded Interface," *Metallurgical and Materials Transactions A: Physical Metallurgy and Materials Science*, vol. 49, no. 3, pp. 899–907, 2018.

[172] A. Berlin, T. Nguyen, M. Worswick, and Y. Zhou, "Metallurgical analysis of magnetic pulse welds of AZ31 magnesium alloy," *Science and Technology of Welding and Joining*, vol. 16, no. 8, pp. 728–734, 2011.

[173] G. Göbel, J. Kaspar, T. Herrmannsdörfer, B. Brenner, and E. Beyer, "Insights into intermetallic phases on pulse welded dissimilar metal joints," *4th International Conference on High Speed Forming*, pp. 127–136, 2010.

[174] H. Paul, J. Morgiel, T. Baudin, F. Brisset, M. Prazmowski, and M. Miszczyk, "Characterization of explosive weld joints by TEM and SEM/EBSD," *Archives of Metallurgy and Materials*, vol. 59, no. 3, pp. 1129–1136, 2014.

[175] J. Li, Q. Yu, Z. Zhang, W. Xu, and X. Sun, "Formation mechanism for the nanoscale amorphous interface in pulse-welded Al/Fe bimetallic systems," *Applied Physics Letters*, vol. 108, no. 20, 2016.

[176] M. Nishida, A. Chiba, Y. Honda, and J. Hirazumi, "Electron microscopy studies of bonding interface in explosively welded titanium/steel clads(communication)," *ISIJ International*, vol. 35, no. 2, pp. 217–219, 1995.

[177] I. A. Bataev, D. V. Lazurenko, S. Tanaka, K. Hokamoto, A. A. Bataev, Y. Guo, and A. M. Jorge, "High cooling rates and metastable phases at the interfaces of explosively welded

materials," *Acta Materialia*, vol. 135, pp. 277–289, 2017.

[178] M. Hammerschmidt and H. Kreye, "The Role of Adiabatic Shearing in Explosive Welding," in *Trudy II Sovershchaniia Po Ubrabotke*, 1982, pp. 117–126.

[179] Y. Zhang, S. S. Babu, and G. S. Daehn, "Interfacial ultrafine-grained structures on aluminum alloy 6061 joint and copper alloy 110 joint fabricated by magnetic pulse welding," *Journal of Materials Science*, vol. 45, no. 17, pp. 4645–4651, 2010.

[180] J. S. Chen, M. Hillman, and S. W. Chi, "Nonlinear meshfree analysis program: User's Manual," *University of California San Diego*, 2013.

[181] F. Grignon, D. Benson, K. S. Vecchio, and M. A. Meyers, "Explosive welding of aluminum to aluminum: Analysis, computations and experiments," *International Journal of Impact Engineering*, vol. 30, no. 10, pp. 1333–1351, 2004.

[182] G. R. Johnson and W. H. Cook, "A constitutive model and data for metals subjected to large strains, high strain rates and high temperatures," *7th International Symposium on Ballistics*. pp. 541–547, 1983.

[183] G. R. Johnson and W. H. Cook, "Fracture characteristics of three metals subjected to various strains, strain rates, temperatures and pressures," *Engineering Fracture Mechanics*, vol. 21, no. 1, pp. 31–48, 1985.

[184] J. E. Kennedy, "Gurney energy of explosives: Estimation of the velocity and impulse imparted to driven metal," Albuquerque, NM, 1970.

[185] R. W. Gurney, "The Initial Velocities of Fragments from Bombs, Shell, Grenades," Aberdeen Proving Ground, MD, 1943.

[186] ASTM International, "A20 Standard Specification for General Requirements for Steel Plates for Pressure Vessels 1," 2004.

[187] ASTM International, "A265 Standard Specification for Nickel and Nickel-Base Alloy-Clad Steel Plate 1," ASTM A265-12, 2012.

[188] ASTM International, "B898 Standard Specification for Reactive and Refractory Metal Clad Plate 1," ASTM B898-11, 2016.

[189] C. R. McKenney and J. G. Banker, "Explosion-Bonded Metals for Marine Structural Applications," *Marine Technology*, vol. 8, no. 3, pp. 285–292, 1971.

[190] Naval Sea Systems Command, "MIL-J-24445A Joint, Bimetallic Bonded, Aluminum to Steel," no. July. Naval Sea Systems Command, 1977.

[191] M. Abbasi, A. Karimi Taheri, and M. T. Salehi, "Growth rate of intermetallic compounds in Al/Cu bimetal produced by cold roll welding process," *Journal of Alloys and Compounds*, vol. 319, no. 1–2, pp. 233–241, 2001.

[192] S. A. A. Akbari Mousavi, S. T. S. Al-Hassani, and A. G. Atkins, “Bond strength of explosively welded specimens,” *Materials and Design*, vol. 29, no. 7, pp. 1334–1352, 2008.

[193] G. Arthur, “Applications of explosive welding to heat exchangers,” *Materials and Design*, vol. 6, no. 1, pp. 37–41, 1985.

[194] L. Bement, “Applying NASA’s Explosive Seam Welding,” in *The Second National Technology Transfer Conference and Exposition, Vol 1*, 1991, pp. 10–23.

[195] D. V Jaramillo, O. T. Inal, and A. Szecket, “An impact weldability domain for the amorphous ribbon/steel system,” *Acta Metallurgica*, vol. 35, no. 7, pp. 1549–1553, 1987.

[196] N. Kahraman, B. Gülenç, and F. Findik, “Joining of titanium/stainless steel by explosive welding and effect on interface,” *Journal of Materials Processing Technology*, vol. 169, no. 2, pp. 127–133, 2005.

[197] O. T. Inal, A. Szecket, D. J. Vigueras, and H. Pak, “Explosive welding of Ti–6Al–4V to mild-steel substrates,” *Journal of Vacuum Science & Technology A: Vacuum, Surfaces, and Films*, vol. 3, no. 6, pp. 2605–2609, 1985.

[198] L. J. Zhang, Q. Pei, J. X. Zhang, Z. Y. Bi, and P. C. Li, “Study on the microstructure and mechanical properties of explosive welded 2205/X65 bimetallic sheet,” *Materials and Design*, vol. 64, pp. 462–476, 2014.

[199] N. Kahraman and B. Gülenç, “Microstructural and mechanical properties of Cu-Ti plates bonded through explosive welding process,” *Journal of Materials Processing Technology*, vol. 169, no. 1, pp. 67–71, 2005.

[200] M. M. Hoseini-Athar and B. Tolaminejad, “Interface morphology and mechanical properties of Al-Cu-Al laminated composites fabricated by explosive welding and subsequent rolling process,” *Metals and Materials International*, vol. 22, no. 4, pp. 670–680, 2016.

[201] A. Durgutlu, B. Gülenç, and F. Findik, “Examination of copper/stainless steel joints formed by explosive welding,” *Materials and Design*, vol. 26, no. 6, pp. 497–507, 2005.

[202] J. Buchar, S. Rolc, and V. Hruby, “On the Explosive Welding of a ring to the axisymmetric body,” *Materials Processing Technology*, vol. 85, pp. 171–174, 1999.

[203] ASTM International, “D3165 Strength Properties of Adhesives in Shear by Tension Loading of Single-Lap-Joint Laminated Assemblies,” D3165-07, 2007.

[204] ASTM International, “B557 − 15 Standard Test Methods for Tension Testing Wrought and Cast Aluminum- and,” B557-15, 2015.

[205] MTS Systems Corporation, “Series 647 hydraulic wedge grips reference manual.” 2013.

[206] Correlated Solutions, “Vic-2D v6 Reference Manual,” 2016.

[207] Correlated Solutions, “Application Note AN -1701 Speckle Pattern Fundamentals,” 2017.

[208] Correlated Solutions, “Digital Image Correlation: Overview of Principles and Software.”

[209] M. A. Sutton, J.-J. Orteu, and H. W. Schreier, *Image Correlation for Shape, Motion and Deformation Measurements: Basic Theory and Applications*. Springer, 2009.

[210] J. R. Davis, Ed., *ASM Specialty Handbook: Aluminum and Aluminum Alloys*, 5th Print. Materials Park, OH, 1993.

[211] K. C. H. Kumar, N. Chakraborti, H. Lukas, O. Bodak, and L. Rokhlin, “Aluminium – Magnesium – Silicon,” *Materials Science International Team, Group IV Physical Chemistry: Ternary Alloy Systems - Phase Diagrams, Crystallographic and Thermodynamic Data: Light Metal Systems, Part 3: Selected Systems from Al-Fe-V to Al-Ni-Zr*. Springer Berlin Heidelberg, pp. 165–177, 2005.

[212] ASTM Standard, “E407-07 Standard Practice for Microetching Metals and Alloys,” *ASTM International*, vol. 07, no. Reapproved 2015, pp. 1–22, 2015.

[213] M. Warmuzek, “Metallographic Techniques for Aluminum and Its Alloys,” in *ASM Handbook Vol 9.: Metallograpy and Microstructures*, vol. 9, G. F. Vander Voort, Ed. ASM International, 2004, pp. 711–751.

[214] Livermore Software Technology Corporation, “LS-DYNA Keyword User’s Manual, Vol I.” LSTC, Livermore, CA, 2017.

[215] Livermore Software Technology Corporation, “LS-DYNA Keyword User’s Manual, Volume II Material Models.” Livermore, CA, 2017.

[216] D. J. Benson, “Computational methods in Lagrangian Eulerian hydrocodes,” *Computer Methods in Applied Mechanics and Engineering*, vol. 99, pp. 235–394, 1992.

[217] T. Belytschko, W. K. Liu, B. Moran, and K. I. Elkhodary, *Nonlinear Finite Elements for Continua and Structures*, 2nd ed. John Wiley & Sons, 2014.

[218] J. Donea, A. Huerta, J. Ponthot, and A. Rodr, “Chapter 14 Arbitrary Lagrangian – Eulerian Methods,” in *Encyclopedia of Computational Mechanics, Vol 1: Fundamentals*, E. Stein, R. de Borst, and T. J. R. Hughes, Eds. John Wiley & Sons, 2004, pp. 1–25.

[219] D. J. Benson and M. Souli, Eds., *Arbitrary Lagrangian-Eulerian and Fluid-Structure Interaction: Numerical Simulation*. Hoboken, NJ: John Wiley & Sons, 2010.

[220] D. J. Benson, “A mixture theory for contact in multi-material Eulerian formulations,” *Computer Methods in Applied Mechanics and Engineering*, vol. 140, no. 1–2, pp. 59–86, 1997.

[221] L. Olovsson, M. Souli, and I. Do, “LS-DYNA – ALE Capabilities Fluid-Structure Interaction Modeling.” Livermore Software Technology Corporation, 2003.

[222] Dassault Systemes, “Abaqus 2016 Analysis User’s Guide.” 2016.

[223] B. Van Leer, “Towards the ultimate conservative difference scheme. IV. A new approach to numerical convection,” *Journal of Computational Physics*, vol. 23, no. 3, pp. 276–299, 1977.

[224] D. J. Benson, “Momentum advection on a staggered mesh,” *Journal of Computational Physics*, vol. 100, no. 1, pp. 143–162, 1992.

[225] B. M. Dobratz and P. C. Crawford, “LLNL Explosives Handbook - Properties of Chemical Explosives and Explosive Simulants,” 1985.

[226] E. Gruneisen, “Handbuch der Physik,” *Vol 10*. Verlag J. Springer, Berlin, p. 22, 1926.

[227] M. H. Rice, R. G. McQueen, and J. M. Walsh, “Compression of Solids by Strong Shock Waves,” *Solid State Physics - Advances in Research and Applications*, vol. 6, no. 1, pp. 1–63, 1958.

[228] J. M. Walsh, M. H. Rice, R. McQueen, and F. L. Yarger, “Shock-Wave Compressions of Twenty-Seven Equations of State of Metals * Metals .,” *Physical Review*, vol. 108, no. 2, pp. 196–216, 1957.

[229] L. E. Schwer, “Aluminum Plate Perforation : A Comparative Case Study using Lagrange with Erosion , Multi-Material ALE , and Smooth Particle Hydrodynamics,” *7th European LS-DYNA Conference*, p. 28, 2009.

[230] J. Baek, K. Arnett, J. S. Chen, and G. Hegemier, “Experimental and Numerical Investigation of Explosive Welding and Weldability Windows,” La Jolla, CA, 2018.

[231] H. J. Melosh and C. P. Sonett, “When Worlds Collide: Jetted Vapor Plumes and the Moon’s Origin,” in *Lunar and Planetary Institute Conference on the Origin of the Moon*, 1984, pp. 22–91.

[232] B. Dolgin, J. Sanok, D. Sevilla, and L. Bement, “Category V Compliant Container For Mars Sample Return Missions,” pp. 1–10, 2000.

[233] V. Philipchuk, “Joining with explosives,” *American Machinist*, vol. 103, no. 8, p. 3, 1959.

[234] D. (Stanford R. I. Davenport, “Explosive Welding (SP 62-67),” in *ASTME Creative Manufacturing Seminars*, 1962, pp. 1–15.

[235] V. Gupta, T. Lee, A. Vivek, K. S. Choi, Y. Mao, X. Sun, and G. S. Daehn, “A robust process-structure model for predicting the joint interface structure in impact welding,” *Journal of Materials Processing Technology*, vol. 264, no. Online August 2018, pp. 107–118, 2019.

[236] W. Xu and X. Sun, “Numerical investigation of electromagnetic pulse welded interfaces between dissimilar metals,” *Science and Technology of Welding and Joining*, vol. 21, no. 7, pp. 592–599, 2016.

[237] Y. Mao, V. Gupta, B. Ufferman, A. Vivek, K. S. CHOI, X. Sun, and G. S. Daehn, “On Process, Structure, Property Relationships in Impact Welding of Aluminum 6061 and Steel 4130,” in *International Conference on High Speed Forming*, 2018.

[238] A. P. & C. Corporation, “Ammonimum Perchlorate Advertisement,” *Aviation Week and Space Technology: 1961 Buyers Guide*, no. Mid December, p. 330, 1960.

[239] R. W. Messler, “Overview of Welding Processes,” in *ASM Handbook*, vol. 6A, no. Fundamentals and Processes, ASM International, 2011, pp. 13-26.

[240] B. Crossland and A. S. Bahrani, “Fundamentals, of explosive welding,” *Contemporary Physics*, vol. 9, no. 1, pp. 71–87, 1968.

[241] B. Crossland, F. McKee, and A. Szecket, “An Experimental Investigation of Explosive Welding Parameters,” in *High Pressure Science and Technology: Sixth AIRAPT Conference. Vol 2. Applications and Mechanical Properties*, K. D. Timmerhaus and M. S. Barber, Eds. New York, NY: Plenum Press, New York, 1979, pp. 805–813.

[242] F. Homann, “Einfluß großer Zähigkeit bei Strömung um Zylinder,” *Forschung auf dem Gebiet des Ingenieurwesens A*, vol. 7, no. 1, pp. 1–10, 1936.

[243] I. A. Bataev, A. A. Bataev, E. A. Prikhodko, V. I. Mali, and M. A. Esikov, “Formation and structure of vortex zones in explosive welding of carbon steel,” *The Physics of Metals and Metallography*, vol. 113, no. 3, pp. 233–240, 2012.

[244] ASTM International, “E290 Bend Testing of Material for Ductility,” ASTM E290-14, 2014.

[245] B. Gulenc, “Investigation of interface properties and weldability of aluminum and copper plates by explosive welding method,” *Materials and Design*, vol. 29, no. 1, pp. 275–278, 2008.